UNIVERSITY OF CALIFORNIA,

IRVINE

# Lipogenesis is an ancestral mechanism used in mammalian cartilage morphogenesis

DISSERTATION

submitted in partial satisfaction of the requirements
for the degree of

DOCTOR OF PHILOSOPHY

in Biological Sciences

by

Raul Ramos M.S.

Dissertation Committee:
Professor Maksim V. Plikus, Chair
Professor Kavita Arora
Professor Peter J. Donovan
Professor Matthew A. Inlay
Professor Grant R. MacGregor

2019

## DEDICATION

Para Irene, quien me lo ha dado todo.

## Table of Contents


| | | Page |
|---|---|---|
| **List of Figures** | | v |
| **List of Tables** | | viii |
| **Acknowledgments** | | ix |
| **Curriculum Vitae** | | x |
| **Abstract of the Dissertation** | | xiii |
| **Chapter I:** | **Introduction and Background** | 1 |
| **Chapter II:** | **Lipochondrocytes are the main cellular component of multiple head and neck cartilages of the mouse** | |
| | Abstract | 15 |
| | Introduction | 16 |
| | Materials and Methods | 19 |
| | Results | 21 |
| | Figures | 25 |
| | Discussion | 34 |
| **Chapter III:** | **Lipochondrocytes possess unique lipidomic and transcriptomic profiles** | |
| | Abstract | 36 |
| | Introduction | 37 |
| | Materials and Methods | 42 |
| | Results | 50 |
| | Figures | 61 |
| | Discussion | 82 |
| **Chapter IV:** | **Lipochondrocytes rely on *de novo* lipogenesis and are insensitive to dietary lipid availability** | |
| | Abstract | 85 |
| | Introduction | 86 |
| | Materials and Methods | 88 |
| | Results | 92 |
| | Figures | 97 |
| | Discussion | 107 |

## Table of Contents


| | | Page |
|---|---|---|
| **Chapter V:** | **Lipochondrocytes are present in the ear cartilage of multiple mammalian orders** | |
| | Abstract | 109 |
| | Introduction | 110 |
| | Materials and Methods | 112 |
| | Results | 116 |
| | Figures | 118 |
| | Discussion | 123 |
| **Chapter VI:** | **Conclusion** | 125 |
| **References** | | 140 |
| **Addendum:** | **Signaling by senescent cells hyper-activates the skin stem cell niche** | 149 |

## List of Figures


| Title | Page |
|---|---|
| Figure 1.1: Portrait of Dr. Franz Leydig and examples of his artwork. | 12 |
| Figure 1.2: First recorded observations on lipid-containing ear cartilage by Dr. Franz Leydig. | 13 |
| Figure 2.1: Representation of mouse head and neck structures analyzed. | 25 |
| Figure 2.2: Cartilaginous elements of the mouse larynx at 1 month of age. | 26 |
| Figure 2.3: Cartilaginous elements of the mouse larynx contain lipochondrocytes. | 27 |
| Figure 2.4: The mouse nasal capsule contains neural crest-derived lipochondrocytes. | 28 |
| Figure 2.5: The mouse ear cartilage plate is comprised of lipochondrocyte and adipocyte populations. | 29 |
| Figure 2.6: Schematic drawing of microdissected ear cartilage. | 30 |
| Figure 2.7: Lipochondrocytes and fenestrae-bound adipocytes differ in size. | 31 |
| Figure 2.8: Lineage tracing and reporter assays reveal differences in embryonic origin and adipokine expression between lipochondrocytes and adipocytes in ear cartilage. | 32 |
| Figure 2.9: Clonogenic analysis of ear cartilage LCs in *Col2a1-CreER$^{T}$;R26R* mice. | 33 |
| Figure 3.0: Summary of the main steps in the adipogenic lineage specification program. | 61 |
| Figure 3.1: The lipidomic profile of ear cartilage is distinct from that of white adipose tissue. | 62 |
| Figure 3.2: Ear cartilage and adipose tissue are differentially enriched for distinct lipid classes. | 63 |
| Figure 3.3: Ear cartilage and adipose tissue show differences in molecular species abundance among different lipid classes. | 64 |
| Figure 3.4: Figure 3. The lipochondrocyte transcriptome is distinct from those of white adipocytes and rib chondrocytes. | 65 |

## List of Figures (Cont'd)


| Title | Page |
|---|---|
| Figure 3.5: Differential gene expression analysis and Gene Ontology shows further distinction between tissues, with an enrichment of cartilage-related terms in the adult lipochondrocyte transcriptome. | 66 |
| Figure 3.6: List of selected marker genes differentially upregulated in LCs, rib chondrocytes, or adipocytes. | 67 |
| Figure 3.7: Expression patterns of selected marker genes in one-month-old ear cartilage. | 68 |
| Figure 3.8: Transcriptome comparisons between lipochondrocytes and notochord cells. | 70 |
| Figure 3.9: Analysis of differentially expressed genes between lipochondrocytes and notochord cells. | 71 |
| Figure 3.10: Analysis of signature genes shared between lipochondrocytes and notochord cells. | 72 |
| Figure 3.11: Phases of ear pinna growth in mice. | 73 |
| Figure 3.12: Expression patterns of SOX9 and PCNA in the developing ear cartilage. | 74 |
| Figure 3.13: Staining of neutral lipids with Oil Red O shows temporal regulation of lipid accumulation. | 76 |
| Figure 3.14: Schematic illustration of the key stages in ear cartilage development. | 77 |
| Figure 3.15: Cell sorting strategy for isolating early lipochondrocytes. | 78 |
| Figure 3.16: Transcriptome analysis of developing LCs at five consecutive time points between P8 and 1 month reveal prominent time-dependent changes. | 79 |
| Figure 3.17: Transcriptome analysis of developing LCs at five consecutive time points between P8 and 1 month reveal prominent time-dependent changes. | 80 |
| Figure 3.18: Verification of relative expression dynamics of differentially expressed genes by qRT-PCR. | 81 |
| Figure 4.1: Schematic drawing of main steps in the *de novo* lipogenesis pathway. | 97 |

## List of Figures (Cont'd)


| Title | Page |
|---|---|
| Figure 4.2: Changes to dietary lipid availability do not alter ear morphology nor lipid droplet size. | 98 |
| Figure 4.3: Fluorescently-labeled fatty acids incorporate into adipocytes, but not LCs. | 99 |
| Figure 4.4: Comparison of FLIM signatures between ear adipocytes and ear lipochondrocytes. | 101 |
| Figure 4.5: SRS microscopy of cultured ear cartilage in the presence of glucose. | 102 |
| Figure 4.6: SRS microscopy detects lipids derived from deuterated glucose. | 103 |
| Figure 4.7: Application of *de novo* lipogenesis inhibitors to the ear leads to misshapen ears and reduced lipid content in ear cartilage. | 104 |
| Figure 4.8: Inducible deletion of *Acaca* in *Col2a1-CreER$^{T}$;Acaca$^{fl/fl}$* mice results in smaller, misshapen ears and smaller LC lipid vacuoles. | 105 |
| Figure 4.9: Gross epiphyseal plate anatomy in *de novo* lipogenesis mutant mice. | 106 |
| Figure 5.1: Partial cladogram of mammalia and representative examples of chiropteran facial diversity. | 118 |
| Figure 5.2: Lipid-laden lipochondrocytes are present in head and neck cartilages of jerboa. | 119 |
| Figure 5.3: Oil Red O-positive lipochondrocytes are present in multiple mammalian species. | 120 |
| Figure 5.4: Summary of the distribution of OilRedO$^{+}$ cartilage in the mammalian clade. | 121 |
| Figure 5.5: Presence of lipid-laden lipochondrocytes in the nasal cartilage of bats. | 122 |
| Figure 6.1: Cartoon of skeletal lineage specification steps. | 138 |
| Figure 6.2: Craniofacial morphological diversity among echolocating bats. | 139 |

## List of Tables


| Title | Page |
|---|---|
| Table 1.1: Summary of main milestones of lipochondrocyte development. | 14 |
| Table 2.1: Primer sequences used for genotyping. | 24 |
| Table 3.1: Primer sequences used in qRT-PCR experiments. | 43 |
| Table 3.2: Definition of lipid class terms used. | 44 |
| Table 6.1: List of mammalian species analyzed. | 115 |

## Acknowledgments

This work could not have been completed without the continued support of my colleagues, friends, and family. I would like to begin by thanking my advisor Max for taking me into his laboratory and encouraging independent scientific thought. Throughout my graduate career, Max has been instrumental with guidance and encouragement; I feel very grateful for crossing paths with him. I would also like to thank the members of my committee, Professors Kavita Arora, Grant MacGregor, Peter Donovan, and Matt Inlay, for their helpful suggestions, support, and patience throughout these years. I also owe a great deal to many of the current and former members of the Plikus Laboratory, for all their technical and intellectual support: Kim, Tom, Xiaojie, Ji Won, Chris, Kosuke, Yingzi, Andrew, Xiaoling, and Sean. I would also like to thank my good friend Nick for his constant support. I would finally like to extend my infinite gratitude to my parents Irene, Mario, Carlos, and Noemi, and to my siblings, Sergio, Emiliano, and Barbara. They may not understand what or why I do the things I do, but support me unconditionally regardless.

# Curriculum Vitae

## Raul Ramos

### EDUCATION

**University of California, Irvine CA**
**Ph.D.** in Biological Sciences with a focus on Developmental and Cell Biology **2012-2019**
**M.S.** in Biological Sciences **2015**

**San Diego State University, San Diego CA**
**B.S.** Biology with and Emphasis in Cell and Molecular Biology **2009-2012**

### AWARDS AND HONORS

**NIH-IMSD Graduate Award**, Univ. of California, Irvine **March 2018**
**Susan V. Bryant Award in Developmental Biology**, Univ. of California, Irvine **June 2017**
**Genesis Award for Best Oral Presentation**, Society for Developmental Biology **March 2017**
West Coast Regional Meeting, Yosemite National Park, CA
**Best Poster**, Society for Developmental Biology **March 2015**
West Coast Regional Meeting, Yosemite National Park, CA
**CIRM Pre-doctoral Fellowship**, Univ. of California, Irvine **Oct. 2014-Sept. 2016**
**MBRS-IMSD Summer Fellowship**, Univ. of California, Irvine **June 2012**

### RESEARCH EXPERIENCE

**Doctoral Research** **Jan. 2013-**
Department of Developmental and Cell Biology, University of California, Irvine
Research Advisor: Maksim Plikus, Ph.D.
**Undergraduate Research** **Aug. 2010-May 2012**
Department of Biology
Research Advisor: Sanford Bernstein, Ph.D.

### UNIVERSITY SERVICE

**Departmental Graduate Student Representative** **Oct. 2016-Oct. 2017**
Department of Developmental and Cell Biology, University of California, Irvine
**Intel Science and Engineering Fair, Judge** **Oct. 2013-2015**
University of California, Irvine

## PRESENTATIONS

**Ramos R,** Prince R, Potma O, Bradley J, Behringer R, Nie Q, Plikus MV (2019) Poster: Characterization of lipid-laden cartilages in mammals. EMBO|EMBL Symposium: The Identity and Evolution of Cell Types; Heidelberg, Germany.

**Ramos R,** Wang X, Peng T, Prince R, MacLean A, Pham KT, Potma E, Bradley J, Behringer R, Nie Q, Plikus MV (2017) Oral Presentation: A cellular and developmental characterization of auricular cartilage. Society for Developmental Biology, West Coast Regional Meeting; Yosemite National Park, CA.

**Ramos R,** Bradley J, Behringer R, Plikus MV (2016) Poster: A characterization of a novel cell type in the mammalian ear pinna. Gordon Research Conference: Craniofacial Morphogenesis and Regeneration; Ventura, CA

**Ramos R,** Bradley J, Behringer R, Plikus MV (2016) Oral Presentation: A characterization of a novel cell type in the mammalian ear pinna. Gordon Research Symposium: Craniofacial Morphogenesis and Regeneration; Ventura, CA

**Ramos R,** Plikus MV (2015). Poster: Rediscovering the lipochondrocyte: a characterization of the mouse external auricular cartilage. Society for Developmental Biology, West Coast Regional Meeting; Yosemite National Park, CA.

**Ramos R**, His TC , Oh JW , Guerrero-Juarez CF, Pham KT, Plikus MV (2014). Oral Presentation: Regulation of ear morphogenesis by macroenvironmental signals from hair follicles. Society for Investigative Dermatology Meeting; Albuquerque, NM.

## PUBLICATIONS

Wang Q, Oh JW, Lee HL, Dhar A, Peng T, **Ramos R**, Guerrero-Juarez CF, Wang X, Zhao R, Cao X, Le J, Fuentes MA, Jocoy SC, Rossi AR, Vu B, Pham K, Wang X, Mali NM, Park JM, Choi JH, Lee H, Legrand J, Kandyba E, Kim JC, Kim M, Foley J, Yu Z, Kobielak K, Andersen B, Khosrotehrani K, Nie Q, Plikus MV. (2017). *Elife* eLife.22772

Plikus MV, Guerrero-Juarez CF, Ito M, Li YR, Dedhia PH, Zheng Y, Shao M, Gay DL, **Ramos R**, Hsi TC, Oh JW, Wang X, Ramirez A, Konopelski SE, Elzein A, Wang A, Supapannachart RJ, Lee HL, Lim CH, Nace A, Guo A, Treffeisen E, Andl T, Ramirez RN, Murad R, Offermanns S, Metzger D, Chambon P, Widgerow AD, Tuan TL, Mortazavi A, Gupta RK, Hamilton BA, Millar SE, Seale P, Pear WS, Lazar MA, Cotsarelis G. (2017). *Science* 355, 748-752.

Chen CC, Wang L, Plikus MV, Jiang TX, Murray PJ, **Ramos R**, Guerrero-Juarez CF, Hughes MW, Lee OK, Shi S, Widelitz RB, Lander AD, Chuong CM. (2015). Organ-level quorum sensing directs regeneration in hair stem cell populations. *Cell* 161, 277-290.

Zhang LJ, Guerrero-Juarez CF, Hata T, Bapat SP, **Ramos R**, Plikus MV, Gallo RL (2015). Dermal adipocytes protect against invasive Staphylococcus aureus skin infection. *Science* 347, 67-71.

Guerrero-Juarez CF, **Ramos R**, Oh JW, Hsi TC, and Plikus MV (2014). Light-emitting hair follicles: studying skin regeneration with in vivo imaging. *J Invest Dermatol* 134, 1496-1498.

Melkani GC, Trujillo AS, **Ramos R,** Bodmer R, Bernstein SI, Ocorr K (2013). Huntington's disease induced cardiac amyloidosis is reversed by modulating protein folding and oxidative stress pathways in the *Drosophila* heart. *PLoS Genet.* 9(12), e1004024.

Oh JW, His TC, Guerrero-Juarez CF, **Ramos R**, and Plikus MV (2013). Organotypic skin culture. *J Invest Dermatol* 133, e14.

**Ramos R**, Guerrero-Juarez CF, and Plikus MV (2013). Hair follicle signaling networks: a dermal papilla-centric approach. *J Invest Dermatol* 133, 2306-2308.

Plikus MV, Vollmers C, de la Cruz D, Chaix A, **Ramos R**, Panda S, Chuong CM (2013). Local circadian clock gates cell cycle progression of transient amplifying cells during regenerative hair cycling. *Proc Natl Acad Sci USA* 110, E2106-2115.

**Abstract of the Dissertation**

Lipogenesis is an ancestral mechanism used in mammalian cartilage morphogenesis

By

Raul Ramos M.S.

Doctor of Philosophy in Biological Sciences

University of California, Irvine, 2019

Professor Maksim V. Plikus, Chair

Cartilages are a diverse group of tissues that form an essential component of the skeletal system. Cartilage-forming cells, *aka* chondrocytes, form cartilage by secreting a diverse array of structural molecules into the extracellular matrix (ECM), including multiple collagens and proteoglycans, conferring the tissue with shock-absorbing and/or elastic properties. In addition to its impact-buffering role in the axial and appendicular skeleton, cartilage plays an important part in the development and proper function of the skull, and many key regulators of chondrocyte specification and development in the head have been found. Conversely, the biology of many adult secondary or accessory cartilages such as those of the external ear or nasal capsule is still understudied. In this work, we show that, in mice, multiple head and neck cartilages, including neural crest-derived ear, nasal, thyroid, and epiglottic cartilages are composed of lipid-laden cartilage cells called lipochondrocytes. Initially identified by famed anatomist Franz von Leydig in the 1850s, lipochondrocytes were the subject of a series of studies in the 1960s and 1970s only to fall back into obscurity, and are still undescribed in modern studies.

Morphologically, lipochondrocytes resemble white adipocytes, but have distinct lipidomic and transcriptomic profiles. Importantly, lipochondrocytes lack many key components of lipid uptake and mobilization pathways, including many fatty acid transporters and lipolytic enzymes. Unlike adipocytes, the lipid droplets in ear lipochondrocytes are insensitive to metabolic stressors, namely obesity and caloric restriction. In ear cartilage, lipid droplet synthesis primarily depends on *de novo* lipogenesis, and its pharmacological or genetic inhibition disrupts proper cartilage formation, leading to mice having smaller and misshapen ears.

Further, we observed lipochondrocytes in several facial cartilages of multiple mammalian species, including in bats, primates, carnivores and even marsupials suggesting that a lipochondrocyte-like cell could have existed in the common ancestor of all extant therians. In this thesis, I bring the lipochondrocyte back into view using modern methods in molecular biology, and open new research avenues in the fields of cellular, developmental, and evolutionary biology.

# Chapter I
# Introduction and Background

Cartilaginous tissues form an essential component of the skeletal system of vertebrates by playing important mechanical and patterning roles (Kaucka and Adameyko, 2017). Structurally similar, cartilage-like tissues also exist in the species of multiple invertebrate groups, including annelids, cephalopods, and arthropods (Cole and Hall, 2004). A recent study revealed homologies in the gene regulatory network of vertebrate and invertebrate chondrogenesis, suggesting an ancient origin for cartilage (Tarazona et al., 2016). In vertebrates, chondrocytes are the differentiated cells that form cartilage. By secreting large quantities of extracellular matrix (ECM) proteins, chondrocytes become encased within *lacunae*, either individually or in groups (Hall, 2015).

Depending on the quantity and the content of their ECM, cartilages are classified as hyaline, fibrous or elastic. Hyaline cartilage, prevalent throughout the skeletal system, contains abundant ECM rich in glycosaminoglycans (Chung et al., 2013). The ECM of fibrous cartilage, found in menisci and musculoskeletal joints, has a dense network of collagenous fibers (Benjamin and Evans, 1990), while that of elastic cartilage, found in the ear, larynx, and epiglottis, contains large amounts of elastin (Montes, 1996). In hyaline cartilages, like those of the growth plate of long bones, chondrocytes commonly undergo hypertrophy, when their cytoplasmic volume prominently expands and multiple organelles increase in size and number (Buckwalter et al., 1986). Chondrocyte hypertrophy is the result of an intricate process of differentiation regulated by multiple molecular pathways, including an Indian hedgehog/parathyroid hormone-related peptide (Ihh/Pthrp) signaling loop, fibroblast growth factor (Fgf), bone morphogenetic protein (BMP), and WNT signaling that

will be covered with more detail further on in this chapter. Together with ECM secretion, chondrocyte hypertrophy contributes to cartilaginous bone growth and shaping (Cooper et al., 2013). The chondrocyte hypertrophic program is also accompanied by distinct signaling that induces chondrocyte apoptosis, ECM degradation, vascular invasion, and osteogenesis, resulting in ossification of cartilaginous bone templates (Gerber et al., 1999). Technological advances of the molecular era of biology have allowed us to better understand some aspects of cartilage development, patterning, and regeneration, but the tissue has a research history that spans millennia.

In the following pages I will provide some background on known important aspects of cartilage biology, from its impact-buffering properties to its role as a patterning unit. In this chapter I will also introduce the *Lipochondrocyte*, an obscure cartilage cell with a lipid droplet so large it resembles white adipose tissue, and for the rest of my dissertation I will provide evidence of its extensive prevalence throughout the mouse skull; an analysis of its neutral lipid content compared to white adipose tissue; an analysis of the adult lipochondrocyte transcriptome compared to *bona fide* white adipose tissue and hyaline cartilage; and evidence for their reliance on the *de novo* lipogenesis pathway to exploit lipogenesis as a tissue patterning mechanism. Lastly, our histological analysis of mammalian ear cartilage show that lipogenesis is an ancestral mechanism of morphological patterning in mammals.

*A Brief History of khondros*

One of the earliest descriptions of cartilage dates back to the 4$^{th}$ century BCE, in Aristotle's groundbreaking treatise *Parts of Animals,* an account on the fauna of the

Mediterranean island of Lesbos (Peck, 1961). Aristotle said that cartilage (Greek: χόνδρος *khondros*) could be "found where it is an advantage that the solid framework should be pliable and glutinous for the benefit of the flesh that surrounds them. This applies to the ears and the nostrils. Such projecting parts quickly get broken if they are brittle. Cartilage and bone are the same in kind and differ only by 'the more and less'" (Peck, 1961). In *History of Animals*, Aristotle makes further mention of cartilage, this time as a way to make a distinction between fishes (bony *vs* cartilage skeletons), noting despite their physical differences, both cartilage and bone served an analogous purpose (Cresswell, 1897).

Roughly 400 years later, In 175 CE, an expanded view on cartilage appeared in the medical texts of the Greek physician and philosopher Aelius Galenus (Galen). He described the shield-like anatomy of the cartilage of the larynx, and coined it with the name θυρεοειδής (*thyreoeidis*), or thyroid, a term we use until this date (Lidell, 1940). Galen further wrote "[cartilages] are spread on some parts of [the bones], such as the joints, to make them smooth, and Nature also uses cartilages occasionally as moderately yielding bodies" (Benedek, 2006). Although other texts of the era offer accounts on cartilage, these mostly reflect Galen's own descriptions; slow advances in technology impeded any further exhaustive empirical studies of the tissue and Galen's paradigm would dominate Western medicine for centuries (Benedek, 2006). It would not be until the first half of the 19$^{th}$ century that sufficient technological and scientific progress allowed for a more detailed examination of cartilage, and important distinctions between different cartilage tissues would become more clearly defined.

In *Lehrbuch der Histologie des Menschen und der Thiere*, the eminent German anatomist Franz von Leydig (Figure 1.1A) makes exhaustive and visionary illustrations on

cytology and the histology of several tissue types, including cartilage (Leydig, 1854, 1857). Despite his lack of speculation, Leydig took special care to highlight the morphological diversity of many connective tissues. For instance, he documented the tissue architecture of the notochord of the bichir (Polypterus), a lungfish endemic to Africa, and found that the tissue contained minimal matrix content and that its cells were vacuolated (Figure 1.1B). Leydig contrasted this architectural strategy with that of his very own fibrous cartilage, which displayed a matrix-rich organization with low cellular content (Figure 1.1C) (Leydig, 1857).

During his analyses of rat ear cartilage, Leydig made an observation that, to our knowledge, had so far gone undocumented. He showed that the cells of the cartilage plate (*aka* chondrocytes) contained lipid droplets so large that they resembled cells of the adipose tissue (Figures 1.2A-B, shaded circles inside the cells represent "drops of fat"). Leydig did not speculate much on the function or purpose of these lipid-laden tissues either, and left multiple questions open for further exploration. Despite this, it would take more than 100 years for Leydig's original observations on cartilage to be recognized.

*Developmental origins of cartilage*

For the last few decades, developmental biology has benefitted from an exponential growth in technological advances, and many questions related to cartilage development have been clarified. For instance, we know that in terms of embryonic origin, cartilages in the mammalian axial and appendicular (limb) skeleton develop from paraxial and lateral plate mesoderm (Umeda et al., 2012) respectively, while those of the frontal head (Bronner

and LeDouarin, 2012; Chai et al., 2000) and the neck (Matsuoka et al., 2005; Tabler et al., 2017) derive from cranial neural crest mesenchyme.

In the head, mesoderm and neural crest derived cartilages converge to form a composite cranium (McBratney-Owen et al., 2008) and while their relative contribution to head cartilages is largely conserved between major vertebrate classes, switches in cellular sources for some cranial structures are known (Piekarski et al., 2014).

*Cartilage in the Molecular Era of Biology*

The advent of molecular cloning has allowed us to gain a better understanding of the transcriptional regulators of chondrogenesis. Formation of diverse cartilages is regulated by a shared transcriptional and signaling program, with *Sox9* serving as the cartilage lineage master-regulator (Bi et al., 1999; Healy et al., 1999), induced early during chondrogenic fate specification by Sonic Hedgehog (Zeng et al., 2002). *Sox5* and *Sox6* expression is induced downstream of *Sox9,* and they work redundantly and cooperatively to regulate early chondrogenesis (Smits et al., 2001). The Hedgehog (Abzhanov and Tabin, 2004; St-Jacques et al., 1999; Zeng et al., 2002) and canonical WNT pathways (Akiyama et al., 2002; Day et al., 2005; Hill et al., 2005) serve as principal activating and inhibitory regulators of chondrogenesis respectively. In addition, signaling by BMP (Murtaugh et al., 1999; Yoon et al., 2005), TGFβ (Oka et al., 2008), FGF (Kumar and Lassar, 2014; Murakami et al., 2000) and Dlk1 (Wang and Sul, 2009) are essential for promoting early chondrogenesis.

Chondrocytes arise from multipotent skeletogenic stem cells, either from the neural crest or from paraxial and lateral plate sources. These stem cell progenitors can form

chondrocytes of the growth plate as well as articular chondrocytes. A significant portion of our understanding of cartilage as a patterning unit comes from the study of growth plate chondrocytes of the long bones. Also known as the epiphyseal plate, the growth plate is a hyaline structure at the tips of multiple long bones such as the femur and tibia that controls bone growth and shaping (Abad et al., 2002). The growth plate harbors a population of chondrocytes at multiple stages of differentiation. At its most distal, chondrocytes form a population of progenitor cells in the 'Resting Zone.' Moving proximally, these progenitors exit quiescence and undergo oriented proliferative expansion in what is known as the 'Proliferative Zone'. In this zone, progenitors form a distinct architectural unit resembling a longitudinal "stack of coins", a morphogenetic phenomenon that controls skeletal growth and shaping (Dodds, 1930; Kaucka and Adameyko, 2017). After several rounds of division, proliferative chondrocytes undergo cell cycle arrest and begin to enlarge, becoming pre-hypertrophic chondrocytes. Pre-hypertrophic chondrocytes continue to expand —a process known as hypertrophy, as they enter the 'Hypertrophic Zone', and deposit a specialized cartilage matrix scaffold for future osteogenesis (Hunziker et al., 1999; Mueller et al., 2010). As stated earlier, a complex network of signaling mechanisms maintain the architecture of the growth plate. The role of BMP signaling in skeletal development is well-established, and many ligands and receptors of the pathway are expressed by all chondrocyte populations in the growth plate as well as in cells of the perichondrium — a tissue that physically envelops many cartilage elements. Although the specific skeletogenic role of each ligand and receptor in the pathway is still a matter of investigation, it is known that BMP signaling is required for the expression and maintenance of the chondrocyte master regulator Sox9 (Pan et al., 2008). In mouse embryos, chondrocyte-specific deletion

of *Bmp2* using *Col2a1-Cre;ER*$^{T2}$ leads to architectural disorganization of the growth plate, as well as defects in chondrocyte proliferation, differentiation, and apoptosis (Shu et al., 2011). Similar to BMP2, the product of *Bmp4* has also been shown to promote chondrocyte lineage specification as well as chondrocyte proliferation and hypertrophy *in vitro* (Kramer et al., 2000). Further deletion of *Bmp4* in *Col2a1-Cre;*ER$^{T2}$;*Bmp2*$^{flox/flox}$;*Bmp4*$^{flox/flox}$ double-mutant embryos exacerbates the phenotypes seen in *Bmp2* mutants alone. Interestingly, cartilage-specific deletion of *Bmp4* only leads to a much milder skeletal phenotype when compared to *Bmp2* mutants, indicating that Bmp4 has a minor role in cartilage development and that its activity complements that of Bmp2 (Kramer et al., 2000).

In the resting zone, expression of Pthrp (encoded by *Pthlh*) maintains transit-amplifying cell proliferation and prevents hypertrophy of chondrocytes in the proliferative zone (Vortkamp et al., 1996). Chondrocytes further away from the Pthrp signal exit the cell cycle and undergo hypertrophy. Importantly, these hypertrophic chondrocytes express *Ihh*, encoding for Ihh, and signal through perichondral cell intermediates to promote the expression of *Pthlh* in resting zone chondrocytes in order to maintain their proliferative state (Mizuhashi et al., 2018; Vortkamp et al., 1996). As proliferative chondrocytes enter the hypertrophic zone, multiple factors including transforming growth factor-β (Tgf-β) family members and Fgf ligands promote their hypertrophy; with the transcription factors runt-related transcription factor 2 (Runx2) and myocyte enhancer factor-2 (Mef2) as key regulators of the program (Arnold et al., 2007; Takeda et al., 2001). The hypertophic program is further characterized by marked production of collagen type X (encoded by *Col10a1*) and collagenase 3 (encoded by *Mmp13*), which remodel the cartilage matrix and

prepare it for osteoblast invasion and calcification (D'Angelo et al., 2000).The mature cartilage matrix is a collagenous network that is comprised by a combination of type II and type IX collagens, encoded by *Col2a1* and *Col9a1/2/3* respectively. Collagen type X is produced in abundance by pre-hypertrophic and hypertrophic chondrocytes. Other connective tissues, including bone, also have significant collagen content in their matrix. However, they contrast the cartilage matrix by being built on a network of collagen types I, III, and V (Lefebvre and Smits, 2005).

In contrast with the transient nature of growth plate chondrocytes, articular chondrocytes form the permanent or "non-ossifying" cartilages seen in the bone joints (Koyama et al., 2008). As opposed to their growth plate counterparts, articular chondrocytes have low cellular turnover rates, and favor instead turnover at the protein level in the ECM (Ortega-Martinez et al., 2013). An important distinction in articular chondrocytes is the lack of activation of a hypertrophic program, which prevents their ossification. Interestingly, upon abnormal or diseased conditions, articular chondrocytes can acquire growth plate chondrocyte characteristics including hypertrophy, as seen in models of osteoarthritis (Decker et al., 2015). However, it is still unclear how growth plate and articular chondrocyte progenitors make their cell fate decisions.

The notochord is another distinct cartilage-like structure of interest in the endoskeleton of chordates. Molecular evidence shows commonalities between cartilage and notochord progenitors (Linsenmayer et al., 1986). It forms early during embryogenesis and serves as a signaling center for surrounding tissue elements along the dorso-ventral

and left-right body axes (Hemmati-Brivanlou et al., 1990; Pourquie et al., 1993; Yamada et al., 1991). It also serves a structural function, persisting throughout adulthood in lancelets, lampreys and at least some ray-finned fishes, while becoming limited after embryogenesis in mammals to the nucleus pulposus of the intervertebral discs (Stemple, 2005). Significantly, the mechanical properties of the notochord are attributed to its large inner vacuolated cells. Pushing against the outer notochord sheath, vacuolated cells generate a hydrostatically pressurized flexible structure that serves as an analogous skeleton (Adams et al., 1990; Ellis et al., 2013).

*Cartilage diversity is under- represented in modern biology*

Although some aspects of chondrogenesis in the growth plate and articular cartilage are well understood, other important aspects behind the maturation of secondary cartilages— like those of the nose, ears, and larynx, remain obscure. The advent of electron microscopy facilitated the study of cartilage ultra-structure, opening a door to a new phase of cartilage research (Little et al., 1958). In the 1970s, a series of electron microscopy studies by Svajger, Reith, and others confirmed Leydig's original claim of lipid-laden ear cartilage (Bradamante et al., 1991; Kostovic-Knezevic et al., 1981; Sanzone and Reith, 1976; Svajger, 1970). Sanzone and Reith (1976), in particular, made important observations on the development of the mouse ear pinna. They organized developmental milestones of the ear into five main "stages" (Table 1.1):

In Stage I, chondroblasts (*aka* cartilage progenitors) condense into a plate and begin to deposit cartilage matrix. This is followed by Stage II, the major mitotic stage, where high, uniform proliferative activity is found across the plate. In Stage III, some cells are still proliferating, but there are now differentiated chondrocytes in the plate as evidenced by

matrix deposition. Interestingly, small intracellular lipid droplets begin to appear in some of these cells. By Stage IV, chondrocytes have deposited more matrix and lipid droplets are now enlarged. Lastly, Stage V echoes the observations that Leydig originally made more than a hundred years prior, with most of the chondrocytes containing a lipid droplet so large they strikingly resemble white adipocytes. Considering the lipid-laden nature of these cartilage cells, the authors coined them with the name *lipochondrocytes* (Sanzone and Reith, 1976).

Despite the relevance of these findings, lipochondrocytes remain obscure and largely unrecognized in modern scientific literature. This presents a unique opportunity to answer many important questions regarding the the cell type, for instance: are lipochondrocytes present in other cartilages? What is the transcriptional program regulating their specification? How do adult lipochondrocytes manage their lipid stores? Are they confined to rodents or are they also found in other vertebrates?

In Chapter II of this dissertation, I show evidence for the presence of multiple cartilages in the mouse head and neck, namely the epiglottis, thyroid, nasal, and ear cartilages, that mainly consist of lipochondrocytes (LCs). I also show that despite their striking physical similarities, LCs and *bona* fide adipocytes differ in developmental origin and cell type-specific reporter expression. In Chapter III, I use high throughput strategies to analyze the lipidomic and transcriptomic profiles of ear LCs. I show that the LC lipidome is distinct from that of WAT, mainly reduced in triglyceride content. In contrast, other lipid classes, including the signaling lipids fatty acid esters of hydroxy fatty acids (FAHFAs) and free fatty acids are over-represented in the LC lipidome. Additionally, I also show that LCs favor the accumulation of lipids with saturated carbon chains, the main product of

endogenous lipid production, as opposed to the mono- or polyunsaturated lipids more abundant in WAT. Transcriptomic analysis of adult and developing LCs shows that they share expression of many genes encoding important chondrogenic regulators, including *Sox5/6/8/9* as well as other genes encoding for structural proteins typical of cartilage cells, including *Col2a1, Col9a1/2, Acan,* and *Chad*. Interestingly, LCs show expression of important adipogenic factors such as *Cebpa, Srebf1,* and *Pparg.* Of note, I also show that LCs do not produce many fatty acid translocases important for lipid scavenging in adipocytes, yet maintain expression of several genes encoding for important enzymes of the *de novo* lipogenesis pathway. These results hinted at a lipid storage strategy employed by LCs distinct from that of WAT. Indeed, in Chapter IV, I show a series of functional experiments including dietary modifications and pulse-chase assays to demonstrate that LCs primarily rely on *de novo* lipogenesis, and are unable to mobilize stored lipids upon systemic metabolic stress. Disrupting *de novo* lipogenesis, either through molecular inhibitors or genetic deletion, interferes with LC maturation and alters adult ear shape and size in mice. Lastly, in Chapter V I profile the facial cartilages of multiple mammalian species, including multiple marsupial species, and show that LCs are not confined to rodents but rather prevalent across the mammalian clade. Here, I demonstrate that lipid vacuolation provides a novel paradigm in cartilage biology, and identifies *de novo* lipogenesis as an ancestral mechanism used in the control of craniofacial cartilage morphogenesis.

**Figures**

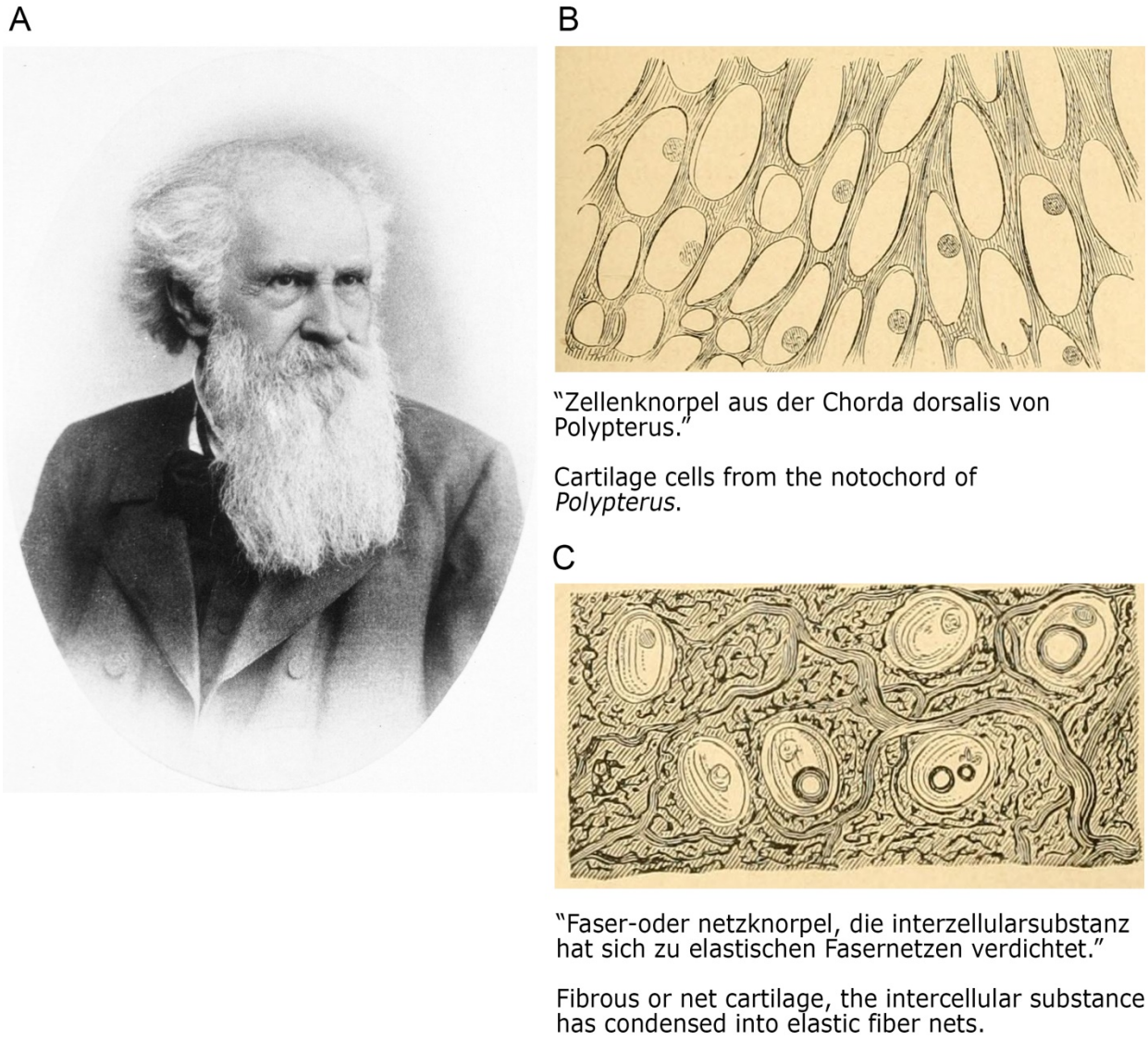


**Figure 1.1: Portrait of Dr. Franz Leydig and examples of his artwork.** (A) Dr. Franz Leydig (1821-1908), eminent zoologist and comparative anatomist. The portrait in was first published in 1908 by J.F. Lehmann; this work is in the public domain. (B-C) Illustrations from his book *Lehrbuch der Histologie des Menschen und der Tiere* (1857). Panels (B) and (C) were modified from (Leydig, 1857); not in copyright.

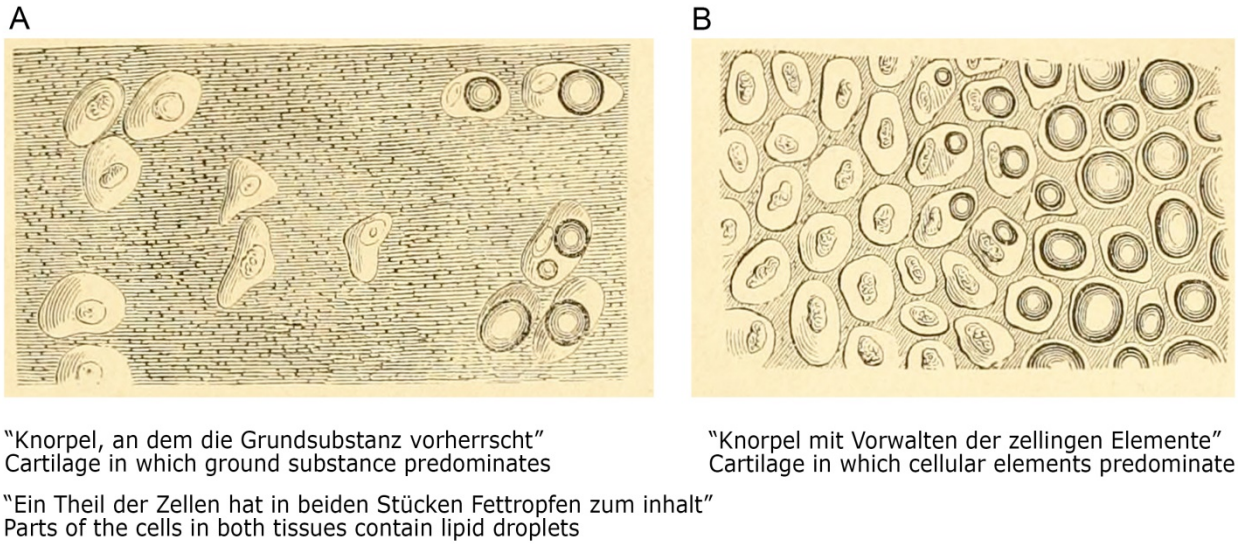


**Figure 1.2: First recorded observations on lipid-containing ear cartilage by Dr. Franz Leydig.** (A-B) Representative drawings of mouse cartilages with low cellularity and high ECM content (A) and high cellularity but low ECM content (B). Leydig noted that some cartilage cells contain large lipid droplets, represented as shaded circles. Modified from (Leydig, 1857); not in copyright.

| STAGE | PD | SUMMARY |
|---|---|---|
| I | P0-P5 | Mesenchymal condensation, production of extracellular matrix (ECM). |
| II | P6~P9 | High, uniform proliferation by chondrocyte progenitors across the plate. |
| III | P10~P12 | Some cells resemble adult chondrocytes and cease to proliferate, but proliferation is still evident in other cells of the plate. Very small lipid droplets are now apparent in many cells. |
| IV | P13~P21 | ECM production continues and is accompanied by enlargement of the intracellular lipid droplets. |
| V | P30 | Most of the intracellular space is occupied by a large lipid droplet. Cells resemble white adipose tissue. These lipid-laden chondrocytes are now termed *lipochondrocytes.* |

**Table 1.1: Summary of main milestones of lipochondrocyte development.** Stages and Summary were adapted from Sanzone and Reith (1976).

## Chapter II
## Lipochondrocytes are the main cellular component of multiple head and neck cartilages of the mouse


### Abstract

The morphogenesis of many elements of the skull, including cartilage, is well documented across multiple model organisms, and is the subject of ongoing research. In contrast, the biology of many adult tissues in the head, including their maintenance and regenerative potential, remains largely under-investigated. Here, I show that many cartilage elements of the adult mouse skull are formed by lipochondrocytes (LCs), a distinct cartilage cell type that possesses a large unilocular lipid droplet and deposits low amounts of extracellular matrix. First described by Franz Leydig in 1854, LCs strikingly resemble adipocytes. In the past five decades, only a handful of studies have explored structural aspects of the ear cartilage plate, and little is known about many cellular aspects of adult LC biology. I show that LCs are the main component of several cartilage structures in the adult mouse skull, ear, nose, larynx. Lineage tracing shows that LCs are derived from the neural crest and that despite their high similarity to adipocytes, LCs are a distinct cell lineage. In the ear, LCs form a sheet, or plate, that is one-to-three cells in thickness with little ECM. The ear is fenestrated and occupied by *bona fide* adipocytes. LCs express *Col2a1*, the main cartilage collagen. In contrast with adipocytes, LCs do not express adipokines. Lastly, mature LCs in the ear plate have low cellular turnover rates, similar to what has been observed in other cartilages.

## Introduction

The development of the head is a complex process that involves multiple signaling mechanisms operating in a three-dimensional space. Studies using a variety of vertebrate model systems have shown that a significant portion of the head is derived from the neural crest, a pluripotent, highly-migratory population of cells that originates at the border between neural- and non-neural ectoderm. Neural crest cells are capable of forming nerves, ganglia, and connective tissues, including cartilage. In mice, most fate mapping studies rely on mouse transgenesis and the *Cre-loxP* system, which utilizes expression of Cre-recombinase to genetically enable the expression of a reporter allele, permanently labeling cells and their progeny. For instance, the *Wnt1-Cre* mouse line has been used to map the cell lineage of the external ear to neural crest cell progenitors of the second pharyngeal arch (Minoux et al., 2013). Further, the *Sox10-Cre* mouse line has been used to show the neural crest origin of many connective tissue elements of the neck, including adipose and laryngeal cartilages (Billon et al., 2007; Matsuoka et al., 2005). However, evidence of ectopic canonical WNT pathway activity and aberrant *Cre* expression in *Wnt1-Cre* and *Sox10-Cre* mice, respectively, calls for more reliable transgenics (Debbache et al., 2018; Lewis et al., 2013b). *Wnt1-Cre2* mice have recently been shown to be useful in fate mapping studies of the neural crest as well, and offer the advantage that they don't show the aberrant phenotypes seen in *Sox10-Cre* and *Wnt1-Cre* lines (Debbache et al., 2018; Lewis et al., 2013b; Tabler et al., 2017). Despite the widespread availability of these transgenic tools, studies have focused on embryonic, immature structures, and the biology of these adult tissues remains largely undescribed.

Previously, studies from the Plikus laboratory showed that the cartilage/muscle complex of the ear may influence skin appendages such as hair follicles via macroenvironmental signaling (Wang et al., 2017). Upon histology, Wang et al. (2017) show that adult ear cartilage cells display large "lipid ghost" artifacts, typically seen in white adipose tissue but not in other healthy tissue types. This intriguing observation prompted us to look for literature on the cell type. First observed in the external ear of the rat, the eminent anatomist Franz Leydig originally described lipid-laden cartilage in the 1850s as "closely resembling adipose tissue" (Leydig, 1854, 1857). More than a hundred years later, electron microscopy studies confirmed the fatty nature of the cartilage of the ear (Sanzone and Reith, 1976; Svajger, 1970). In these, the authors documented the accumulation of intracellular lipids in the mouse and rat external ear, and coined their cells with the name *Lipochondrocytes*. Despite Franz Leydig's original observation of lipid-laden cartilage and the structural studies that followed it more than a century later, little is known about their prevalence throughout the adult mouse head; to the point that recent publications have inadvertently identified them as skin adipocytes (Egawa et al., 2013).

Previous studies have shown that the nasal and larynx cartilages in the mouse head rely on BMP and Hh signaling mechanisms for early embryogenesis, as expected in cartilage tissues (Hayano et al. 2015; Kaucka et al. 2018; Tabler et al. 2017), but it is currently unknown whether these elements contain lipochondrocytes in adult stages. In this chapter, I use a variety of histological methods in combination with mouse lineage tracing lines to probe into the biology of many adult head and neck cartilages. I show that cartilage elements of the larynx, namely those of the epiglottis, thyroid and arytenoid

cartilages, as well as the cartilage in the nasal capsule and ear pinna are comprised of lipid-laden lipochondrocytes.

In the ear pinna, lipochondrocytes form a thin two-to-three cell-diameter thin sheet that is naturally fenestrated, with each fenestrae occupied by *bona fide* lipid-laden adipocytes. Despite their initial resemblance, lipochondrocytes and adipocytes show distinct characteristics. For example, lipochondrocytes are uniform in size across the plate compared to fenestrae-bound adipocytes, which show a wider size distribution. Considering these observations, I wondered if the physical similarities between LCs and adipocytes extended to other aspects of their biology, including their developmental origin and lifespan. In neural crest specific *Wnt1-Cre2* reporter mice, lipochondrocytes but not fenestrae adipocytes show reporter activity, indicating that the two have distinct developmental origins. Similarly, cartilage-specific, tamoxifen-inducible *Col2a1-CreER$^T$;R26R* reporter mice show activity in plate lipochondrocytes, but not in adipocytes. This pattern is mirrored in adipocyte-restricted *Retn-LacZ* or *Adipoq-Cre;R26R* reporter mice, which show reporter activity only in fenestrae-bound cells but not in cells of the plate, indicating distinct regulation of adipokine expression by LCs. Lastly, I use a low-induction tamoxifen treatment in *Col2a1-CreER$^T$;R26R* animals to track the fate of distinct lipochondrocyte clones, and show that ear cartilage has little cellular turnover.

## Materials and Methods

| REAGENT or RESOURCE | SOURCE | IDENTIFIER |
|---|---|---|
| Chemicals, Peptides, and Recombinant Proteins | | |
| BODIPY 493/503 | ThermoFisher | D3922 |
| Oil Red O | AMRES CO | 0684-100G |
| Tamoxifen | Sigma-Aldrich | T5648 |
| Experimental Models: Organisms/Strains | | |
| Mouse: *Wnt1-Cre2* | The Jackson Laboratory | JAX: 022137 |
| Mouse: *mT/mG (aka ROSA$^{mTmG}$)* | The Jackson Laboratory | JAX: 007576 |
| Mouse: *R26R* | The Jackson Laboratory | JAX: 003474 |
| Mouse: *Col2a1-CreER$^{I}$* | The Jackson Laboratory | JAX: 006774 |
| Mouse: *Retn-lacZ (aka Retn$^{tm1Laz}$)* | (Banerjee et al., 2004) | |
| Mouse: *Adipoq-Cre* | The Jackson Laboratory | JAX: 010803 |
| Oligonucleotides | | |
| PCR primers. See Table S9 | | |
| Software and Algorithms | | |
| Fiji | (Schindelin et al., 2012) | https://imagej.net/Fiji |

For this chapter, I performed all sections, dissections, stainings, imaging and mouse work. Cell size and clone quantifications were performed in collaboration with Tom Burns B.S..

***Experimental mouse models.*** All mouse experiments were performed in accordance with UC Irvine's Institutional Animal Care and Use Committee (IACUC) guidelines. *Wnt1-Cre2* (Lewis et al., 2013b), *mT/mG* (Muzumdar et al., 2007), *R26R* (Soriano, 1999b), *tdTomato* (Madisen et al., 2010), *Col2a1-CreER$^{T}$* (Nakamura et al., 2006), *Retn-lacZ* (Banerjee et al., 2004), and *Adipoq-Cre* (Eguchi et al., 2011) were used. In *Col2a1-CreER$^{T}$;R26R* mice, tamoxifen in corn oil was injected IP for four consecutive days starting at P7 at a dose of 75 mg/kg for full induction. For low-dose tamoxifen induction, a single dose of tamoxifen in corn oil at 7.5 mg/kg was injected IP at P7.

***Histochemistry, immunostaining, and imaging.*** For LacZ staining, tissues were fixed in 4% PFA for 30 minutes at room temperature and rinsed 3 times in PBS. Samples were

incubated in LacZ buffer at 37 °C for 5 minutes, then transferred to LacZ buffer with X-Gal (VWR) and incubated at 37 °C until signal developed. For Oil Red O staining, tissues were fixed in 4% PFA for 8 hrs at 4 °C and rinsed 3 times in PBS. Specimens were submerged in 60% isopropanol for 1 min followed by 6.25 mg/ml Oil Red O in isopropanol for 30 min. Tissues were rinsed in 60% isopropanol and imaged in 1X PBS. For BODIPY staining, tissues were incubated in 200 μmolar BODIPY 493/503 (Thermo Fisher) in 1X PBS for 30 min before imaging. Tissue sections were obtained by dissecting and thoroughly rinsing tissues followed by embedding in OCT compound and freezing at <-20° C. Sections were cut at a thickness of 12 μm.

***Measurements.*** Cell area and cell counts were performed using the Fiji app, using the Measure tool and the Cell-Counter plug-in, respectively.

## Results

I analyzed multiple cartilages for the presence of lipid laden chondrocytes in mice of 1 month of age (1 mo) (Figure 2.1). Previous cell fate studies have established the embryonic origin of many cranial cartilages in mice (McBratney-Owen et al., 2008) (Piekarski et al., 2014; Tabler et al., 2017). To determine the embryonic origin of lipochondrocytes, I used the *Wnt1-Cre2;ROSA*$^{mT/mG}$ mouse line (hereafter *Wnt1-Cre2;mT/mG*), in which pre-migratory neural crest cells and their progeny are labeled by membrane-bound GFP, and cells outside the lineage by membrane-bound tdTomato (Lewis et al., 2013a; Muzumdar et al., 2007).

The *Wnt1-Cre2;mT/mG* larynx is a complex structure composed of cartilaginous elements of mixed embryonic origin, consisting, from anterior to posterior, of neural crest-derived epiglottic cartilage, composite thyroid cartilage, and non-neural crest cricoid and arytenoid cartilages (n=5) (Figure 2.2A). Hematoxylin and eosin (H&E) staining of the cartilage elements of the larynx shows that its cells contain distinct "lipid ghost" artifacts, voids left behind by lipid droplets after histological processing (Figure 2.3B-C). Indeed, upon Oil Red O staining, epiglottic cartilage, the neural crest portion of thyroid cartilage (Figure 2.3A-C) and arytenoid cartilage (Figure 2.3D-G) have many unilocular lipid-laden cells (n=3). On average, lipid vacuoles are larger in the epiglottic compared to thyroid cartilage, and in the latter they decrease in size toward the posterior end, eventually leading to a non-neural crest-derived region devoid of lipid droplets (Figure 2.3C).

In *Wnt1-Cre2;mT/mG* mice, frozen tissue sections of the nasal capsule show GFP-positive chondrocytes, confirming their neural crest origin (n=5) (Figure 2.4A). Upon

staining with the neutral lipid dye Oil Red O, it is apparent that the tissue is composed of lipochondrocytes (n=3) (Figures 2.4B-C).

In the ear, dissected cartilage stains strongly with Oil Red O (n=8) (Figure 2.5A). In many places, the ear cartilage plate is naturally fenestrated, with more fenestrations in the lateral compared to the medial side (Figure 2.5B-C, 2.6). Individual fenestrae are commonly occupied by clusters of lipid-filled cells that are, on average, 175±7% larger than adjacent plate cells (Figure 2.7A-B). To address the embryonic origin of lipochondrocytes in ear cartilage, I used the *Wnt1-Cre2;R26R* mouse reporter line, in which *lacZ* is expressed upon Cre activity in pre-migratory neural crest cells and their progeny, (n=4) (Lewis et al., 2013b; Soriano, 1999a). I observe lacZ activity in lipochondrocytes of the cartilage plate, but not in the cells inside the fenestrations (Figure 2.8A).

To test whether lipochondrocytes express *bona fide* cartilage genes, I used the cartilage-specific *Col2a1-CreER$^{T}$;R26R* mice (n=3), in which Cre recombinase activity depends upon tamoxifen induction (Chen et al., 2007). Mice were injected at postnatal day 5 (P5) intraperitoneally (IP) for 3 days with tamoxifen to induce full Cre activity. Similar to our *Wnt1-Cre2;R26R* results, lipochondrocytes of the plate, but not fenestrae-bound cells are lacZ-positive (Figure 2.8B). In contrast, in the adipocyte-specific nuclear reporter *Retn-lacZ* (n=4) (Figure 2.8C) and *Adipoq-Cre;R26R* mice (n=6) (Figure 2.8D) only the cells inside the fenestrae, but not those of the plate, label with lacZ (Banerjee et al., 2004; Eguchi et al., 2011).

Cartilage has been established as a tissue with low cellular turnover, instead favoring a turnover of its ECM components (Ortega-Martinez et al., 2013; Umlauf et al.,

2010). I investigated if lipochondrocytes, like other mature chondrocytes, are also long-lived cells. To do so, I designed a pulse-chase experiment in which I used a low dose tamoxifen treatment of *Col2a1-CreER$^{T}$;R26R* mice at P6. This permitted labeling of individual cartilage progenitors, allowing for discretely labeled lipochondrocyte clones to be evaluated in adult ears at different ages. I studied lipochondrocyte clone sizes 3 weeks (n=1,253 clones) (Figure 2.9A-B) and 23 weeks after labeling (n=423 clones) (Figure 2.9C) and found no significant reductions in clone size (Figure 2.9D).

| Target | Forward Primer | Reverse Primer | Mutant Primer |
|---|---|---|---|
| *Cre* | GGTGTCCAATTTACTGACCGTACA | CGGATCCGCCGCATAACCAGTG | |
| *Rosa-Lacz* | AAAGTCGCTCTGAGTTGTTAT | GGAGCGGGAGAAATGGATATG | GCGAAGAGTTTGTCCTCAACC |
| *Retn-Lacz* | TGTCGGTCAGTTGAGAACTGA | ACTGTGCAACAATTCCCACAC | |
| *Acaca-fl* | CTTTCCAATTCAAGGTTCTGAC | TACAAACGCAAGAGTCATACTGG | |

**Table 2.1: Primer sequences used for genotyping**

## Figures

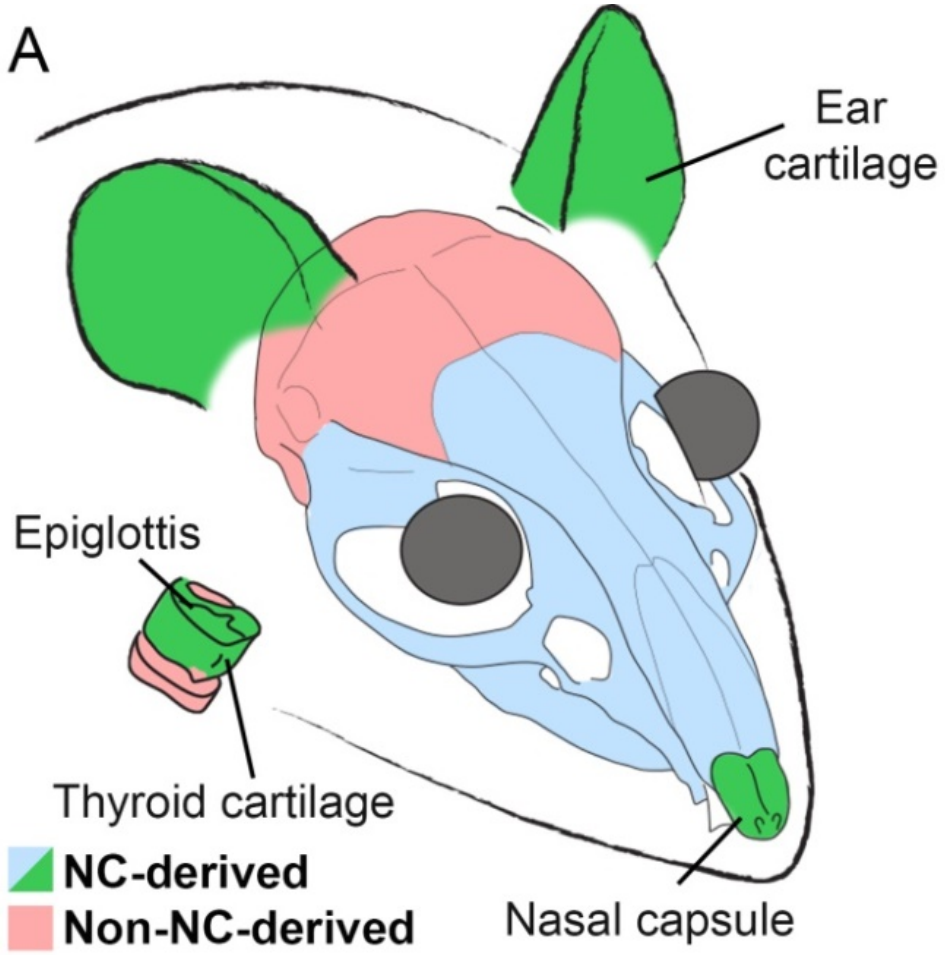


**Figure 2.1: Representation of mouse head and neck structures analyzed.** (A) Cartoon of a mouse head and neck; neural crest derived elements are color coded blue/green, non-neural crest-derived elements are highlighted in pink. The cartilages analyzed in this work are highlighted in green.

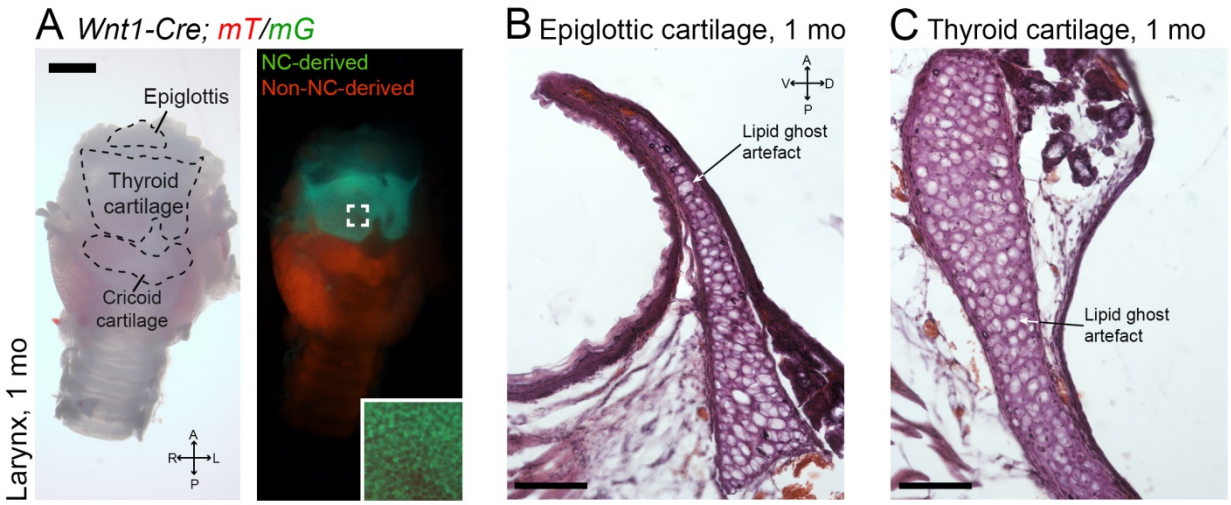


**Figure 2.2: Cartilaginous elements of the mouse larynx at 1 month of age.** (A) Whole-mount, dissected larynx of a Wnt1-Cre2;mTmG mouse at one month of age with cartilage elements annotated (left panel). Neural crest-derived tissues are GFP-positive, while non-neural crest-derived elements are tdTomato-positive (right panel). (B-C) H&E staining of epiglottic and thyroid cartilage sections. Both elements contain large, empty vacuole artifacts known as "lipid ghosts", common in adipose tissues. Scale bars: B,C – 100 µm; A – 1 mm.

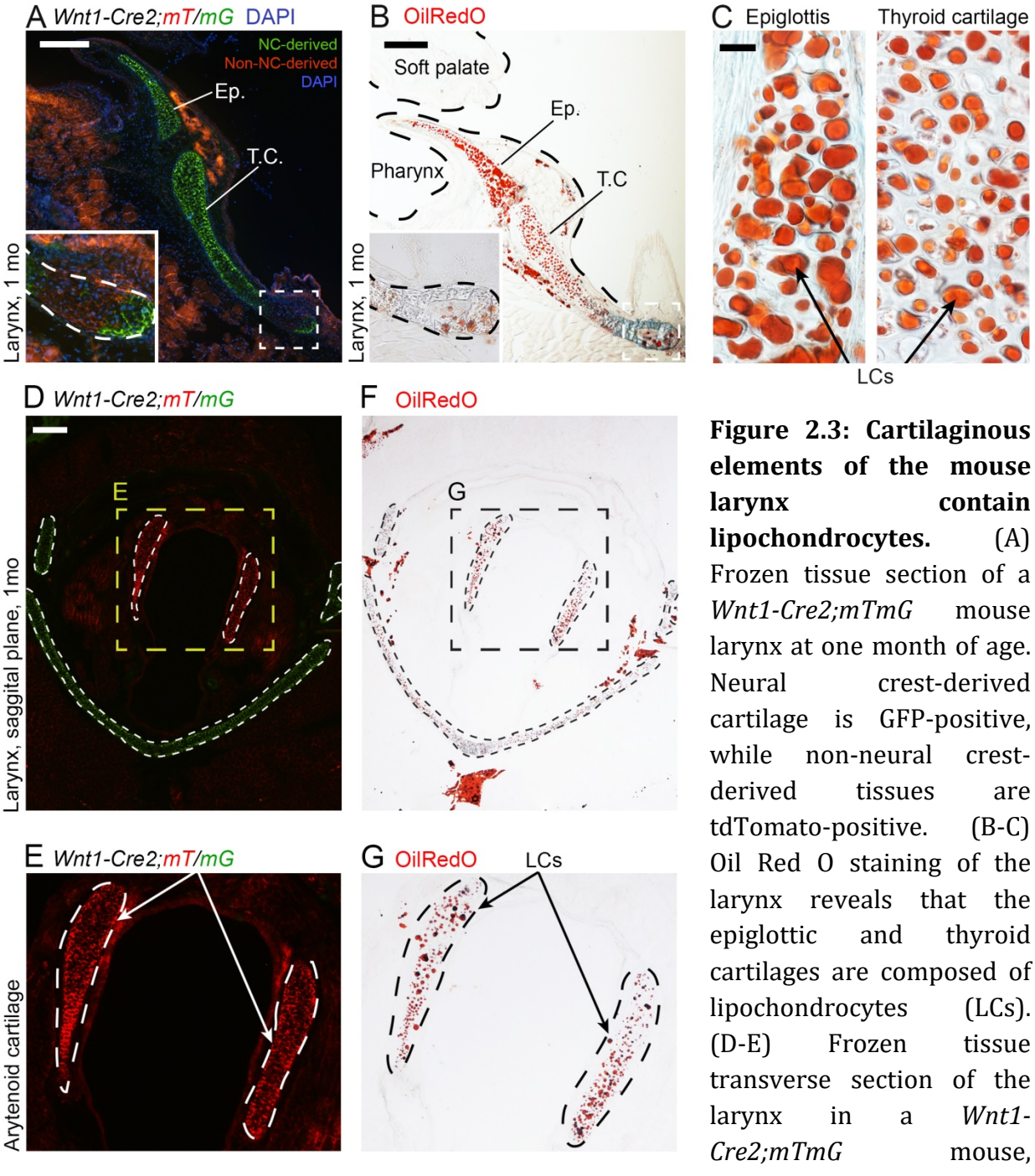


**Figure 2.3: Cartilaginous elements of the mouse larynx contain lipochondrocytes.** (A) Frozen tissue section of a *Wnt1-Cre2;mTmG* mouse larynx at one month of age. Neural crest-derived cartilage is GFP-positive, while non-neural crest-derived tissues are tdTomato-positive. (B-C) Oil Red O staining of the larynx reveals that the epiglottic and thyroid cartilages are composed of lipochondrocytes (LCs). (D-E) Frozen tissue transverse section of the larynx in a *Wnt1-Cre2;mTmG* mouse, showing the arytenoid originates outside the neural crest. Size bars: C – 25 µm; A – 200 µm; B – 250 µm; D – 500 µm.

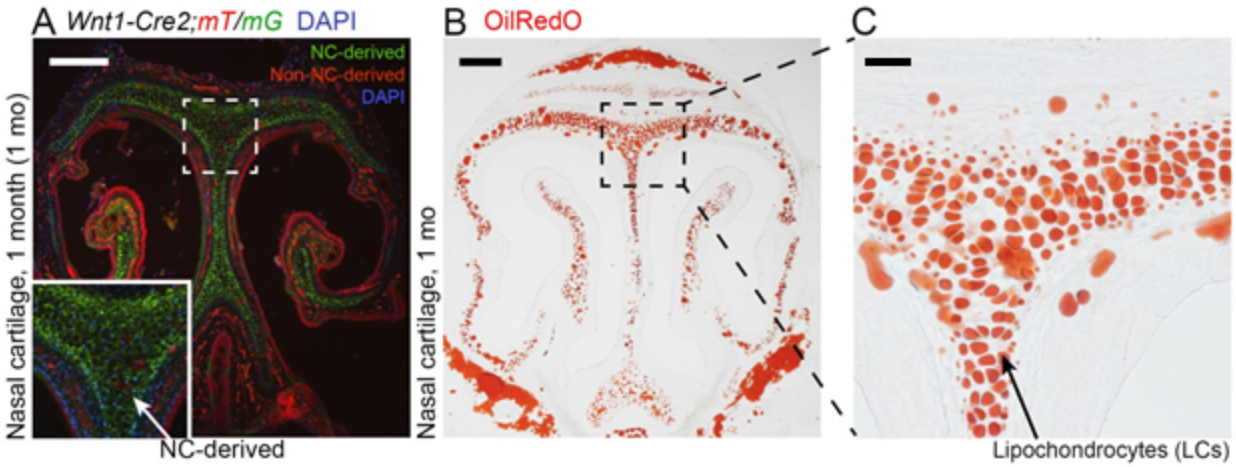


**Figure 2.4: The mouse nasal capsule contains neural crest-derived lipochondrocytes.** (A) Frozen tissue section of a Wnt1-Cre2;mTmG mouse nasal capsule at one month of age. Neural crest-derived cartilage is GFP-positive, while non-neural crest-derived tissues are tdTomato-positive. (B-C) Oil Red O staining of the nasal capsule reveals that the majority of the cartilaginous element is composed of tightly-packed lipochondrocytes (LCs). Scale bars: C – 50 μm A, B – 200 μm. Scale bar needed for 'C'

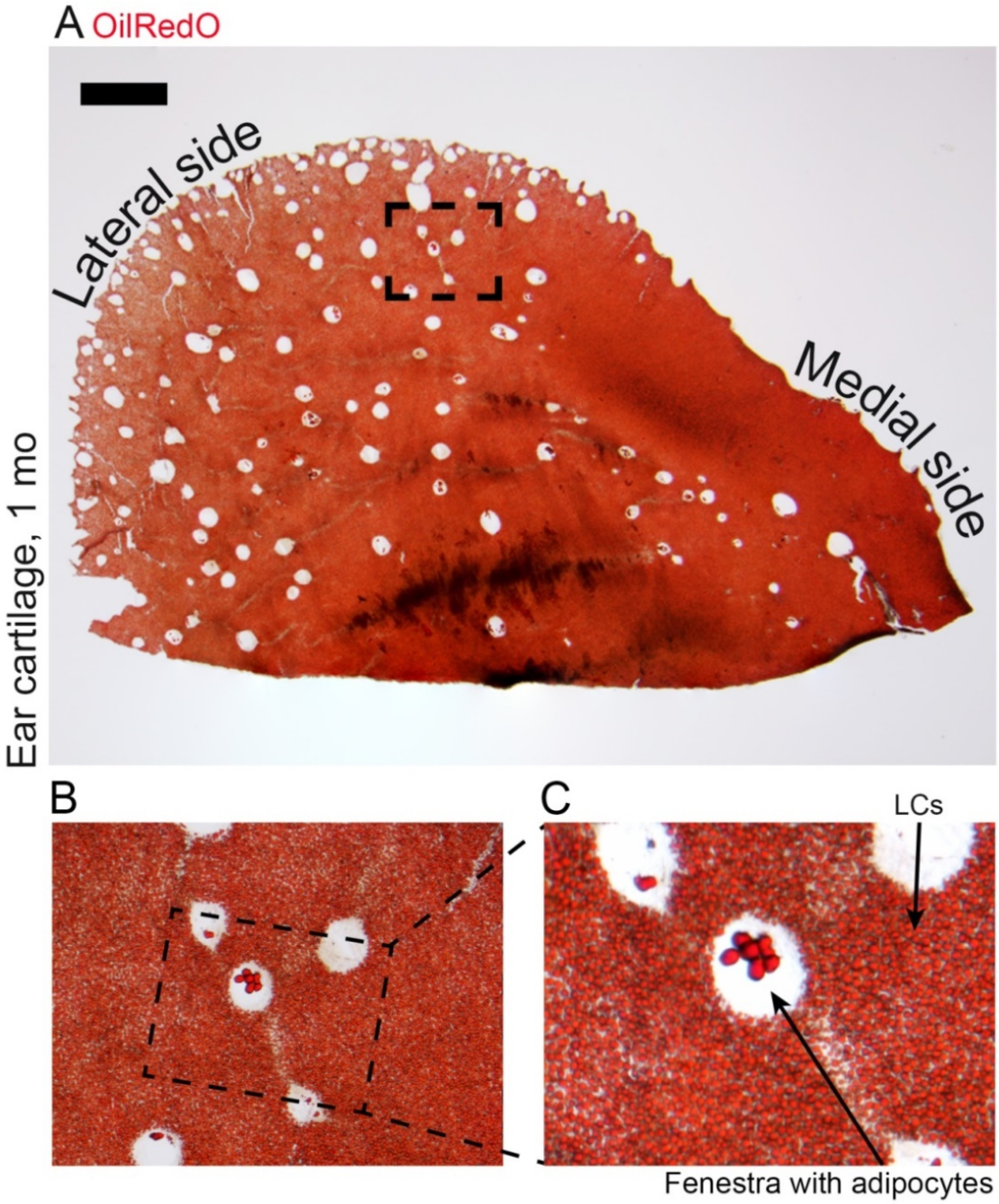


**Figure 2.5: The mouse ear cartilage plate is comprised of lipochondrocyte and adipocyte populations.** (A) Whole-mount OilRedO staining (n=8) shows that ear cartilage in 1-month-old mice consists of LCs, organized into a nearly two-dimensional plate that is two-to-three cell layers thick. (B) In many places ear cartilage is fenestrated, with more fenestrae on the lateral than the medial side. (C) Fenestrae are commonly occupied by small clusters of lipid-filled unilocular adipocytes. Scale bar: 1mm.

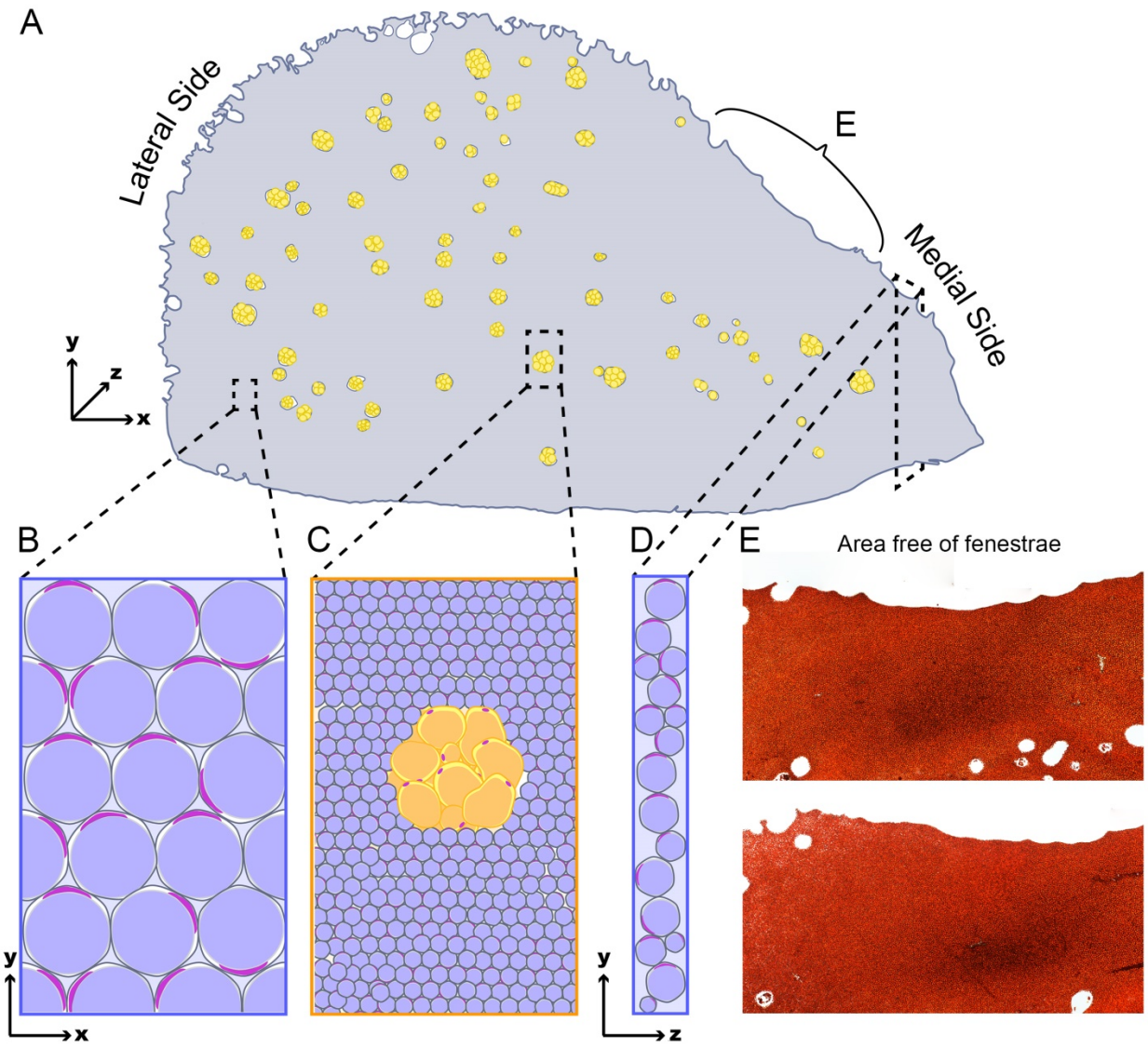


**Figure 2.6: Schematic drawing of microdissected ear cartilage. (A-D)** Ear cartilage in mice has the appearance of a fenestrated sheet, consisting of tightly packed lipochondrocytes (blue cells on **B, C, D**). White adipocytes (yellow cells on **A, C**) are located within cartilage fenestrae. **(E)** Along its medial side, the cartilage plate contains an area that is consistently free from fenestrations; this area was microdissected and used in lipidomic and RNA-sequencing studies to avoid sample contamination from adipocytes. Two OilRedO-stained whole mount examples area **(E)** are shown.

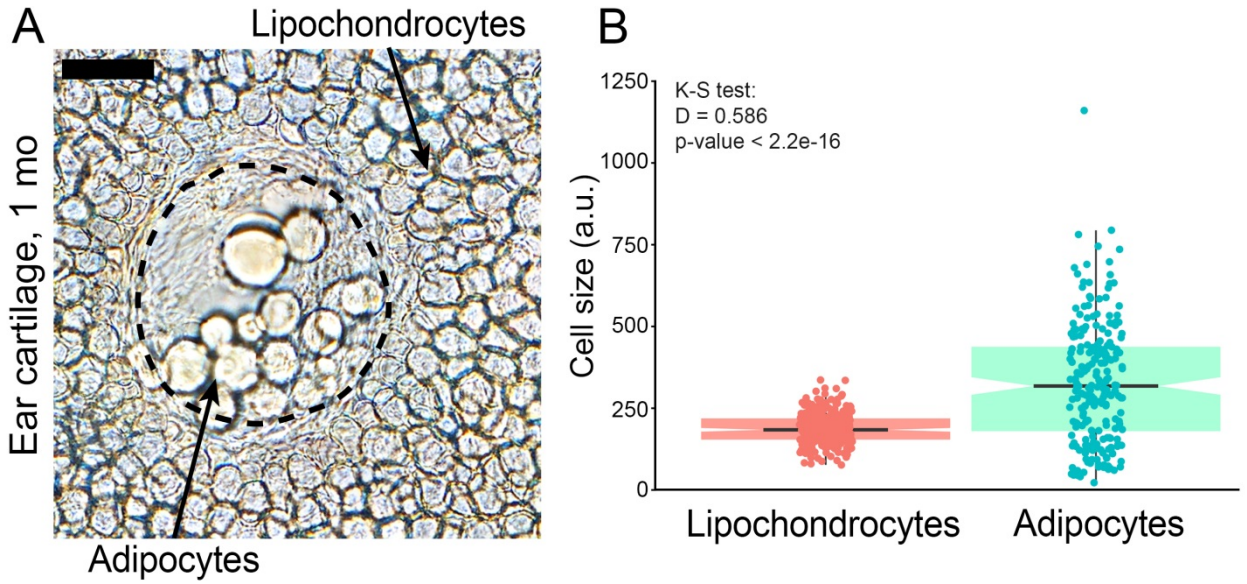


**Figure 2.7: Lipochondrocytes and fenestrae-bound adipocytes differ in size. (A)** Lipochondrocytes and adjacent adipocytes within ear cartilage fenestrae have similar morphologies in one-month-old mice. **(B)** Despite their similar appearance, the distribution of lipochondrocyte size is consistently uniform throughout the ear cartilage plate (red) compared to the broadly varying size distribution of adipocytes in ear fenestrae (teal). Two-sample Kolmogorov-Smirnov test: D= 0.586, p-value $<2.2*10^{-16}$. Size bar: A – 50 μm.

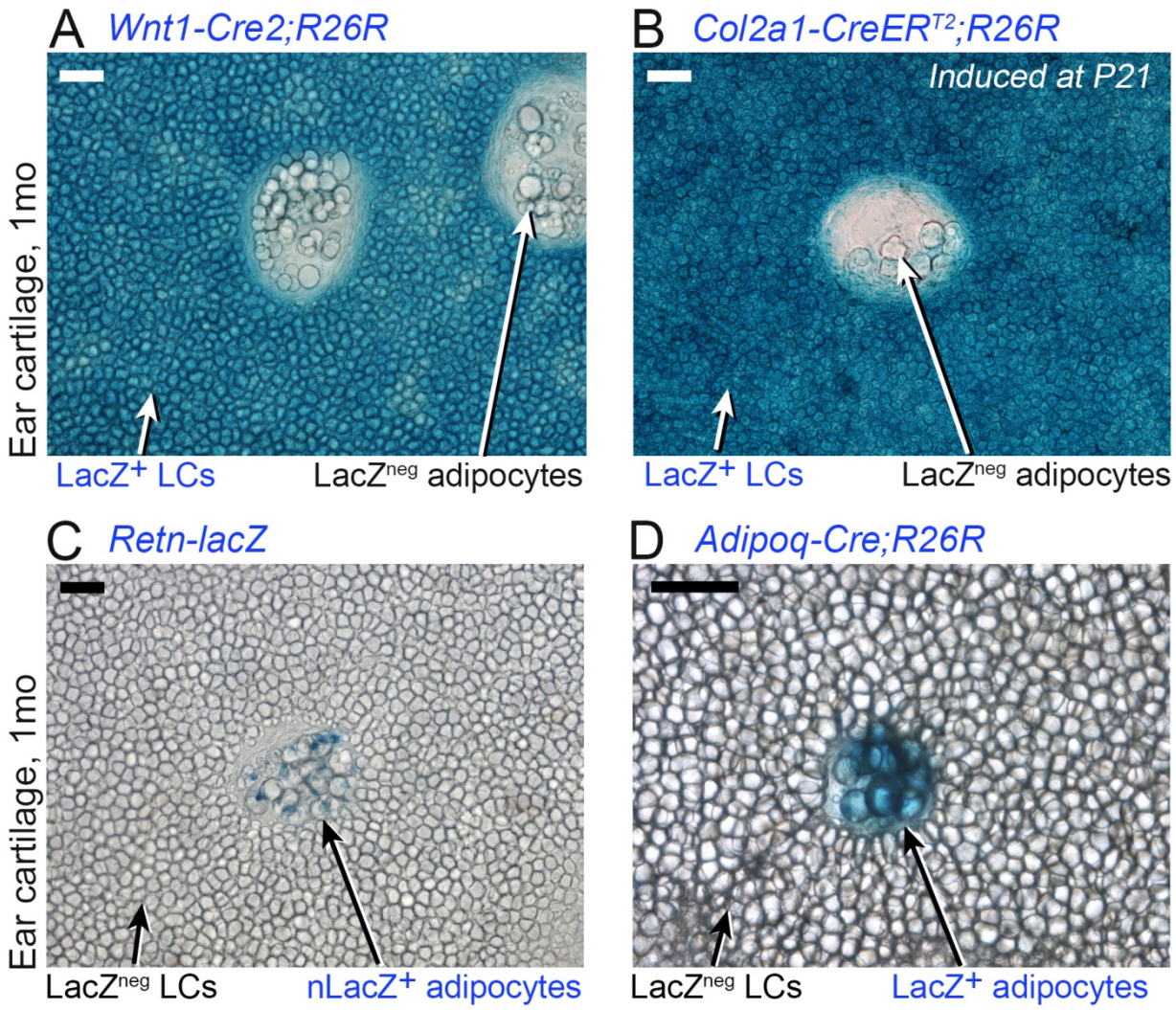


**Figure 2.8: Lineage tracing and reporter assays reveal differences in embryonic origin and adipokine expression between lipochondrocytes and adipocytes in ear cartilage.** (A-B) Lineage tracing in 1-month-old mice shows that ear LCs, but not fenestra adipocytes, label lacZ-positive with the neural crest-specific *Wnt1-Cre2* driver (n=4) (A) and cartilage-specific *Col2a1-CreER$^{T}$* driver (n=3) after tamoxifen induction at P21 (B). (C-D) On lacZ staining of ear cartilage, only fenestra adipocytes label positive in *Retn-lacZ* reporter mice (n=4) (C) and in *Adipoq-Cre;R26R* mice (n=6) (D). Scale bars: A-D – 100 µm.

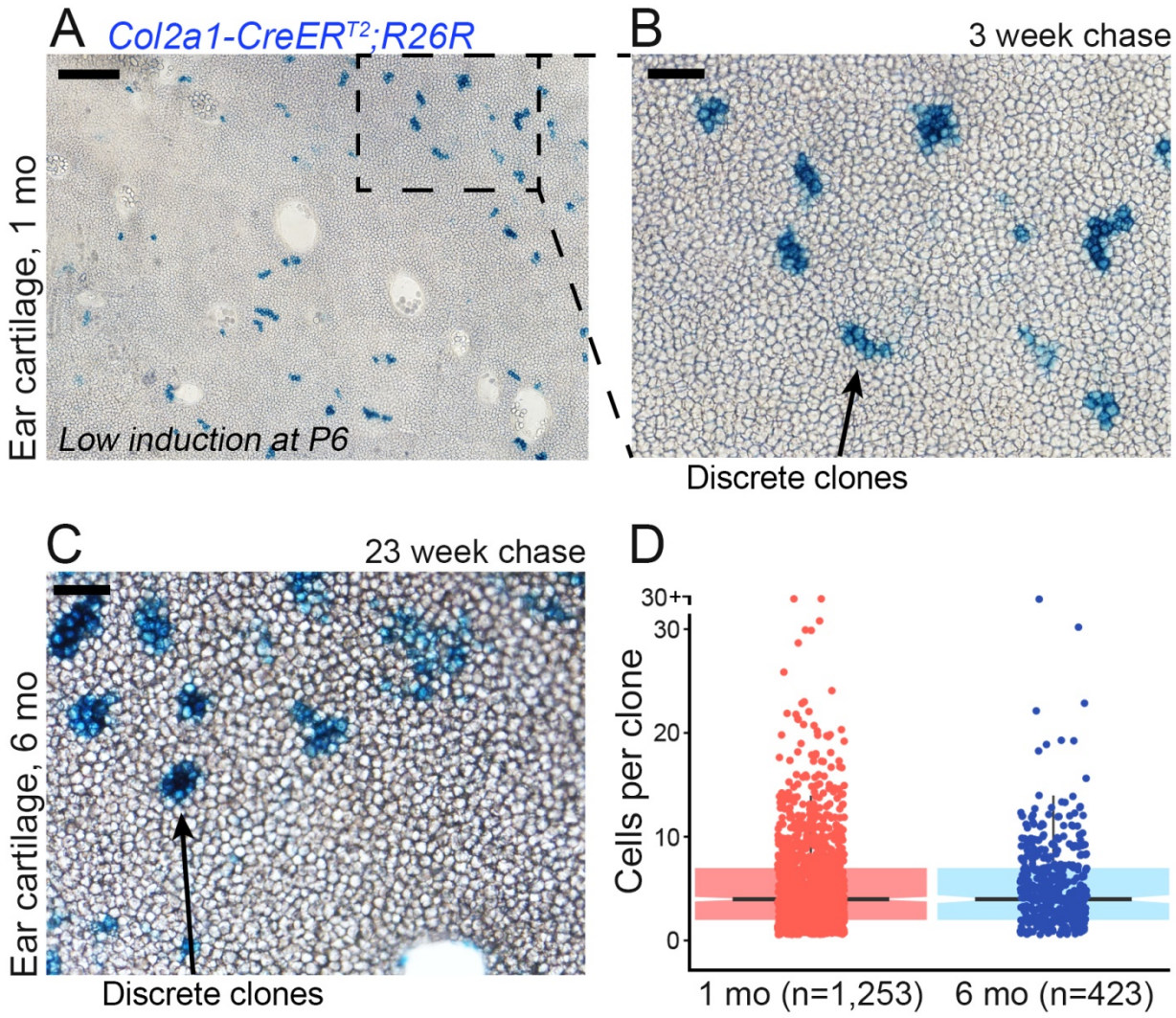


**Figure 2.9: Clonogenic analysis of ear cartilage LCs in *Col2a1-CreER$^{T}$;R26R* mice.** (A-C) Ear cartilage LacZ staining patterns after low tamoxifen induction at P6, followed by a 3- (A, B) or 23-week chase. Average size of lacZ-labeled LC clones does not change significantly between 1 month (B) and 6 months of age (C). Panel (D) shows size distribution of lacZ-labeled LC clones at both time points. Scale bars: A – 500 μm; B,C – 100 μm.

## Discussion

In this chapter, I show that multiple adult cartilages of the head and neck, including those of the nose and external ear, are formed by neural crest-derived lipochondrocytes (LCs): lipid-filled cartilage cells that deposit a thin extracellular matrix (ECM) and have a low cellular turnover. The head is one of the most complex parts of the vertebrate body. Primary cartilages of the skull have been extensively studied across a spectrum of taxa, including mice. In contrast, adult secondary cartilages like those of the nose and ears of mammals remain largely understudied. Recent studies have begun to look into the development of the primordia of several of these cartilages (Hayano et al., 2015; Heude et al., 2018; Kaucka et al., 2018; Tabler et al., 2017), but many aspects of the biology of these adult tissues remain unknown. Using a combination of histological methods and transgenic reporter mice, I show that multiple adult accessory cartilages of the skull, namely the ears, nasal capsule, and several cartilage elements of the larynx are comprised of (LCs). Additionally, LC-based cartilages display little extracellular matrix (ECM) content, which contrasts with the typical histology of hyaline and fibrous cartilages: ECM-rich structures sparsely populated by chondrocytes (Hall, 2015). This architectural strategy may be favored by these tissues in order to maximize flexibility without compromising rigidity, as seen in the similarly vacuolated notochord (Stemple, 2005), a tissue that will be further discussed in Chapters III and VI.

In terms of embryonic origin, LCs can be derived from neural crest and non-neural crest mesenchymal progenitors in *Wnt1-Cre2;mTmG* mice (Figures 2.3A-G, 2.4A-C) (Tabler et al., 2017). In contrast to our observations, Matsuoka et al. (2005) show that, in *Sox10-Cre* mice the entire anterior larynx, down to the cricoid cartilage, originates from neural crest.

Further, ear adipocytes of *Wnt1-Cre2* mice do not trace back to neural crest in my experiments, whereas *Sox10-Cre* mice, in which post-migratory neural crest cells are labeled, have been used to establish the adipogenic potential of the neural crest (Billon et al., 2007). It is possible that all of the anterior elements of the larynx as well as adipose depots of the head map to a neural crest progenitor, but that lower recombination frequencies in *Wnt1-Cre2 vs Sox10-Cre* mouse lines confound our results. Carefully staged lineage tracing experiments will be needed to establish that. If so, this would mean that LCs are found only in neural crest-derived cartilage, and that LCs could have evolved as a novelty in the neural crest-derived skeleton. Studies have shown that despite their potential for evolutionary diversification, the skeletal program of neural-crest derived cells evolved via co-option of the more ancient vertebrate cartilage program *SoxE*, which includes the genes *Sox8, Sox9,* and *Sox10* (Jandzik et al., 2015). However, this basal program may have been used as a template for novel mechanisms of morphogenesis, including lipid accumulation as seen in LCs.

These initial observations have prompted us to ask a number of questions regarding the biology of LCs: What is the role of lipids in these cells? What is the transcriptional program controlling LC differentiation? Are LCs confined to rodents, or are they prevalent in other taxa? To answer these questions, a combination of high throughput and functional experiments across various tissues and species will be necessary.

# Chapter III
# Lipochondrocytes possess unique lipidomic and transcriptomic profiles


## Abstract

Previous anatomic analyses of the mouse head revealed many cartilages comprised of adipocyte-like cells termed lipochondrocytes (LCs). Despite their similar fatty appearance, lineage tracing and reporter mouse lines have shown intrinsic differences between LCs and white adipose tissue, namely in embryonic origins and adipokine expression. High-throughput methods have proven very useful in the identification of molecules and gene expression patterns across a variety of tissues and organisms. To better understand the differences between LCs and *bona fide* adipocyte and cartilage cells, I performed a series of high-throughput experiments, including lipidomics by mass spectrometry, and RNA-sequencing at multiple developmental time points. Our lipidomic studies show that the lipid content of adult LCs is significantly different to that of adipocytes, namely tissue-specific differences in triglycerides (TAG), diacylglycerols (DAG), free fatty acids (FFA), and fatty acid hydroxyl-fatty acids (FAHFA) exist, suggesting differences in lipid droplet biogenesis, utilization, or both. RNA-seq analysis reveals LCs are largely distinct from adipocytes and rib chondrocytes across multiple gene ontology categories, including extracellular matrix, transcription factors, signaling pathways and lipid metabolism genes. Compared to adipocytes, LCs show downregulation of multiple key genes involved in lipid uptake and mobilization, and yet maintain expression of a core set of genes involved in the *de novo* lipogenesis pathway also present during postnatal development, which may be necessary to maintain tissue homeostasis and maintain the LC phenotype.

## Introduction

Adipose tissues play a variety of roles that range from core regulators of energetics to non-metabolic roles (Guerrero-Juarez and Plikus, 2018). At its most simple, adipose tissue can be described as a connective tissue comprised in great part by adipocytes, which store lipids from a variety of dietary and endogenous sources. Mammals have a variety of adipose tissue types that each have distinct histological properties and functional roles.

*White Adipose Tissue*:

WAT is the main energy-storing tissue in mammals, and has important physiological roles. WAT adipocytes store energy as lipids —either endogenously-produced via *de novo* lipogenesis or absorbed from circulation— as unilocular lipid droplets, or mobilize them in response to energy demands. As such, WAT is capable of significant expansion, by means of hyperplasia and hypertrophy. In the former, pre-adipocyte progenitors differentiate to become mature, metabolically-responsive adipocytes, thus increasing adult cell numbers in the tissue. WAT hypertrophy involves the physical expansion of adult adipocytes by enhanced lipid storage. In mammals, multiple WAT depots exist distributed throughout the body, and show significant distinctions between them at multiple levels, including metabolic sensitivity, developmental origin, and response to hormonal stimuli (Montague et al., 1998; Palou et al., 2009; Wu et al., 2008; Santosa et al., 2015).

*Brown Adipose Tissue:*

BAT is another depot that is prevalent in most mammals, albeit as a transitional tissue in some. As with WAT, the role of BAT is also tightly linked to metabolic control, in this case as an energy dissipater and thermoregulator. Abundant iron-rich mitochondria —responsible

for the gross coloration and name of the tissue— and multilocular lipid-droplets are the most distinct physical characteristics of BAT adipocytes. BAT is especially prevalent among hibernating animals, and although BAT depots exist in humans (e.g. between the shoulder blades in newborn infants), they exist mostly around the perinatal period and are significantly reduced in adults. By collapsing the mitochondrial proton gradient, uncoupling protein 1 (Ucp1) allows the electron-transport system to be used to generate heat instead of ATP, acting as the main functional protein responsible for energy dissipation in BAT (Crichton et al., 2017).

*Beige/BRITE Adipose Tissue:*

Recent evidence in mouse and humans shows the existence of a developmentally distinct subpopulation of BAT adipocytes known as beige or BRITE (**Br**own/wh**ite**) (Barquissau et al., 2016). Brite adipocytes originate as pre-existing WAT adipocytes with basal expression levels of Ucp1. Upon stimulation, these adipocytes increase Ucp1 production and cellular respiration rates. There are also significant developmental and transcriptional differences between BRITE adipocytes and their WAT and BAT counterparts that will be described briefly.

Adipogenesis is the process of cell differentiation from pre-adipocyte precursors to mature adipocytes. Pre-adipocytes arise from mesenchymal progenitors of diverse embryonic sources, including somatic mesoderm and neural crest (Billon et al., 2007; Sebo et al., 2018). Because definite markers to exclusively label BAT progenitors but not those of WAT remain elusive, most of the research in adipose tissue development is confined to the analysis of general adipogenic progenitors common to both BAT and WAT, regardless of

origin (Schulz and Tseng, 2013). Following lineage commitment by the expression and nuclear activity of the zinc-finger protein 423 (ZFP423, encoded by *Zfp423*) (Shao et al., 2016), adipogenic differentiation is accompanied by a series of morphological changes to committed pre-adipocytes, including rounding and the gradual accumulation of lipid, that result from a transcriptional cascade driven by three main classes of transcription factors: C/EBPs, SREBPs, and PPAR-family members (Figure 3.0).

*The C/EBP family*

CCAAT/enhancer binding proteins (C/EBPs) belong to the basic-leucine zipper class of transcription factors, with six isoforms described to date: C/EBPs α, β, γ, δ, ϵ, and ζ, expressed across a variety of tissues (Flodby et al., 1996; Zhang et al., 1997). *In vitro* studies in 3T3-L1 cells —a well-established pre-adipocyte cell line (Green and Kehinde, 1975)— have shown that expression of *Cebpb* and *Cebpd*, genes encoding C/EBPs β and δ respectively, is induced rapidly after the addition of adipogenic hormonal stimuli, and their activation is responsible for a burst of clonal expansion, followed by the expression of *Cebpa* and peroxisome proliferator-activated receptor γ (*Pparg*) (Tang and Lane, 1999). Further, knockdown of *Cebpb* in 3T3-L1 cells inhibits adipogenesis, whereas its overexpression stimulates it independent from extracellular adipogenic cues (Yeh et al., 1995; Zhang et al., 2011). In mice, knockout of *Cebpb* and *Cebpd* leads to impaired adipogenesis (Tanaka et al., 1997).

*SREBP1c*

Sterol regulatory element binding protein-1 (SREBP-1) is a member of the basic helix-loop–helix (bHLH) family of transcription factors along with other SREBPs. SREBPs are membrane-bound in the ER and, upon their cleavage by S1P, they regulate cholesterol and fatty acid biosynthesis and uptake (Patra et al., 2007). SREBP1c is highly expressed in BAT, followed by liver, and WAT (Rosen et al., 2000).

*PPARγ.*

Peroxisome proliferator-activated receptor gamma (PPARγ) is a member of the nuclear hormone receptor superfamily, and its activity transcriptional activity requires heterodimerization with the nuclear hormone receptor retinoid X receptor (RXR) (Rosen et al., 2000). Like other nuclear receptors, PPARγ acts as a key regulator of adipogenesis, transactivating multiple target genes involved in lipid metabolic pathways, including *Lpl, Fabp1/4, Plin, Angptl4,* and *Ucp1* (Nakachi et al., 2008). PPARγ expression increases during adipocyte differentiation. Ectopic expression of PPARγ induces the accumulation of lipid droplets in mouse embryonic fibroblasts, whereas its genetic ablation impairs adipocyte differentiation (Ge et al., 2002; Rosen et al., 1999).

Recent high throughput approaches have been used to compare the biology of different adipose tissue types. For example, a lipidomic analysis revealed that although the lipidome of BAT and WAT is mostly comprised of triglycerides (<99%), significant differences separate the tissues (Grzybek et al., 2019; May et al., 2017). Diglycerides are the next most abundant lipid class in the WAT lipidome, but in BAT they were not significantly more or less abundant, an important observation supporting the view that that lipid synthesis is central to WAT, but not BAT biology. The differential abundance of

mitochondria between BAT and WAT adipocytes is also reflected in their lipidome. Cardiolipins, important components of the mitochondrial membrane, are more abundant in the BAT lipidome compared to that of WAT, owed to the increased mitochondrial content in the former tissue. Interestingly, May et al. (2017) also observe that upon metabolic stress induced by high fat diet, BAT adipocytes shift their lipidomic composition to one more similar to that of different WAT depots under the same stress; namely, longer and highly unsaturated species increase, as expected from elevated levels of dietary lipids available for uptake from circulation (Grzybek et al., 2019). This is an important observation that highlights the high metabolic sensitivity of adipose tissues and their ability to compensate for dynamic energy demands.

In Chapter II, I show that LCs are lipid-filled cells, and that, in fact, past studies have overlooked LCs because of their striking resemblance with adipocytes (Egawa et al., 2013). I also show that LCs do not express the metabolic regulators Resistin or Adiponectin, suggesting that LCs may have a distinct, non-metabolic role for their lipids. Recently, mass spectrometry approaches have been used to analyze the lipidome of distinct adipose tissue populations under normal, chronic exercise, and disease conditions, an approach that would be very fruitful in LCs. Further, several details behind the regulation of lipogenesis in adipocytes at the transcription level are known, and an unbiased comparison between adipose tissues, rib chondrocytes, and LCs could shed light on the mechanisms behind LC maturation. Considering our observations on LC, I compared its lipidomic and transcriptomic profile to those of *bona fide* white adipose tissue and rib cartilage.

## Materials and Methods

| REAGENT or RESOURCE | SOURCE | IDENTIFIER |
|---|---|---|
| Rabbit anti-SOX9 | Millipore | AB5535 |
| Rabbit anti-FASN | Cell Signaling Technology | 3180S |
| Rabbit anti-PLIN1 | Cell Signaling Technology | 9349S |
| Rabbit anti-COL8A1 | Antibodies-Online | ABIN1718654 |
| Mouse anti-MYOC | ProteinTech | 60357-1-Ig |
| Rabbit anti-ACACA | Cell Signaling Technology | 3676S |
| Rabbit anti-CEBPA | Cell Signaling Technology | 8178S |
| Rabbit anti-CEBPB | Cell Signaling Technology | 3084S |
| Mouse anti-PCNA | Abcam | AB29 |
| Goat anti-rabbit Alexa Fluor 488 | ThermoFisher | A11008 |
| Goat anti-rabbit Alexa Fluor 555 | ThermoFisher | A21428 |
| Goat anti-mouse Alexa Fluor 555 | ThermoFisher | A21422 |
| Mounting medium with DAPI | Vector Labs | H-1200 |
| Critical Commercial Assays | | |
| M.O.M. Kit | Vector Labs | BMK-2202 |
| NextSeq 500/550 High Output v2 kit (75 cycles) | Illumina | FC-404-2002 |
| NextSeq 500/550 High Output v2 kit (150 cycles) | Illumina | FC-404-2005 |
| Deposited Data | | |
| Mouse ear-derived lipochondrocytes and inguinal adipocytes bulk RNA-seq data | This work | GEO: GSE116119 |
| Rib-derived chondrocyte bulk RNA-seq data | He et al. (2016) | GEO: GSE73372 |
| Notochord-derived cells and nucleus pulposus bulk RNA-seq data | Peck et al. (2017) | GEO: GSE100934 |
| Experimental Models: Organisms/Strains | | |
| Mouse: *Wnt1-Cre2* | The Jackson Laboratory | JAX: 022137 |
| Mouse: *tdTomato (aka Ai9(RCL-tdT))* | The Jackson Laboratory | JAX: 007909 |
| Oligonucleotides | | |
| PCR primers. See Table 3.1 | | |
| Software and Algorithms | | |
| STAR v.2.4.2a | Dobin et al. (2013) | https://github.com/alexdobin/STAR/releases?after=2.5.0c |
| RSEM v.1.2.25 | (Eguchi et al., 2011) | https://github.com/deweylab/RSEM/releases |
| edgeR v.3.2.2 | (Robinson et al., 2010) | http://bioconductor.org/packages/stats/bioc/edgeR/ |

| Target | Forward Primer | Reverse Primer |
|---|---|---|
| *Col8a1* | AGAGTGCACCCAGCCCCAGT | TGGGTGGCACAGCCATCACATTT |
| *Myoc* | CCACCCAGTACCCCTCTCAG | AGCGCTCCACATCCTTTGTCT |
| *Mkx* | CGGACGTTCAGTGGTTTCCTG | GCTTATGCCTTACCTTCCCTCC |
| *Fasn* | GGGTGTGAGTGGTTCAGAGG | AGGGCAATGCTTGGTCCTTT |

**Table 3.1: Primer sequences used in qRT-PCR experiments**

| Abbrev. | Name |
|---|---|
| AC | Acyl Carnitines |
| Cer | Ceramides |
| CE | Cholesteryl Esters |
| Co Q | Coenzyme Q |
| CL | Cardiolipin |
| DAG | Diacylglycerols |
| FFA | Free Fatty Acids |
| FAHFA | Fatty Acid Hydroxy-Fatty Acids |
| Gly | Glycolipids |
| MAG | Monoacylglycerols |
| LPA | Lysophosphatidic Acids |
| PA | Phosphatidic Acids |
| LPC | Lysophosphatidylcholines |
| PC | Phosphatidylcholines |
| LPE | Lysophosphatidylethanolamines |
| PE | Phosphatidylethanolamines |
| LPG | Lysophosphatidylglycerols |
| PG | Phosphatidylglycerols |
| LPI | Lysophosphatidylinositols |
| PI | Phosphatidylinositols |
| LPS | Lysophosphatidylserines |
| PS | Phosphatidylserines |
| SM | Sphingomyelins |
| TAG | Triacylglycerols |

**Table 3.2: Definition of lipid class terms used.**

For this chapter, I performed all tissue dissections, sections, immunohistochemistry, imaging, quantitative RT-PCR, data analysis, and mouse work. Fluorescence-activated cell sorting (FACS) was performed by Vanessa Scarfone at the UC Irvine Stem Cell Research Center's Flow Cytometry Core. RNA libraries used in RNA-sequencing experiments were generated in collaboration with Xiaojie Wang PhD. RNA-sequencing and data demultiplexing was performed by Nicole El-Ali. Morphometric analysis of ear pinna was performed by Katie Nigh. Lipidomics, including all mass spectrometry methods as well as partial data analysis was performed in by Michael Kiebish PhD and his colleagues, who have established a lipid extraction and identification pipeline for a variety of tissues, including white adipocytes.

***Lipidomic Profiling.*** All lipid standards were acquired from Cayman Chemical Company, Matreya, Cambridge Isotope Laboratories, NuChek Prep, Avanti Polar Lipid, or Sigma-Aldrich. All solvents are of high-performance liquid chromatography (HPLC) or liquid chromatography-mass spectrometry (LC/MS) grade and were acquired from Sigma-Aldrich, Fisher Scientific, or VWR International.

*Liquid/Liquid Extraction of Structural Lipids.*

Medial, fenestra-free zones of the ear cartilage plate were dissected from adult P33 C57BL/6J female mice (n=5, at least 10mg per n), carefully avoiding adipocytes. For white adipose tissue control, inguinal fat was collected (n=5, at least 10mg per n). All tissues were rinsed thoroughly in fresh PBS and flash frozen for downstream use. Tissues were thawed in ten times diluted PBS and homogenized in Omni bead tubes with 2.8-mm ceramic beads in the Omni Bead Ruptor 24 with Cryo Cooling Unit (Omni International) at 4 °C for 2 min.

Protein concentration was determined by the bicinchoninic acid assay. One mg of protein from each sample was aliquoted, and a cocktail of deuterium-labeled and odd chain phospholipid standards from diverse lipid classes was added. Standards were chosen so that they represented each lipid class and were at designated concentrations chosen to provide the most accurate quantitation and dynamic range for each lipid species. 4 mL chloroform:methanol (1:1, by volume) was added to each sample, and lipidomic extractions were performed as previously described (Kiebish et al., 2010). Lipid extraction was automated using a customized sequence on a Hamilton Robotics STARlet system (Hamilton). Lipid extracts were dried under nitrogen and reconstituted in chloroform:methanol (1:1, by volume). Samples were flushed with nitrogen and stored at -20C°.

*Direct Infusion MS/MSALL Structural Lipidomics Platform.*

Samples were diluted 50 times in isopropanol:methanol:acetonitrile:water (3:3:3:1, by volume) with 2 mM ammonium acetate in order to optimize ionization efficiency in positive and negative modes. Electrospray ionization-MS was performed on a TripleTOF 5600+ (SCIEX), coupled to a customized direct injection loop on an Ekspert microLC200 system (SCIEX). Fifty ml of sample was injected at a flow rate of 6 ml/min. Lipids were analyzed using a customized data independent analysis strategy on the TripleTOF 5600+ allowing for MS/MSALL high-resolution and high-mass-accuracy analysis as previously described (Simons et al., 2012). Quantification was performed using an in-house library on MultiQuant software (SCIEX) and normalized to 1 mg protein.

***Histochemistry, immunostaining, and imaging.*** The primary antibodies used were rabbit anti-SOX9 (1:250; Millipore AB5535 QVP135108), rabbit anti-FASN (1:250; Cell Signaling Technology 3180S), rabbit anti-PLIN1 (1:750; Cell Signaling Technology 9349S), rabbit anti-COL8A1 (1:500; Antibodies-Online ABIN1718654), mouse anti-MYOC (1:250; ProteinTech 60357), rabbit anti-ACACA (1:50; Cell Signaling Technology 3676S), rabbit anti-CEBPA (1:100; Cell Signaling Technology 8178S), rabbit anti-CEBPB (1:200; Cell Signaling Technology 3084S), mouse anti-PCNA (1:200; Abcam AB29). Secondary antibodies used were goat anti-rabbit Alexa Fluor 488 and 555 (ThermoFisher A11008 and A21428 respectively), Goat anti-mouse (ThermoFisher A21422) at 1:1000. Stained sections were mounted with non-hardening mounting medium with DAPI (Vector Labs). For mouse anti-PCNA and rabbit anti-SOX9, immunostaining was performed on paraffin sections with heat-based antigen retrieval in citrate buffer (10mM Citric Acid, pH 6.0); for other antibodies, frozen tissue sections were used. A Mouse-on-Mouse (M.O.M.) kit (Vector Labs) was used when necessary and according to manufacturer's instructions.

***RNA extraction and RNA-sequencing.*** Ear cartilage tissues were collected from male *Wnt1-Cre2;tdTomato* mice at several developmental time points. In P8, P10, and P13 mice, red fluorescence-positive ear cartilage was microdissected and incubated in 0.75 mg/ml Collagenase I (Sigma-Aldrich) in 10% FBS DMEM for 3 hrs at 37°C in 5% CO2 with constant motion. The cell suspension was passed through a 40 μm nylon cell strainer (Corning) and centrifuged at 290 g for 5 minutes at 4 °C. The cell pellet was reconstituted in PBS and stained with Zombie Violet Cell Viability Kit (BioLegend) according to the manufacturer's protocol. Single, live cell fractions were then FACS-sorted as tdTomato-hi using a BD FACSAria II flow cytometer (BD Biosciences). In P21 and P33 mice, the ear cartilage plate

was microdissected and the medial and distal portions of the plate were separated and incubated in Collagenase I. Dissected inguinal adipose tissue was also treated to isolate single adipocytes. Cells were passed through a 100 μm nylon cell strainer (Corning) and centrifuged at 290 g for 10 minutes at 4 °C. Following centrifugation, the buoyant, lipid-filled cell fraction was collected. Sorted tdTomato$^{hi}$ cells (from P8, P10, and P13) and buoyant cells (from P21 and P33) were re-suspended in RLT buffer, a cell lysis buffer property of Qiagen, with added 1% beta-mercaptoethanol and mechanically homogenized using a Hard Tissue Homogenizing Ceramic Beads Kit (Precellys, CK28), following manufacturer's instructions. Total RNA was isolated using the RNeasy Micro-Kit (QIAGEN). Optimal-quality RNAs with RIN scores more than 8.8 were considered for cDNA library preparation. Full-length cDNA library amplification was performed as previously described (Picelli et al., 2014) with minor modifications. Briefly, 1 ng of total RNA was reversed-transcribed, and resulting cDNA was pre-amplified for 13 cycles. Tagmentation was carried out on 18 ng cDNA using the Nextera DNA Sample Preparation Kit (Illumina) at 55°C for 5 min and purified using PCR Purification Kit (Qiagen). Transposed cDNA was used for limited cycle enrichment PCR using previously published Nextera PCR primers (Buenrostro et al., 2013). Libraries were amplified for 7 continuous cycles and purified with AMPure XP beads (Beckman Coulter). Library quantification was done using KAPA for Illumina Sequencing Platforms (Illumina). Libraries were multiplexed and sequenced as paired-end on an Illumina Next-Seq500 platform (Cluster density = 296K/mm2, Clusters PF = 71.2%, Q30 = 87.6%). The libraries were sequenced to an average depth of 10-30 million reads per library using paired 43bp reads. Reads were first aligned using STAR v.2.4.2a with parameters '--outFilterMismatchNmax 10 --

outFilterMismatchNoverReadLmax 0.07 --outFilterMultimapNmax 10' to the reference mouse genome (mm10/genocode,vM8). Gene expression levels were quantified using RSEM v.1.2.25 with expression values normalized into Fragments Per Kilobase of transcript per Million mapped reads (FPKM). Samples with >1,000,000 uniquely mapped reads and >60% uniquely mapping efficiency were used for downstream analyses. Differential expression analysis was performed using edgeR v.3.2.2 on protein-coding genes and lncRNAs. Differentially expressed genes were selected by using fold change (FC)≥2, false discovery rate (FDR)<0.05 and counts per million reads (CPM)≥2.

**Results**

We asked if the similarities between LCs and adipocytes extend beyond their morphological and ultrastructural resemblance (Bradamante et al., 1991; Kostovic-Knezevic et al., 1981; Mallinger and Bock, 1985). We compared the lipidomic profiles of microdissected ear cartilage (n=5) and perigonadal white adipose tissue (WAT; n=5) from one-month old female wild type mice, an age at which morphometric analyses show the ear is stable in size and shape (Figure 3.11). WAT was trimmed and collected from around the ovary. To prevent cartilage contamination with adipocytes, we used only part of the medial portion consistently devoid of fenestrae (Figure 2.6E). Principal component analysis (PCA) of our lipidomics data partitioned the samples into specific clusters, mainly separated by tissue type on principal component 1 (PC1) (Figure 3.1). Whereas the ear cartilage samples cluster into a well-defined region, WAT samples appear more "spread-out" across PC2 and PC3. Adipocytes, even when isolated from a single source, have been shown to be heterogeneous in terms of developmental origin, insulin sensitivity, and lipid uptake(Reviewed in Luong et al. (2019)). Although tissues were dissected by carefully avoiding any surrounding non-adipose tissue and exclusively from around the ovary, differences in dissection extent and/or in the actual source within the perigonadal fat pad among samples could exaggerate the already heterogeneous WAT lipidome. Despite this, our WAT lipidome data is in line with other lipidome studies (May et al., 2017) and the LC lipidome is significantly distinct from these *bona fide* adipose tissues. While neutral lipids, the primary molecular species of lipid droplets, constitute the majority of the tissue's lipids in both ear cartilage and WAT, the relative abundance of major lipid classes is different across tissues (Figure 3.2A-B).

Specifically, the WAT lipidome is dominated by triglycerides (86.5+/-12.36%), followed by fatty acid hydroxyl-fatty acids (FAHFAs; 9.4+/-2.5%) and diglycerides (1.7+/-0.001%). Interestingly, triglycerides constitute only 43.3+/-0.78% of cartilage lipids, half of that of WAT, while FAHFAs make a considerably larger contribution, at 31.1+/-3.1%. The low relative abundance of triglycerides in ear cartilage indicates that their synthesis, utilization, or both are suppressed. Consistent with the first possibility, several molecular classes that serve as precursors in triglyceride synthesis, namely free fatty acids (FFAs) (7.6+/-0.2% *vs.* 0.9+/-0.1%), lysophosphatidic acids (1.2+/-0.2% *vs.* 0.04+/-0.007%) and phosphatidic acids (5.0+/-0.4% *vs.* 0.5+/-0.05%), preferentially accumulate in ear cartilage compared to WAT.

Beyond neutral lipids, the ear cartilage lipidome differs from that of WAT across several other lipid classes. For instance, the ear cartilage has a more diverse composition of glycolipids (60 species in cartilage *vs.* 48 in WAT); phosphatidylethanolamines, a class of phospholipids (90 *vs.* 73); sphingomyelins (34 *vs.* 21); cholesteryl esters (24 *vs.* 17); and acyl carnitines (31 *vs.* 19) (Figure 3.3A). Moreover, compared to WAT, the cartilage lipidome as a whole is enriched for saturated fatty acid chains, the main product of *de novo* lipogenesis (19.7% *vs.* 3.8%), as well as for monounsaturated fatty acid chains (13.2% *vs.* 8.2%) (Figure 3.3B). Together, lipidomic analysis suggests that despite morphological similarities, LCs and adipocytes rely on distinct lipid vacuole biogenesis, maintenance and/or utilization pathways.

Next, we asked what gene expression patterns could explain the observed physical characteristics of LCs. We performed RNA-sequencing (RNA-seq) to compare the

transcriptomes of ear cartilage LCs (n=3 biological replicates) with inguinal WAT adipocytes from one-month old wild type mice (n=3) and hyaline rib cartilage chondrocytes (n=3) reported by He et al. (2016). PCA shows that the transcriptome of LCs is distinct from those of adipocytes and hyaline chondrocytes (Figure 3.4A), with 8,422 differentially expressed genes (Figure 3.5A) and each cell type is enriched for unique Gene Ontology terms. As expected, adipocytes are enriched for terms including lipid storage, fatty acid synthesis and oxidation, insulin response, as well as angiogenesis (Figure 3.5B, blue). Rib chondrocytes are enriched for terms anticipated for hyaline cartilage, including chondrocyte differentiation, apoptosis, ossification, TGFβ and WNT signaling (Figure 3.5B, red). Interestingly, ear LCs are simultaneously enriched for cartilage and metabolic terms, highlighting their distinct nature. Top terms for LCs include cartilage development, facial morphogenesis, ECM organization, cell growth and TGFβ signaling (Figure 3.5B, green).

Next, we analyzed top differentially expressed genes across three cell types, focusing on extracellular matrix, secreted signals, transcriptional regulators and metabolic factors (Figure 3.6A-C). Both LCs and rib chondrocytes express many of the same extracellular matrix genes, otherwise minimally present in adipocytes. However, cartilage type-specific enrichment patterns were also observed. Compared to rib chondrocytes, LCs express high levels of *Aspn, Cilp2, Col8a1, Col8a2, Dcn, Eln, Fmod, Mgp, Myoc*, *Smoc2* and *Ucma* (Figure 3.6A). At the same time, they express lower levels of *Acan, Col2a1, Col9a2, Col10a1, Col11a2, Dmp1, Fn1, Matn1* and *Tnn* that are otherwise highly expressed in rib cartilage (Figure 3.6B). In terms of secreted signals, both cartilage cell types express BMP ligands, but LCs are enriched for *Bmp5*, while rib chondrocytes – for *Bmp4/6/7/8a*. Among TGFβ ligands, LCs express *Gdf5* and *Tgfb3*, while rib chondrocytes express *Gdf10/15* and

*Tgfb1.* In terms of the WNT pathway, LCs are enriched for WNT antagonists *Dkk3, Sfrp1/2/5, Wif1*, while rib chondrocytes – for WNT ligands *Wnt5a/5b/10b/11*. Rib chondrocytes also prominently express *Ihh, Spp1, Tnf, Vegfa* and a large number of chemokines *Ccl2/3/4/5/7/8/9/12/24*, *Cxcl1/2/3/10/16* and interleukins *Il1b/1f9/17b/17d*. Other secreted signals specifically enriched in LCs include angiopoietins *Angpt4, Angptl7*, FGF ligands *Fgf7* and *Fgf18*, IGF binding proteins *Igfbp2/4/5/6/7* and cytokine-like protein *Cytl1*.

LCs and rib chondrocytes show distinct expression patterns for transcriptional regulators, including homeobox and homeobox-like genes. Reflecting their thoracic origin, rib chondrocytes are enriched for *Hoxa3/5/6/7*, *Hoxb2/7*, and *Hoxc5/6/8*. In a similar fashion, ear LCs are enriched for *Hoxa2*, *Dlx5/6*, and *Msx1*, reflecting their origin from neural crest mesenchyme of the second pharyngeal arch (Minoux et al., 2013). Both cartilage cell types share expression of known chondrogenic regulators, including *Id2, Smad4, Snai1/2, Sox5/6/8/9* and *Twist1*. At the same time, only rib chondrocytes express high levels of the following established regulators of chondrogenesis: *Foxa3, Foxo4, Nkx3-2, Runx1/3, Smad7, Sox4, Sp7* and *Vdr*. LCs specifically express *Cbx6, Foxn3, Glis2/3, Lhx8, Mkx, Scx, Tbx15.* Intriguingly, they also express several known transcriptional regulators of adipogenesis: *Cebpa, Klf9, Nfia, Pparg, Srebf1* and *Zfp423*, albeit at lower levels than adipocytes.

Despite sharing some similarities, major differences are present between LCs and adipocytes. Unlike adipocytes, LCs do not express well-established secreted adipokines *Adipoq, Cfd (adipsin), Lep, Retn, Retnla* and pro-adipogenic transcriptional regulators *Ebf1,*

*Ebf2, Cebpb, Ppara, Rxrg, Thrsp* (Figure 3.6C). Further differences extend to multiple key genes involved in lipid synthesis, lipid catabolism and lipid vacuole formation and maintenance. For instance, LCs do not express *Cd36* and express low levels of *Slc27a1*, two major fatty acid transporters in adipocytes. However, glucose transporters, including *Slc2a1* and *Slc2a4*, which can be utilized in *de novo* lipogenesis, are expressed, albeit with cell type-specific differences. Similar to adipocytes, LCs express, although at lower levels, key *de novo* lipogenesis enzymes: *Acly*, *Acaca*, *Fasn* and *Scd1*. LCs also express many key enzymes required at all steps of triglyceride synthesis: *Gpat4, Agpat1/2/3/4*, triglyceride-producing *Ppap2a/2b/2c, Ppapdc1b/2/3* and *Lpin2*, and triglyceride-producing *Dgat1* and *Dgat2*. Importantly, *Pnpla2*, *Lipe* and *Mgll*, key enzymes required for triglyceride mobilization and breakdown are prominently downregulated in LCs. Also, not expressed and downregulated respectively are *Plin1* and *Abhd5*, both of which are critical for Pnpla2 activation and hormone-stimulated lipolysis in adipocytes. Finally, LCs express several key proteins implicated in lipid vacuole assembly, fusion and stability, albeit many of them at reduced levels as compared to adipocytes: *Arf1, Bscl2 (seipin), Cav1, Cav2, Cidea, Plin2, Plin3, Ptrf (cavin1), Prkcdbp (cavin3), Rab18, Snap23, Stx5a* and *Vamp4*. At the same time, other related proteins are not expressed or expressed at very low levels: *Cidec, Fitm2, Plin1, Plin5* and *Sdpr (cavin2)*.

Immunohistochemistry confirms many of the expression patterns seen in adult LC RNA-sequencing experiments, but also shows interesting patterns not immediately apparent from our sequencing results. For example, despite its downregulation compared to rib chondrocytes, LCs show nuclear SOX9 activity, essential for the cartilage differentiation and tissue maintenance (Figure 3.7A). ECM proteins COL8A1 and MYOC are

markedly expressed in LCs, with COL8A1 localizing to the surface of the plate and MYOC to the LC periphery (Figure 3.7B-C). Also in agreement with our RNA-sequencing results, lipochondrocytes show expression of adipogenic transcription factor CEBPA, but not CEBPB (Figure 3.7D-E). Interestingly, despite its downregulation compared to adipocytes, expression of *de novo* lipogenesis enzymes FASN and ACACA is apparent in individual LCs and other fatty tissues such as sebaceous glands (Figure 3.7F-G). Further, the prominent downregulation of *Plin* in LCs against adipose tissue is also reflected by the absence of PLIN from LCs in the plate, but not in adjacent skin adipocytes (Figure 3.7H). Negative control staining using purified rabbit IgG, BSA only (no primary antibody), or a M. O. M. protein diluent only, further confirm these expression patterns (Figure 3.7I-K)

To further explore the relationship between LCs and other cartilages, we compared the transcriptome of adult LCs to that of notochord cells, a cartilage–like tissue (Tarazona et al., 2016) that displays architecture similar to that of LC-based cartilages —low ECM content and vacuolated cells—, and found them to be distinct. The notochord is a midline structure that defines the phylum *Chordata*. It becomes specified early during embryonic development as a rod-like structure that runs along the anterior-posterior body axis. It serves as an essential signaling center for proper patterning of the surrounding embryonic elements (Pourquie et al., 1993). Its differentiated cells are large and contain distinct vacuoles of hydrated material (Stemple, 2005). When they are surrounded by a sheath, such as in the zebrafish embryo, its inner cells generate osmotic pressure that provides the notochord with stiffness and cartilage-like mechanical properties (Ellis et al., 2013). However, despite functional similarities, the relationship of the notochord with other cartilages remains a debated topic (Hall, 2015; Stemple, 2005; Witten et al., 2010). In

mammals, the continuous embryonic notochord becomes fragmented in adults, and depending on their position along the midline, notochord cells can ossify and contribute to the vertebral anlagen or become encased in the intervertebral disc and form the *nucleus pulposus*. Cells in the latter structure continue to be prominently vacuolated and structurally resemble mature vacuolated LCs, although their vacuoles do not contain lipid. To better understand the relationship between LCs and cells of the notochord, we compared the transcriptome of adult mouse LCs with those of day E12.5 notochord-derived cells (NDCs) and day P0 nucleus pulposus (NP) from a previously published mouse study (Peck et al., 2017).

PCA shows that all three transcriptomes are distinct (Figure 3.8A) with 5,593 genes differentially expressed across the samples and organizing into 6 clusters, N1 through N6 (Figure 3.8B). Genes in clusters N1 and N6 are up- and downregulated, respectively, in adult LCs compared to both NDCs and NP (Figure 3.9A-B). Clusters N4 and N5 contain upregulated genes shared by LCs and NP and LCs and NDCs, respectively. LCs are enriched for gene ontology terms that include collagen fibril production, cartilage development, lipid metabolism, response to oxidative stress, and several bioenergetics processes (Figure 3.9C), highlighting their specialized cartilage nature. NDCs and NP are enriched for terms including Cell cycle, transcription, chromatin modification, and protein phosphorylation, pointing to their highly proliferative, embryonic nature (Figure 3.9D). Next, we analyzed top differentially expressed genes across all cell types, with a focus on extracellular matrix, metabolic genes, and transcriptional regulators. In LCs, extracellular matrix genes *Aspn, Bgn, Cilp2, Col8a1, Col8a2, Fbn1, Myoc, Sparc, Thbs4* and *Ucma* are highly upregulated compared to NDCs and NP (Figure 3.9A). On the other hand, *Col15a1, Col22a1, Col24a1* and

*Ncan* are downregulated when compared against cells of the notochord (Figure 3.9B). Next, we asked which ECM genes are shared between LCs and notochord cells. Upregulated in both LCs and NDCs compared to NP are *Chadl, Col9a1, Col9a2, Col11a1, Emilin1, Emilin3, Mfap2* and *Matn4* (Figure 3.10A). In LCs and NP, *Acan, Col5a3, Col10a1, Ecm1* and *Timp2* are upregulated against NDCs (Figure 3.10B). Similar to what we observe when compared to rib chondrocytes, many genes involved in lipid synthesis and metabolism are upregulated in LCs, namely *Apod, Apoe, Cidea, Dgat2, Insig1, Ldhd, Mogat1* and *Pcx,* (Figure 3.9A), although LCs and NP both upregulate *Aldh2, Acot7, Fabp4* and *Fah* when compared to NDCs (Figure 3.10B). In contrast, genes involved in other metabolic processes outside lipid synthesis, such as *Gsk3a* and *Mogs* are down, when compared to NDCs and NP (Figure 3.9B). In terms of transcriptional regulators, compared to NP, LCs and NDCs upregulate *Dlx2, Emx2, Gsc, Irx2, Id1, Msx1,* as well as signature cartilage factors *Sox5* and *Sox9* (Figure 3.10A).

Taken together, LCs have a unique transcriptome, with certain features shared with hyaline chondrocytes, such as extracellular matrix, signaling and transcription factor genes, and other feature shared with adipocytes, including essential lipogenesis and lipid storage genes. Further, our analysis also shows multiple differences between LC and notochord cells. Considering the mechanical and supportive role of the notochord during embryogenesis, it is not surprising to see expression of structural genes also expressed by chondrocytes, such as *Col9a1/2* and *Chadl,* or transcriptional regulators of such genes, including *Sox9* and *Sox5.*

To further probe into the LC biology, we asked when, during ear development, do LCs activate the lipogenesis program and which transcriptional changes accompany it. First, we established key events in LC formation in the ear. External ears in mice (Anthwal and Thompson, 2016; Mallinger and Bock, 1985), including ear hair follicles (Wang et al., 2017) develop after birth. Using ear surface measurements in wild type mice (n=5), we observe two consecutive growth phases. During the early phase of slow growth, between postnatal days P1 and P15, ears unfold and grow approximately nine times in size. During a later phase, between P15 and one month of age, ears expand rapidly before reaching plateau, becoming approximately 25 times larger than P1 ears (Figure 3.11A-B). Next, we studied expression patterns of cartilage lineage marker SOX9 and proliferation marker PCNA, as well as the neutral lipid stain Oil Red O. SOX9 is absent from ear mesenchyme on and before P2, sparsely appears at P4, and broadly activates at P7 and onward. Many SOX9-positive cells are PCNA-positive between P4 and P10, but become mostly PCNA-negative by P13 and onward (Figure 3.12 A-F). Oil Red O-positive lipid vacuoles first appear in the ear cartilage between P10 and P13 and then rapidly enlarge between P13 and one month (Figure 3.13A-E). Thus, commitment to the LC lineage occurs between P4 and P7 and committed LC progenitors proliferate between P4 and P13. Post-mitotic LCs then differentiate and form lipid vacuoles starting at P10, and reach adult size by one month of age. Proliferation and lipogenesis partially overlap in the developing ear cartilage between P10 and P13 (Figures 3.11 and 3.12) (Sanzone and Reith, 1976).

On this basis, we defined the following time points for our RNA-seq experiment: P8 and P10 as the early and late proliferative phases, respectively; P13 as the transition between proliferation and differentiation; and P21 and one month as the early and late

differentiation phases, respectively (Figure 3.14). At P8, P10 and P13, we isolated LC progenitors as tdTomato$^{hi}$ cells by sorting from microdissected cartilage primordia in *Wnt1-Cre2;tdTomato* mice (Figure 3.15A-B). At P21 and one month, lipid-containing LCs were isolated using a buoyancy approach. We note that buoyant cells at P13 and non-buoyant cells at P21 were depleted from their respective samples upon processing. PCA analysis reveals that the transcriptome of LC lineage prominently changes as a function of time (n=3 per time point; Figure 3.16A).

A total of 2,397 genes were found to be differentially expressed and they organize into four temporally-dependent clusters (Figure 3.16B). Cluster T1 genes upregulate during the proliferative phase, at P8 and P10; cluster T2 genes transiently upregulate at P13 and P21; while cluster T3 and T4 genes upregulate during the differentiation phase, peaking at P21 and one month, respectively. Gene category and Gene Ontology enrichment analyses show that cell cycle activators, including *Ccna2, Ccnb1, Ccnb2, Cdk1, Cdk2*, and pro-mitotic factors, such as *Aurkb, Cdc16, Cdca3, Mad2l1* and *Prc1* are abundant in LC progenitors, and then largely shut down upon differentiation (Figure 3.16C, teal, 3.17A). In contrast, cell cycle inhibitors *Ccndbp1, Cdkn1a, Cgrrf1* and *Mrpl41* are enriched in differentiated LCs in cluster T4. Lipogenesis genes, including *Dgat2, Fasn, Lpin1* and *Mogat1* prominently increase in cluster T2, marking the onset of LC differentiation (Figure 3.16C, orange, 3.17B). Cluster T3 and Cluster T4 mark differentiated LCs, and are also enriched for critical lipogenesis genes, including *Agpat2, Agpat3, Bscl2, Cidea, Dgat1, Fabp5, Mogat2* and *Plin2* (Figure 3.16C, orange, 3.17C-D). Expression of known lipogenesis regulators, including *Klf15, Srebf1, Stat5a* and *Stat5b* is also upregulated in cluster T4 (Figure 3.17E). Transcription factors (3.16C, jade) and extracellular matrix genes (Figure

3.16C, purple) show two enrichment peaks, early, in cluster T1 and late, in clusters T3 and T4. Transcription factors upregulated in cluster T1 include *Hes1*, a regulator of neural crest-derived mesenchyme and chondrogenesis regulators *Sox6* and *Sox8* (Figure 3.17E). In terms of extracellular matrix genes, cluster T1 is enriched for established cartilage-specific collagens, including *Col2a1, Col9a1, Col9a2, Col11a2*, as well as *Eln, Fbln5, Fbn2, Nid2* and *Postn*, while cluster T4 is enriched for cornea-specific collagen *Col8a1*, hypertrophic cartilage-associated *Col10a1,* as well as *Chad, Fbn1* and *Omd*. (Figure 3.17E). Expression of signaling factors shows complex temporal patterns across several major pathways, including BMP, IGF, TGFβ and WNT (Figure 3.17E). To validate our time course RNA-sequencing results we performed qRT-PCR, targeting selected, differentially expressed genes *Fasn, Col8a1, Mkx,* and *Myoc*. We see that the expression dynamics from our RNA-sequencing experiments closely match those observed by means of qRT-PCR (Figure 3.18A-B). Taken together, the LC lineage displays a dynamic gene expression profile, with an early phase being dominated by cell cycle genes and pro-chondrogenic transcriptional regulators and extracellular matrix factors, and with the late phase being dominated by lipogenesis machinery genes and its transcriptional regulators, as well as specialized extracellular matrix factors.

## Figures

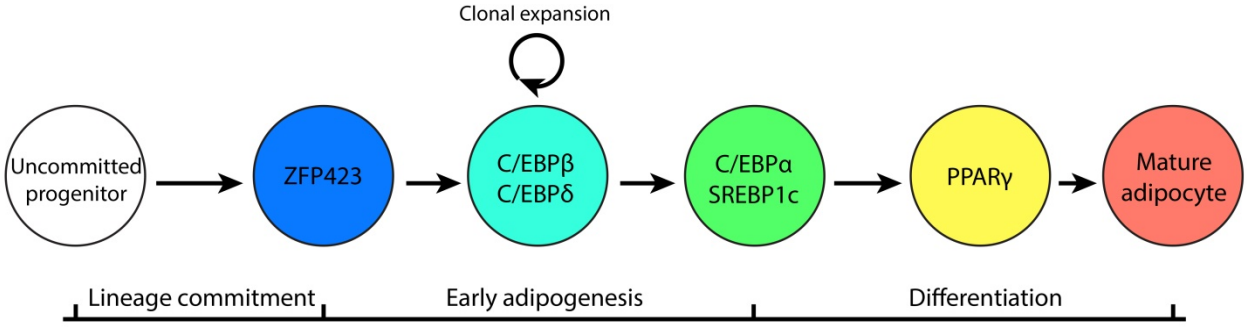


**Figure 3.0: Summary of the main steps in the adipogenic lineage specification program.** Uncommitted progenitors (in white above) express and activate ZFP423, a key transcriptional lineage determination factor to become pre-adipocyte precursors (Blue). Activation of C/EBPs β and δ induces a burst of clonal expansion (Cyan), necessary for further progression into the adipogenic differentiation program. Activity of C/EBPα and SREBP1c (Green) marks the onset of adipogenesis. PPARγ activity marks the last step of adipocyte differentiation (Yellow), and it is maintenance in mature adipocytes (Red) is important for major metabolic functions, including lipid metabolism, hormone secretion, and insulin sensitivity.

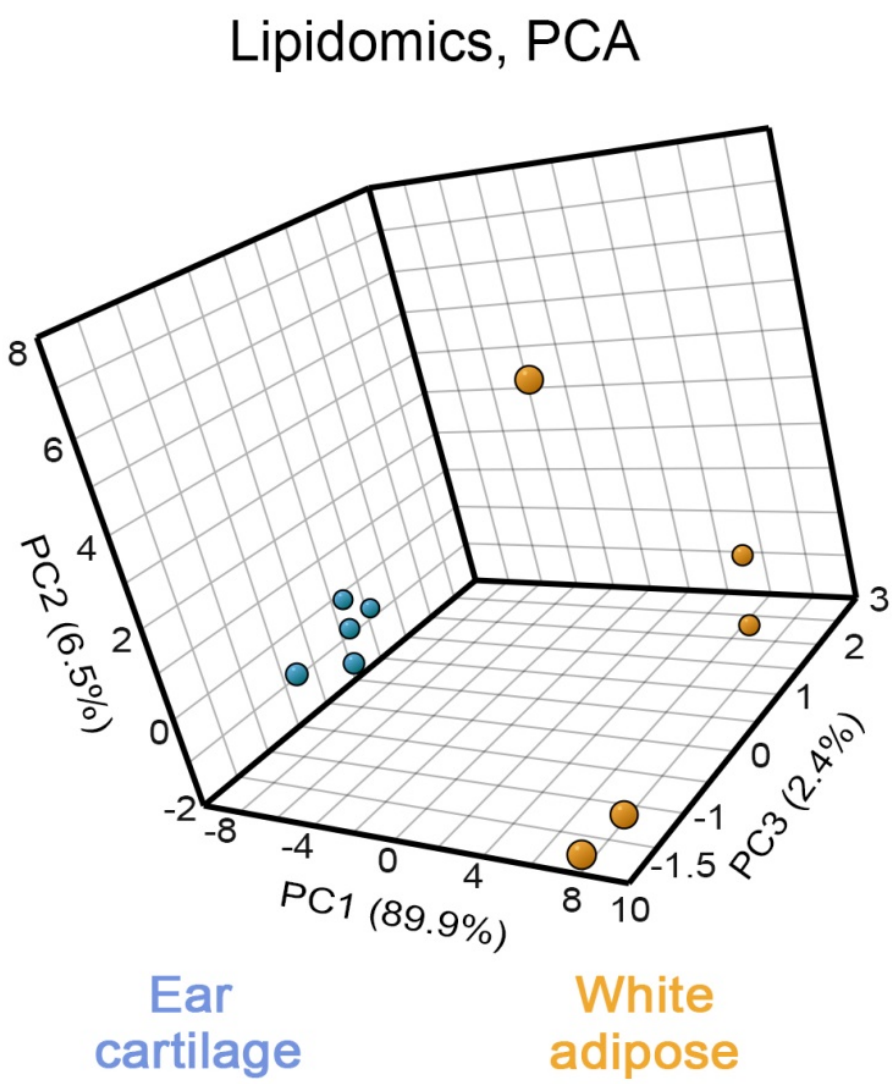


**Figure 3.1: The lipidomic profile of ear cartilage is distinct from that of white adipose tissue** Principal component analysis shows that the lipidomic profile of one-month-old ear cartilage (blue, n=5) is distinct from that of inguinal white adipose tissue (yellow, n=5).

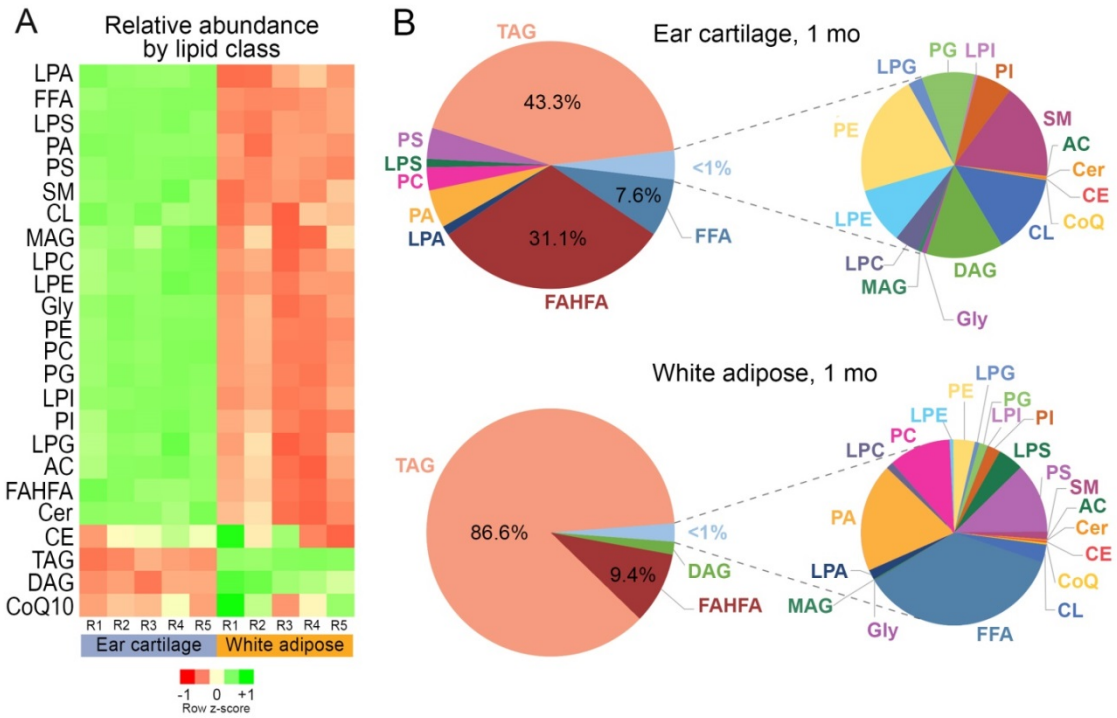


**Figure 3.2: Ear cartilage and adipose tissue are differentially enriched for distinct lipid classes. (A, B)** Ear cartilage and adipose tissue are differentially enriched for distinct lipid classes, as shown on the heatmap **(A)** and pie charts **(B).** See Table 2.2 for the definition of lipid classes. Prominently, among neutral lipids, ear cartilage is enriched for free fatty acids (FFA) and fatty acid hydroxyl-fatty acids (FAHFA), while adipose tissue is enriched for triacylglycerols (TAG) and diacylglycerols (DAG). See Table 3.2 for the definition of all lipid classes.

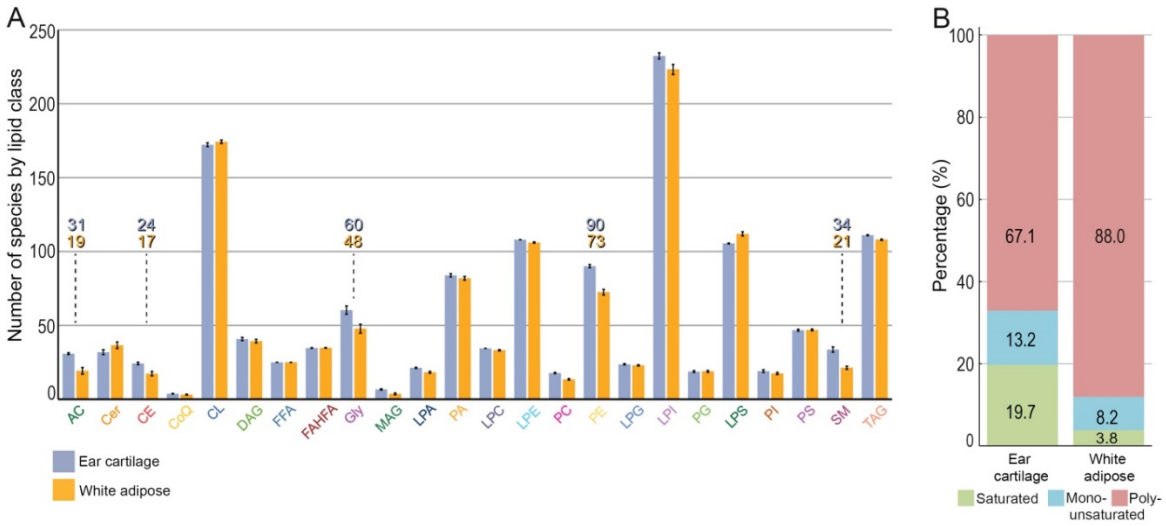


**Figure 3.3: Ear cartilage and adipose tissue show differences in molecular species abundance among different lipid classes. (A)** Bar chart shows that in comparison with adipose tissue (yellow), ear cartilage (blue) has a more diverse lipid composition (i.e. more detected molecular species), especially within the classes of acyl carnitines (AC), cholesteryl esters (CE), glycolipids (Gly), phosphatidylethanolamines (PE) and sphingomyelins (SM). See Table 3.2 for the definition of all lipid classes. **(B)** Compared to adipose tissue, ear cartilage contains a substantially higher proportion of lipids with saturated fatty acid tails (green).

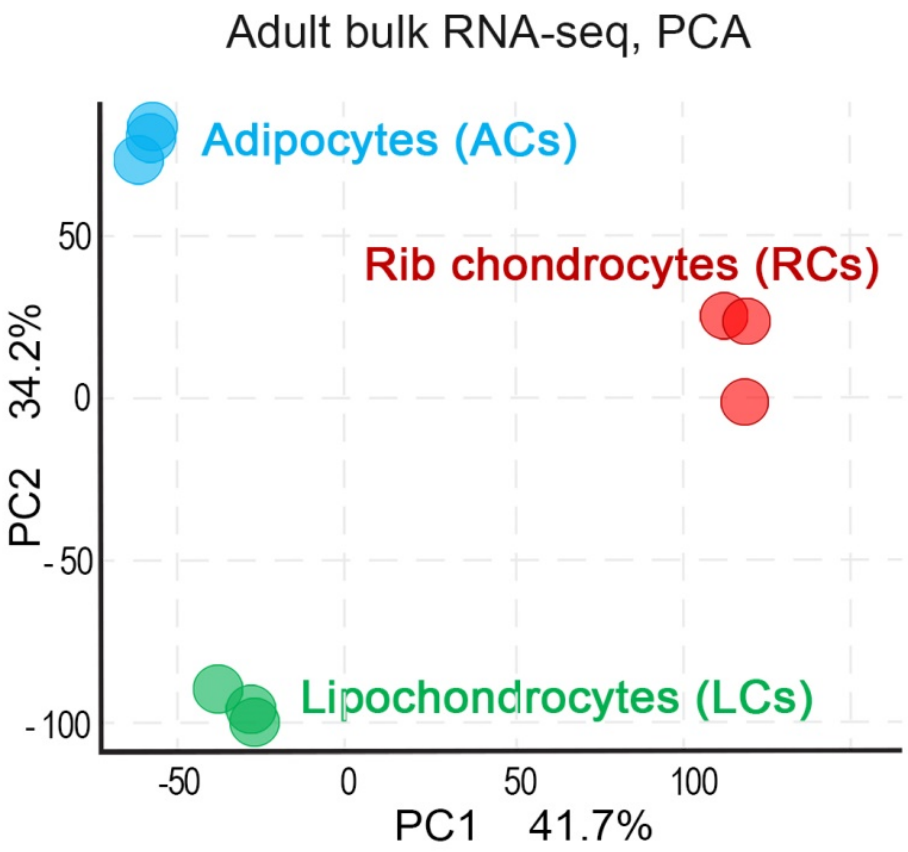


**Figure 3.4: Figure 3. The lipochondrocyte transcriptome is distinct from those of white adipocytes and rib chondrocytes. (A)** Principal component analysis shows that the transcriptional signature of ear LCs from 1-month-old mice (green, n=3) is distinct from these of inguinal white adipocytes (blue, n=3) and hyaline rib cartilage chondrocytes (red, n=3).

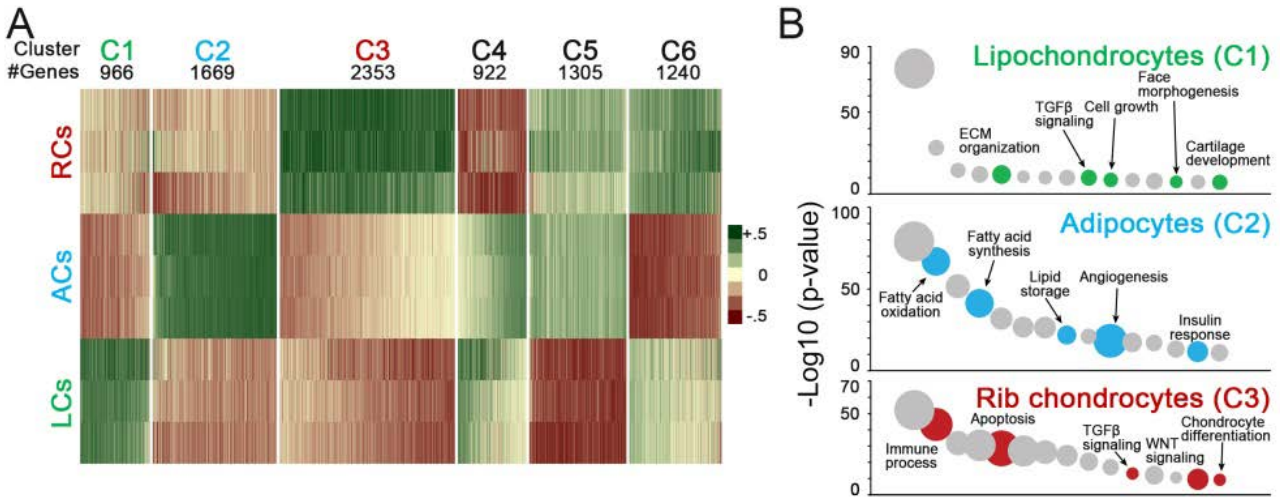


**Figure 3.5: Differential gene expression analysis and Gene Ontology shows further distinction between tissues, with an enrichment of cartilage-related terms in the adult lipochondrocyte transcriptome. (A)** Heatmap shows that a total of 8,422 genes are differentially expressed between three cell types and they group into six clusters, C1 through C6. **(B)** Bubble charts of Gene Ontology terms enriched in LC-specific C1 cluster (green), adipocytes-specific C2 cluster (blue) and rib chondrocyte-specific C3 cluster (red). Selected bubbles are colored and annotated. Bubble sizes correlate with gene numbers and their vertical position corresponds to significance.

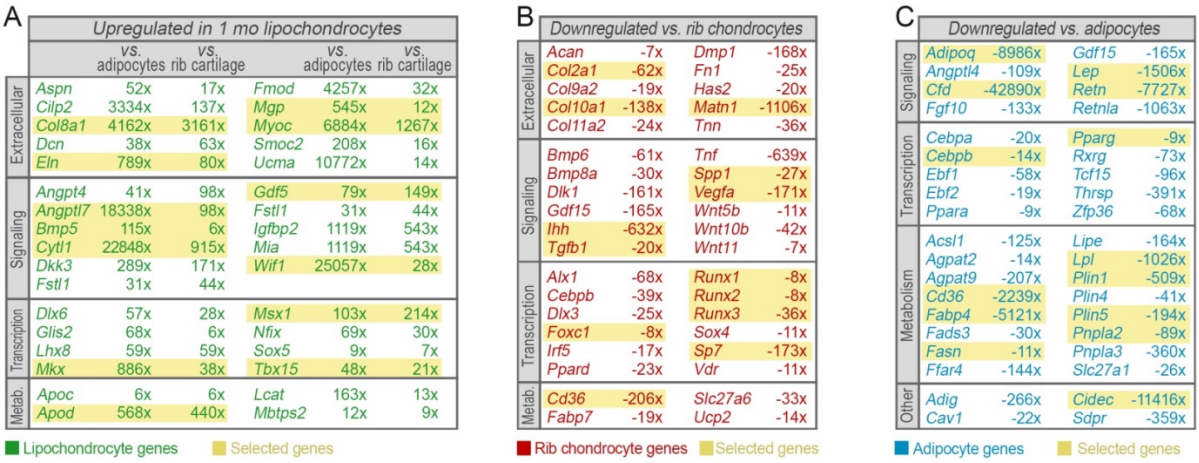


**Figure 3.6: List of selected marker genes differentially upregulated in LCs, rib chondrocytes, or adipocytes.** Select differentially expressed genes were sorted into *Extracellular Matrix, Signaling, Transcription, and Metabolism* categories, depending on their known roles. **(A-C)** Upregulated genes in 1 month old LCs vs rib chondrocytes and adipocytes (A), and downregulated genes in 1 month old LCs vs rib chondrocytes (B) and adipocytes (C) are shown.

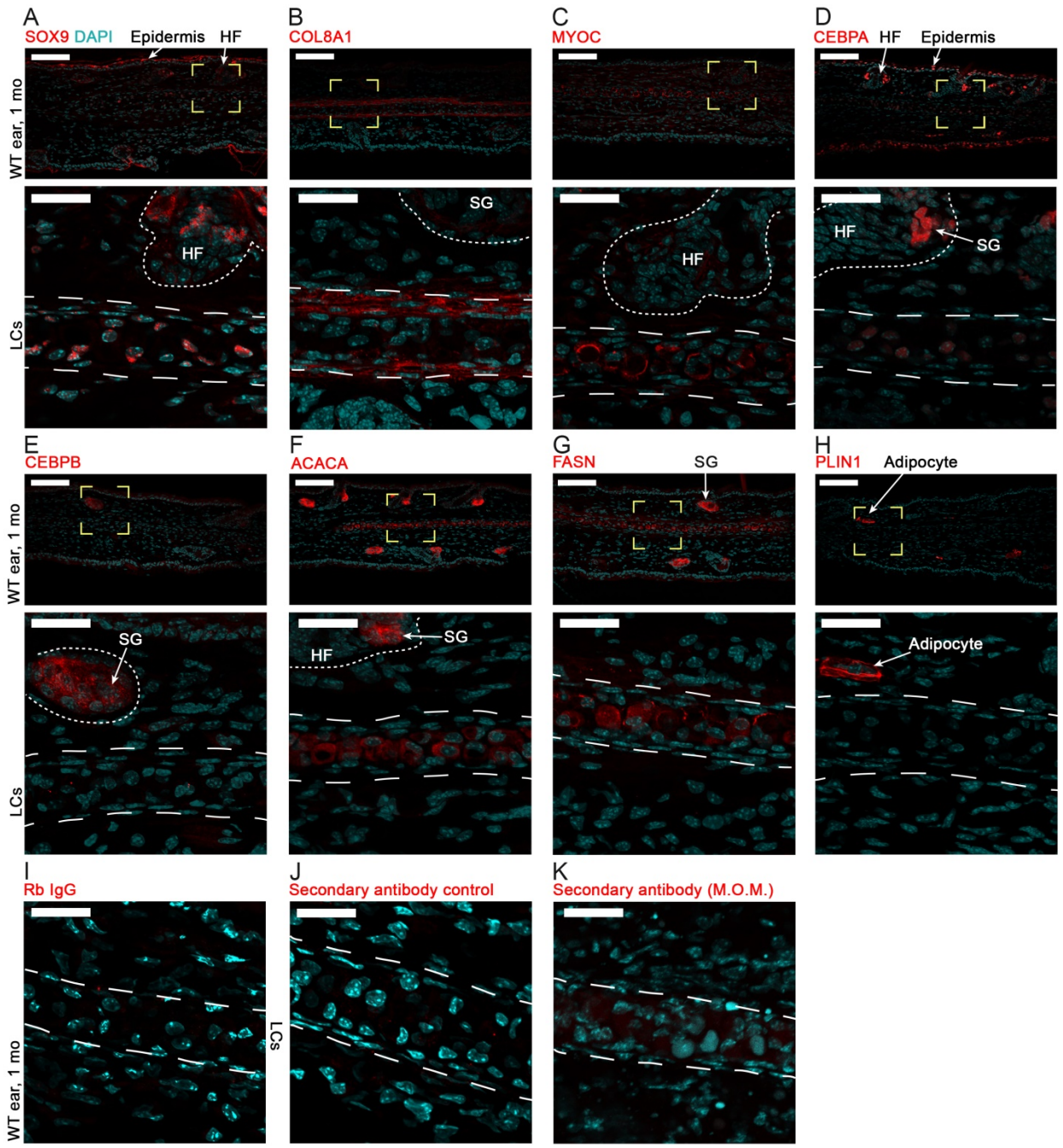


**Figure 3.7: Expression patterns of selected marker genes in one-month-old ear cartilage. (A-H)** LCs show nuclear expression of cartilage lineage master-regulator SOX9 **(A)**. LC-enriched extracellular matrix factors COL8A1 **(B)** and MYOC **(C)** are expressed at the periphery and in the center of the ear cartilage, respectively. LCs express low levels of adipogenesis-associated transcription factor CEBPA **(D)**, and do not express CEBPB **(E)**. LCs also express ACACA **(F)** and FASN **(G)**, key enzymes required for *de novo* lipogenesis, but do not express PLIN1, a lipid droplet-coating protein involved in lipid mobilization and a marker of white adipocytes **(H)**. **(I)** Negative controls show minimal non-specific staining

that contrasts the staining patterns of previous panels **(I-K)**. Epidermis, hair follicles (HF) and sebaceous glands (SG) in the surrounding ear skin are marked and outlined. Immunostaining images shown on **A-I** are representative of the marker staining patterns observed in three or more independently stained samples. Scale bars: G-N (top panels) – 100 μm; G-N (top panels) – 30 μm.

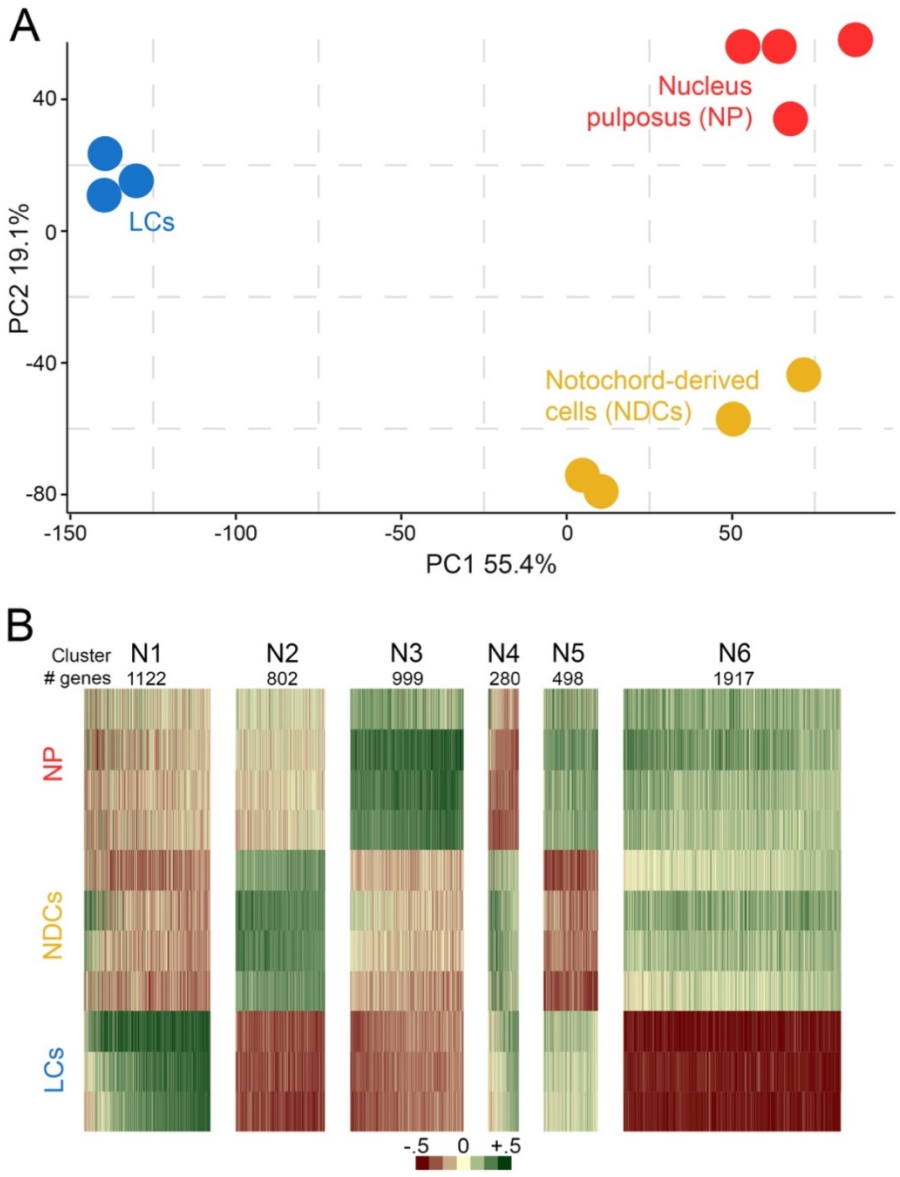


**Figure 3.8: Transcriptome comparisons between lipochondrocytes and notochord cells. (A)** Principal component analysis shows that the transcriptional signature of one-month-old mouse lipochondrocytes (blue, n=3) significantly differs from that of notochord derived cells (NDCs) from E12.5 mouse embryos (yellow, n=4) and nucleus pulposus cells (NP) from P0 mice (n=4). Meta-analysis was performed using RNA-seq data from Peck et al. (2017). **(B)** Heatmap shows that a total of 5,593 genes are differentially expressed between three cell types and they group into six clusters, N1 through N6. LCs – lipochondrocytes, NDCs – Notochord Derived Cells, NP – Nucleus Pulposus.

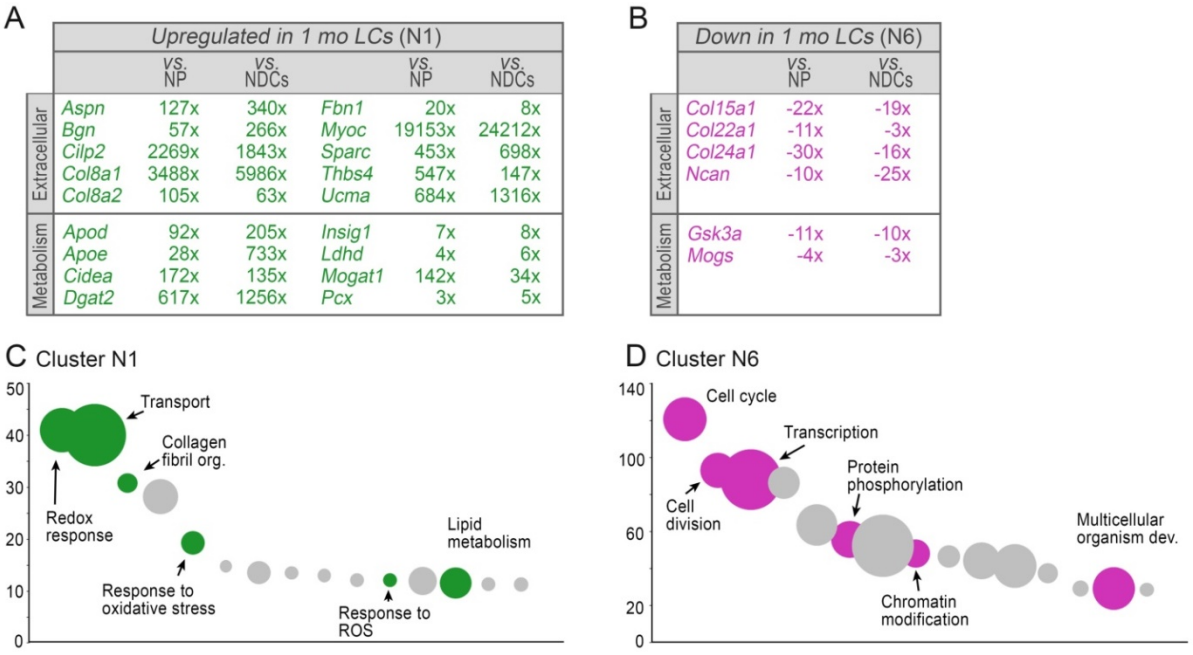


**Figure 3.9: Analysis of differentially expressed genes between lipochondrocytes and notochord cells. (A, B)** List of selected extracellular matrix molecules and metabolic genes differentially upregulated **(A)** and downregulated **(B)** in LCs relative to both E12.5 notochord derived cells and P0 nucleus pulposus cells. **(C, D)** Bubble charts of Gene Ontology terms enriched in cluster N1 from **(C)** – genes upregulated in LCs, and cluster N6 **(D)** – genes downregulated in LCs. Selected bubbles are colored and annotated. Bubble sizes correlate with gene numbers and their vertical position corresponds to significance. LCs – lipochondrocytes, NDCs – notochord derived cells, NP – nucleus pulposus.

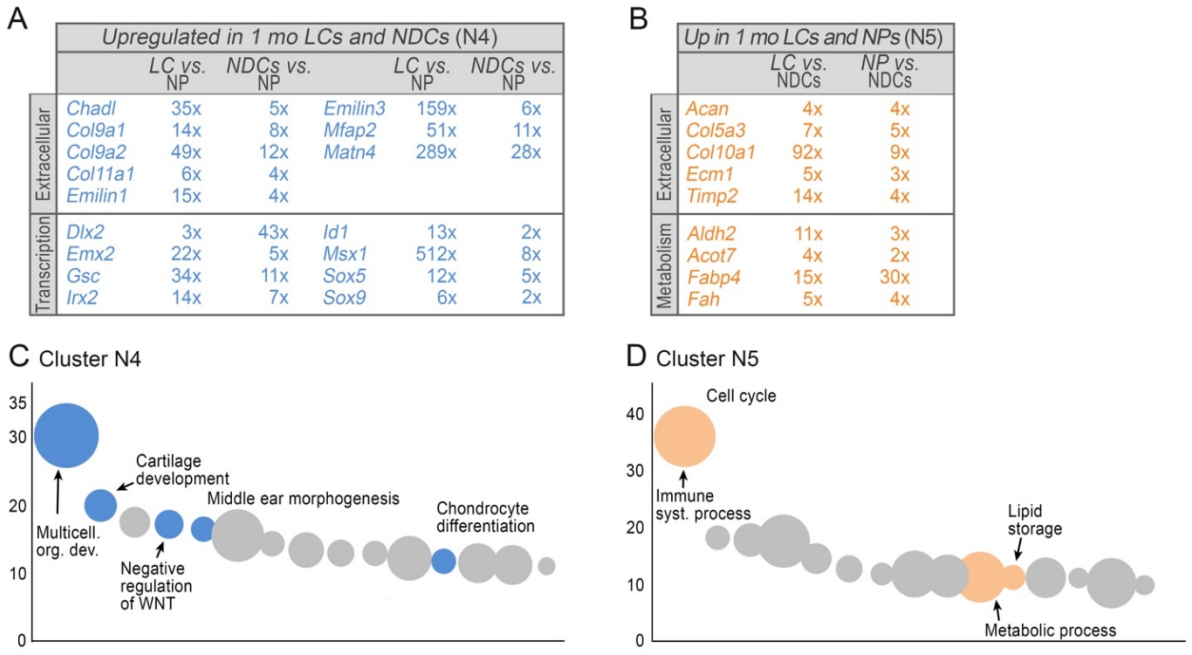


**Figure 3.10: Analysis of signature genes shared between lipochondrocytes and notochord cells. (A, B)** List of selected extracellular matrix molecules and transcription factors shared between one-month-old LCs and E12.5 NDCs, corresponding to cluster N4 in Figure S9B **(A)**. List of selected extracellular matrix molecules and metabolic genes shared between one-month-old LCs and P0 NP, corresponding to cluster N5 in Figure S9B **(B)**. **(C, D)** Bubble charts of Gene Ontology terms enriched in clusters N4 **(C)**, and N5 **(D)**. Selected bubbles are colored and annotated. Bubble size correlates with gene count and their vertical position corresponds to significance. LCs – lipochondrocytes, NDCs – notochord derived cells, NP – nucleus pulposus.

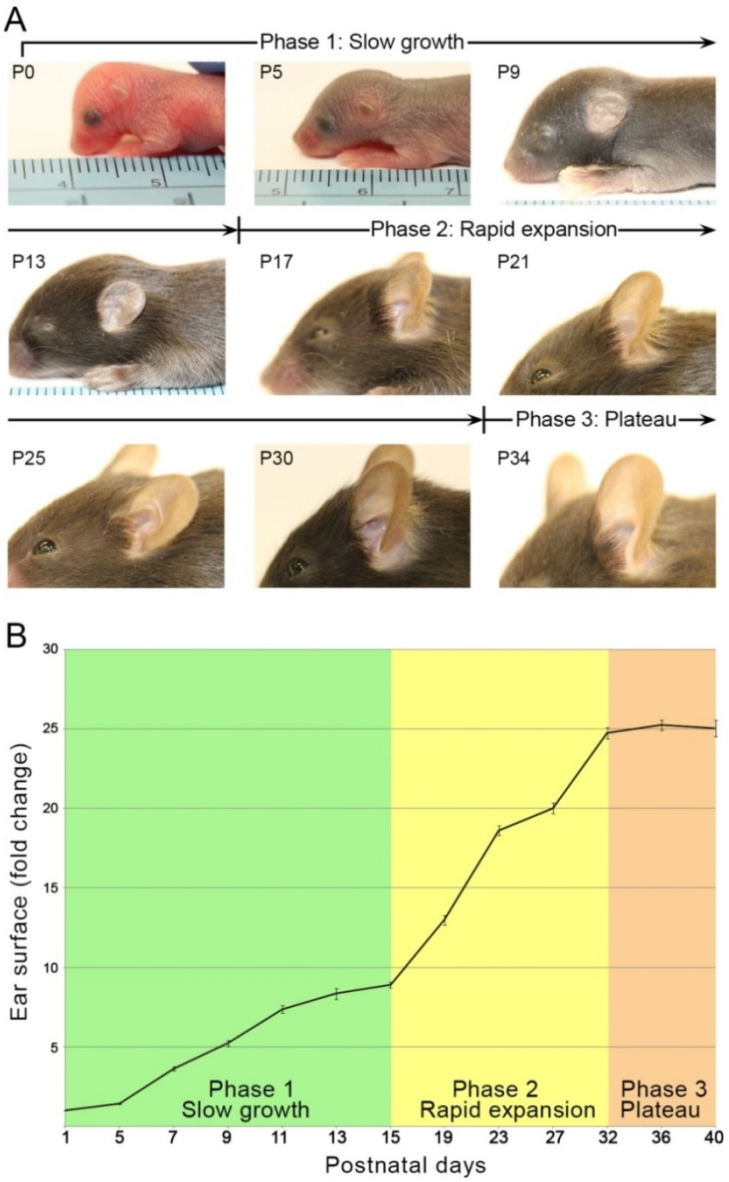


**Figure 3.11: Phases of ear pinna growth in mice. (A)** Ear pinna in mice undergoes significant size and shape changes during the first postnatal month. Images are shown to scale and are marked with postnatal days. **(B)** Quantification of ear surface measurements reveals three phases of ear pinna grows: Phase 1 of slow growth between days P1 and P15, when ears enlarge by approximately nine times (green); Phase 2 of rapid expansion between days P15 and P32 (yellow); and plateau Phase 3 (orange), when ears stop further expansion and become approximately 25 times larger than P1 ears.

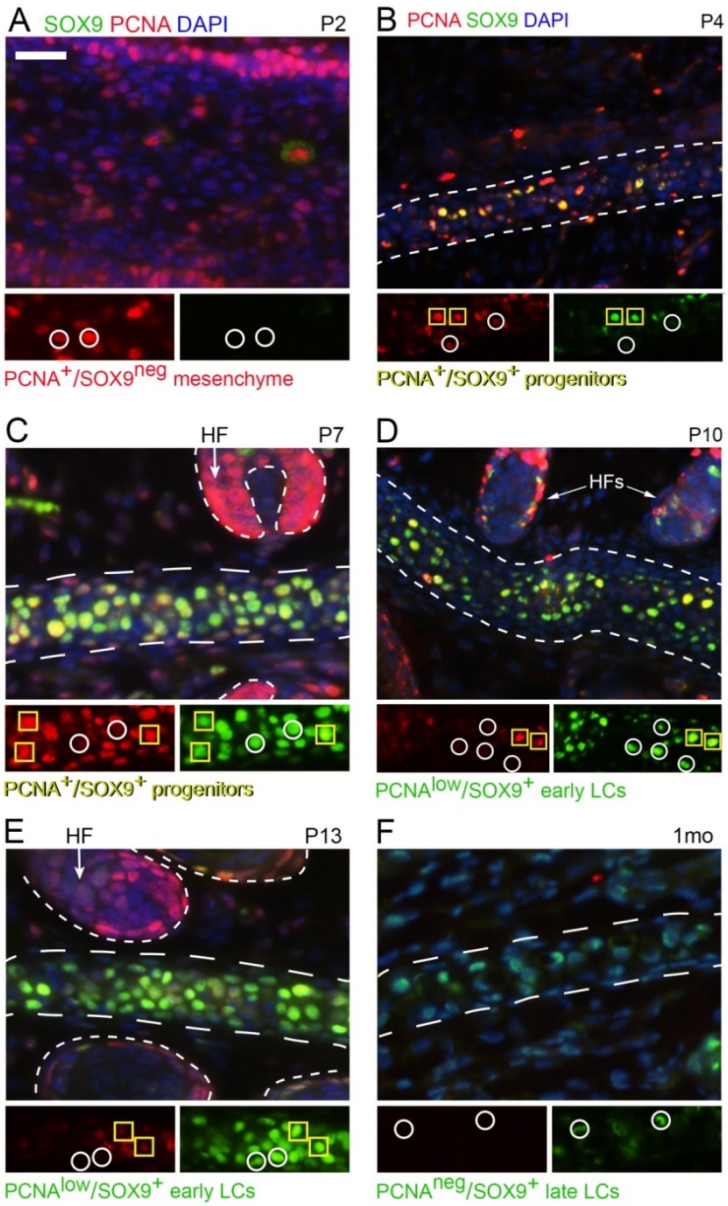


**Figure 3.12: Expression patterns of SOX9 and PCNA in the developing ear cartilage. (A)** Expression patterns of SOX9 (green) and proliferation marker PCNA (red) in the developing ear cartilage at four consecutive postnatal time points, days P2, P4, P7, P10, P13 and 1 month of age. For each time point shown, co-localization of markers is shown on the top panels. Bottom panels show PCNA and SOX9 expression separately within the same region. Single-positive cells are marked with white circles and double-positive cells with yellow squares. At P2, mesenchymal condensate at the site of future ear cartilage (outlined) contains many PCNA-positive cells, but does not express SOX9. At P7, many SOX9-positive LC progenitors appear and a large portion of them co-expresses PCNA. At P13, early LCs remain strongly SOX9-positive, but sharply downregulate PCNA expression. At 1 month, many mature LCs maintain SOX9 expression, but are negative for PCNA. Hair follicles (HF) in the surrounding ear skin are marked and outlined. HFs – hair follicles, LCs –

lipochondrocytes. Images are representative of the marker staining patterns observed in three or more independently stained samples. Scale bar: 25 μm.

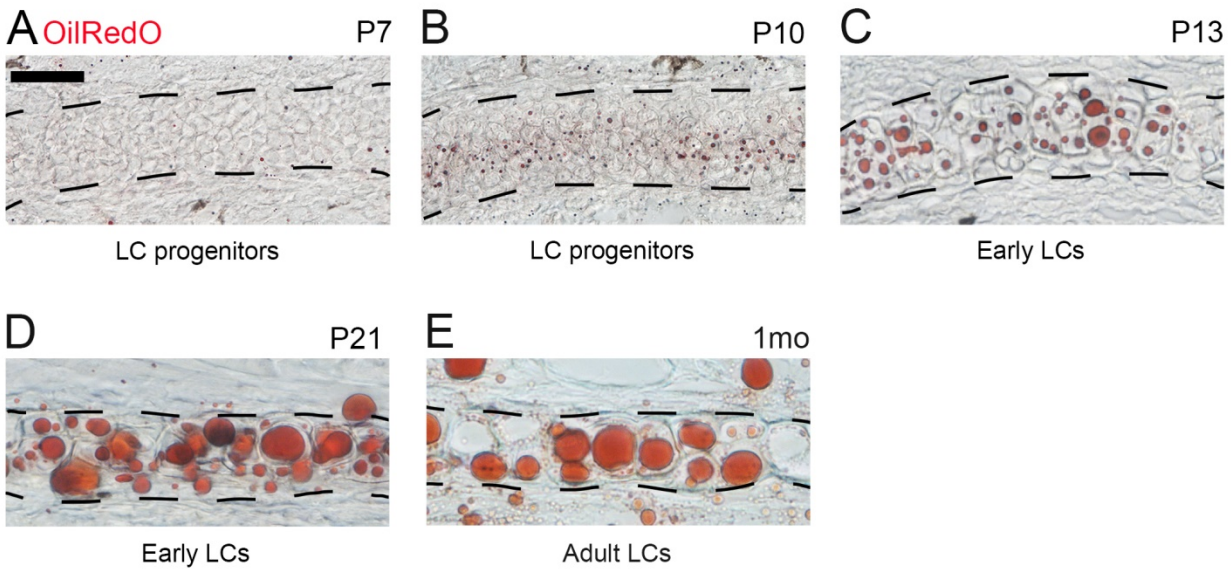


**Figure 3.13: Staining of neutral lipids with Oil Red O shows temporal regulation of lipid accumulation. (A-E)** Oil Red O staining in the developing ear cartilage at five consecutive postnatal time points, days P7, P10, P13, P21 and 1 month of age. First Oil Red O-positive lipid droplets appear between P10 and P13 and then prominently increase in size by P21 and 1 month. Images are representative of the marker staining patterns observed in three or more independently stained samples. Scale bar: 25 μm.

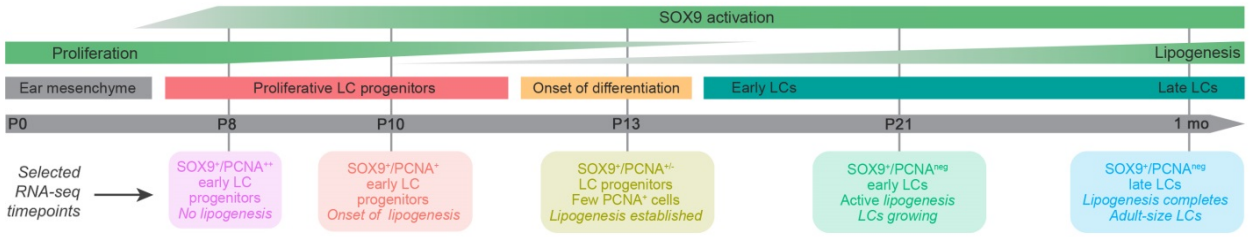


**Figure 3.14: Schematic illustration of the key stages in ear cartilage development.** Major cellular events, such as proliferation and onset of lipogenesis were based on previous documentation by Sanzone and Reith (1976). Although we disagree with some of the postnatal time points assigned by them to each of their 'Stages', their observations serve as an inspiration for our own described here. Patterns of proliferation, SOX9 expression, and lipogenesis are represented as green gradients, depending on their onset or activation, on top. Key stages in ear cartilage development are in the middle (colored bars). Selected RNA-seq time points are at the bottom as colored boxes.

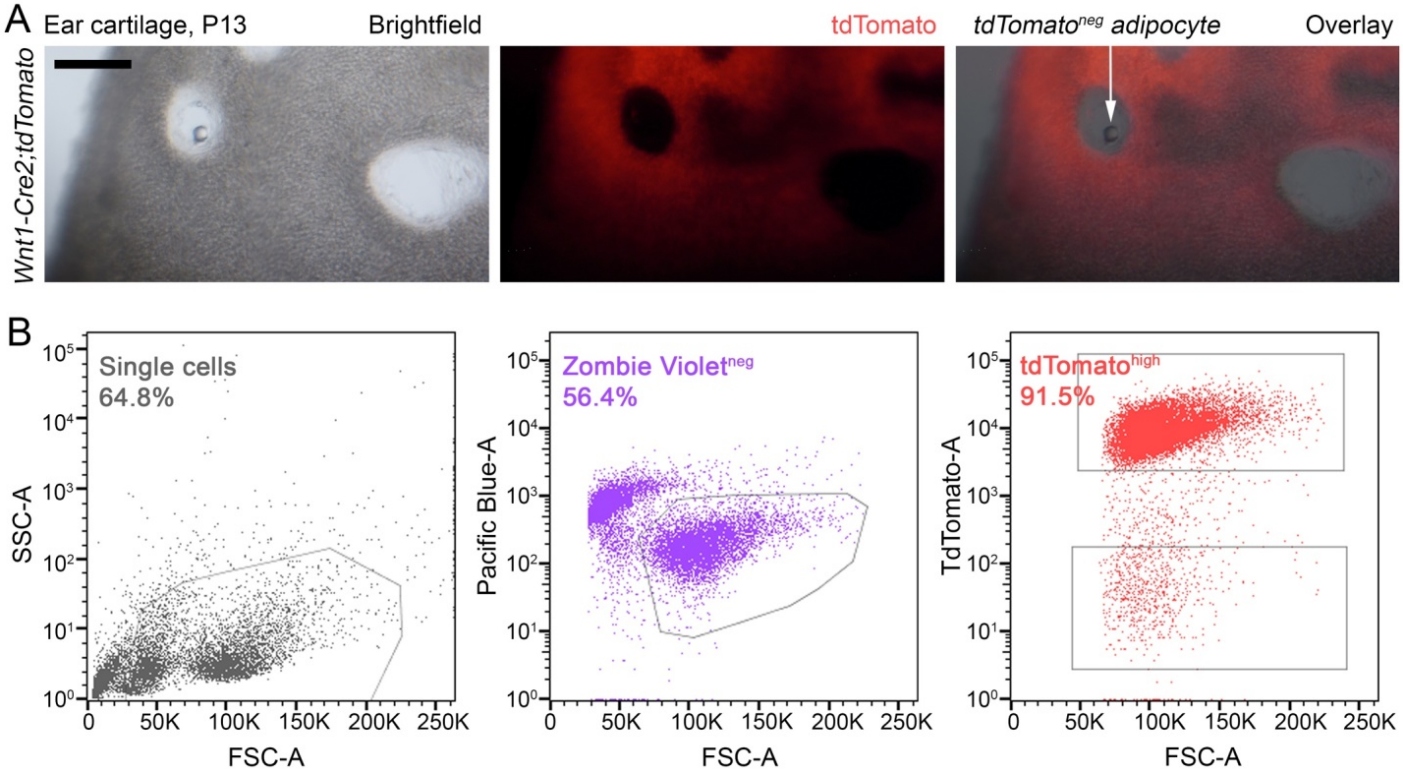


**Figure 3.15: Cell sorting strategy for isolating early lipochondrocytes. (A)** Whole-mount view of microdissected ear cartilage from P13 *Wnt1-Cre2;tdTomato* mouse. Brightfield (left), tdTomato expression (center) and overlay (right) images are shown. A large portion of the ear cartilage is tdTomato$^{+}$. Adipocytes within ear fenestrae are tdTomato$^{neg}$ (arrow on the right). **(B)** Gating strategy for sorting tdTomato$^{high}$ viable (Zombie Violet$^{neg}$) early lipochondrocytes from P13 *Wnt1-Cre2;tdTomato* ear cartilage. Scale bar: A – 500 µm.

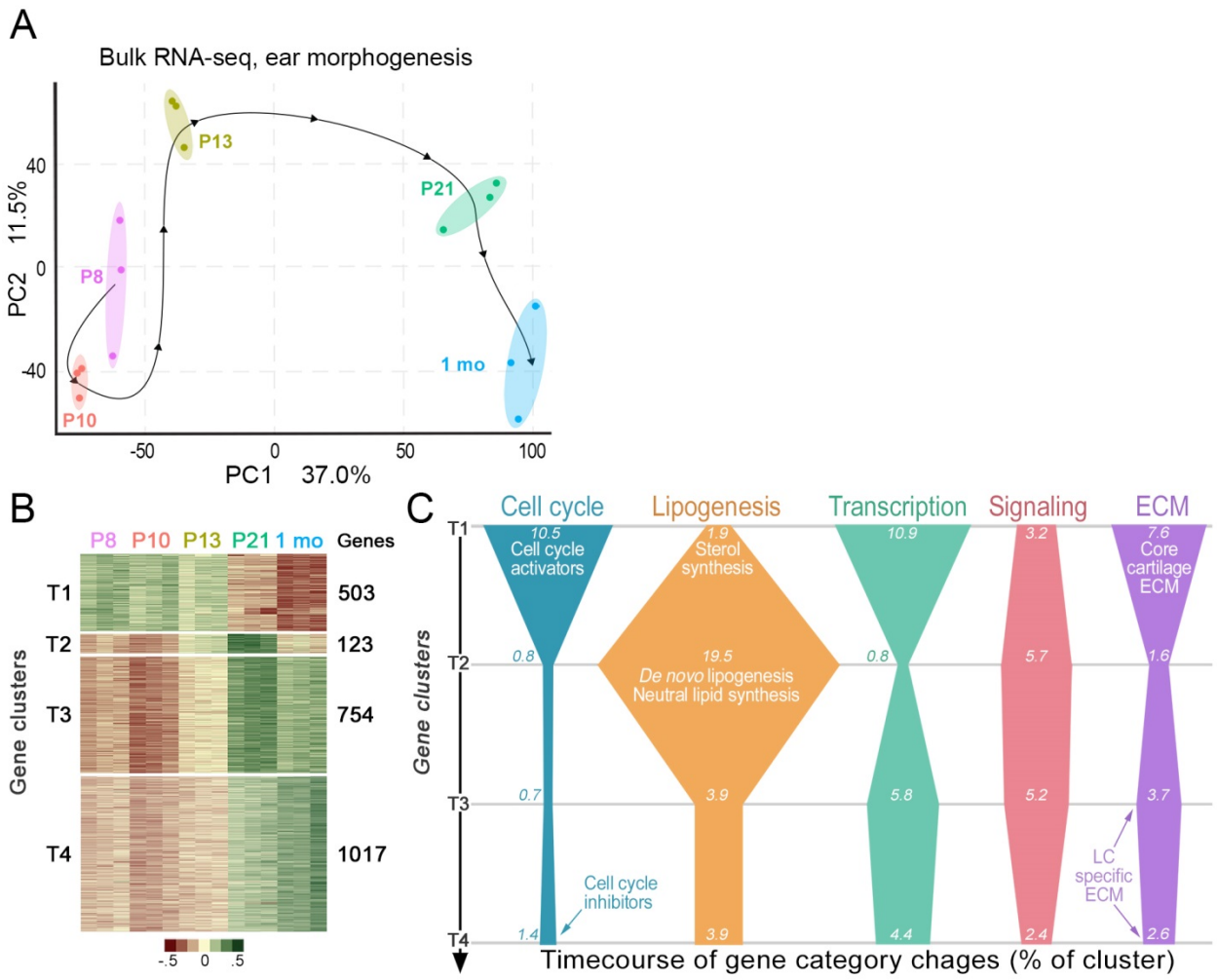


**Figure 3.16: Transcriptome analysis of developing LCs at five consecutive time points between P8 and 1 month reveal prominent time-dependent changes.** Panel (A) shows principal component analysis and panel (B) shows a heatmap of the 2,397 differentially expressed genes that organize into four temporally-dependent clusters. Time points are colored according to panel **Figure 3.14**. Genes upregulated on P8 and P10 constitute cluster T1, transiently upregulated genes on P13 and P21 form cluster T2, and genes peaking at P21 and 1 month constitute clusters T4 and T5, respectively. Relative abundance of genes across clusters T1 (top) through T4 (bottom) within the following categories: cell cycle (teal), lipogenesis (orange), transcription (jade), signaling (red) and extracellular matrix genes (ECM, purple). Graph width corresponds to the percentage of cluster genes.

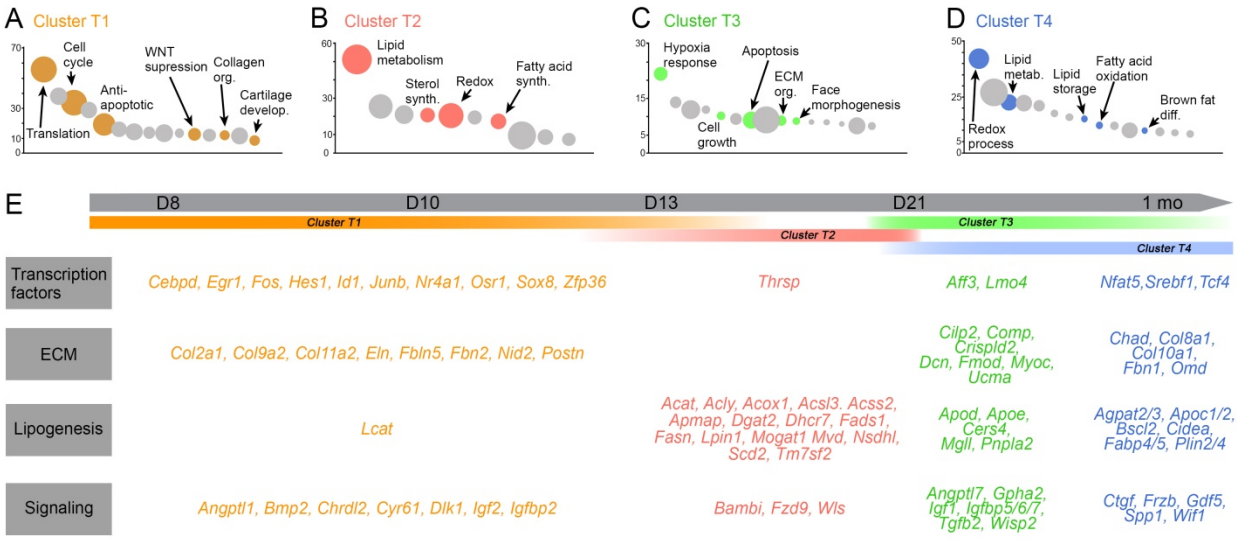


**Figure 3.17: Gene signature analysis of developing LCs at five consecutive time points between P8 and 1 month reveal prominent time-dependent changes.** Table showing selected cluster-specific upregulated genes within the following categories: transcription factors, extracellular matrix genes (ECM), lipogenesis genes and signaling genes. Genes are color-coded by cluster: T1 (orange), T2 (red), T3 (green), T4 (blue).

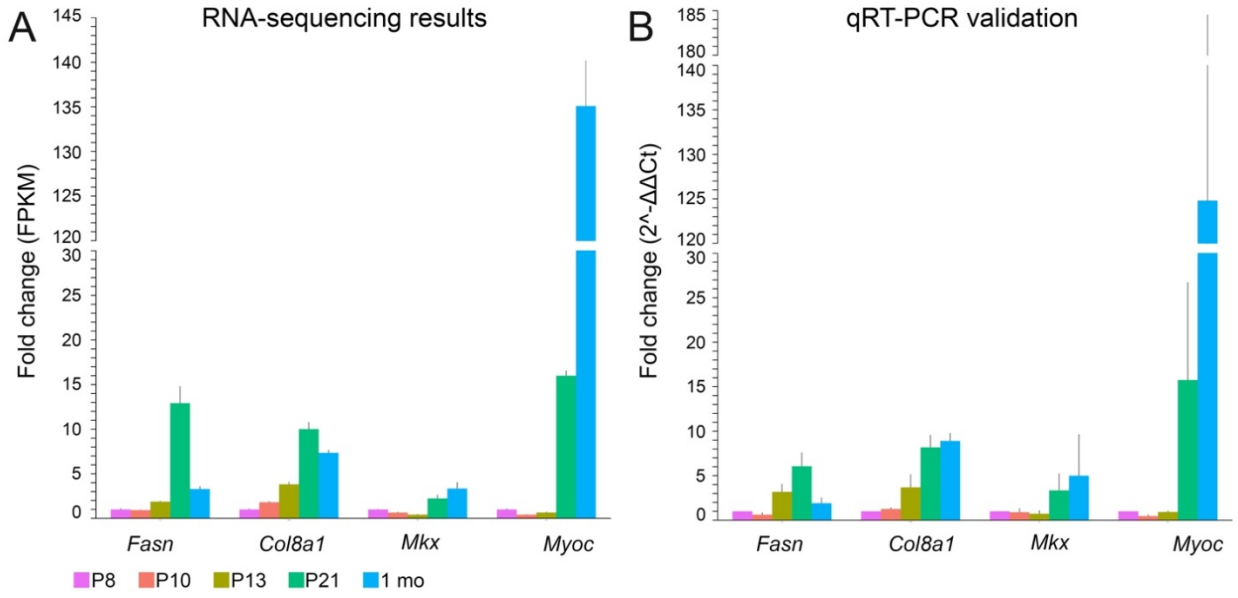


**Figure 3.18: Verification of relative expression dynamics of differentially expressed genes by qRT-PCR. (A)** Fold change of FPKM values of four differentially expressed genes, *Fasn, Col8a1, Mkx* and *Myoc,* during lipochondrocyte development compared to day P8. **(B)** Relative expression of the same four genes during lipochondrocyte development by qRT-PCR. The expression dynamics revealed in our RNA-seq experiments closely match those seen by qRT-PCR.

**Discussion**

LCs, adipocytes, and rib chondrocytes possess intrinsic differences that could be detected by high-throughput approaches. Lipidomics analysis revealed significant differences in the overall abundance of TAG, DAG, and FFAs between LCs and white adipose tissue. Studies have shown that the lipidome of white adipose tissue is dominated by TAGs (<99%), which can be readily mobilized and broken down for future energy use. Our WAT results agree with these observations. Interestingly, the LC lipidome contains a significantly lower proportion of TAGs to other lipid classes, which suggests differences in TAG production, utilization, or both. We also see an increased presence of DAG, FFAs, and other lipids in LCs that serve as precursors of TAG synthesis.

The FFA content in LCs is surprisingly high, however. *In vivo* studies have shown that chronically elevated free fatty acid (FFA) levels can cause apoptosis of pancreatic β-cells via the formation of ceramides, which induce nitric oxide (NO)-dependent cell death and has been proposed to explain the development of type 2 diabetes in obese individuals. Interestingly, TAG buildup has been shown to be an effective "buffer" against FFA lipotoxicity, but TAG levels in LCs are significantly lower in LCs than they are in adipocytes. Further, despite increased ceramide levels in LCs compared to adipocytes, our RNA-sequencing results show that nitric oxide synthase (*Nos2*), which catalyzes the production of NO and is responsible for NO-dependent cell death, is not expressed at any of the developmental time points we studied. Importantly, *in vitro* studies have shown that antioxidant molecules and enzymes can help ameliorate NO-mediated cell death. Our RNA-seq analysis shows that antioxidant enzymes such as superoxide dismutase (*Sod1*) and

glutathione peroxidase (*Gpx*) are expressed at adipocyte levels or higher. This could point to a mechanism by which LCs deal with high FFA buildup. Fluorescence lifetime imaging microscopy has been shown to be able to detect reactive oxygen species (ROS) in an adipocyte model (Datta et al., 2015), and its application to LC biology could prove useful.

In terms of transcriptional program, LCs express many of the genes involved in chondrogenesis, namely expression of SOX family factors *Sox9, Sox5, Sox6*, and *Sox8* during development and in adults. Importantly, P10 LCs express the anti-adipogenic protein Pref-1 (Dlk1), which induces the binding of Sox9 to the promoter regions of C/EBPβ and C/EBPδ and suppress their promoter activity (Wang and Sul, 2009). This is a crucial stage at which LCs begin to accumulate lipids; by using a combination of pro- and anti-adipogenic factors, LCs may achieve their final differentiation program.

Importantly, many of the enzymatic and cell membrane transport elements involved in *de novo* lipogenesis, that is, the production of lipids from glucose precursors, are active during LC development, whereas fatty acid translocases such as CD36 remain off. This could be a mechanism to protect LCs from further, uncontrolled lipid accumulation, which may tie to a highly regulated mechanism to control the final, uniform cell size of LCs.

In terms of structural proteins, LCs express a battery of *bona fide* cartilage collagens, namely *Acan, Col2a1, Col9a2, Col10a1,* and *Col11a2.* Additionally, LCs express specific ECM marker proteins such as *Col8a1/*2, and *Myoc*, otherwise expressed in the retinal epithelium. These proteins may confer the LC with novel elastic or buffering properties that, along with lipids, may give ear cartilage, epiglottis, and nasal capsule their biomechanical properties. Lastly, our meta-analysis of vacuolated notochord cell transcriptome *vs* LCs reveals many similarities in terms of structural proteins. Previously, studies have identified the

notochord as a cartilage-like structure (Tarazona et al., 2016). To better understand the position of all these tissues in the "connective-tissue" lineage tree, more detailed *in silico* approaches will be necessary.

# Chapter IV
# Lipochondrocytes rely on *de novo* lipogenesis and are insensitive to changes in systemic metabolic stress


## Abstract

Our previous lipidomic and RNA-sequencing experiments identified important differences in lipid content and transcriptional control of lipid accumulation, respectively, in LCs compared to WAT, and pointed to a possible mechanism for lipid accumulation in LCs through *de novo* lipogenesis. When challenged with a high fat diet (HFD) or caloric restriction (RCI), adipocytes readily internalize or mobilize lipids, respectively, to compensate for the metabolic changes. We show that lipid-laden LCs have a very stable lipid droplet that remains undisturbed even after chronic metabolic stress. Here, by coupling functional experiments with stimulated Raman scattering (SRS) and fluorescence lifetime imaging microscopy (FLIM), we were able to identify LCs as insensitive to changes in dietary lipids in circulation, trace the dynamic metabolism of glucose in LCs, and observe differences in lipid oxidation between LCs and adipocytes. Chemical inhibition of acetyl CoA-carboxylase 1 (ACACA) and fatty acid synthase (FAS), key enzymes for fatty acid synthesis, we confirmed the reliance of LCs on the pathway. Further, genetic deletion of *Acaca* leads to small, misshapen ears and smaller lipid droplets in ear cartilage. Together, our results demonstrate that LCs rely on *de novo* lipogenesis as a mechanism for morphogenesis, and show that the LC can be used as a valuable tool to study dynamic glucose and lipid metabolism.

## Introduction

LDs are ubiquitous organelles in most cells and most organisms. However, the size of most of these is constrained to a few hundred nm, and they have been shown to be highly dynamic in response to cellular energetic demands. Adipocytes, on the other hand, are able to store lipid droplets of up to a few hundred μm, and mobilize them for further energetic use (Walther and Farese, 2012). Our previous high-throughput analyses have shown that many of the fatty acid transporters used for lipid uptake by adipocytes are not expressed in LCs. Further, saturated fatty acids, the main product of *de novo* lipogenesis, are much more abundant in LCs than they are in adipose tissues. These observations hint at a possible mechanism of lipid accumulation in LCs by *de novo* lipogenesis.

In mammalian cells, glucose serves as one of the most important energy sources, providing the metabolite precursors for *de novo* synthesis of other molecules such as lipids. After glucose internalization, pyruvate is produced as a product of glycolysis. Pyruvate enters mitochondria, and through the tricarboxylic acid cycle (TCA), it is converted to acetyl-CoA and exported to cytosol. Acetyl-CoA, in turn, is used as a precursor for lipid synthesis via the *de novo* lipogenesis pathway through the action of multiple enzymes, including acetyl-CoA carboxylase 1(ACACA) and fatty acid synthase (FAS) (Figure 4.1).

Newly synthesized fatty acids are further esterified and stored in lipid droplets. In contrast, lipid droplet buildup can also be achieved from the incorporation of free fatty acids from lysed triglycerides or by direct uptake from lipids in circulation (Walther and Farese, 2012). *De novo* lipogenesis remains a therapeutically relevant target, as many cancers have been shown to rely on this mechanism for their metabolic need. Because they

are non-metabolizable, fluorescent analogs of glucose can only be used to study glucose uptake, and visualization of *de novo* lipogenesis has remained a challenge. However, recent studies have allowed for the direct visualization of *de novo* lipogenesis *in vitro* using stimulated Raman scattering (SRS), an imaging technique based on the vibrational properties of atom bonds in molecules (Li and Cheng, 2014).

To better understand the mechanisms of lipid accumulation in LCs, we performed a series of functional experiments in combination with novel imaging methods to visualize lipid droplet and glucose dynamics in adult and developing LCs.

## Materials and Methods

| REAGENT or RESOURCE | SOURCE | IDENTIFIER |
|---|---|---|
| Chemicals, Peptides, and Recombinant Proteins | | |
| BODIPY 493/503 | ThermoFisher | D3922 |
| C1-BODIPY-C12 (BODIPY 500/510 C1,C12) | ThermoFisher | D3823 |
| Glucose-d7 | Cambridge Isotope Laboratories | DLM-2062-PK |
| Tamoxifen | Sigma-Aldrich | T5648 |
| Dulbecco's Modified Eagle Medium | ThermoFisher | 11965092 |
| Dulbecco's Modified Eagle Medium (glucose free) | ThermoFisher | 11966025 |
| NaHCO3 | Sigma-Aldrich | S6297 |
| Fetal Bovine Serum | Atlanta Biologicals | S11150H |
| PenStrep | ThermoFisher | 15070063 |
| C75 | Cayman Chemical | 191282-48-1 |
| ND-646 (*aka* ND) | MedChem Express | HY-101842 |
| PF 05175157 (*aka* PF) | TOCRIS | 5790 |
| DMSO | VWR | BDH1115-1LP |
| Experimental Models: Organisms/Strains | | |
| Mouse: *db/db (aka Lepr$^{db/db}$)* | The Jackson Laboratory | JAX: 000697 |
| Mouse: *Acaca$^{fl}$ (aka Acaca$^{tm1Dejs}$)* | (Lee et al., 2014) | |
| Software and Algorithms | | |
| Lipid Droplets Tool for Fiji | http://dev.mri.cnrs.fr/projects/imagej-macros/wiki/Lipid_Droplets_Tool | |

For this chapter, I performed tissue dissections, C1-BODIPY-C12 pulse-chase assays, *ex vivo* ear cultures, chemical inhibition of *de novo* lipogenesis and morphometric analyses. Fluorescence lifetime imaging and its analysis was performed by Rupsa Datta PhD. Spontaneous Raman spectroscopy imaging and measurements were performed by Richard C. Prince. Modified diet experiments were performed in collaboration with Prof. Chao-Chun Yang. Mouse work was performed in collaboration with Tom Burns B.S..

***Experimental mouse models.*** In *Col2a1-CreER$^{T}$; Acaca$^{fl}$* mice, tamoxifen in corn oil was injected IP for four consecutive days starting at P10 at a dose of 75 mg/kg for full induction.

***Modified diet experiments.*** Male C57BL/6J mice were fed *ad libitum* with a high fat chow (n=4) for 39 weeks, starting at P21, or placed under caloric restriction (n=3) for 72 hrs with water only starting at P33. Control mice were fed *ad libitum* with normal chow for 39 weeks starting at P21 (n=3). The obesity mouse model *Lepr$^{db}$* (*db/db*) was fed *ad libitum* with normal chow for 39 weeks starting at P21 (n=3).

***C1-BODIPY-C12 pulse-chase assays.*** One month old male C57BL/6J mice were injected with 200 µl of 20 mM C1-BODIPY-C12 (ThermoFisher) in 1% BSA in PBS via IP, and its incorporation into tissues was analyzed 6 hrs later. For longer term pulse-chase experiments, P10 mice were injected with 200 µl of 20 mM C1-BODIPY-C12 in 1% BSA in PBS via IP every 24 hrs for 8 consecutive days. Tissues were analyzed 6 hrs after the last injection.

***Topical drug treatment.*** C75 (Cayman Chemical), ND-646 (MedChemExpress), and PF 05175157 (TOCRIS) were dissolved individually in DMSO at 40 mM, 5 mM, and 50 mM concentrations, respectively. Twenty µl of either drug were painted on the ears of WT mice for 10 consecutive days, starting at P11. Changes to ear morphology were monitored daily, and final size was measured on day 10 of treatment, at P21. Control mice received topical treatment of DMSO vehicle only (VWR).

***Fluorescence lifetime imaging (FLIM).*** Adult one-month-old mouse ear cartilage plates were microdissected, rinsed in 1X PBS, and mounted in microscope slides. Inguinal adipose tissue was rinsed in 1X PBS, cut into 5 mm squares and mounted. All dissections were performed within 1 hr of imaging. FLIM data was acquired as previously described (Datta

et al., 2015). All FLIM data acquisition and processing were performed with software developed at the Laboratory for Fluorescence Dynamics (LFD, UC Irvine).

***Glucose-d7 ex vivo ear culture.*** Glucose-d7 was purchased from Cambridge Isotope Laboratories. P14 ears were partially dissected by removing the caudal skin flap and exposing the cartilage, then cultured in glucose-d7 containing media. Briefly, glucose-d7 containing media was prepared with glucose-free DMEM (ThermoFisher Scientific), 25 μM glucose-d7, 10% FBS (Atlanta Biologicals), and 1X PenStrep. Tissue was cultured for 72 hours (hrs). Control samples were cultured for 72 hrs in high glucose (25 μM glucose) DMEM, 10% FBS, 1X PenStrep without glucose-d7 added. Samples were changed into fresh media every 24 hrs. All samples were rinsed with 1X PBS twice for 5 min and fixed with 4% PFA for 1 hr before imaging.

***SRS microscopy.*** These experiments were performed in collaboration with Richard C. Prince and Dr. Eric Potma at UC Irvine. For simplicity, a brief description of the experimental setup is included. *Ex vivo* cultured ears were imaged through stimulated Raman scattering to visualize lipid content and track deuterium incorporation into lipid droplets. Stimulated Raman loss was measured using a combination of a fixed stokes beam at 1064nm generated by a 76-MHZ mode-locked Nd:Vanadate laser (Picotrain, High-Q) delivering 7 picosecond pulses and a variable pump beam generated through an optical parametric oscillator (OPO; Levante Emerald, APE) pumped by the second harmonic of the laser at 532nm. For imaging of the CH2 lipid mode, the OPO was tuned to 817nm and for deuterated imaging it was tuned to 868 nm. For stimulated Raman loss, the stokes beam was modulated at 10MHz using an acousto-optic modulator (AOM, Crystal Technology).

After modulation, the two beams are combined and directed into a laser scanning inverted microscope (Fluoview 300 & IX71, Olympus). The SRS signal was collected on an output channel of the lock-in by the synced Fluoview system to form the intensity image. Additionally, linear Raman spectra were acquired for the P14+72hrs ear samples and pure standards using a confocal Raman microscope (InVia Confocal, Renishaw).

***Lipid Droplet size quantification.*** Ear cartilage was dissected and stained with BODIPY as previously described. After imaging and Z-stack acquisition, maximum intensity projections were obtained and the Lipid Droplet Tool plug-in for Fiji was used to calculate lipid droplet size distribution. A Two-sample Kolmogorov-Smirnov test was performed to compare droplet size distributions.

**Results**

Compared to adipocytes, LCs do not express translocase *Cd36* and prominently downregulate transporter *Slc27a1*, both necessary for intracellular absorption of dietary fatty acids. They also do not express perilipin *Plin1* and hormone sensitive lipase *Lipe*, and strongly downregulate *Abhd5, Pnpla2, Mgll,* genes that are necessary for mobilization of neutral lipid vacuoles. This prompted us to ask whether changes in the availability of dietary lipids would affect lipid vacuole morphology and LC size. We placed adult mice for twelve weeks onto high fat diet (HFD) or subjected them to 36 hrs of restricted calorie intake (RCI) and then analyzed ear morphology and lipid vacuole appearance. Compared to regular chow (RC) control mice (n=6), ear area size and LC lipid vacuole morphology do not change significantly in HFD mice (n=6) (Figure 4.2A-A',. 4.2B-B', 4.1E). This is despite significant increases in body weight (Figure 4.2F) as well as dermal and perigonadal WAT size (Figure 4.2G). Moreover, RCI mice (n=3) also do not show significant changes in ear area and LC size compared to control mice (Figure 4.2C-C'), even though their body weight (Figure 4.2E) and WAT depots reduce significantly (Figure 4.1F). We also examined $Lepr^{db/db}$ *(db/db)* mice (n=6), which develop early-onset obesity (Coleman, 1978). Similar to HFD mice, *db/db* animals show a significant increase in body weight and WAT size (Figure 4.2E-F), but no significant changes to ear size or LC lipid vacuole morphology (Figure 4.2D-D', 4.2E).

Considering the low expression of fatty acid transporters *Cd36* and *Slc27a1* from our RNA-sequencing experiments, we hypothesized that lipid uptake rate in LCs would be significantly lower than its adipocyte counterparts. To test this, we compared the uptake of

dietary fatty acids between WAT and ear cartilage by imaging the incorporation of C1-BODIPY-C12, a fluorescently-labeled long chain fatty acid, onto tissues after intra-peritoneal injection pulses (Li et al., 2005). We performed a short pulse-chase experiment by tracking C1-BODIPY-C12 incorporation 6 hrs after a single injection to one-month old mice (n=3). Despite substantial incorporation of C1-BODIPY-C12 into perigonadal WAT (Figure 4.3A, right panels), the probe is not detected in LCs or in fenestrae-bound adipocytes (Figure 4.3A, left panels). We also performed a longer pulse-chase experiment by injecting for 8 consecutive days from P10 to P17, a time window we previously established as critical for lipogenesis (Figure 3.13A-E), imaging 6 hrs after the last pulse (n=3). The probe broadly incorporated into perigonadal WAT (Figure 4.3B, right panels) and also into ear cartilage fenestra-bound adipocytes, but not into LCs of the plate (Figure 4.3B, left panels).

Next, we compared lipid catabolism between adipocytes and ear LCs by performing fluorescence lifetime imaging microscopy (FLIM) on freshly-isolated tissues. Previously, Datta et al. (2015) showed that the phasor approach to FLIM following tissue excitation at 740 nm wavelength can identify an endogenously fluorescent molecular species with long lifetime properties (LLS), and that LLS serve as a reliable label-free marker of lipid oxidation. We used the phasor FLIM approach to compare the LLS distribution between ear LCs, adjacent adipocytes and perigonadal adipocytes. Consistent with Datta et al. (2015), at 740 nm excitation, a strong LLS is detected in ear adipocytes (n=4) (Figure 4.4A, red cursor on left) that localizes to lipid vacuoles (Figure 4.4B, red cursor on bottom panel). In contrast, the LLS signature is absent in ear LCs (n=5) (Figure 4.4A, red cursor on right, Figure 4.4C, red cursor on bottom panel). We conclude that in contrast to adipocytes, adult

LCs form stable lipid vacuoles, insensitive to systemic fluctuations in dietary fatty acid availability, and shielded from lipid mobilization and catabolism even under extreme fasting conditions. Gene expression signature of adult LCs, depleted of key fatty acid transporters and neutral lipid mobilization factors, is consistent with the observed biology.

Our results suggest that despite morphological similarities, lipid metabolism in LCs is distinct from that of adipocytes, and that LCs may form stable lipid vacuoles that are shielded from systemic fluctuations in lipid availability and expenditure. In particular, gene expression data (Figure 3.6C), modified diet experiments (Figure 4.2A-D, 4.2A'-D'), and C1-BODIPY-C12 pulse-chase experiments (Figure 4.3A-B) all suggest that the biogenesis of lipid vacuoles in developing LCs primarily occurs via *de novo* lipogenesis. Therefore, we examined *de novo* lipogenesis in developing ear LCs by imaging the incorporation of glucose-derived deuterium into lipid vacuoles with stimulated Raman scattering (SRS) microscopy, a technique that images molecules on the basis of their vibrational properties (Li and Cheng, 2014; Prince et al., 2016). We cultured microdissected P14 mouse ears for 72 hrs in high glucose media (n=3) or in glucose-free media supplemented with deuterated glucose (G-d7) (n=3). Using SRS microscopy, we can directly visualize LC lipid vacuoles on the basis of a high carbon-hydrogen (C-H) signal (Figure 4.6A), as well as any G-d7 derived lipids on the basis of a carbon-deuterium (C-D) signal (Figure 4.6B). In the Raman spectrum of G-d7 exposed LCs, we observe a C-D stretch signal that matches the C-D stretch signal of pure G-d7, otherwise absent in control glucose exposed LCs (Figure 4.6D, red region). Spatially, C-D signal in G-d7 exposed LCs overlaps with the strong C-H signal, typical of lipid-enriched regions (Figure 4.6D, blue region), indicating that the signal comes

from lipid vacuoles, rather than cytoplasm or extracellular space. This data confirms that differentiating LCs grow lipid vacuoles via *de novo* lipogenesis.

Next, we tested the functional significance of *de novo* lipogenesis during ear cartilage development, by studying changes in ear morphology in mice treated with chemical inhibitors of the *de novo* lipogenesis pathway. Mouse ears were topically treated daily for 11 days starting at P10 (Figure 3.13C-E) with Acetyl-CoA carboxylase inhibitors PF-05175157 (PF) and ND-646 (ND) (Griffith et al., 2014; Svensson et al., 2016) or with C75, a fatty acid synthase inhibitor (Flavin et al., 2010) separately, and compared to DMSO-treated control ears at P21. In all cases we observed reduction in ear sizes (Figure 4.7A-D), with ND and C75 inducing prominently smaller, misshapen ears, 88±2% and 55±7% in size (Figure 4.7E) compared to DMSO vehicle control, respectively. Upon BODIPY staining, P21 ear cartilage from C75-treated mice contained large areas devoid of lipid vacuoles (Figure 4.7F).

We also disrupted *de novo* lipogenesis genetically by inducing cartilage-specific deletion of *Acaca*, one of two acetyl-CoA carboxylases (Lee et al., 2014), in homozygous *Col2a1-CreER$^{T}$;Acaca$^{fl/fl}$* mice. Mice were induced with four daily intra-peritoneal tamoxifen injections starting at P10, and ears were examined at P17. Compared to tamoxifen treated *Col2a1-CreER$^{T}$;Acaca$^{+/+}$* control mice (n=3) (Figure 4.7A-B), and consistent with our chemical inhibition experiments, *Col2a1-CreER$^{T}$;Acaca$^{fl/fl}$* mice (n=3) (Figures 4.8C-D) develop misshapen ears that are 51±12% smaller compared to tamoxifen treated *Col2a1-CreER$^{T}$;Acaca$^{+/+}$* control mice (n=3) (Figure 4.8E). Analysis of lipid droplets in LCs shows a significant reduction in lipid droplet size distribution in mutant LCs compared to control

(Figure 4.8F-H). Gross examination of other chondrocytes in the epiphyseal plate shows that both mutant and control mice display a similar plate architecture (Figure 4.8A-B).

## Figures

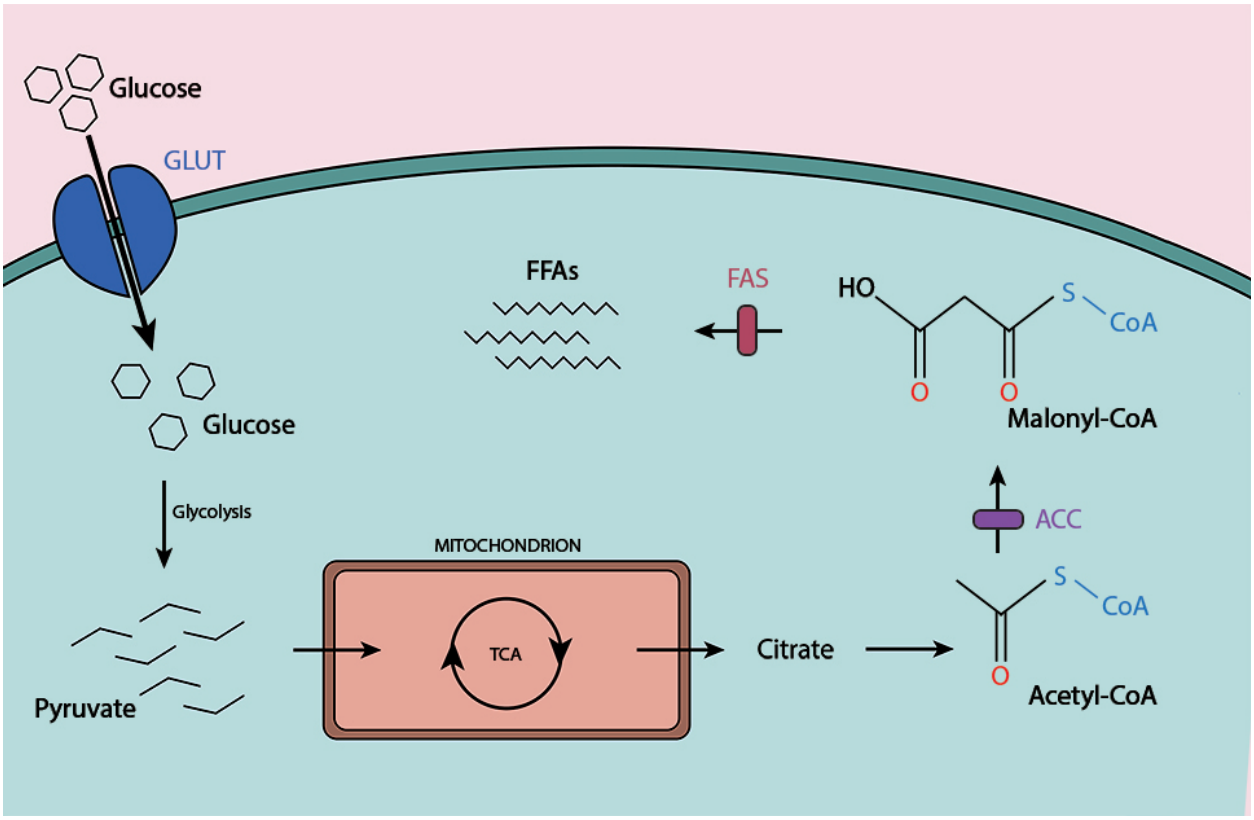


**Figure 4.1: Schematic drawing of main steps in the *de novo* lipogenesis pathway.**

Excess glucose molecules are incorporated into the cell via glucose transporters (GLUT). Glucose breakdown by multiple enzymes during glycolysis releases energy and yields the three-carbon molecule pyruvate, a key intermediate in several metabolic pathways throughout the cell. Pyruvate can then be transported into mitochondria and used as a substrate in the tricarboxylic acid (TCA) cycle, *aka* citric acid cycle to further generate energy. The citrate produced exits the mitochondrion and is converted back into acetyl-CoA by ATP-citrate lyase. Acetyl-CoA carboxylase (ACC) acts on acetyl-CoA to yield malonyl-CoA, which is then utilized by fatty acid synthase (FAS) to generate palmitic acid and other free fatty acids (FFAs).

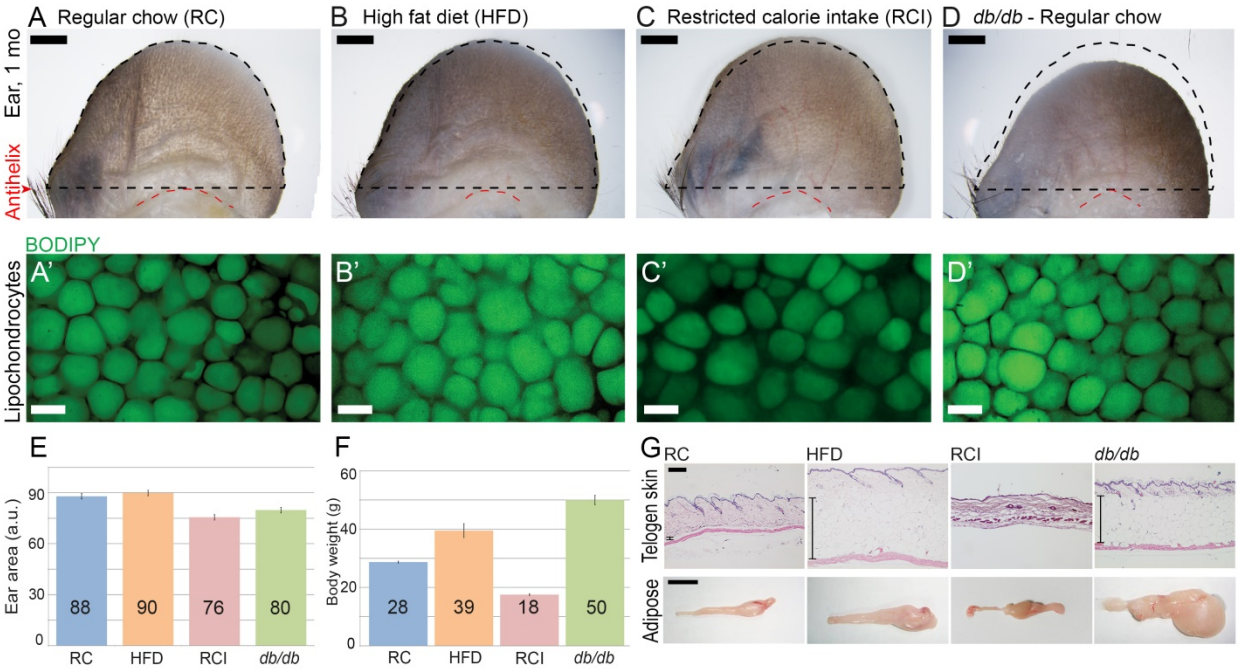


**Figure 4.2: Changes to dietary lipid availability do not alter ear morphology nor lipid droplet size. (A-G)** LC-containing ear cartilage in mice does not significantly change in response to systemic differences in nutrient availability. As compared to control mice on regular chow (RC, n=6) **(A, A')**, ear size as well as the size of individual LCs do not change in mice on high fat diet (HFD, n=6) **(B, B')**, mice on restricted calorie intake (RCI, n=3) **(C, C')** and *db/db* mice (n=6), the model for obesity **(D, D')**. Panels **A-D** show whole mount images of the representative ears, microdissected to expose the cartilage. Panels **A'-D'** show confocal images of ear cartilage stained with BODIPY. **(E)** Ear area measurements (a.u., arbitrary units) confirm absence of significant size differences in HFD, RCI and *db/db* mice as compared to control RC mice. Average ear area values are provided. **(F)** In contrast to ear size, body weight significantly increases in HFD and *db/db* mice and significantly decreases in RCI mice as compared to control RC mice. Average body weight values (in grams) are provided. **(G)** Consistent with the changes in body weight, HFD and *db/db* mice show prominently increased dermal WAT (top panels, histology) and perigonadal WAT (bottom panels, whole mount).

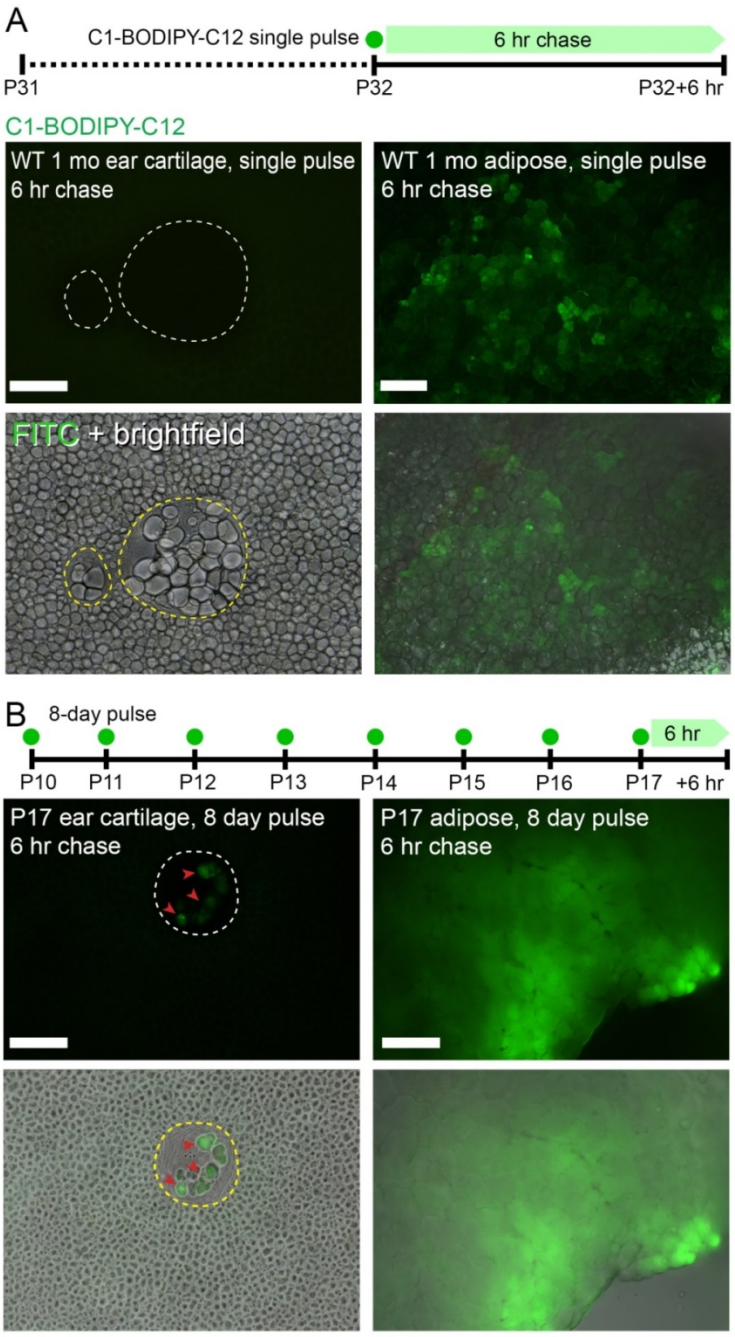


**Figure 4.3: Fluorescently-labeled fatty acids incorporate into adipocytes, but not LCs.** **(A)** Results of the C1-BODIPY-C12 intake experiment 6 hrs following single intra-peritoneal injection to 1-month-old mice (n=3). Top panel shows schematic drawing of the experimental design. Middle panels show FITC fluorescence (green) in the ear cartilage (left) and perigonadal WAT (right). Bottom panels show FITC and brightfield overlays. C1-BODIPY-C12 substantially incorporates into perigonadal WAT, but is undetectable in LCs and fenestra adipocytes. **(B)** Results of long pulse-chase experiment with C1-BODIPY-C12, which was supplied for eight consecutive days, between P10 and P17, and chased for 6 hrs

(n=3). Experimental schematic is shown on the top. Middle and bottom panels show FITC and FITC plus brightfield images, respectively, of ear cartilage (left) and perigonadal WAT (right). C1-BODIPY-C12 incorporates into perigonadal adipocytes, fenestra adipocytes (red arrowheads no the left), but not into LCs.

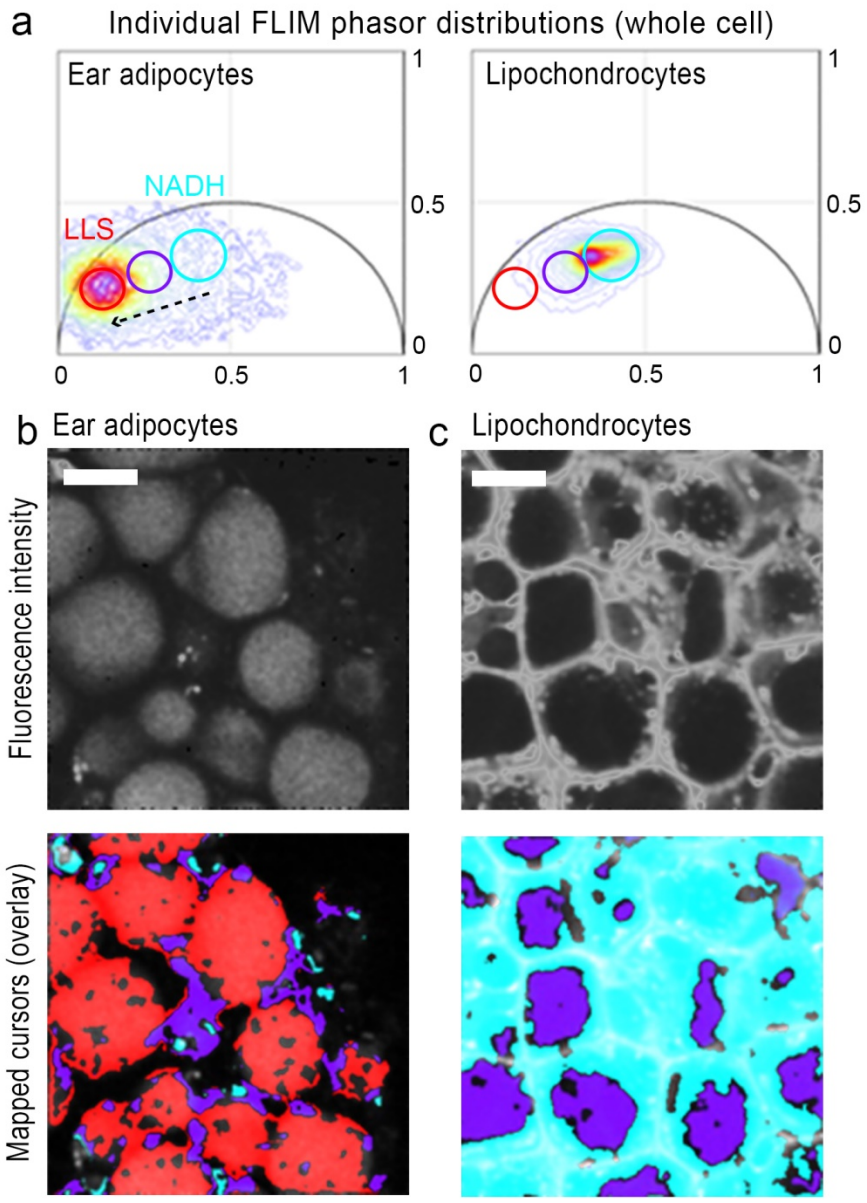


**Figure 4.4: Comparison of FLIM signatures between ear adipocytes and ear lipochondrocytes. (A)** Individual fluorescence lifetime imaging microscopy (FLIM) phasor plots on freshly-isolated ear adipocytes (left) and ear lipochondrocytes (right) following tissue excitation at 740 nm wavelength. Key endogenously fluorescent molecular species, NADH and long lifetime species (LLS), are marked and color-coded. Ear adipocytes, but not ear lipochondrocytes display strong LLS signature. **(B, C)** Mapped cursor overlays of FLIM data onto ear adipocytes **(B)** and ear lipochondrocytes **(C)**. Top panels show endogenous fluorescence intensity and bottom panels show cursor overlays with NADH (blue) and LLSs (red). LLSs map to adipocytes. Purple cursor indicates a fluorescence lifetime distribution in between that of NADH and the LLS. Scale bars: A,B – 20 um.

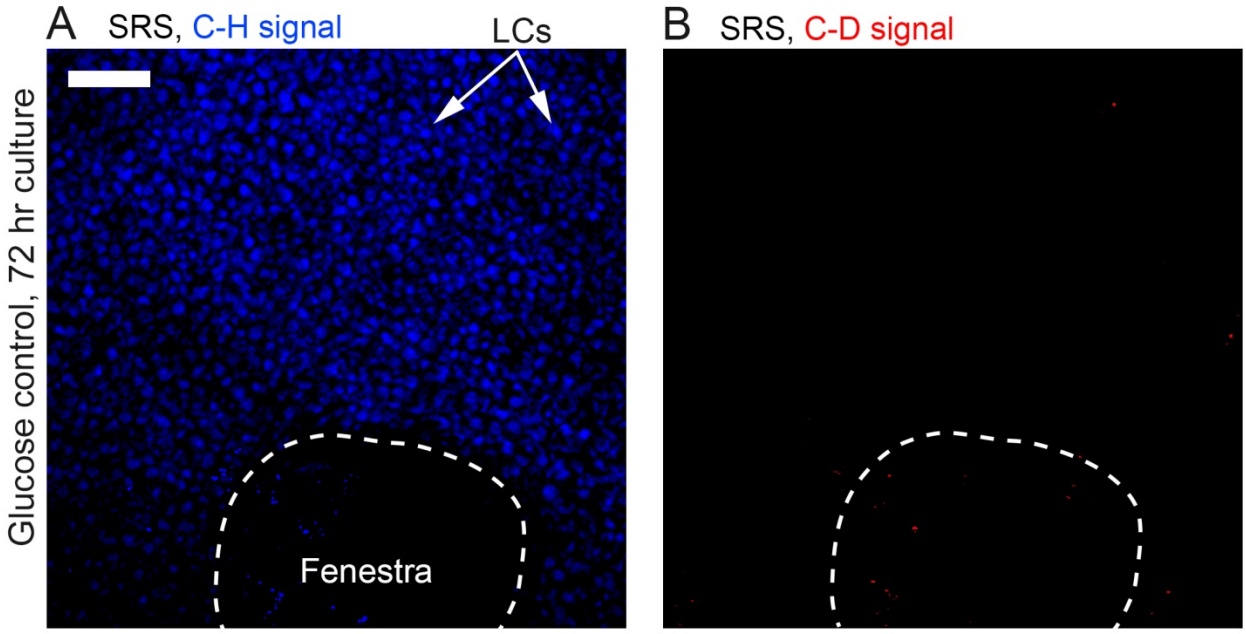


**Figure 4.5: SRS microscopy of cultured ear cartilage in the presence of glucose.** Color-coded stimulated Raman scattering (SRS) microscopy images of P14 ear cartilage after 72 hr of culture in the presence of glucose control. **(A)** Positive SRS signal within the C–H vibration range (~2800-3000 $cm^{-1}$) indicative of lipids and **(B)** SRS signal within the C–D vibration range (~2000-2400 $cm^{-1}$) indicative of deuterated lipids are shown. As expected for this sample, SRS signal within the C-D vibration range is negative. Dashed lines outline ear fenestra. LCs – lipochondrocytes. Scale bar: 50 um.

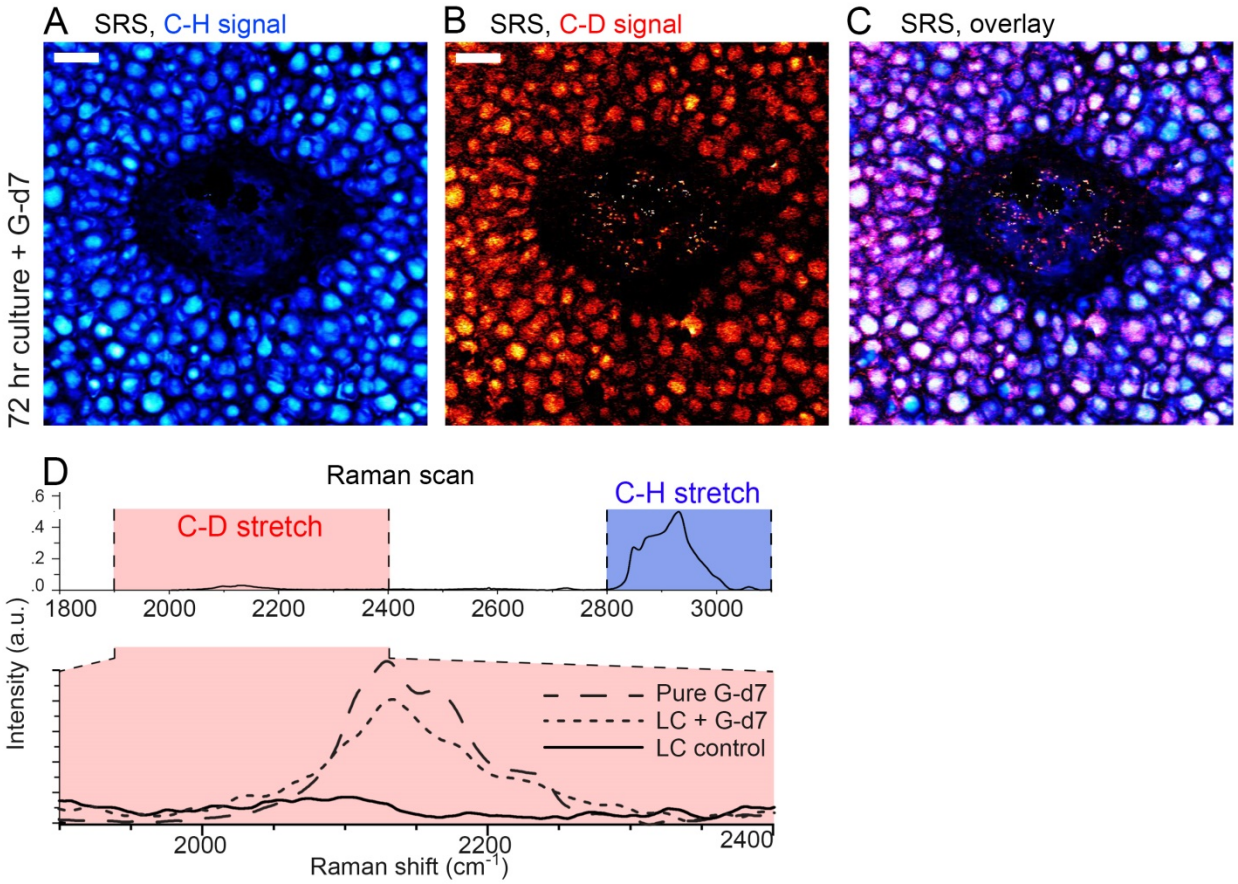


**Figure 4.6: SRS microscopy detects lipids derived from deuterated glucose. (A-C)** Color-coded stimulated Raman scattering (SRS) microscopy images of P14 ear cartilage after 72 hr of culture in the presence of deuterated glucose. Data reveals that glucose-derived deuterium incorporates into lipid vacuoles of developing ear LCs. Color-coded ear cartilage images at C-H vibration range **(A)**, C-D vibration range **(B)** and the overlay **(C)**. Raman scan from deuterated glucose-cultured LC lipid vacuoles shows C-D stretch peak overlaps with C-D stretch peak of pure deuterated glucose **(D, red region)**. Scale bars: A, B – 25 um.

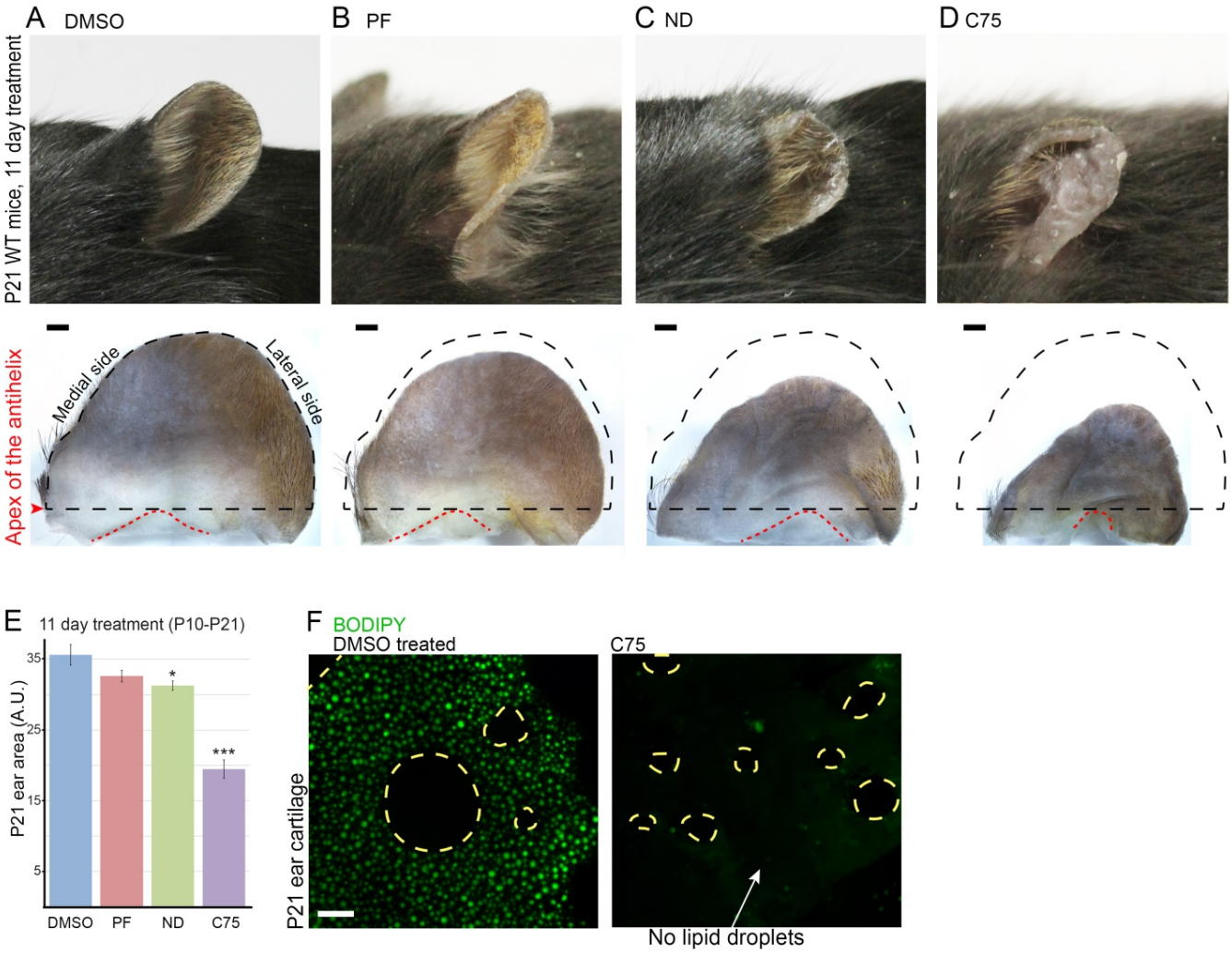


**Figure 4.7: Application of *de novo* lipogenesis inhibitors to the ear leads to misshapen ears and reduced lipid content in ear cartilage. (A-D)** Ears become smaller in mice topically treated with *de novo* lipogenesis inhibitors PF-05175157 (PF), ND-646 (ND) and C75 as compared to DMSO control. Representative mice and ears are shown. **(E)** ND and C75 show significant size reduction compared to control (* represents a p-value < 0.05 and *** represents a p-value of < 0.01 by t-test). **(F)** Portions of C75-treated ears show a prominent decrease in BODIPY$^{+}$ lipid vacuoles. Scale bars: F – 50 um; A-D (bottom) – 1mm.

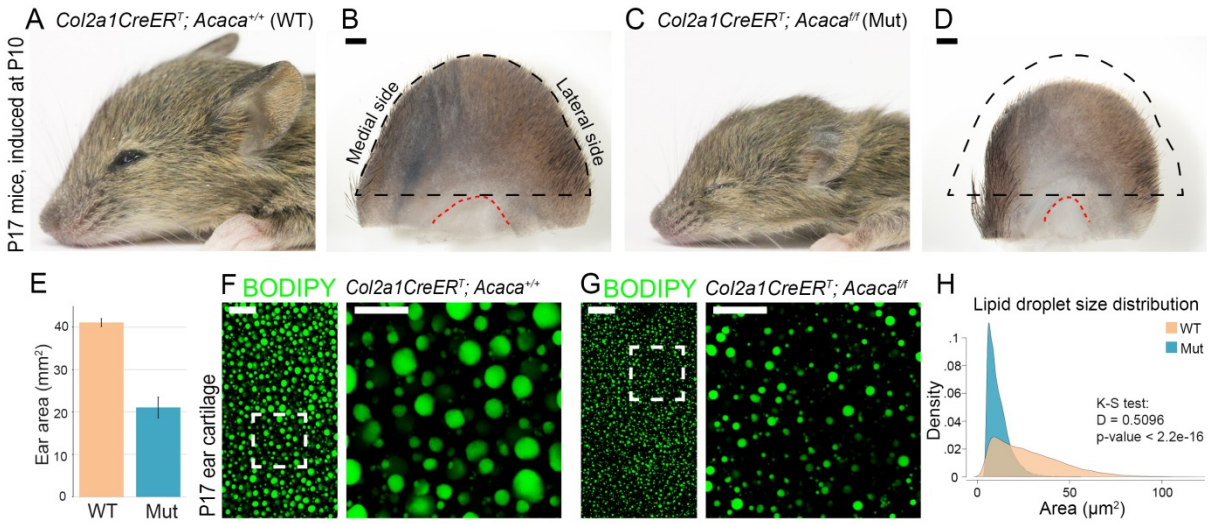


**Figure 4.8: Inducible deletion of *Acaca* in *Col2a1-CreER$^T$;Acaca$^{fl/fl}$* mice results in smaller, misshapen ears and smaller LC lipid vacuoles.** Representative control and mutant mice (**A, C**), ears (**B, C**) and BODIPY-stained ear cartilage (**F, G**) are shown. Size quantification for ear area is on **E** and for ear LC lipid vacuoles is on **H.** Two-sample Kolmogorov-Smirnov test: D= 0.509, p-value <$2.2*10^{-16}$. Scale bars: F, G – 40 µm, inset – 20 µm; B, D – 1mm.

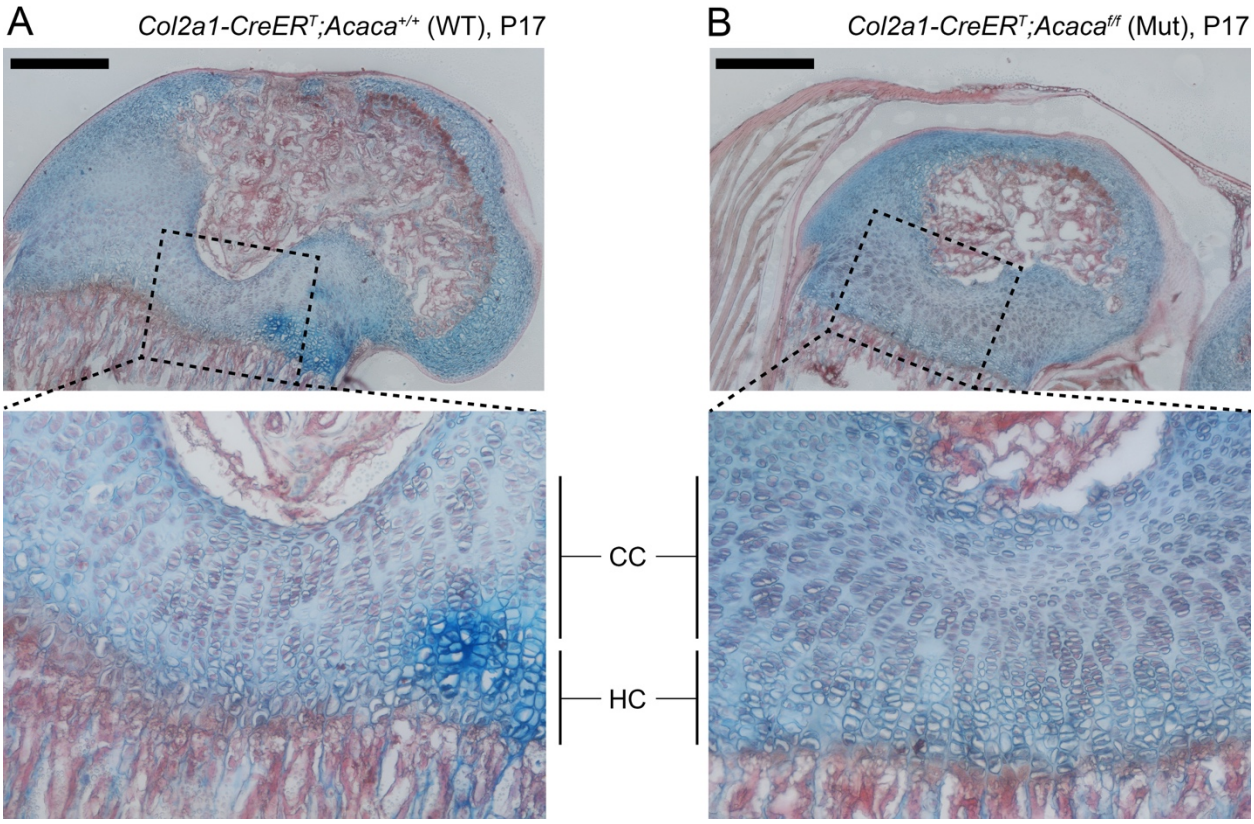


**Figure 4.9: Gross epiphyseal plate anatomy in *de novo* lipogenesis mutant mice.** Representative sections of femoral heads in tamoxifen-induced P17 control *Col2a1-CreER$^{T}$;Acaca$^{+/+}$* **(A)** and homozygous mutant *Col2a1-CreER$^{T}$;Acaca$^{fl/fl}$* mice **(B)** are shown. Both mice display similar epiphyseal architecture, with no gross defects in columnar chondrocyte (CC) or hypertrophic chondrocyte (HC) populations. Sections were stained with Alcian Blue (blue) to detect hyaline cartilage, and counterstained with Nuclear Fast Red (brown nuclei). Scale bars: A, B – 500 μm.

## Discussion

Normally, adipose tissues accumulate energy-rich lipid in lipid droplets, depending on energetic demands. Here we show that LCs are insensitive to changes in dietary lipid availability, failing to incorporate or mobilize lipids out into the bloodstream as a metabolic response, and that LCs use *de novo* lipogenesis as a mechanism for lipid buildup. The fact that these lipids remain undisturbed points to a non-energetic role for them, perhaps as a structural element *per se* or also as a result of lipid signaling. Adjacent, fenestrae-bound ear adipocytes remain metabolically active based on our mouse reporter, fluorescent lipid pulse-chase experiments, and FLIM results, so the location of LCs is not an impediment for them to interact with central metabolic cues. Importantly, and tied to our lipidomics results, FLIM shows a distinct absence of LLS species in LCs compared to adipocytes. These LLS species have been hypothesized to be ROS, and have been proposed as an endogenous biomarker of oxidative stress. In combination with lipidomics and RNA-sequencing, LCs appear to have a highly antioxidant profile, essential for lipid stability and longevity observed.

Because many fluorescently-labeled metabolites are non-metabolizable by the cell, visualizing metabolism in single living cells has remained a significant challenge. By using deuterium labeled glucose and SRS microscopy, we have demonstrated the capability of LCs to accumulate lipids via *de novo* lipogenesis. Recently, *de novo* lipogenesis has been increasingly linked to the metabolism of cancer cells. Higher sensitivity experiments such as mass spectrometry could be used to study energetics and metabolite dynamics in LCs, offering a higher resolution of this mechanism. With higher detection sensitivity, SRS

imaging of LCs could be a powerful tool to study glucose and lipid metabolism in the cell under different conditions in future studies.

Chemical or genetic inhibition of *de novo* lipogenesis leads to misshapen ears, in some cases showing regions of the cartilage plate devoid of lipids. By comparing lipid-laden and lipid-depleted LCs, our model could prove useful to elucidate the structural role of lipids in the ear.

# Chapter V
# Lipochondrocytes are present in the ear cartilage of multiple mammalian orders


## Abstract

The external ear, *aka* pinna, is a distinguishing feature of most extant mammals, with its earliest paleontological evidence dating back to *Eutriconodonta*, an extinct mammalian clade from the Early Cretaceous period. Changes to ear pinna shape and size vary greatly, even among closely-related species, making the ear pinna an ideal model to study the genetic and cellular mechanisms that drive morphological diversity. Our previous analyses as well as past studies by others have revealed many LC-based cartilages in the head of rodents, but the evolutionary prevalence of these cells is still unknown. Here, we show that LCs are a common feature of the mammalian skull in general, present in the majority of all mammalian orders, including several marsupials. Interestingly, LCs can organize into the ridges and valleys in the ears that many echolocating bats rely on for survival, pointing to their ability to build highly precise structures using tightly controlled cell growth mechanisms. Considering their significant presence in marsupials and eutherians, but not in monotremes, we posit that LCs evolved in the last common ancestor to all therians some time during the mid- to late Jurassic.

## Introduction

Mammals (class Mammalia) constitute one of the major vertebrate groups, and are represented across diverse habitats throughout the world with more than 6,000 extant species (Burgin, 2018). Mammals are characterized by the presence of milk-producing glands, middle ear bones, and hair. Within the class, three major groups of extant mammals exist: the monotremes (Monotremata), which includes the billed, egg-laying platypus and echidna; the marsupials (Marsupialia), which nurture their underdeveloped young in a fold or pouch called *marsupium* and include kangaroos, koalas, bandicoots, and possums; and the eutherians (Eutheria), which includes all primates, carnivores, rodents, and many others, making up the majority of all extant mammalian diversity.

Within this last group, four major orders have been established by recent phylogenetic studies: Afrotheria, which includes all species of hyraxes, elephant shrews, elephants, and sea cows; Euarchontoglires, which, among others, includes all primates and rodents —the most speciose order of mammals; Laurasiatheria, of which all species of even- and odd-toed ungulates, whales, carnivores, and bats form a part of; and Xenarthra, constituted by all armadillos and anteaters (Figures 5.1A [Primates labeled with a blue dot for reference] and 5.2). Mammals have adapted to almost every ecosystem on Earth, and as such have evolved a remarkable array of head and body morphologies to overcome distinct evolutionary pressures.

Because of its central role in sensing and feeding, the mammalian head has also been subject to significant morphological diversification. This variation in shape and size arises from multiple different morphogenetic mechanisms. For example, extant

monotremes have a toothless bill and lack external ears. Both marsupial and eutherian animals display variations in skull length between its members, some attributed to known morphogenetic mechanisms. For example, Runx2, which plays important roles in bone development, has been found to also control mammalian facial length. The Runx2 protein contains a repetitive glutamine (Q) and alanine (A) domain. The Q:A tandem repeat ratio has been found to be correlated with facial length in carnivora and primates: species with high Q:A ratios have longer faces than those with lower ratios. This correlation is not present in other mammalian groups like marsupials, xenarthra, or afrotheria.

Fascinated by natural shape and form, German biologist and illustrator Ernst Haeckel paid special attention to bats (order Chiroptera), as the group displays an enormous diversity in craniofacial morphology among its members (Figure 5.1B) (Haeckel, 1904). Modern phylogenetics has greatly complemented the field of evolutionary biology by molecularly defining taxonomic relationships. The study of non-model mammal species can not only help us better understand many of the mechanisms of morphogenesis already established in model mammals, but also aid in the identification of novel cellular and molecular mechanisms of morphogenesis. Meta studies show that despite our confidence in the established taxonomy, most of these relationships have been set based on molecular evidence only, and a significant portion of the mammalian clade remains anatomically uncharacterized (Guillerme and Cooper, 2016). To better understand the prevalence of lipogenesis as a morphogenetic mechanism, we asked what other mammals, in addition to rodents (Anderson, 1964; Bradamante et al., 1991; Kostovic-Knezevic et al., 1981), form LC-based cartilages.

## Materials and Methods

| REAGENT or RESOURCE | SOURCE | IDENTIFIER |
|---|---|---|
| Oil Red O | AMRES CO | 0684-100G |
| Software and Algorithms | | |
| Figtree v.1.4.2 | http://evolve.zoo.ox.ac.uk/software.html?id = figtree | |
| Tissue specimens | | |
| List of species analyzed. See Table 6.1 | See below | |

Tissue dissections, Oil Red O staining, imaging and cataloguing was performed in collaboration with Yuchen Liu B.S., and Cindy Vu. Mammalian ear and facial tissues were kindly provided by Prof. Kimberly Cooper, Prof. Sharlene Santana, Jeffrey Bradley PhD, Prof. Andrew McKechnie, Prof. Frank Breukelen, Prof. Richard Behringer, Scott Weldy DVM, Sandra Schoeniger PhD, and Sandy Ingleby PhD.

***Tissue dissections, Oil Red O staining, and imaging.*** Mammalian tissues were obtained from multiple sources. All tissues were preserved in 10% buffered formalin upon arrival. When possible, whole pinna dissections were performed by removing the rostral and caudal skin flaps, exposing the cartilage plate. For large ears (e.g. Grant's gazelle), 1 $cm^2$ ear pinna pieces were cut, rinsed thoroughly in fresh PBS and mounted in Optimal Cutting Temperature (OCT) medium for frozen sections. Sections were cut at a thickness of 12 μm. After whole mount dissection or sectioning, specimens were submerged in 60% isopropanol for 1 min followed by submersion in 6.25 mg/ml Oil Red O in Isopropanol for 30 min. Specimens were then brought back to PBS through a series of isopropanol reverse gradients, starting at 60% isopropanol, and then imaged.

***Cladograms and phylograms.*** Partial cladograms and phylograms were constructed based on previously curated and published data (Bininda-Emonds et al., 2007). Briefly, Bininda-Emonds generated supertree topologies by combining previously existing trees for Carnivora, Afrosoricida, Eulipotyphla, and Chiroptera with previously published phylogenetic hypotheses based on molecular data and fossil records. Graphics were generated using FigTree version 1.4.2.

| # | ORDER | FAMILY | GENUS | SPECIES | Common name | LCs? |
|---|---|---|---|---|---|---|
| 1 | Afrosoricida | Tenrecidae | *Tenrec* | *ecaudatus* | Tenrec | - |
| 2 | Cetartiodactyla | Bovidae | *Oryx* | *gazella* | Gemsbok | - |
| 3 | Cetartiodactyla | Cervidae | *Odocoileus* | *hemionus* | Mule Deer | - |
| 4 | Cetartiodactyla | Bovidae | *Cephalophus* | *rufilatus* | Red-Flanked Duiker | - |
| 5 | Cetartiodactyla | Bovidae | *Nanger* | *granti* | Grant's Gazelle | - |
| 6 | Carnivora | Felidae | *Puma* | *concolor* | Cougar | - |
| 7 | Carnivora | Felidae | *Leopardis* | *pardalis* | Ocelot | - |
| 8 | Carnivora | Canidae | *Canis* | *rufus* | Red Wolf | + |
| 9 | Carnivora | Ursidae | *Ursus* | *americanus* | American Black Bear | - |
| 10 | Carnivora | Ursidae | *Melursus* | *ursinus* | Sloth Bear | - |
| 11 | Carnivora | Procyonidae | *Procyon* | *lotor* | Raccoon | + |
| 12 | Carnivora | Ailuridae | *Ailurus* | *fulgens* | Red Panda | - |
| 13 | Carnivora | Viverridae | *Arctictis* | *binturong* | Binturong | + |
| 14 | Carnivora | Mustelidae | *Taxidea* | *taxus* | American Badger | - |
| 15 | Carnivora | Canidae | *Canis* | *rufus* | Red Wolf | + |
| 16 | Carnivora | Otariidae | *Zalophus* | *californianus* | Californian Sea Lion | - |
| 17 | Carnivora | Mustelidae | *Lontra* | *canadensis* | North American River Otter | - |
| 18 | Carnivora | Felidae | *Uncia* | *uncia* | Snow Leopard | - |
| 19 | Chiroptera | Phyllostomidae | *Brachyphylla* | *nana* | Cuban Fruit-Eating Bat | - |
| 20 | Chiroptera | Phyllostomidae | *Desmodus* | *rotundus* | Common Vampire Bat | - |
| 21 | Chiroptera | Phyllostomidae | *Micronycteris* | *microtis* | Common Big-Eared Bat | + |
| 22 | Chiroptera | Phyllostomidae | *Trachops* | *cirrhosus* | Fringe-Lipped Bat | + |
| 23 | Chiroptera | Phyllostomidae | *Carollia* | *perspicillata* | Seba'S Short-Tailed Bat | + |
| 24 | Chiroptera | Phyllostomidae | *Glossophaga* | *sorcina* | Pallas'S Long-Tongued Bat | + |
| 25 | Chiroptera | Phyllostomidae | *Artibeus* | *lituratus* | Great Fruit-Eating Bat | + |
| 26 | Chiroptera | Phyllostomidae | *Macrotus* | *waterhousii* | Waterhouse'S Leaf-Nosed Bat | + |
| 27 | Chiroptera | Pteropodidae | *Eidolon* | *helvum* | Straw-Coloured Fruit Bat | - |
| 28 | Cingulata | Dasypodidae | *Dasypus* | *sabanicola* | Llanos long-nosed Armadillo | - |
| 29 | Dasyuromorphia | Dasyuridae | *Dasyuroides* | *byrnei* | Kowari | + |
| 30 | Didelphimorpha | Didelphidae | *Didelphis* | *virginiana* | North American opossum | + |
| 31 | Diprotodontia | Macropodidae | *Dendrolagus* | *matschiei* | Matschie's Tree-Kangaroo | + |
| 32 | Diprotodontia | Macropodidae | *Macropus* | *robustus* | Common Wallaroo | - |
| 33 | Eulipotyphla | Erinaceidae | *Erinaceus* | *europaeus* | European Hedgehog | - |
| 34 | Hyracoidea | Procaviidae | *Dendrohyrax* | *arboreus* | Southern Tree Hyrax | - |

| # | ORDER | FAMILY | GENUS | SPECIES | Common name | LCs? |
|---|---|---|---|---|---|---|
| 35 | Lagomorpha | Leporidae | *Brachylagus* | *idahoensis* | Pygmy Rabbit | + |
| 36 | Lagomorpha | Leporidae | *Oryctolagus* | *cuniculus* | Rabbit | + |
| 37 | Macroscelidea | Macroscelididae | *Elephantulus* | *myurus* | Eastern Rock Elephant Shrew | + |
| 38 | Perissodactyla | Tapiridae | *Tapirus* | *terrestris* | South American Tapir | - |
| 39 | Pholidota | Manidae | *Manis* | *javanica* | Pangolin | - |
| 40 | Primates | Atelidae | *Alouatta* | *caraya* | Howler monkey | - |
| 41 | Primates | Cebidae | *Cebus* | *apella* | Brown capuchin | + |
| 42 | Primates | Cercopithecidae | *Macaca* | *silenus* | Lion-Tailed Macaque | + |
| 43 | Primates | Cercopithecidae | *Erythrocebus* | *patas* | Patas Monkey | + |
| 44 | Primates | Herpestidae | *Suricata* | *suricatta* | Meerkat | - |
| 45 | Primates | Lemuridae | *Lemur* | *catta* | Ring-tailed lemur | + |
| 46 | Primates | Lemuridae | *Varecia* | *variegata* | Black-And-White Ruffed Lemur | - |
| 47 | Primates | Lorisidae | *Nycticebus* | *coucang* | Sunda Slow Loris | - |
| 48 | Primates | Cercopithecidae | *Macaca* | *silenus* | Lion-Tailed Macaque | + |
| 49 | Primates | Cercopithecidae | *Colobus* | *guereza* | Mantled Guereza | + |
| 50 | Primates | Hominidae | *Homo* | *Sapiens* | Human | - |
| 51 | Primates | Atelidae | | *Ateles* | Spider Monkey | + |
| 52 | Rodentia | Castoridae | *Castor* | *canadensis* | North American Beaver | - |
| 53 | Rodentia | Caviidae | *Dolichotis* | *salinicola* | Mara | - |
| 54 | Rodentia | Dipodidae | *Jacus* | *jaculus* | Three-toed lesser Egyptian jerboa | + |
| 55 | Rodentia | Muridae | *Rattus* | *norvegicus* | Rat | + |
| 56 | Rodentia | Muridae | *Acomys* | *cahirinus* | African Spiny Mouse | + |
| 57 | Rodentia | Cricetidae | *Mesocricetus* | *auratus* | Hamster | + |
| 58 | Scandentia | Tupaiidae | *Tupaia* | | Tupaia | + |
| 59 | Soricomorpha | Soricidae | *Sorex* | *araneus* | Shrew | - |
| 60 | Tubulidentata | Orycteropodidae | *Orycteropus* | *afer* | Aardvark | - |
| 61 | Peramelemorphia | Peramelidae | *Perameles* | *nasuta* | Long-Nosed Bandicoot | + |
| 62 | Peramelemorphia | Peramelidae | *Isoodon* | *macrourus* | Northern Brown Bandicoot | + |
| 63 | Diprotodontia | Petauridae | *Petaurus* | *breviceps* | Sugar Glider | + |
| 64 | Diprotodontia | Petauridae | *Petaurus* | *norfolcencis* | Squirrel Glider | + |
| 65 | Monotremata | Tachyglossidae | *Tachyglossus* | *aculeatus* | Short-Beaked Echidna | - |

**Table 6.1: List of mammalian species analyzed.**

## Results

We began by analyzing the secondary head cartilages of the lesser Egyptian jerboa (*Jaculus jaculus)* (Figure 5.2A), a small rodent endemic to Africa and the middle East, and found extensive evidence of LCs in ear, nasal capsule, and laryngeal cartilages (Figure 5.2B-E). Interestingly, some chondrocytes in cartilage elements of the jerboa larynx are negative for Oil Red O (Figure 5.2E, yellow arrowheads in inset). Due to its ease of collection from preserved museum archives, we focused most of our remaining studies on the cartilage of the external ear. Further, the external ear is a distinguishing feature of most extant marsupial and eutherian mammals, and its earliest paleontological evidence dates back to Eutriconodonta, an extinct mammalian group from the Early Cretaceous period (~145 million years ago) (Martin et al., 2015).

We examined microdissected ears from a total of 68 species, covering 4 orders of marsupials, 18 orders of eutherians, and one monotreme, and found ample morphological evidence for LC-based cartilage across the mammalian clade (Table 6.1). Generally, LCs are common in mammalian species with thin, membrane-like ears, irrespective of their phylogeny. Prominent LCs were detected in the kowari *(Dasyuroides byrnei)*, a small, carnivorous marsupial endemic to central Australia. Its ear cartilage features Oil Red $O^+$ LCs arranged in a plate, with large fenestrae occupied by adipocytes (Figure 5.3A, green arrows).

The squirrel glider *(Petaurus norfolcensis)*, another marsupial species, also features Oil Red $O^+$ ear LCs (Figure 5.3B). Many fenestrae in the ear plate of the squirrel glider are occupied by a single hair follicle, a feature rarely observed in other species we examined.

The kowari-like ear cartilage anatomy, with many LCs and large, adipocyte-filled fenestrae is also seen in North American opossum *(Didelphis virginiana)* (Figure 5.3C). Within eutherians, prominent LCs are observed in membrane-like ear cartilages of rufous elephant shrew *(Elephantulus rufescens)* (Figure 5.3D), Cairo spiny mouse *(Acomys cahirinus)* (Figure 5.3E) and several species of bats, including Pallas's long-tongued bat *(Glossophaga soricina)* (Figure 5.3F).

In the latter, LCs are differentially distributed across the cartilage, sparsely along the medial side and in shape of prominent parallel ridges along the lateral side. Each such ridge appears to form via "stacking" of several layers of LCs on top of the base cartilage plate, giving the ear its "ruffled" appearance. Further, we detected Oil Red $O^+$ lipid droplets, indicative of LCs, on histology of the ear cartilage of some primates, including ring-tailed lemur *(Lemur catta)* and brown capuchin *(Cebus paella)* (Figures 5.3G-H). In adult humans, ear cartilage does not contain detectable lipid droplets (Figure 5.3I). In summary, LC-based ear cartilages are widely distributed across the mammalian clade, and are common to both marsupials and eutherians, pinpointing its evolutionary origin to the common ancestor of all therians (Figure 5.4) (Bininda-Emonds et al., 2007). Lastly, and in addition to our results in the lesser Egyptian jerboa, we find evidence of LC-based cartilage in the nasal capsule of the Fringe-lipped bat (*Trachops cirrhosus*) (Figure 5.5A) and the common big-eared bat (*Micronycteris microtis*) (Figure 5.5B)

## Figures

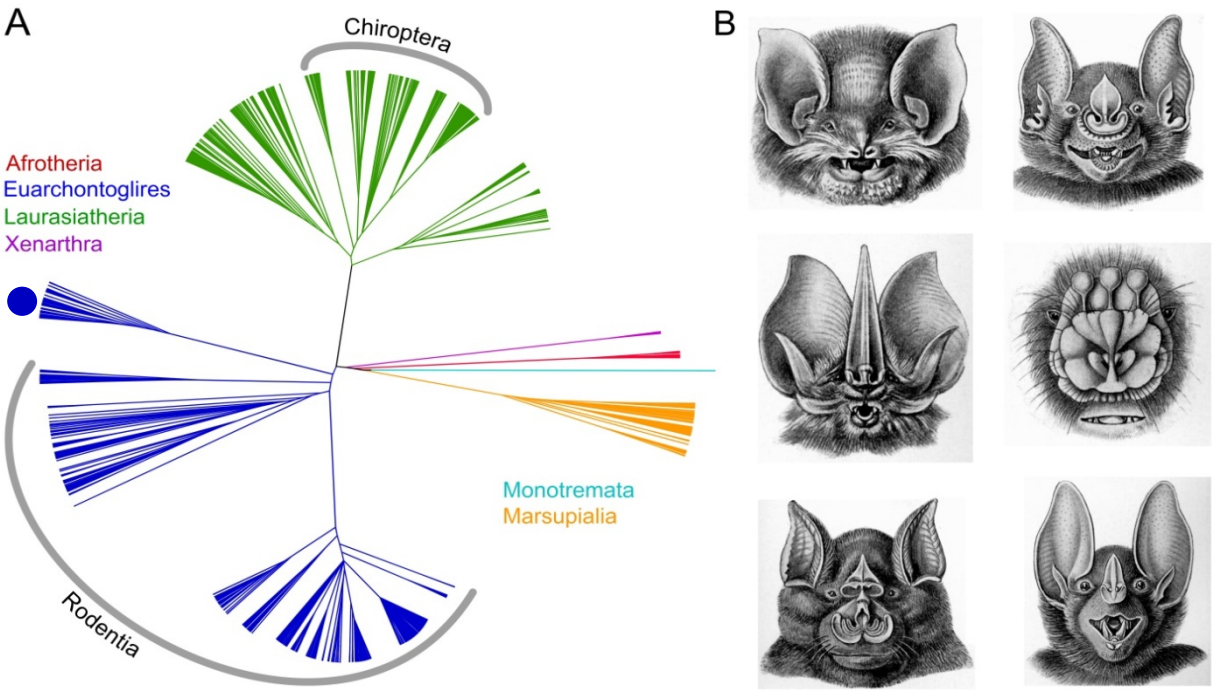


**Figure 5.1: Partial cladogram of mammalia and representative examples of chiropteran facial diversity.** (A) Partial cladogram of mammalia, highlighting major taxa. Rodentia and chiroptera, the first and second most specious mammal clades, respectively, are in grey brackets. Primates are highlighted with a blue dot for reference. (B) Craniofacial diversity in bats (chiroptera), as illustrated by Ernst Haeckel in *Kunstformen der Natur* (Haeckel, 1904). Not in copyright.

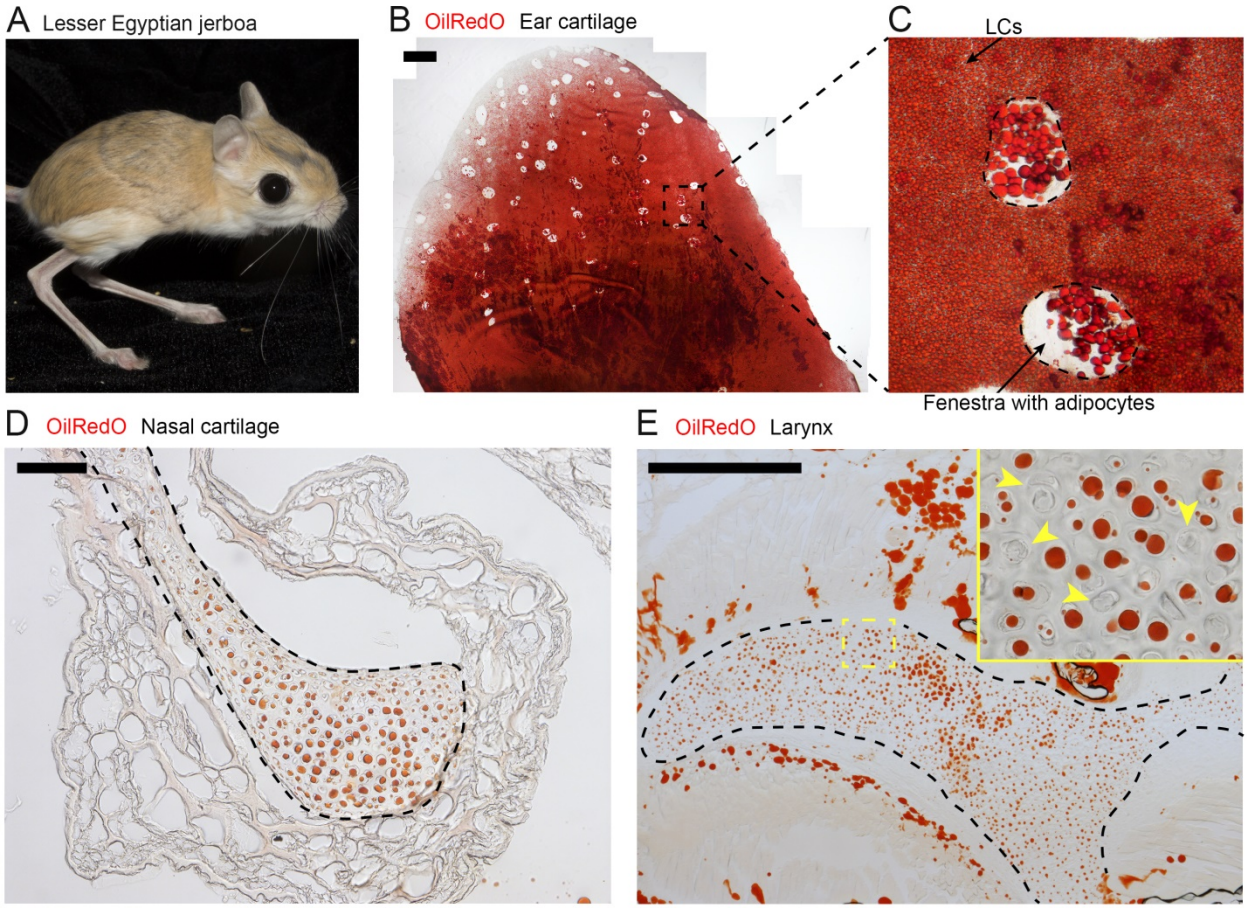


**Figure 5.2: Lipid-laden lipochondrocytes are present in head and neck cartilages of jerboa.** Ear cartilage of the Lesser Egyptian jerboa (*Jaculus jaculus*) **(A)** was stained with OilRedO for neutral lipids **(B)**. The jerboa ear cartilage plate contains lipochondrocytes and is fenestrated **(C)**, in a manner similar to that of mouse ear cartilage. OilRedO staining of frozen sections of nasal tissue **(D)** and larynx **(E)** shows distinct lipid-laden lipochondrocytes. In the epiglottis, multiple chondrocytes lack OilRedO-positive vacuoles (yellow arrowheads in inset), pointing to a "mixed" population of chondrocytes in the tissue. LC – lipochondrocyte. Scale bars: D – 100 µm, E –500 µm, A – 1 mm.

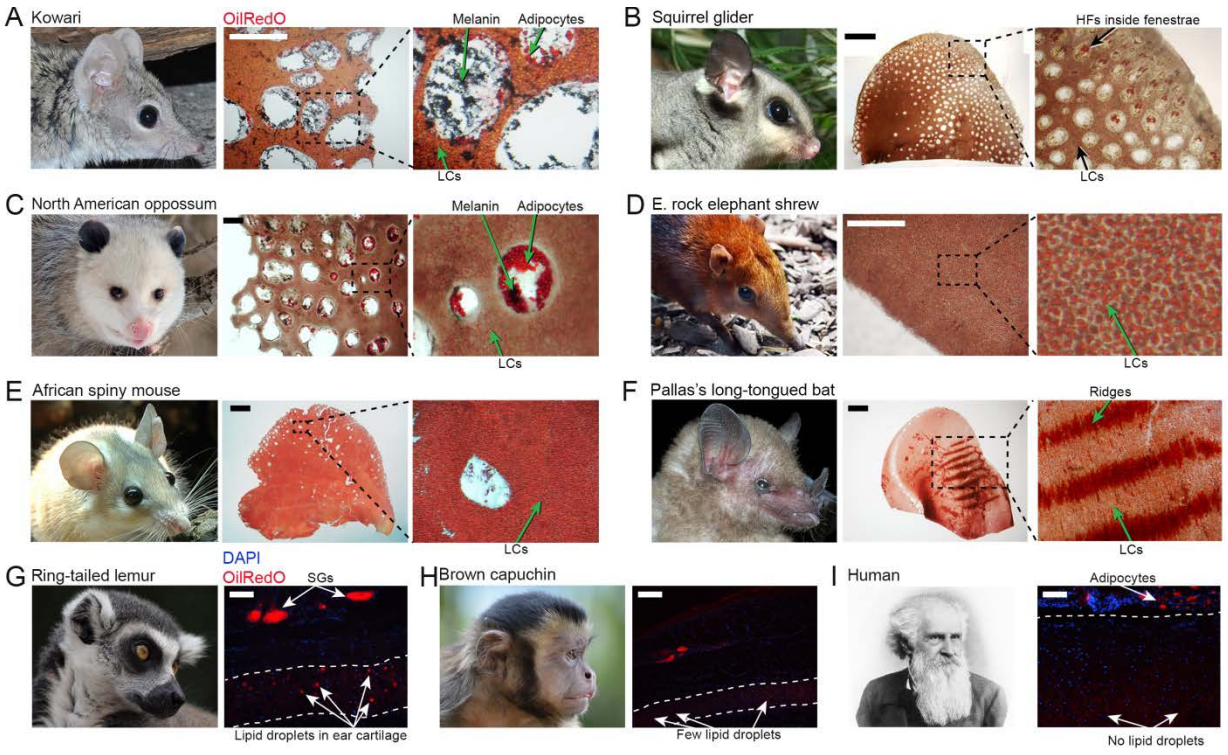


**Figure 5.3: Oil Red O-positive lipochondrocytes are present in multiple mammalian species.** Representative examples of mammalian species that contain OilRedO$^+$ LCs in their ear cartilage. Whole mount OilRedO-stained ear cartilages are shown. Common species names are provided, binomial names are provided in text. HF, hair follicle. **(G-I)** On histology, OilRedO$^+$ LCs are observed in several primate species, but not in humans. Scale bars, **a** – 20 million years; **G-I** – 50 μm; **A, D** – 1 mm; **C, E, F** – 2 mm; **B** – 5 mm.

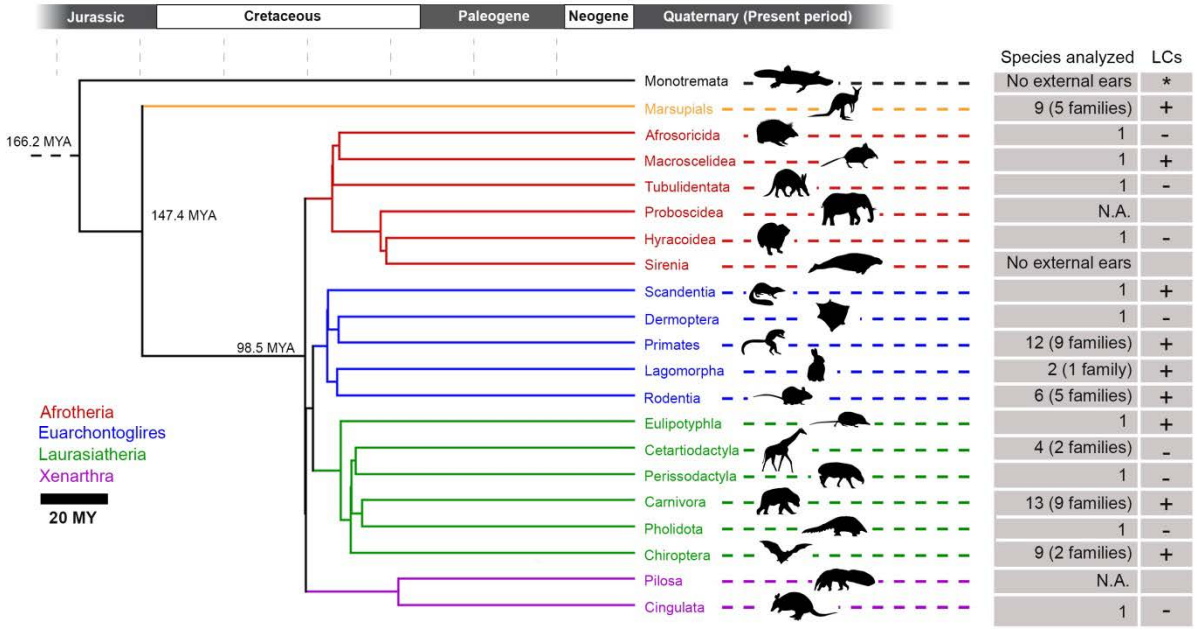


**Figure 5.4: Summary of the distribution of OilRedO⁺ cartilage in the mammalian clade.** Partial mammalian phylogenetic supertree is shown along with information on the number of analyzed species and evidence of OilRedO$^+$ LCs (right box). Scale bar: 20 million years.

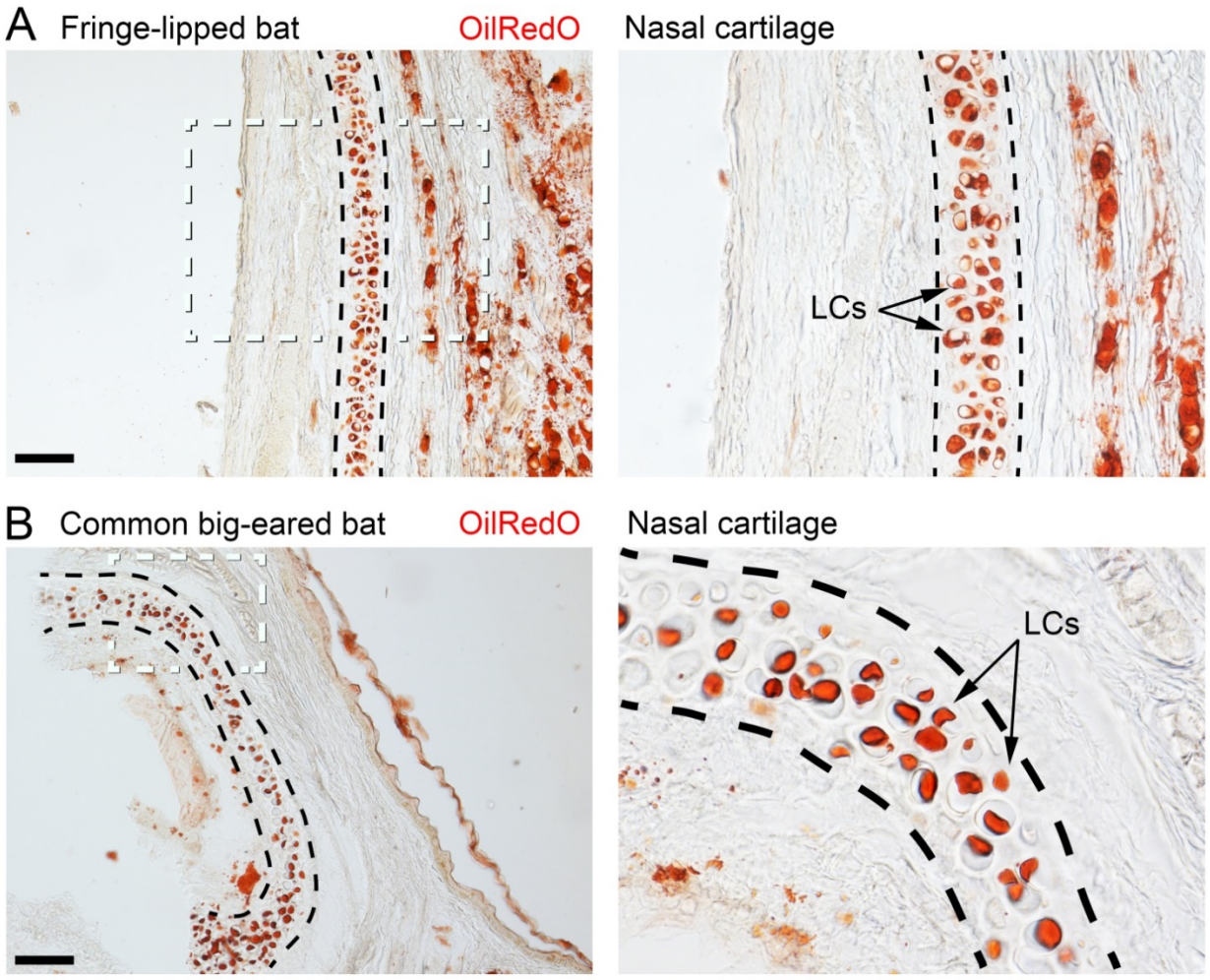


**Figure 5.5: Presence of lipid-laden lipochondrocytes in the nasal cartilage of bats.** OilRedO staining of frozen sections of nasal tissue from **(A)** Fringe-lipped bat *(Trachops cirrhosis)* and **(B)** Common big-eared bat *(Micronycteris microtis)* reveals the presence of distinct lipid-laden lipochondrocytes. LC – lipochondrocyte. Scale bars: A, B – 200 µm.

## Discussion

Here, we show that LCs are a prevalent cell type widely distributed in the mammalian clade. We notice a tendency for LCs to comprise cartilages of thin, membrane-like ears but not in thick, fleshy ears. This points to an architectural role for LCs that maintains the rigidity of these thin structures, but without compromising their flexibility. As pointed out by Socrates more than two millennia ago, prominent structures like those of the ears and nose need to be pliable. As tissues scale down in size, ECM-based cartilages become an unfeasible option, as the shape and size of the ECM cannot be directly controlled, which would lead to amorphous structures.

Interestingly, the so called melon in the head of cetaceans is also rich in lipids. Used as an acoustic lens, the cetacean melon also relies on the stability of intracellular lipid droplets, and it has been shown that the tissue maintains its adiposity even in starving animals (Cranford et al., 1996). Considering that LCs are present in many structures important for the production, amplification, or pickup of sound signals, it's possible that the lipids in LCs are also playing an important acoustic role. Future functional and behavioral experiments could prove very useful in determining this.

Studies in invertebrates have revealed the presence of vacuolated cartilages in the gill book of horseshoe crabs (*Limulus*) as well as the zebrafish fin. These cells, to our knowledge, do not accumulate lipids in the same manner that mammalian LCs do. However, other studies in zebrafish have identified *bona fide* adipocyte populations derived from hypertrophic chondrocyte populations, highlighting the intimate relationship

between these two cell lineages. Future studies are still needed to completely identify the evolutionary origin of LCs in vertebrates.

# Chapter VI
# Conclusion

The skeletal system has been a matter of interest for millennia. To the researcher, it offers an excellent model to study mechanisms of cellular differentiation, tissue morphogenesis, and programmed cell death (Hall, 2015). Cartilage is an essential component to the system, as it serves important patterning and supporting roles in both embryonic and adult life stages. Much of our understanding about the morphogenesis of the skeleton comes from studies on endochondral cartilages: those that form the embryonic templates of future bones. However, endochondral cartilage is only one of the many types of cartilage tissues found across vertebrates. A more thorough understanding of cartilage biology, from its mechanisms of embryonic specification to its maintenance and repair in adult organisms requires the study of other chondrocyte types. In the preceding chapters, I presented novel findings regarding lipochondrocytes (LCs) —lipid-filled cartilage cells present in multiple facial cartilages across the mammalian taxon, including a characterization of their lipid stores, their transcriptome, and lipid metabolism. Further investigation of this cell type will lead to important insights into the mechanisms behind cartilage lineage specification, metabolism, and phenotypic maintenance. Moreover, unlike bone, cartilage tissues regenerate very poorly *in vivo,* and an established model for the study of cartilage regeneration is currently lacking. Partial evidence of ear cartilage regeneration exists in some animal models (e.g. increased proliferation and collagen deposition after injury) (Seifert et al., 2012; Zhang et al., 2017), but a thorough analysis of the LC regenerative potential remains to be performed. Such a study could establish LCs as a convenient model system for the study of mechanisms of adult cartilage regeneration – an

important but yet unmet medical need. Below, I will discuss some of the most recent knowledge regarding chondrocyte lineage specification, regeneration, and evolution, as well as propose further experiments to better understand LC differentiation, repair, metabolism, and function.

Abbreviations:
SSC – Skeletal Stem Cell
OCP – Osteochondroprogenitor
JCP – Joint Chondroprogenitor
LCP – Lipochondroprogenitor
GPC – Growth plate chondrocytes
ACC – Articular chondrocytes
LCs – Lipochondrocytes

*How are LCs in the head specified?*

Many details on the fine molecular and/or mechanical signaling mechanisms that induce downstream differentiation of skeletal stem cells (SSCs) into distinct cartilage populations are still unclear (Figure 6.1). The RNAseq experiments shown in Chapter II give an important insight into the regulatory program responsible for the maturation of LCs, but further analysis of earlier developmental stages would clarify important early regulators of the development of LC and of secondary cartilages in general. In Chapter II I show that before P4 most LC progenitors in the mouse ear do not exhibit nuclear SOX9 activity, indicating that the cells have not yet committed to the chondrocyte lineage (Cole,

2011). This makes P4 or earlier an ideal postnatal stage for future single cell RNAseq (scRNAseq) studies. Additionally, PCNA and SOX9 immunohistochemistry as well as Oil Red O staining patterns (Figures 3.12 and 3.13) show that the developing cartilage plate is comprised of a heterogeneous population of LCs at close but different stages of maturation, which creates a short developmental continuum. Single cell resolution experiments, including scRNAseq and single cell ATAC (Assay for Transposase Accessible Chromatin), of LCs could reveal some of the fine steps taken by LC progenitors during the initial stages of LC fate specification. To account for the large size of LCs in adult stages, single nuclei (sNuc-seq and sNuc-ATAC) strategies —which uses isolated nuclei instead of whole cells to profile gene expression or transcriptional landscapes in cells that are hard to purify— could be used (Habib et al., 2017). These strategies could also be used with other LC-based cartilages in the head such as the nasal capsule and larynx.

*How does the 'bona fide' chondrocyte lineage achieve its phenotypic diversity?*

As previously stated, the diversity of cartilage and cartilage-like tissues is quite broad, even when only considering vertebrate cartilages. As Cole (2011) suggests, the numerous overlaps between shared transcriptional regulators, developmental phases, and phenotypic traits make cartilage a complex tissue to study. In mammals, three classic types of cartilage have been generally defined: hyaline cartilage, sparsely populated with a matrix rich in collagens and glycosaminoglycans; elastic cartilage, with additional elastic fiber content; and fibrocartilage, which contains dense and highly organized collagenous fibers within its extracellular matrix (ECM) (Cole, 2011).

We know that these cartilage types are found in distinct areas of the skeleton, and that their respective chondrocytes arise from known progenitors: hyaline growth plate chondrocytes (GPCs) arise from osteochondroprogenitors (OCPs), and fibrous articular chondrocytes (ACCs) arise from joint chondroprogenitors (JCPs) (Figure 6.1). At the same time, OCPs and JCPs arise from a common skeletogenic stem cell (SSC) from neural crest or mesoderm sources (Liu et al., 2017). Importantly, OCPs and JCPs are multipotent: OCPs give rise to bone and cartilage cells; JCPs to synovial and cartilage cells (Figure 6.1). Despite identification of important transcriptional regulators for bone and cartilage lineages (e.g. *Runx2* for bone and *Sox9* for cartilage), the regulatory mechanisms behind SSC fate specification are still unclear. Further, in zebrafish models, hypertrophic GPCs have been shown to directly convert into bone cells and bone marrow adipocytes, adding further complexity to the differentiation mechanisms used by the skeletal system (Giovannone et al., 2019). Considering that all known chondrocytes arise from a common skeletogenic stem cell (Liu et al., 2017), how, then, is phenotypic diversity achieved across the cartilage spectrum? LC based cartilages can offer new perspectives on mechanisms of cartilage specification and phenotypic maintenance.

In past studies, Wang et al. (2017) established that the ear skin macroenvironment is rich in signaling elements from sources including dermal fibroblasts, adipocytes, and the cartilage/muscle complex that act on cells of hair follicles (HFs) in the vicinity, influencing their developmental and regenerative behavior. Vascular tissues of the skin have also been shown to be a source of inhibitory signals to the stem cells of the HFs they surround (Li et al., 2019). Similarly, sonic hedgehog (SHH) cross-talking between neural tissues and chondrocyte progenitors in the face enables the morphogenesis of the nasal capsule; a

tissue we show is comprised of LCs later in mouse development (Figure 2.4A-C) (Kaucka et al., 2018). Considering the close distance at which HFs and LC progenitors co-develop in ear skin, molecular signals sourced from skin cells likely play an important role in the fate specification of LC progenitors in the ear pinna. Indeed, many genes encoding for chondrogenic signals like *Bmp2, Bmp4,* and *Shh*, are expressed by many cells of the mature HF (Sennett et al., 2015). Modulation of these pathways by means of transgenic mice would be a good approach to better understand the molecular players involved in LC specification. For example, K14-CreERT mice show tamoxifen-inducible Cre recombinase activity in dividing cells of the epidermis, and can be readily used to generate conditional mutations to disrupt SHH (*B6;129-Shh$^{tm2Amc}$/J*), BMP (*B6;129S4-Bmp2$^{tm1Jfm}$/J*, *B6;129S4-Bmp4$^{tm1Jfm}$/J*) and other relevant signaling pathways in the ear skin.

Another interesting research avenue would be to test if the skeletogenic progenitors that give rise to chondrocytes in the axial and appendicular skeleton also have the ability to form LCs. Recent work from the Weissman and Longaker research groups has led to the molecular identification and characterization of bone marrow-derived mouse and human skeletal stem cell populations with distinctive tissue potential including bone, cartilage and bone marrow stroma (Chan et al., 2015; Chan et al., 2018). Importantly, the authors show that these SSCs yield heterotopic skeletal tissues upon subcutaneous or sub-renal transplantation, and that modulation of signals involved in skeletal development can alter the fate decisions of the heterotopically transplanted SSCs. Specifically, increased BMP promotes cartilage differentiation at the expense of bone. Considering the BMP signaling-rich environment of the developing ear (Wang et al., 2017) as well as its high levels of vascularization compared to most avascular cartilages (Egawa et al., 2013), the ear pinna

niche offers a unique model to study cartilage lineage specification. To test the ability of SSCs to form LCs, heterotopic grafts of purified bone marrow-derived mouse SSCs onto embryonic and early postnatal ears of severe combined immunodeficient mice (e.g. NOD *scid* gamma) followed by histological and gene expression studies of the mature explanted grafts could shed light onto the ability of SSCs to form LCs. Further, LC progenitors could be grafted intradermally in the mouse dorsal back skin, where HFs regenerate continuously throughout the mouse adult life.

In line with the ideas above, one interesting possibility is that OCPs and JCPs further specify in response to differential mechanical forces. In the skull, for example, OCPs of the mandibular condyle require mechanical loading to properly differentiate into chondrocytes (Robinson et al., 2015). Indeed, phenotypic characteristics of hyaline and fibrous cartilage such as low cellularity and highly collagenous ECM content can be correlated with their impact- or shear stress-dampening properties. In contrast, the LC-based larynx, nose, and ear do not undergo these types of mechanical stress, and are instead required for the proper bending and support of soft tissues. Interestingly, recent *in vitro* studies have shown that SREBP-1, a key transcription factor for adipogenesis (Figure 3.1, Green), regulates stem cell commitment based on cytoskeletal contraction and ECM stiffness (Bertolio et al., 2019). Specifically, Bertolio et al. (2019) show that soft substrates are permissive to SREBP-dependent lipogenesis across a variety of human, mouse, and fly tissues and cell lines, whereas stiffer substrates prevent its activation. The RNAseq experiments in Chapter II show that *Srebp1a* is upregulated during mouse LC maturation and maintenance (Figure 3.17), but the mechanisms behind its activation in LCs is still unknown. To test the role of mechanical stimuli independently from molecular signaling on

SSC fate specification, purified appendicular SSCs as well as LCPs from ear primordia could be isolated and cultured *in vitro* in chondrogenic media under different substrate stiffness conditions; lipid synthesis as well as changes to expression of ECM related genes could be assayed across conditions. In combination with the SSC grafts described previously, these *in vitro* studies could provide us with an even deeper understanding of the *bona fide* chondrocyte regulatory network.

This is an important pursuit, as current research on cartilage repair and regeneration, including tissue engineering efforts, would benefit from an expanded view on the gene regulatory networks of cartilage tissues and their progenitor cells.

*LCs as a tool to study lipoexpediency*

Despite their fatty resemblance, LCs and *bona fide* adipocytes produce and manage their neutral lipids differently. Although excessive lipid intracellular pools are known to be cytotoxic, the benefits of such the abundant lipid content in LCs may outweigh their known negative effects in a notion known as lipoexpediency, an important area of research considering current rates of obesity and metabolic disease. For example, multiple lipid signaling molecules such as diacylglyceride have been shown to regulate rates of lipid production and breakdown to maintain lipid homeostasis, and that the disruption of diacyglyceride signaling leads to increased obesity and reduced lipolytic activity in mice (Nakano et al., 2018).

Irrespective of the specific roles that neutral lipid plays in LCs, our data clearly shows that it is primarily non-metabolic. How, then, does the cell "know" how to manage these lipids? The ear cartilage has a distinct neutral lipid composition from that of adipose tissue, and, in contrast with mouse adipocytes, LCs rely heavily on *de novo* lipogenesis for free fatty acid synthesis, unable to uptake them from peripheral circulation. While the exact reason for their nearly-exclusive reliance on *de novo* lipogenesis is currently unclear, I speculate that such a highly controlled mechanism can provide a tight control over the rate of lipid vacuole growth during LC differentiation as well as provide a pool of signaling lipids that could be involded in normal cell processes in LCs. Indeed, our measurements show that ear LC size is highly uniform, in contrast to fenestrae-bound adipocyte counterparts (Figure S4B). Thus, it is conceivable LC-based cartilages exploit this tight control to fine-tune the adult tissue's morphology, which can be essential for their function.

Unlike typical white adipocytes, adult LCs not only fail to uptake, but also fail to release lipids from their vacuoles upon systemic metabolic demand. They also downregulate key genes of the molecular machinery required for those functions. Importantly, non-metabolic roles, including mechanical role, are being rapidly recognized for adipose tissue as well. For example, white adipose tissue within hip and knee joints is thought to buffer mechanical friction between bones and does not atrophy even upon extreme starvation (reviewed in Zwick et al., 2018). Our RNA-seq data on LCs shows that, in principle, resistance to lipid vacuole mobilization can be achieved at the molecular level. LCs express very low levels of lipid droplet-associated protein *Plin1* and hormone-sensitive lipase *Lipe*, both of which critical for initiating triglyceride mobilization in adipocytes.

As previously discussed, PPARs are essential for adipocyte differentiation, and their modulation has been an attractive therapeutic target. For instance, PPARα has been used as a target to treat multiple disorders of lipid metabolism. Past studies show that PPARα is able to sense nutritional changes via lipid signals and respond by promoting the expression of some of its target genes. Although the mechanisms of lipid signaling and PPARα activation are still unknown, it has been speculated that FAS, which is nutritionally responsive, may mediate this process through the tight control of diacylglyceride production (Chakravarthy et al., 2005). Indeed, palmitic acid, the main product of FAS, has been reported to have insulin-sensitizing effects on muscle as well as improve the rates of glucose metabolism in other tissues (Dimopoulos et al., 2006; Passos et al., 2016; Yang et al., 2011).

In Chapter V, I show that pharmacological and genetic disruption of the *de novo* lipogenesis pathway leads to ear cartilage malformations; however, it would be very interesting to measure metabolite content and transcriptional responses to these insults via mass spectrometry and RNA-sequencing/qPCR methods. Specifically, besides altering their final shape, how are LCs dealing with the disruption to the pathway? Transcriptionally, a plethora of metabolic genes have been shown to respond to glucose and insulin signaling, including *Cyps1, Dgat2, Elovl5,* and *Fasn,* which become upregulated during the "rapid expansion" phase of LC maturation. It would be interesting to see how these genes are transcribed upon disruption of *de novo* lipogenesis as well as analyzing LC development and maintenance in insulin-resistant and obesity mouse models such as the leptin receptor mutant mice ($Lepr^{db}$).

In terms of lipotoxicity, current research has focused on the effects of antioxidants in multiple models of fat steatosis (Verma et al., 2014; Yang et al., 2018). My RNA-seq experiments in Chapter II show LC upregulation of antioxidant enzyme genes such as *Sod* and *Gpx1* compared to both *bona fide* adipocytes and chondrocytes, which may be another mechanism how LCs deal with the cytotoxic effects of excessive free fatty acids. Indeed, FLIM data in Chapter IV shows a striking difference in terms of oxidative stress levels between adipose tissues and LCs. Genetic or pharmacological disruption of these enzymes in LCs may prove very informative with regards to the role of antioxidant levels and lipid management.

*Is lipogenesis a form of cartilage hypertrophy?*

RNA-seq analysis clearly shows that during their development LCs express many core chondrogenic transcription factors, including several SOX family members and many cartilage-specific ECM genes, including collagens type II, IX, X and XI. Analogous to LCs, other cartilage and cartilage like-cells can increase their volume dramatically upon differentiation. For example, inner cells of the notochord develop large aqueous vacuole and prominently expand in size. Pushing against the outer sheath, hypertrophic notochord cells produce what is thought to be a hydrostatic pressure (Adams et al., 1990; Ellis et al., 2013). Hyaline chondrocytes in the growth plate of long bones also undergo hypertrophy via a distinct mechanism of cytoplasmic volume and organelle size and number expansion (Buckwalter et al., 1986) and this contributes to bone growth and shaping (Cooper et al., 2013). Although we never see the cell death or mineralization that accompanies the hypertrophic program of growth plate chondrocytes, we posit that lipid vacuolation is a form of cartilage hypertrophy, and that the *de novo* lipogenesis pathway, with its rate-

limiting enzymes, provides LCs with a high-precision mechanism of size and shape control. For this mechanism to remain precise at the tissue level, the total number of adult LCs in the plate should be fixed, long-lived, and protected from lipid loss. Indeed, all of these features are supported by our studies. Physical measurements such as tensile strength and compressive tolerance using atomic force microscopy in normal and defective LCs (pharmacological inhibiton or genetic disruption of *de novo* lipogenesis) would clarify the mechanical roles that "lipid hypertrophy" plays on normal cartilage function.

*What is the evolutionary origin of LCs?*

In Chapter V, members of the order Chiroptera display a high degree of craniofacial morphological variation, despite their close evolutionary relatedness (Figure 6.2A-D). the precise morphology of external ears, that broadly varies among species, has been linked to specialization of their sonar system (Ma and Muller, 2011). Certain, highly precise ear features, such as parallel ridges, which we now show to be composed of stacks of LCs (Figure 7G), can aid in diffraction-based sound perception (Keeley et al., 2018). Acoustic properties of neutral lipids can further aid in sound modulation by LC-rich cartilage, analogous to the proposed role of neutral lipids in the so called melon, an adipocyte-rich organ that acts as an acoustic lens in echolocating Cetaceans (reviewed in Zwick et al., 2018). In order to clarify the evolutionary role of lipid-filled cartilages throughout the mammalian clade, and especially on their acoustic role, echolocating species of bats could be treated topically with pharmacological inhibitors of FAS and ACC as shown in Chapter IV, and their behavioral response to changes in ear morphology measured under lab conditions.

Focusing on the ear cartilage, our studies show that LCs are prominent through the mammalian clade, even represented in extant marsupials. We posit that the mammalian LC evolved in the last common ancestor of marsupials and eutherians ancestor. Because we observe LCs in multiple head and neck cartilages and not only in external ears, it is very possible that LCs originated earlier and exist in other animal phyla. For example, the cartilage of the gill book in horseshoe crabs (*Limulus*) shows prominent vacuolation similar to LCs, but their lipid content or transcriptional activity of lipid metabolism genes has not been researched so far. Future large-scale comparative morphological studies of cartilage will be needed to address this important evolutionary question.

*Conclusion*

Our rediscovery and characterization of LCs opens new opportunities for future studies across the range of disciplines. With their unique lipid biology, LCs can prove as a fruitful model system for studying regulation of *de novo* lipogenesis and lipid vacuole synthesis and maintenance. These studies can lend new insights into the causes, pathogenesis and therapies for the metabolic syndrome. Along these lines, LCs can likely be used to study cellular resistance to the toxic effect of FFAs. Indeed, our lipidomic studies show that mouse ear cartilage contains large quantities of FFAs, which are typically highly toxic to many cells types, including pancreatic islet cells (Cnop et al., 2001). LC-rich cartilages can prove to be uniquely positioned to address the relative role that cells *vs.* ECM play in endowing connective tissues with their biomechanical properties of stiffness and elasticity. LCs undergo repositioning during ear cartilage morphogenesis and might prove to be useful in studying developmental mechanism of cartilage mechanisms, such as convergent extension. This can be further aided by a fairly simple, nearly two-dimensional morphology

of ear cartilage, distinct anatomic features, such as fenestrae and exceptional ease with which ears can be examined and imaged. Lastly, ear cartilage is known for its ability to regenerate in adult rodents following ear punch hole injury (Seifert et al., 2012), but the mechanisms behind cartilage repair remain unknown. The LC lineage can become a novel system for studying mechanisms of adult cartilage regeneration – an important but yet unmet medical need.

## Figures

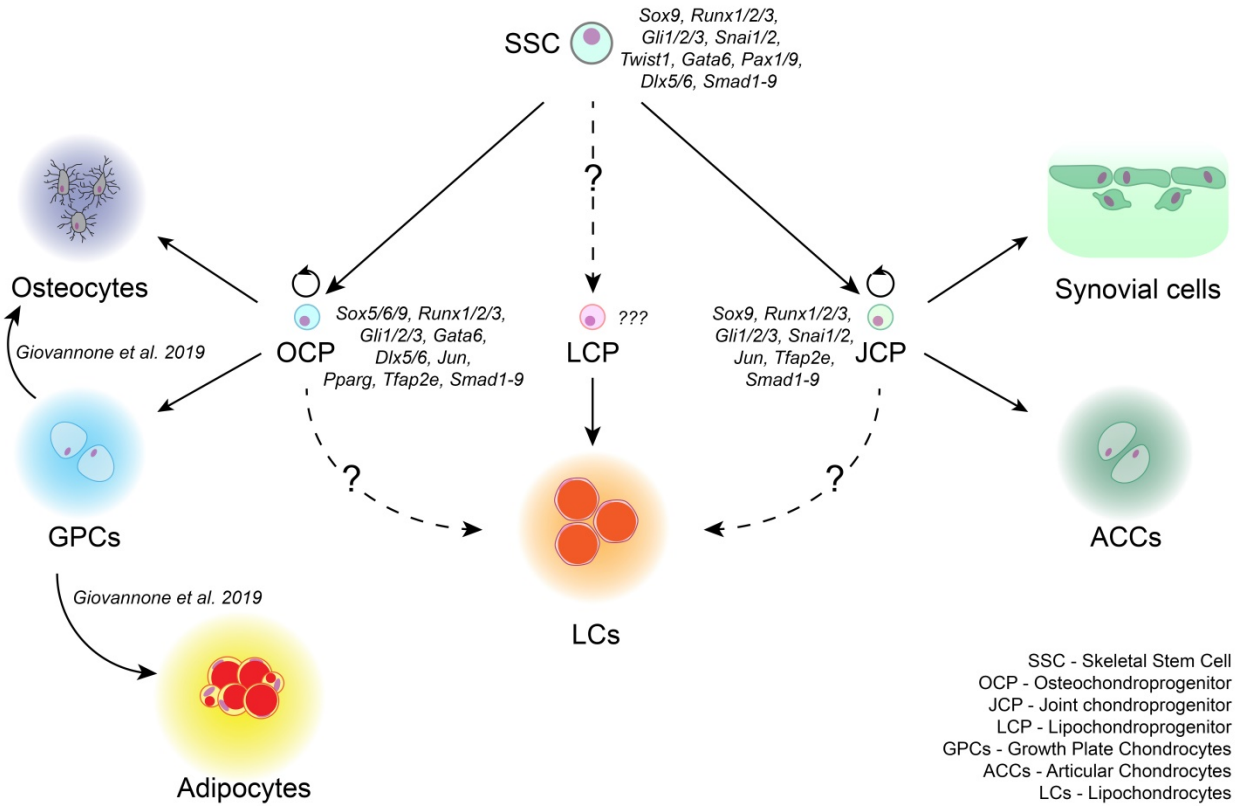


**Figure 6.1: Cartoon of skeletal lineage specification steps.** Bone marrow-resident SSCs (TOP) differentiate into OCPs or JCPs through mechanisms that are still unclear. These OCPs and JCPs express distinct transcription factors that further differentiate them into multiple skeletal tissues, including bone and cartilage for OCPs, and synovium and cartilage for JCPs. Further, mature GPCs in zebrafish have been shown to differentiate into bone cells as well as bone marrow-resident adipocytes. It is currently unknown if SSCs from the axial or appendicular skeleton can generate LCs directly or through an LCP cell.

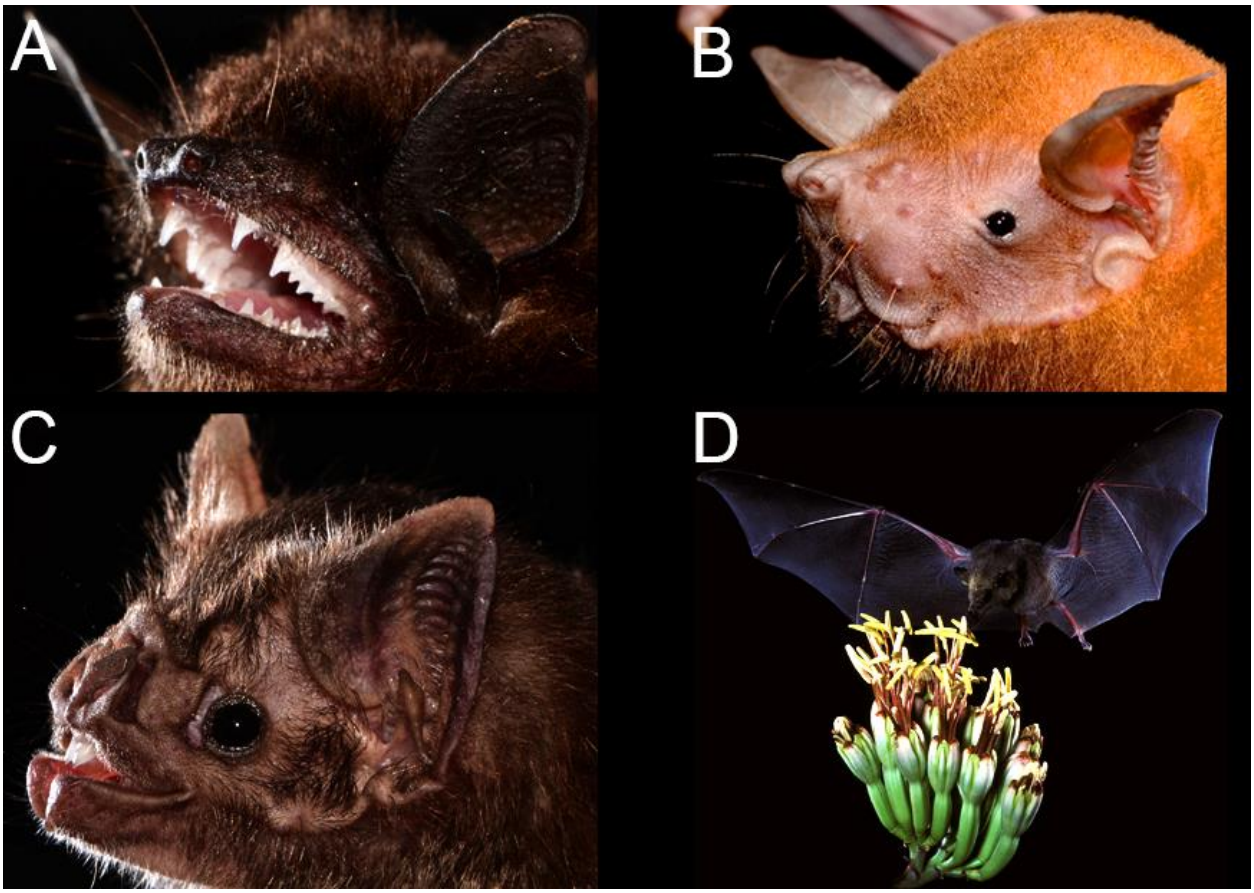


**Figure 6.2: Craniofacial morphological diversity among echolocating bats.** (A-C) Gross facial appearance of echolocating members of chiroptera. The black myotis (*Myotis nigricans*) **(A)**, lesser bulldog bat (*Noctilio albiventris*) **(B)**, common vampire bat (*Desmodus rotundus*) **(C),** and long-tongued Mexican bat (*Choeronycteris mexicana*) **(D)** show distinct craniofacial morphologies that correlate with distinct feeding behaviors. Images A-C are a courtesy of Dr. Marco Mello (marcomellolab.wordpress.com). Image in (D) is in the public domain in the U.S.A.

## References


Abad, V., Meyers, J.L., Weise, M., Gafni, R.I., Barnes, K.M., Nilsson, O., Bacher, J.D., and Baron, J. (2002). The role of the resting zone in growth plate chondrogenesis. Endocrinology *143*, 1851-1857.

Abzhanov, A., and Tabin, C.J. (2004). Shh and Fgf8 act synergistically to drive cartilage outgrowth during cranial development. Developmental biology *273*, 134-148.

Adams, D.S., Keller, R., and Koehl, M.A. (1990). The mechanics of notochord elongation, straightening and stiffening in the embryo of Xenopus laevis. Development *110*, 115-130.

Akiyama, H., Chaboissier, M.C., Martin, J.F., Schedl, A., and de Crombrugghe, B. (2002). The transcription factor Sox9 has essential roles in successive steps of the chondrocyte differentiation pathway and is required for expression of Sox5 and Sox6. Genes Dev *16*, 2813-2828.

Anderson, D.R. (1964). The Ultrastructure of Elastic and Hyaline Cartilage of the Rat. The American journal of anatomy *114*, 403-434.

Anthwal, N., and Thompson, H. (2016). The development of the mammalian outer and middle ear. Journal of anatomy *228*, 217-232.

Banerjee, R.R., Rangwala, S.M., Shapiro, J.S., Rich, A.S., Rhoades, B., Qi, Y., Wang, J., Rajala, M.W., Pocai, A., Scherer, P.E.*, et al.* (2004). Regulation of fasted blood glucose by resistin. Science *303*, 1195-1198.

Barquissau, V., Beuzelin, D., Pisani, D.F., Beranger, G.E., Mairal, A., Montagner, A., Roussel, B., Tavernier, G., Marques, M.A., Moro, C.*, et al.* (2016). White-to-brite conversion in human adipocytes promotes metabolic reprogramming towards fatty acid anabolic and catabolic pathways. Mol Metab *5*, 352-365.

Benedek, T.G. (2006). A history of the understanding of cartilage. Osteoarthritis Cartilage *14*, 203-209.

Benjamin, M., and Evans, E.J. (1990). Fibrocartilage. Journal of anatomy *171*, 1-15.

Bi, W., Deng, J.M., Zhang, Z., Behringer, R.R., and de Crombrugghe, B. (1999). Sox9 is required for cartilage formation. Nat Genet *22*, 85-89.

Billon, N., Iannarelli, P., Monteiro, M.C., Glavieux-Pardanaud, C., Richardson, W.D., Kessaris, N., Dani, C., and Dupin, E. (2007). The generation of adipocytes by the neural crest. Development *134*, 2283-2292.

Bininda-Emonds, O.R., Cardillo, M., Jones, K.E., MacPhee, R.D., Beck, R.M., Grenyer, R., Price, S.A., Vos, R.A., Gittleman, J.L., and Purvis, A. (2007). The delayed rise of present-day mammals. Nature *446*, 507-512.

Bradamante, Z., Kostovic-Knezevic, L., Levak-Svajger, B., and Svajger, A. (1991). Differentiation of the secondary elastic cartilage in the external ear of the rat. Int J Dev Biol *35*, 311-320.

Bradamante, Z., and Svajger, A. (1977). Pre-elastic (oxytalan) fibres in the developing elastic cartilage of the external ear of the rat. Journal of anatomy *123*, 735-743.

Bronner, M.E., and LeDouarin, N.M. (2012). Development and evolution of the neural crest: an overview. Developmental biology *366*, 2-9.

Buckwalter, J.A., Mower, D., Ungar, R., Schaeffer, J., and Ginsberg, B. (1986). Morphometric analysis of chondrocyte hypertrophy. J Bone Joint Surg Am *68*, 243-255.

Buenrostro, J.D., Giresi, P.G., Zaba, L.C., Chang, H.Y., and Greenleaf, W.J. (2013). Transposition of native chromatin for fast and sensitive epigenomic profiling of open chromatin, DNA-binding proteins and nucleosome position. Nat Methods *10*, 1213-1218.

Burgin, C.J., Colella, J.P., Kahn, P.L., Upham, N.S. (2018). How many species of mammals are there? . Journal of Mammalogy *99*, 1-14.

Chai, Y., Jiang, X., Ito, Y., Bringas, P., Jr., Han, J., Rowitch, D.H., Soriano, P., McMahon, A.P., and Sucov, H.M. (2000). Fate of the mammalian cranial neural crest during tooth and mandibular morphogenesis. Development *127*, 1671-1679.

Chen, M., Lichtler, A.C., Sheu, T.J., Xie, C., Zhang, X., O'Keefe, R.J., and Chen, D. (2007). Generation of a transgenic mouse model with chondrocyte-specific and tamoxifen-inducible expression of Cre recombinase. Genesis *45*, 44-50.

Chung, E.J., Shah, N., and Shah, R.N. (2013). 11 - Nanomaterials for cartilage tissue engineering. In Nanomaterials in Tissue Engineering (Woodhead Publishing), pp. 301-334.
Cnop, M., Hannaert, J.C., Hoorens, A., Eizirik, D.L., and Pipeleers, D.G. (2001). Inverse relationship between cytotoxicity of free fatty acids in pancreatic islet cells and cellular triglyceride accumulation. Diabetes *50*, 1771-1777.
Cole, A.G., and Hall, B.K. (2004). The nature and significance of invertebrate cartilages revisited: distribution and histology of cartilage and cartilage-like tissues within the Metazoa. Zoology (Jena) *107*, 261-273.
Coleman, D.L. (1978). Obese and diabetes: two mutant genes causing diabetes-obesity syndromes in mice. Diabetologia *14*, 141-148.
Cooper, K.L., Oh, S., Sung, Y., Dasari, R.R., Kirschner, M.W., and Tabin, C.J. (2013). Multiple phases of chondrocyte enlargement underlie differences in skeletal proportions. Nature *495*, 375-378.
Cranford, T.W., Amundin, M., and Norris, K.S. (1996). Functional morphology and homology in the odontocete nasal complex: implications for sound generation. J Morphol *228*, 223-285.
Cresswell, R. (1897). Aristotle's History of Animals in Ten Books (London: George Bell and Sons).
Crichton, P.G., Lee, Y., and Kunji, E.R. (2017). The molecular features of uncoupling protein 1 support a conventional mitochondrial carrier-like mechanism. Biochimie *134*, 35-50.
Datta, R., Alfonso-Garcia, A., Cinco, R., and Gratton, E. (2015). Fluorescence lifetime imaging of endogenous biomarker of oxidative stress. Scientific reports *5*, 9848.
Day, T.F., Guo, X., Garrett-Beal, L., and Yang, Y. (2005). Wnt/beta-catenin signaling in mesenchymal progenitors controls osteoblast and chondrocyte differentiation during vertebrate skeletogenesis. Dev Cell *8*, 739-750.
Debbache, J., Parfejevs, V., and Sommer, L. (2018). Cre-driver lines used for genetic fate mapping of neural crest cells in the mouse: An overview. Genesis *56*, e23105.
Decker, R.S., Koyama, E., and Pacifici, M. (2015). Articular Cartilage: Structural and Developmental Intricacies and Questions. Curr Osteoporos Rep *13*, 407-414.
Dobin, A., Davis, C.A., Schlesinger, F., Drenkow, J., Zaleski, C., Jha, S., Batut, P., Chaisson, M., and Gingeras, T.R. (2013). STAR: ultrafast universal RNA-seq aligner. Bioinformatics *29*, 15-21.
Dodds, G.S. (1930). Row formation and other types of arrangement of cartilage cells in endochondral ossification. The Anatomical Record.
Egawa, G., Miyachi, Y., and Kabashima, K. (2013). Identification of perivascular adipose tissue in the mouse skin using two-photon microscopy. J Dermatol Sci *70*, 139-140.
Eguchi, J., Wang, X., Yu, S., Kershaw, E.E., Chiu, P.C., Dushay, J., Estall, J.L., Klein, U., Maratos-Flier, E., and Rosen, E.D. (2011). Transcriptional control of adipose lipid handling by IRF4. Cell Metab *13*, 249-259.
Ellis, K., Bagwell, J., and Bagnat, M. (2013). Notochord vacuoles are lysosome-related organelles that function in axis and spine morphogenesis. J Cell Biol *200*, 667-679.
Flavin, R., Peluso, S., Nguyen, P.L., and Loda, M. (2010). Fatty acid synthase as a potential therapeutic target in cancer. Future oncology *6*, 551-562.
Flodby, P., Barlow, C., Kylefjord, H., Ahrlund-Richter, L., and Xanthopoulos, K.G. (1996). Increased hepatic cell proliferation and lung abnormalities in mice deficient in CCAAT/enhancer binding protein alpha. J Biol Chem *271*, 24753-24760.
Ge, K., Guermah, M., Yuan, C.X., Ito, M., Wallberg, A.E., Spiegelman, B.M., and Roeder, R.G. (2002). Transcription coactivator TRAP220 is required for PPAR gamma 2-stimulated adipogenesis. Nature *417*, 563-567.
Gerber, H.P., Vu, T.H., Ryan, A.M., Kowalski, J., Werb, Z., and Ferrara, N. (1999). VEGF couples hypertrophic cartilage remodeling, ossification and angiogenesis during endochondral bone formation. Nat Med *5*, 623-628.

Green, H., and Kehinde, O. (1975). An established preadipose cell line and its differentiation in culture. II. Factors affecting the adipose conversion. Cell *5*, 19-27.
Griffith, D.A., Kung, D.W., Esler, W.P., Amor, P.A., Bagley, S.W., Beysen, C., Carvajal-Gonzalez, S., Doran, S.D., Limberakis, C., Mathiowetz, A.M.*, et al.* (2014). Decreasing the rate of metabolic ketone reduction in the discovery of a clinical acetyl-CoA carboxylase inhibitor for the treatment of diabetes. Journal of medicinal chemistry *57*, 10512-10526.
Grzybek, M., Palladini, A., Alexaki, V.I., Surma, M.A., Simons, K., Chavakis, T., Klose, C., and Coskun, U. (2019). Comprehensive and quantitative analysis of white and brown adipose tissue by shotgun lipidomics. Mol Metab *22*, 12-20.
Guerrero-Juarez, C.F., and Plikus, M.V. (2018). Emerging nonmetabolic functions of skin fat. Nat Rev Endocrinol *14*, 163-173.
Guillerme, T., and Cooper, N. (2016). Assessment of available anatomical characters for linking living mammals to fossil taxa in phylogenetic analyses. Biol Lett *12*.
Haeckel, E. (1904). Kunstformen der Natur (Leipzig).
Hall, B.K. (2015). Bones and Cartilage, pp. 650-655.
Hayano, S., Komatsu, Y., Pan, H., and Mishina, Y. (2015). Augmented BMP signaling in the neural crest inhibits nasal cartilage morphogenesis by inducing p53-mediated apoptosis. Development *142*, 1357-1367.
He, X., Ohba, S., Hojo, H., and McMahon, A.P. (2016). AP-1 family members act with Sox9 to promote chondrocyte hypertrophy. Development *143*, 3012-3023.
Healy, C., Uwanogho, D., and Sharpe, P.T. (1999). Regulation and role of Sox9 in cartilage formation. Dev Dyn *215*, 69-78.
Hemmati-Brivanlou, A., Stewart, R.M., and Harland, R.M. (1990). Region-specific neural induction of an engrailed protein by anterior notochord in Xenopus. Science *250*, 800-802.
Heude, E., Tesarova, M., Sefton, E.M., Jullian, E., Adachi, N., Grimaldi, A., Zikmund, T., Kaiser, J., Kardon, G., Kelly, R.G.*, et al.* (2018). Unique morphogenetic signatures define mammalian neck muscles and associated connective tissues. eLife *7*.
Hill, T.P., Spater, D., Taketo, M.M., Birchmeier, W., and Hartmann, C. (2005). Canonical Wnt/beta-catenin signaling prevents osteoblasts from differentiating into chondrocytes. Dev Cell *8*, 727-738.
Hunziker, E.B., Kapfinger, E., and Saager, C. (1999). Hypertrophy of growth plate chondrocytes in vivo is accompanied by modulations in the activity state and surface area of their cytoplasmic organelles. Histochem Cell Biol *112*, 115-123.
Jandzik, D., Garnett, A.T., Square, T.A., Cattell, M.V., Yu, J.K., and Medeiros, D.M. (2015). Evolution of the new vertebrate head by co-option of an ancient chordate skeletal tissue. Nature *518*, 534-537.
Kaucka, M., and Adameyko, I. (2017). Evolution and development of the cartilaginous skull: From a lancelet towards a human face. Semin Cell Dev Biol.
Kaucka, M., Petersen, J., Tesarova, M., Szarowska, B., Kastriti, M.E., Xie, M., Kicheva, A., Annusver, K., Kasper, M., Symmons, O.*, et al.* (2018). Signals from the brain and olfactory epithelium control shaping of the mammalian nasal capsule cartilage. eLife *7*.
Keeley, B.W., Keeley, A.T.H., and Houlahan, P. (2018). Ridge number in bat ears is related to both guild membership and ear length. PLoS One *13*, e0200255.
Kiebish, M.A., Bell, R., Yang, K., Phan, T., Zhao, Z., Ames, W., Seyfried, T.N., Gross, R.W., Chuang, J.H., and Han, X. (2010). Dynamic simulation of cardiolipin remodeling: greasing the wheels for an interpretative approach to lipidomics. J Lipid Res *51*, 2153-2170.
Kostovic-Knezevic, L., Bradamante, Z., and Svajger, A. (1981). Ultrastructure of elastic cartilage in the rat external ear. Cell Tissue Res *218*, 149-160.
Kostovic-Knezevic, L., Bradamante, Z., and Svajger, A. (1986). On the ultrastructure of the developing elastic cartilage in the rat external ear. Anatomy and embryology *173*, 385-391.

Koyama, E., Shibukawa, Y., Nagayama, M., Sugito, H., Young, B., Yuasa, T., Okabe, T., Ochiai, T., Kamiya, N., Rountree, R.B*., et al.* (2008). A distinct cohort of progenitor cells participates in synovial joint and articular cartilage formation during mouse limb skeletogenesis. Developmental biology *316*, 62-73.
Kumar, D., and Lassar, A.B. (2014). Fibroblast growth factor maintains chondrogenic potential of limb bud mesenchymal cells by modulating DNMT3A recruitment. Cell Rep *8*, 1419-1431.
Lee, J., Walsh, M.C., Hoehn, K.L., James, D.E., Wherry, E.J., and Choi, Y. (2014). Regulator of fatty acid metabolism, acetyl coenzyme a carboxylase 1, controls T cell immunity. Journal of immunology *192*, 3190-3199.
Lefebvre, V., and Smits, P. (2005). Transcriptional control of chondrocyte fate and differentiation. Birth Defects Res C Embryo Today *75*, 200-212.
Lewis, A.E., Vasudevan, H.N., O'Neill, A.K., Soriano, P., and Bush, J.O. (2013a). The widely used Wnt1-Cre transgene causes developmental phenotypes by ectopic activation of Wnt signaling. Dev Biol *379*, 229-234.
Lewis, A.E., Vasudevan, H.N., O'Neill, A.K., Soriano, P., and Bush, J.O. (2013b). The widely used Wnt1-Cre transgene causes developmental phenotypes by ectopic activation of Wnt signaling. Developmental biology *379*, 229-234.
Leydig, F. (1854). Kleinere Mittheilungen zur thierischen Gewebelehre (Berlin).
Leydig, F. (1857). Lehrbuch der Histologie des Menschen und der Thiere (Frankfurt a.M.: Meidinger).
Li, H., Black, P.N., and DiRusso, C.C. (2005). A live-cell high-throughput screening assay for identification of fatty acid uptake inhibitors. Analytical biochemistry *336*, 11-19.
Li, J., and Cheng, J.X. (2014). Direct visualization of de novo lipogenesis in single living cells. Scientific reports *4*, 6807.
Lidell, H.G.S., R. (1940). A Greek-English Lexicon (Oxford: Clarendon Press).
Linsenmayer, T.F., Gibney, E., and Schmid, T.M. (1986). Segmental appearance of type X collagen in the developing avian notochord. Developmental biology *113*, 467-473.
Little, K., Pimm, L.H., and Trueta, J. (1958). Osteoarthritis of the hip: an electron microscope study. The Journal of bone and joint surgery British volume *40-B*, 123-131.
Ma, J., and Muller, R. (2011). A method for characterizing the biodiversity in bat pinnae as a basis for engineering analysis. Bioinspir Biomim *6*, 026008.
Madisen, L., Zwingman, T.A., Sunkin, S.M., Oh, S.W., Zariwala, H.A., Gu, H., Ng, L.L., Palmiter, R.D., Hawrylycz, M.J., Jones, A.R*., et al.* (2010). A robust and high-throughput Cre reporting and characterization system for the whole mouse brain. Nat Neurosci *13*, 133-140.
Mallinger, R., and Bock, P. (1985). Differentiation of extracellular matrix in the cellular cartilage ("Zellknorpel") of the mouse pinna. Anatomy and embryology *172*, 69-74.
Martin, T., Marugan-Lobon, J., Vullo, R., Martin-Abad, H., Luo, Z.X., and Buscalioni, A.D. (2015). A Cretaceous eutriconodont and integument evolution in early mammals. Nature *526*, 380-384.
Matsuoka, T., Ahlberg, P.E., Kessaris, N., Iannarelli, P., Dennehy, U., Richardson, W.D., McMahon, A.P., and Koentges, G. (2005). Neural crest origins of the neck and shoulder. Nature *436*, 347-355.
May, F.J., Baer, L.A., Lehnig, A.C., So, K., Chen, E.Y., Gao, F., Narain, N.R., Gushchina, L., Rose, A., Doseff, A.I*., et al.* (2017). Lipidomic Adaptations in White and Brown Adipose Tissue in Response to Exercise Demonstrate Molecular Species-Specific Remodeling. Cell Rep *18*, 1558-1572.
McBratney-Owen, B., Iseki, S., Bamforth, S.D., Olsen, B.R., and Morriss-Kay, G.M. (2008). Development and tissue origins of the mammalian cranial base. Developmental biology *322*, 121-132.
Minoux, M., Kratochwil, C.F., Ducret, S., Amin, S., Kitazawa, T., Kurihara, H., Bobola, N., Vilain, N., and Rijli, F.M. (2013). Mouse Hoxa2 mutations provide a model for microtia and auricle duplication. Development *140*, 4386-4397.

Montague, C.T., Prins, J.B., Sanders, L., Zhang, J., Sewter, C.P., Digby, J., Byrne, C.D., and O'Rahilly, S. (1998). Depot-related gene expression in human subcutaneous and omental adipocytes. Diabetes *47*, 1384-1391.
Montes, G.S. (1996). Structural biology of the fibres of the collagenous and elastic systems. Cell biology international *20*, 15-27.
Mueller, M.B., Fischer, M., Zellner, J., Berner, A., Dienstknecht, T., Prantl, L., Kujat, R., Nerlich, M., Tuan, R.S., and Angele, P. (2010). Hypertrophy in mesenchymal stem cell chondrogenesis: effect of TGF-beta isoforms and chondrogenic conditioning. Cells Tissues Organs *192*, 158-166.
Murakami, S., Kan, M., McKeehan, W.L., and de Crombrugghe, B. (2000). Up-regulation of the chondrogenic Sox9 gene by fibroblast growth factors is mediated by the mitogen-activated protein kinase pathway. Proc Natl Acad Sci U S A *97*, 1113-1118.
Murtaugh, L.C., Chyung, J.H., and Lassar, A.B. (1999). Sonic hedgehog promotes somitic chondrogenesis by altering the cellular response to BMP signaling. Genes Dev *13*, 225-237.
Muzumdar, M.D., Tasic, B., Miyamichi, K., Li, L., and Luo, L. (2007). A global double-fluorescent Cre reporter mouse. Genesis *45*, 593-605.
Nakachi, Y., Yagi, K., Nikaido, I., Bono, H., Tonouchi, M., Schonbach, C., and Okazaki, Y. (2008). Identification of novel PPARgamma target genes by integrated analysis of ChIP-on-chip and microarray expression data during adipocyte differentiation. Biochem Biophys Res Commun *372*, 362-366.
Nakamura, E., Nguyen, M.T., and Mackem, S. (2006). Kinetics of tamoxifen-regulated Cre activity in mice using a cartilage-specific CreER(T) to assay temporal activity windows along the proximodistal limb skeleton. Dev Dynam *235*, 2603-2612.
Oka, K., Oka, S., Hosokawa, R., Bringas, P., Jr., Brockhoff, H.C., 2nd, Nonaka, K., and Chai, Y. (2008). TGF-beta mediated Dlx5 signaling plays a crucial role in osteo-chondroprogenitor cell lineage determination during mandible development. Developmental biology *321*, 303-309.
Ortega-Martinez, M., Romero-Nunez, E., Niderhauser-Garcia, A., de-la-Garza-Gonzalez, C., Ancer-Rodriguez, J., and Jaramillo-Rangel, G. (2013). Evidence of chondrocyte turnover in lung cartilage, with the probable participation of nestin-positive cells. Cell biology international *37*, 239-241.
Palou, M., Priego, T., Sanchez, J., Rodriguez, A.M., Palou, A., and Pico, C. (2009). Gene expression patterns in visceral and subcutaneous adipose depots in rats are linked to their morphologic features. Cell Physiol Biochem *24*, 547-556.
Patra, D., Xing, X., Davies, S., Bryan, J., Franz, C., Hunziker, E.B., and Sandell, L.J. (2007). Site-1 protease is essential for endochondral bone formation in mice. J Cell Biol *179*, 687-700.
Peck, A.L. (1961). Aristotle Parts of Animals (London: William Heinemann Ltd).
Peck, S.H., McKee, K.K., Tobias, J.W., Malhotra, N.R., Harfe, B.D., and Smith, L.J. (2017). Whole Transcriptome Analysis of Notochord-Derived Cells during Embryonic Formation of the Nucleus Pulposus. Scientific reports *7*, 10504.
Picelli, S., Faridani, O.R., Bjorklund, A.K., Winberg, G., Sagasser, S., and Sandberg, R. (2014). Full-length RNA-seq from single cells using Smart-seq2. Nature protocols *9*, 171-181.
Piekarski, N., Gross, J.B., and Hanken, J. (2014). Evolutionary innovation and conservation in the embryonic derivation of the vertebrate skull. Nat Commun *5*, 5661.
Pourquie, O., Coltey, M., Teillet, M.A., Ordahl, C., and Le Douarin, N.M. (1993). Control of dorsoventral patterning of somitic derivatives by notochord and floor plate. Proc Natl Acad Sci U S A *90*, 5242-5246.
Prince, R.C., Frontiera, R.R., and Potma, E.O. (2016). Stimulated Raman Scattering: From Bulk to Nano. Chemical reviews.
Robinson, M.D., McCarthy, D.J., and Smyth, G.K. (2010). edgeR: a Bioconductor package for differential expression analysis of digital gene expression data. Bioinformatics *26*, 139-140.

Rosen, E.D., Sarraf, P., Troy, A.E., Bradwin, G., Moore, K., Milstone, D.S., Spiegelman, B.M., and Mortensen, R.M. (1999). PPAR gamma is required for the differentiation of adipose tissue in vivo and in vitro. Mol Cell *4*, 611-617.
Rosen, E.D., Walkey, C.J., Puigserver, P., and Spiegelman, B.M. (2000). Transcriptional regulation of adipogenesis. Genes Dev *14*, 1293-1307.
Sanzone, C.F., and Reith, E.J. (1976). The development of the elastic cartilage of the mouse pinna. The American journal of anatomy *146*, 31-71.
Schindelin, J., Arganda-Carreras, I., Frise, E., Kaynig, V., Longair, M., Pietzsch, T., Preibisch, S., Rueden, C., Saalfeld, S., Schmid, B*., et al.* (2012). Fiji: an open-source platform for biological-image analysis. Nat Methods *9*, 676-682.
Sebo, Z.L., Jeffery, E., Holtrup, B., and Rodeheffer, M.S. (2018). A mesodermal fate map for adipose tissue. Development *145*.
Seifert, A.W., Kiama, S.G., Seifert, M.G., Goheen, J.R., Palmer, T.M., and Maden, M. (2012). Skin shedding and tissue regeneration in African spiny mice (Acomys). Nature *489*, 561-565.
Smits, P., Li, P., Mandel, J., Zhang, Z., Deng, J.M., Behringer, R.R., de Crombrugghe, B., and Lefebvre, V. (2001). The transcription factors L-Sox5 and Sox6 are essential for cartilage formation. Dev Cell *1*, 277-290.
Soriano, P. (1999a). Generalized lacZ expression with the ROSA26 Cre reporter strain. Nat Genet *21*, 70-71.
Soriano, P. (1999b). Generalized lacZ expression with the ROSA26 Cre reporter strain. Nature Genetics *21*, 70-71.
St-Jacques, B., Hammerschmidt, M., and McMahon, A.P. (1999). Indian hedgehog signaling regulates proliferation and differentiation of chondrocytes and is essential for bone formation. Genes Dev *13*, 2072-2086.
Stemple, D.L. (2005). Structure and function of the notochord: an essential organ for chordate development. Development *132*, 2503-2512.
Svajger, A. (1970). Chondrogenesis in the external ear of the rat. Zeitschrift fur Anatomie und Entwicklungsgeschichte *131*, 236-242.
Svensson, R.U., Parker, S.J., Eichner, L.J., Kolar, M.J., Wallace, M., Brun, S.N., Lombardo, P.S., Van Nostrand, J.L., Hutchins, A., Vera, L*., et al.* (2016). Inhibition of acetyl-CoA carboxylase suppresses fatty acid synthesis and tumor growth of non-small-cell lung cancer in preclinical models. Nat Med *22*, 1108-1119.
Tabler, J.M., Rigney, M.M., Berman, G.J., Gopalakrishnan, S., Heude, E., Al-Lami, H.A., Yannakoudakis, B.Z., Fitch, R.D., Carter, C., Vokes, S*., et al.* (2017). Cilia-mediated Hedgehog signaling controls form and function in the mammalian larynx. eLife *6*.
Tanaka, T., Yoshida, N., Kishimoto, T., and Akira, S. (1997). Defective adipocyte differentiation in mice lacking the C/EBPbeta and/or C/EBPdelta gene. EMBO J *16*, 7432-7443.
Tang, Q.Q., and Lane, M.D. (1999). Activation and centromeric localization of CCAAT/enhancer-binding proteins during the mitotic clonal expansion of adipocyte differentiation. Genes Dev *13*, 2231-2241.
Tarazona, O.A., Slota, L.A., Lopez, D.H., Zhang, G., and Cohn, M.J. (2016). The genetic program for cartilage development has deep homology within Bilateria. Nature *533*, 86-89.
Umeda, K., Zhao, J., Simmons, P., Stanley, E., Elefanty, A., and Nakayama, N. (2012). Human chondrogenic paraxial mesoderm, directed specification and prospective isolation from pluripotent stem cells. Scientific reports *2*, 455.
Umlauf, D., Frank, S., Pap, T., and Bertrand, J. (2010). Cartilage biology, pathology, and repair. Cell Mol Life Sci *67*, 4197-4211.
Vortkamp, A., Lee, K., Lanske, B., Segre, G.V., Kronenberg, H.M., and Tabin, C.J. (1996). Regulation of rate of cartilage differentiation by Indian hedgehog and PTH-related protein. Science *273*, 613-622.

Walther, T.C., and Farese, R.V., Jr. (2012). Lipid droplets and cellular lipid metabolism. Annu Rev Biochem *81*, 687-714.
Wang, Q., Oh, J.W., Lee, H.L., Dhar, A., Peng, T., Ramos, R., Guerrero-Juarez, C.F., Wang, X., Zhao, R., Cao, X.*, et al.* (2017). A multi-scale model for hair follicles reveals heterogeneous domains driving rapid spatiotemporal hair growth patterning. eLife *6*.
Wang, Y., and Sul, H.S. (2009). Pref-1 regulates mesenchymal cell commitment and differentiation through Sox9. Cell Metab *9*, 287-302.
Witten, P.E., Huysseune, A., and Hall, B.K. (2010). A practical approach for the identification of the many cartilaginous tissues in teleost fish. J Appl Ichthyol *26*, 257-262.
Wu, Y., Kim, J.Y., Zhou, S., and Smas, C.M. (2008). Differential screening identifies transcripts with depot-dependent expression in white adipose tissues. BMC Genomics *9*, 397.
Yamada, T., Placzek, M., Tanaka, H., Dodd, J., and Jessell, T.M. (1991). Control of cell pattern in the developing nervous system: polarizing activity of the floor plate and notochord. Cell *64*, 635-647.
Yeh, W.C., Cao, Z., Classon, M., and McKnight, S.L. (1995). Cascade regulation of terminal adipocyte differentiation by three members of the C/EBP family of leucine zipper proteins. Genes Dev *9*, 168-181.
Yoon, B.S., Ovchinnikov, D.A., Yoshii, I., Mishina, Y., Behringer, R.R., and Lyons, K.M. (2005). Bmpr1a and Bmpr1b have overlapping functions and are essential for chondrogenesis in vivo. Proc Natl Acad Sci U S A *102*, 5062-5067.
Zeng, L., Kempf, H., Murtaugh, L.C., Sato, M.E., and Lassar, A.B. (2002). Shh establishes an Nkx3.2/Sox9 autoregulatory loop that is maintained by BMP signals to induce somitic chondrogenesis. Genes Dev *16*, 1990-2005.
Zhang, D.E., Zhang, P., Wang, N.D., Hetherington, C.J., Darlington, G.J., and Tenen, D.G. (1997). Absence of granulocyte colony-stimulating factor signaling and neutrophil development in CCAAT enhancer binding protein alpha-deficient mice. Proc Natl Acad Sci U S A *94*, 569-574.
Zhang, Y.Y., Li, X., Qian, S.W., Guo, L., Huang, H.Y., He, Q., Liu, Y., Ma, C.G., and Tang, Q.Q. (2011). Transcriptional activation of histone H4 by C/EBPbeta during the mitotic clonal expansion of 3T3-L1 adipocyte differentiation. Mol Biol Cell *22*, 2165-2174.
Zwick, R.K., Guerrero-Juarez, C.F., Horsley, V., and Plikus, M.V. (2018). Anatomical, Physiological, and Functional Diversity of Adipose Tissue. Cell Metab *27*, 68-83

Arnold, M.A., Kim, Y., Czubryt, M.P., Phan, D., McAnally, J., Qi, X., Shelton, J.M., Richardson, J.A., Bassel-Duby, R., and Olson, E.N. (2007). MEF2C transcription factor controls chondrocyte hypertrophy and bone development. Dev Cell *12*, 377-389.
Bertolio, R., Napoletano, F., Mano, M., Maurer-Stroh, S., Fantuz, M., Zannini, A., Bicciato, S., Sorrentino, G., and Del Sal, G. (2019). Sterol regulatory element binding protein 1 couples mechanical cues and lipid metabolism. Nat Commun *10*, 1326.
Chakravarthy, M.V., Pan, Z., Zhu, Y., Tordjman, K., Schneider, J.G., Coleman, T., Turk, J., and Semenkovich, C.F. (2005). "New" hepatic fat activates PPARalpha to maintain glucose, lipid, and cholesterol homeostasis. Cell Metab *1*, 309-322.
Chan, C.K., Seo, E.Y., Chen, J.Y., Lo, D., McArdle, A., Sinha, R., Tevlin, R., Seita, J., Vincent-Tompkins, J., Wearda, T.*, et al.* (2015). Identification and specification of the mouse skeletal stem cell. Cell *160*, 285-298.
Chan, C.K.F., Gulati, G.S., Sinha, R., Tompkins, J.V., Lopez, M., Carter, A.C., Ransom, R.C., Reinisch, A., Wearda, T., Murphy, M.*, et al.* (2018). Identification of the Human Skeletal Stem Cell. Cell *175*, 43-56 e21.
Cole, A.G. (2011). A review of diversity in the evolution and development of cartilage: the search for the origin of the chondrocyte. Eur Cell Mater *21*, 122-129.

D'Angelo, M., Yan, Z., Nooreyazdan, M., Pacifici, M., Sarment, D.S., Billings, P.C., and Leboy, P.S. (2000). MMP-13 is induced during chondrocyte hypertrophy. J Cell Biochem *77*, 678-693.
Dimopoulos, N., Watson, M., Sakamoto, K., and Hundal, H.S. (2006). Differential effects of palmitate and palmitoleate on insulin action and glucose utilization in rat L6 skeletal muscle cells. Biochem J *399*, 473-481.
Egawa, G., Miyachi, Y., and Kabashima, K. (2013). Identification of perivascular adipose tissue in the mouse skin using two-photon microscopy. J Dermatol Sci *70*, 139-140.
Giovannone, D., Paul, S., Schindler, S., Arata, C., Farmer, D.T., Patel, P., Smeeton, J., and Crump, J.G. (2019). Programmed conversion of hypertrophic chondrocytes into osteoblasts and marrow adipocytes within zebrafish bones. eLife *8*.
Habib, N., Avraham-Davidi, I., Basu, A., Burks, T., Shekhar, K., Hofree, M., Choudhury, S.R., Aguet, F., Gelfand, E., Ardlie, K.*, et al.* (2017). Massively parallel single-nucleus RNA-seq with DroNc-seq. Nat Methods *14*, 955-958.
Hall, B.K. (2015). Bones and Cartilage.
Kaucka, M., Petersen, J., Tesarova, M., Szarowska, B., Kastriti, M.E., Xie, M., Kicheva, A., Annusver, K., Kasper, M., Symmons, O.*, et al.* (2018). Signals from the brain and olfactory epithelium control shaping of the mammalian nasal capsule cartilage. eLife *7*.
Kramer, J., Hegert, C., Guan, K., Wobus, A.M., Muller, P.K., and Rohwedel, J. (2000). Embryonic stem cell-derived chondrogenic differentiation in vitro: activation by BMP-2 and BMP-4. Mech Dev *92*, 193-205.
Li, K.N., Jain, P., He, C.H., Eun, F.C., Kang, S., and Tumbar, T. (2019). Skin vasculature and hair follicle cross-talking associated with stem cell activation and tissue homeostasis. eLife *8*.
Liu, C.F., Samsa, W.E., Zhou, G., and Lefebvre, V. (2017). Transcriptional control of chondrocyte specification and differentiation. Semin Cell Dev Biol *62*, 34-49.
Luong, Q., Huang, J., and Lee, K.Y. (2019). Deciphering White Adipose Tissue Heterogeneity. Biology (Basel) *8*.
Mizuhashi, K., Ono, W., Matsushita, Y., Sakagami, N., Takahashi, A., Saunders, T.L., Nagasawa, T., Kronenberg, H.M., and Ono, N. (2018). Resting zone of the growth plate houses a unique class of skeletal stem cells. Nature *563*, 254-258.
Nakano, T., Seino, K., Wakabayashi, I., Stafforini, D.M., Topham, M.K., and Goto, K. (2018). Deletion of diacylglycerol kinase epsilon confers susceptibility to obesity via reduced lipolytic activity in murine adipocytes. FASEB J *32*, 4121-4131.
Pan, Q., Yu, Y., Chen, Q., Li, C., Wu, H., Wan, Y., Ma, J., and Sun, F. (2008). Sox9, a key transcription factor of bone morphogenetic protein-2-induced chondrogenesis, is activated through BMP pathway and a CCAAT box in the proximal promoter. J Cell Physiol *217*, 228-241.
Passos, M.E., Alves, H.H., Momesso, C.M., Faria, F.G., Murata, G., Cury-Boaventura, M.F., Hatanaka, E., Massao-Hirabara, S., and Gorjao, R. (2016). Differential effects of palmitoleic acid on human lymphocyte proliferation and function. Lipids Health Dis *15*, 217.
Robinson, J., O'Brien, A., Chen, J., and Wadhwa, S. (2015). Progenitor Cells of the Mandibular Condylar Cartilage. Curr Mol Biol Rep *1*, 110-114.
Schulz, T.J., and Tseng, Y.H. (2013). Brown adipose tissue: development, metabolism and beyond. Biochem J *453*, 167-178.
Seifert, A.W., Kiama, S.G., Seifert, M.G., Goheen, J.R., Palmer, T.M., and Maden, M. (2012). Skin shedding and tissue regeneration in African spiny mice (Acomys). Nature *489*, 561-565.
Sennett, R., Wang, Z., Rezza, A., Grisanti, L., Roitershtein, N., Sicchio, C., Mok, K.W., Heitman, N.J., Clavel, C., Ma'ayan, A.*, et al.* (2015). An Integrated Transcriptome Atlas of Embryonic Hair Follicle Progenitors, Their Niche, and the Developing Skin. Dev Cell *34*, 577-591.

Shao, M., Ishibashi, J., Kusminski, C.M., Wang, Q.A., Hepler, C., Vishvanath, L., MacPherson, K.A., Spurgin, S.B., Sun, K., Holland, W.L.*, et al.* (2016). Zfp423 Maintains White Adipocyte Identity through Suppression of the Beige Cell Thermogenic Gene Program. Cell Metab *23*, 1167-1184.
Shu, B., Zhang, M., Xie, R., Wang, M., Jin, H., Hou, W., Tang, D., Harris, S.E., Mishina, Y., O'Keefe, R.J.*, et al.* (2011). BMP2, but not BMP4, is crucial for chondrocyte proliferation and maturation during endochondral bone development. J Cell Sci *124*, 3428-3440.
Takeda, S., Bonnamy, J.P., Owen, M.J., Ducy, P., and Karsenty, G. (2001). Continuous expression of Cbfa1 in nonhypertrophic chondrocytes uncovers its ability to induce hypertrophic chondrocyte differentiation and partially rescues Cbfa1-deficient mice. Genes Dev *15*, 467-481.
Verma, M.K., Yateesh, A.N., Smitha, R., Neelima, K., Pallavi, P.M., Reddy, M., Poornima, J., Oommen, A.M., Jagannath, M.R., and Somesh, B.P. (2014). Integrated analysis of chronic lipotoxicity on muscle metabolism and stress and its reversal by antioxidants. Springerplus *3*, 251.
Vortkamp, A., Lee, K., Lanske, B., Segre, G.V., Kronenberg, H.M., and Tabin, C.J. (1996). Regulation of rate of cartilage differentiation by Indian hedgehog and PTH-related protein. Science *273*, 613-622.
Wang, Q., Oh, J.W., Lee, H.L., Dhar, A., Peng, T., Ramos, R., Guerrero-Juarez, C.F., Wang, X., Zhao, R., Cao, X.*, et al.* (2017). A multi-scale model for hair follicles reveals heterogeneous domains driving rapid spatiotemporal hair growth patterning. eLife *6*.
Yang, J.P., Shin, J.H., Seo, S.H., Kim, S.G., Lee, S.H., and Shin, E.H. (2018). Effects of Antioxidants in Reducing Accumulation of Fat in Hepatocyte. Int J Mol Sci *19*.
Yang, Z.H., Miyahara, H., and Hatanaka, A. (2011). Chronic administration of palmitoleic acid reduces insulin resistance and hepatic lipid accumulation in KK-Ay Mice with genetic type 2 diabetes. Lipids Health Dis *10*, 120.
Zhang, Q.S., Kurpad, D.S., Mahoney, M.G., Steinbeck, M.J., and Freeman, T.A. (2017). Inhibition of apoptosis signal-regulating kinase 1 alters the wound epidermis and enhances auricular cartilage regeneration. PLoS One *12*, e0185803.

## Addendum

# Signaling by senescent cells hyper-activates the skin stem cell niche

Xiaojie Wang[1,2], Raul Ramos[1,2], Anne Q. Phan[3], Kosuke Yamaga[1,2], Xiaoling Cao[1,2,4], Jessica Flesher[5], Shan Jiang[1,6], Ji Won Oh[1,2,7,8,9], Suoqin Jin[6,11], Truman Kt Nguyen[1,2], Heidi Y. Liang [1,2], Andrew Nguyen[1,2], Kimberly N. Vu[1,2], Jennie L. Phung[1,2], Kevin H. Tran[1,2], Yingzi Liu[1,2,12,13], Zhili Deng[12,13], Nobuhiko Taguchi[14], Vanessa M. Scarfone[2], Guangfang Wang[2], Kara Nicole Paolilli[2], Xiaoyang Wang[2], Christian F. Guerrero-Juarez[1,2,6,10,11], Ryan T. Davis[15], Elyse Noelani Greenberg[5], Rolando Ruiz-Vega[5], Sohail Jahid[5], Priya Vasudeva[5], Rabi Murad[1,6], Lily Halida Putri Widyastuti[2], Hye-Lim Lee[1,2], Kevin J. McElwee[16], Alain-Pierre Gadeau[17], Devon A. Lawson[15], Bogi Andersen[2,5,10,18], Ali Mortazavi[1,6], Qing Nie[1,6,10,11], Takahiro Kunisada[14], Michael Karin[19], Jan Tuckermann[20,11], Jeffrey D. Esko[3], Anand K. Ganesan[5,22], Ji Li[12,13], Maksim V. Plikus[1,2,6,10,#]

[1] Department of Developmental and Cell Biology, University of California, Irvine, Irvine, CA 92697, USA
[2] Sue and Bill Gross Stem Cell Research Center, University of California, Irvine, Irvine, CA 92697, USA
[3] Glycobiology Research and Training Center, Department of Cellular and Molecular Medicine, University of California, San Diego, La Jolla, CA 92093, USA
[4] Department of Burn Surgery, The First Affiliated Hospital, Sun Yat-sen University, Guangzhou, China
[5] Department of Biological Chemistry, University of California, Irvine, Irvine, CA 92697, USA
[6] Center for Complex Biological Systems, University of California, Irvine, Irvine, CA 92697, USA
[7] Department of Anatomy, School of Medicine, Kyungpook National University, Daegu, Korea
[8] Biomedical Research Institute, Kyungpook National University Hospital, Daegu, Korea
[9] Hair Transplantation Center, Kyungpook National University Hospital, Daegu, Korea

[10] NSF-Simons Center for Multiscale Cell Fate Research, University of California, Irvine, Irvine, CA, 92697, USA

[11] Department of Mathematics, University of California, Irvine, Irvine, CA, 92697, USA

[12] Department of Dermatology, Center for Molecular Medicine, Xiangya Hospital, Central South University, Changsha, China

[13] Key Laboratory of Organ Injury, Aging and Regenerative Medicine of Hunan Province, Changsha, China

[14] Department of Tissue and Organ Development, Regeneration and Advanced Medical Science, Gifu University Graduate School of Medicine, Gifu 5011194, Japan

[15] Department of Physiology and Biophysics, University of California, Irvine, Irvine, CA 92697, USA
[16] Centre for Skin Sciences, University of Bradford, West Yorkshire, UK

[17] INSERM U1034, Adaptation cardiovasculaire à l'ischémie, F-33600 Pessac, France

[18] Department of Medicine, University of California, Irvine, Irvine, CA 92697, USA
[19] Laboratory of Gene Regulation and Signal Transduction, Departments of Pharmacology and Pathology, University of California San Diego, School of Medicine, La Jolla, CA 92093, USA
[20] Institute for Comparative Molecular Endocrinology (CME), University of Ulm, Helmholtzstrasse 8/1, 89081 Ulm, Germany

[21] Leibniz Institute of Age Research-Fritz Lipmann Institute, Beutenbergstrasse 11, 07745 Jena, Germany

[22] Department of Dermatology, University of California, Irvine, Irvine, CA 92697, USA

**# Author for correspondence:**

Maksim V. Plikus, PhD

Department of Developmental and Cell Biology,

Sue and Bill Gross Stem Cell Research Center,

University of California Irvine, Irvine, California 92697, USA

E-mail: plikus@uci.edu

**Summary**

Niche signals maintain stem cells in a prolonged quiescence or transiently activate them for proper regeneration. Altering signaling within the niche affects stem cell behavior and can lead to regenerative disorders. We show that senescent melanocytes drive hair follicle stem cells to exit quiescence and change their transcriptome and composition, dramatically enhancing hair regeneration. Senescent melanocytes activate a distinct secretome, containing pro-inflammatory factors. Osteopontin is a newly identified senescent secretome factor required for hair regeneration. Osteopontin injection is sufficient to induce new hair growth and to recruit myeloid cells, which amplify osteopontin levels and further enhance hair regeneration. Deletion of osteopontin, its receptor, or depletion of myeloid cells, all markedly limit enhanced hair regeneration induced by senescent melanocytes. While conventionally senescent cells are viewed as being detrimental for tissue regeneration, here we show that they can enhance regeneration via paracrine effects on the stem cell niche and immune cell modulation.

**Highlights**

- Paracrine signaling by senescent melanocytes prominently enhances hair regeneration
- Responding to senescent cell signals, hair follicles activate their stem cell niche
- Osteopontin is essential and sufficient for enhanced hair regeneration
- Osteopontin recruits myeloid cells that further amplify hair regeneration

**Introduction**

Stem cells (SCs) are critically required for long-term tissue maintenance and regeneration. To perform their function, SCs remain quiescent and transiently activate only when warranted, a switch that is tightly controlled. Immediate control is exerted by the short-range signaling niche (Scadden, 2014). Additionally, activities of thousands of individual SC niches are coordinated by long-range signaling cues from the surrounding tissues (Hsu and Fuchs, 2012; Plikus and Chuong, 2014). Because long-range signals coordinate activities of many SC niches at once, any changes in them can profoundly alter the overall regenerative potential of an organ. However, what cell types can function as efficient long-range regulators of SCs is poorly understood.

Skin offers a valuable model system for studying these fundamental aspects of SC biology. Skin contains progenitor-rich hair follicles (HFs) that regenerate in cycles (Muller-Rover et al., 2001). Each cycle starts with SC activation (Cotsarelis et al., 1990; Hsu et al., 2014), and requires signaling by the niche, featuring specialized dermal papilla (DP) fibroblasts (Sennett and Rendl, 2012). While HFs are able in principle to regenerate cyclically without external signaling inputs, many thousands of HFs physiologically coordinate their hair-making activities for the common goal of proper fur "manufacturing" (Wang et al., 2017a). Coordination is achieved via shared signaling between neighboring HFs (Plikus et al., 2011) and with other non-hair skin cell types. The most prominent effects on hair regeneration are exerted by skin adipocytes (Plikus et al., 2008) and adipose progenitors (Festa et al., 2011). This is possible because HFs and adipose tissue are close to each other and because they use some of the same signaling pathways – WNT, BMP, Hedgehog and PDGF – to regulate their cellular lineages. Innate and adaptive immune cells are also potent modifiers of hair regeneration dynamics (Ali et al., 2017; Castellana et al., 2014; Chen et al., 2015; Wang et al., 2019).

Here, we discover that senescent cells use their unique secretome to drive exit of tissue SCs from quiescence. We show that senescent melanocytes in pigmented nevi (*aka* moles) signal via paracrine factors to hyper-activate hair SCs, leading to prominently enhanced hair regeneration. A senescent secretome also recruits myeloid cells which, in turn, amplify and enrich it for additional pro-regenerative signaling factors. We identify osteopontin as a novel senescent secretome factor responsible for enhanced hair regeneration. Activation of tissue progenitors by aged cells provides a

novel paradigm in SC biology and identifies senescent cells as an attractive therapeutic target in regenerative disorders.

**Results**

***Hair regeneration is hyper-activated in the presence of senescent melanocytes***

As cyclic hair regeneration is tightly controlled at the level of SC quiescence, naturally occurring conditions of excessive hair growth are rare. Hairy pigmented nevi, a type of a benign skin lesion in humans, are peculiar as they show prominently enhanced hair growth (Figure 1A, 1B). Despite being well known clinically, the mechanism behind excessive hair growth in nevi is not understood. Oncogene mutations, commonly in *Nras* or *Braf*, in skin melanocytes induce nevi (Roh et al., 2015). Mutant cells first transiently expand but subsequently activate oncogene-induced senescence (OIS) (Dhomen et al., 2009), giving rise to a spatially restricted lesion enriched for senescent cells. Once in full senescence, cells express a specialized secretome, the senescence-associated secretory phenotype (SASP) (Coppe et al., 2008). Several inflammatory cytokines and growth factors are part of the SASP, and their essential signaling roles are being rapidly recognized in normal embryonic development (Storer et al., 2013), cellular reprogramming (Mosteiro et al., 2016; Ritschka et al., 2017), injury repair (Chiche et al., 2017; Demaria et al., 2014; Feng et al., 2019; Sarig et al., 2019), and cancer progression (Laberge et al., 2015; Ruhland et al., 2016; Yoshimoto et al., 2013). We hypothesized that enhanced hair growth in hairy nevi is driven by activating signaling from senescent melanocytes in HF SC niches.

First, we asked whether mouse models for melanocyte OIS replicate enhanced hair regeneration. We studied two models for melanocyte OIS: constitutive *Tyr-Nras*$^{Q61K}$ (Pawlikowski et al., 2013) and inducible *Tyr-CreER*$^{T2}$*;Braf*$^{V600E}$ mice (Michaloglou et al., 2005). In both models, oncogenes are overexpressed from the *Tyrosinase (Tyr)* enhancer/promoter regulatory region, that is highly specific to neural-crest derived melanocyte lineage (Ackermann et al., 2005; Bosenberg et al., 2006). Normal hair regeneration in mice is coordinated; large groups of HFs jointly transition from resting (telogen) to active growth phase (anagen) and then via regression (catagen) back into telogen (Plikus et al., 2008; Wang et al., 2017a). This coordination causes HF SCs to spend a large portion of their lifecycle in quiescence, only transiently activating to regenerate new hairs within discrete HF groups. Intriguingly, *Tyr-Nras*$^{Q61K}$ mice, whose skin contains many senescent melanocytes, identified as non-proliferative γH2AX$^{+}$ melanocytes (53.5% on average at P56; Figures 1C, 1D; S1), p21$^{+}$ melanocytes (Figure 1E, 1F) or senescent β-Gal+ cells (Figure 1G), show dramatically accelerated hair regeneration, with many ectopic anagen HFs present at any given time (Figures 1H-L; S2, S3). In control mice, dorsal HFs are in first anagen at postnatal day P15 (Figure S3A), first telogen by P23 (Figure S3B), and second anagen by P36 (Figure 1I). After that, HFs enter a lengthy second telogen spanning days P44-P69 (Figures 1J, 1K; S3). Intriguingly, at all time points examined, *Tyr-Nras*$^{Q61K}$ skin contained ectopic anagen HFs (n=3/time point) (Figures 1H-K; S3C-E), which were numerous even at P100 (n=3) (Figure S3F). The ectopic anagen phenotype is especially visible in *Tyr-Nras*$^{Q61K}$*;TOPGAL* mice, where all anagen HFs strongly activate *TOPGAL* WNT reporter and stain

positive for lacZ (Figure 1L). Ectopic anagen HF density in *Tyr-Nras*$^{Q61K}$ mice varied between the time points (Figures 1H), but on average it was 35.4% relative to synchronous anagen HF density in P30 wild type (WT) skin (Figure S2B).

Next, we crossed *Tyr-Nras*$^{Q61K}$ mice onto an albino *Tyr(C-2J)* background carrying a mutation in the tyrosinase gene. Despite the lack of melanin, albino *Tyr-Nras*$^{Q61K}$ mice displayed ectopic anagen both at P56 and P100 (Figure S4), indicating that is not excessive melanogenesis, but rather senescent melanocytes that are necessary for the nevus hair phenotype. Further, we induced senescent melanocytes in *Tyr-CreER*$^{T2}$*;Braf*$^{V600E}$ mice (n=4 per time point). Induced animals displayed prominent ectopic anagen at P44, P56, P69 and P100 (Figures 2A, 2B; S5) averaging 35.7% anagen HFs relative to P30 WT skin, which closely phenocopies *Tyr-Nras*$^{Q61K}$ mutants. We also asked if injection of senescent melanocytes into normal telogen skin would be sufficient to induce ectopic anagen. We sorted melanocyte lineage from *Tyr-Nras*$^{Q61K}$*;Tyr-CreER*$^{T2}$*;tdTomato* skin as tdTomato$^{+}$ cells (Figures 2C, 2D; S6). Intradermal injection of sorted cells from mutant mice into telogen skin of *SCID* mice induced new anagen within 21 days (18.7±4.9 anagen HFs/injection site; n=5; ~20,000 cells/injection) (Figure 2E, 2G). In contrast, injection of sorted cells from control *Tyr-CreER*$^{T2}$*;tdTomato* mice did not activate new anagen (0±0 anagen HFs/injection site; n=4) (Figure 2F). We also generated senescent melanocytes by exposing primary CD117$^{+}$ newborn mouse melanocytes to $H_2O_2$ (Figure 2H). High levels of $H_2O_2$-induced senescence were confirmed by senescent β-Gal staining (Figure 2I, 2J). DiI-labeled, $H_2O_2$-treated melanocytes induced new anagen in telogen *SCID* skin 21 days after injection (19.8±7.6 anagen HFs/injection site; n=6). In contrast, normal control melanocytes did not induce anagen (0±0 anagen HFs/injection site; n=7) (Figure 2K-M). We also treated *Tyr-Nras*$^{Q61K}$ mice with two subcutaneous injections of ABT-737, a small-molecule BCL-2/W/XL inhibitor and a potent senolytic drug (Yosef et al., 2016), at P10 and P12. Compared to vehicle control (n=6), ABT-737 treatment (n=6) visibly decreased pigmentation and significantly reduced ectopic anagen HFs at P56 (6.8±3.6 anagen HFs/mm$^2$ *vs.* 12.3±2 in control) (Figure 2N, 2O). Lastly, we studied *K14-Edn3* (Aoki et al., 2015) and *K14-Kitl* (Kunisada et al., 1998) mice, which, respectively, show dermal and epidermal expansion of non-senescent melanocytes. Both mouse models showed normal hair cycle progression, with synchronized anagen at P36 (n=3/model) and synchronized telogen at P56 (n=3/model) (Figure S7, S8). Taken together, our data shows that mouse models for melanocyte OIS reproduce the enhanced hair growth clinically observed in hairy pigmented nevi and that senescent melanocytes, but not normal melanocytes, are necessary and sufficient to hyper-activate HF regeneration.

***Senescent melanocytes disrupt hair stem cell quiescence***

We next asked how senescent melanocytes affect key HF cell populations: bulge SCs, hair germ progenitors and DP fibroblasts. We profiled their transcriptomes by RNA-sequencing (RNA-seq). Bulge (GFP$^{+}$/CD34$^{+}$/Pcad$^{low}$) and hair germ (GFP$^{+}$/CD34$^{neg}$/Pcad$^{hi}$) cells (Greco et al., 2009) were isolated from *K14-H2B-GFP* control and *Tyr-Nras*$^{Q61K}$*;K14-H2B-GFP* mutant mice, where CD34 and Pcad maintain WT

expression patterns (Figure S9). Subsets of DP fibroblasts were isolated as $GFP^+/CD133^+$ cells from *Tyr-Nras$^{Q61K}$;Sox2-GFP* mutant and *Sox2-GFP* control mice (Driskell et al., 2009). We profiled bulge and DP cells at P30 and P56, when WT HFs are in anagen and telogen, respectively. Hair germ cells were profiled at P56, since they exist only during telogen.

RNA-seq on bulge SCs revealed prominent gene expression differences between *Tyr-Nras$^{Q61K}$* and control mice (Figure 3A, 3B; Table S1). The largest differences were seen at P56, with mutant SCs down- and up-regulating 973 and 1,159 genes, respectively. Depleted gene ontology (GO) categories for mutant SCs included cell cycle block, circadian rhythm, and WNT and JAK-STAT suppression, while enriched categories contained cell cycle, cell migration, WNT signaling and skin development (Figure 3C; Table S1). These GO signatures indicate that *Tyr-Nras$^{Q61K}$* bulge SCs lose quiescence.

To confirm that the *Tyr-Nras$^{Q61K}$* bulk RNA-seq signature is not simply dominated by near-normal activated SCs from ectopic anagen HFs, we compared P56 mutant with P30 anagen and P56 telogen WT bulge cells by single-cell RNA-seq (scRNA-seq). WT cells from P30 and P56 formed a shared cluster C1 and two phase-specific clusters: anagen-specific C2 and telogen-specific C3 (Figure 3F-H). Upon marker analysis, C1 cells match the signature of inner bulge cells, which includes *Chit1, Krt6a* and *Krt80*, while both C2 and C3 cells match that of outer bulge *bona fide* SCs, which includes *Col18a1, Krt17, Lhx2, Tcf7l2* and *Vdr* (Figures 3J; S10-S12; Tables S2, S3) (Joost et al., 2016; Yang et al., 2017). P56 mutant bulge cells dramatically altered their composition relative to WT cells – some cells contributed to the shared inner bulge cluster C1, others to WT anagen-specific outer bulge cluster C2, while many cells formed two new mutant-specific clusters C4 and C5, which retained a core outer bulge signature (Figures 3H; S10). Importantly, no mutant cells contributed to WT telogen-specific outer bulge cluster C3, which has a quiescent gene expression signature, including *Bmp2, Col17a1, Ctgf, Grem1, Nfatc1, Tgm5* and *Wif1* (Figure 3H; S11). Loss of quiescence by mutant-specific outer bulge SCs is further evident from inferred cell cycle analysis – C5 cells were exclusively in S and G2/M phases (Figure 3I) with prominently upregulated mitotic markers (Figure 3J; Table S3) Additionally, mutant-specific outer bulge SCs upregulated a unique set of genes, including *Cux1, Msx2* and *Fgf5* (Figure 3J; Table S3). Given that P56 *Tyr-Nras$^{Q61K}$* skin contains many telogen HFs (Figure S2), the disappearance of WT telogen-specific C3 outer bulge cells supports the loss of quiescence by mutant telogen SCs. Outer bulge marker similarities between clusters C2 through C5 suggest that in the presence of senescent melanocytes, normally quiescent telogen SCs transition to a uniquely activated state.

Next, we confirmed loss of quiescence in functional assays. For pulse and pulse-chase experiments, mice were treated with EdU between P27-P34, when WT HFs are in anagen and their SCs proliferate. Four hrs after the EdU pulse, *Tyr-Nras$^{Q61K}$* mice displayed bulge SC labeling efficiency that was compatible to WT SCs (Figure S13). However, in a pulse-chase assay, there was a prominent loss of EdU-retaining SCs in *Tyr-Nras$^{Q61K}$* mice as noted by analysis at P92 (0.06% mutant *vs.* 0.5% WT $EdU^+$

bulge cells; n=4 per genotype) (Figure 3K). Depletion of EdU label-retaining SCs in mutants was confirmed by co-staining for SOX9 (Figure 3L). In a long-term clonogenic assay, the attachment ability of *Tyr-Nras$^{Q61K}$* bulge SCs was similar to that of WT SCs, but their serial passaging potential was compromised: mutant SCs supported 6 passages (n=3) compared to 13.7 passages for WT SCs (n=3) (Figure 3M, 3O). Attachment rates and passaging potential, however, did not differ between mutant (n=3) and WT hair germ progenitors (n=3) (Figure 3N, 3O).

Next, we returned to the bulk RNA-seq data and profiled it for signaling changes that accompany loss of quiescence by *Tyr-Nras$^{Q61K}$* bulge SCs. We confirmed that quiescence markers from single-cell analysis, including *Bmp2, Col17a1, Ctgf, Grem1, Nfatc1* and *Wif1,* were also downregulated in P56 *Tyr-Nras$^{Q61K}$* SCs on bulk analysis (Figure 3D; Table S1). Other known quiescence markers were also downregulated in *Tyr-Nras$^{Q61K}$* SCs: *Axin2*, *Fgf18* and *Foxc1* (Figure 3D, 3E). In addition, *Nras$^{Q61K}$* SCs downregulated multiple components of the BMP pathway *(Fst, Dand5, Nbl1, Nog, Smad9, Sostdc1)* and the WNT pathway *(Dkk3, Dkkl1, Fzd2/3/7/9, Wnt10a/3/7b),* as well as *Fgf1* and *Hhip*. Conversely, they upregulated TGFβ pathway members: *Bmp1, Gdf10, Inhba, Inhbb, Tgfb1;* WNT pathway factors: *Fzd4/5, Rspo1, Wnt9a;* as well as *Fgf5, Fgf21, Ccl21a, Cxcl9/10/12, Il1f5* and *Spp1* (Figure 3D). Interestingly, *Spp1* (osteopontin) showed the largest fold change (73.9x) and high expression values in P56 *Tyr-Nras$^{Q61K}$* compared to WT SCs. It was also highly expressed by P30 *Tyr-Nras$^{Q61K}$* SCs but not expressed by P30 WT SCs. Thus, *Spp1* is specifically upregulated in *Tyr-Nras$^{Q61K}$* bulge SCs. We also examined the expression pattern changes in hair germ and DP cells and found them to be complex, involving several important signaling pathways (Text S1; Figures S14, S15). Among other changes, *Tyr-Nras$^{Q61K}$* DP cells upregulated *Spp1*, similar to mutant bulge SCs (Figure S15).

***Nevus melanocytes express hair growth-inducing osteopontin***

Next, we asked which signaling factors nevus melanocytes express. We isolated the melanocyte lineage as tdTomato$^{+}$ cells from tamoxifen-induced *Tyr-Nras$^{Q61K}$;Tyr-CreER$^{T2}$;tdTomato* mutant and *Tyr-CreER$^{T2}$;tdTomato* control skin. P56 mutant cells were compared to both P30 anagen and P56 telogen WT cells on bulk RNA-seq (Figure 4A, 4B). This strategy identified 598 mutant-specific upregulated genes, and also excluded genes regulated as part of the normal hair cycle. Mutant-specific genes were enriched for GO terms, including aging, WNT suppression, cell cycle block and mitotic division (Figure 4C; Table S6). Consistent with mutant melanocytes undergoing OIS, they upregulated tumor suppressors *Cdkn2b (aka p15)*, *Lzts1,* as well as *Cdkn3, H2afx* and mitosis-associated genes *Aurka/b, Cdca3/8, Cdc20/25c, Cenpa, Mad2l1, Ncaph, Knstrn, Plk1, Psrc1* and *Reep4* (Figure 4D; Table S6). Upregulation of the latter genes is consistent with extended mitotic arrest by OIS melanocytes (Dikovskaya et al., 2015). Focusing on the secretome, we identified 27 signaling factors specifically upregulated in nevus

melanocytes, including BMP members *Bmp4, Fstl1;* WNT members *Frzb, Wif1, Wisp1;* IGF regulators *Igfbp2/4/7;* as well as *Dhh, Fgf7, Spp1* and *Tnf* (Figure 4F). Notably, 68% of the secretome genes enriched in *BRAF*$^{V600E}$-induced human senescent melanocytes *in vitro* (Pawlikowski et al., 2013) and 71% of the core *in vitro* SASP factors (Coppe et al., 2008; Freund et al., 2010) were represented in the transcriptome of P56 *Tyr-Nras*$^{Q61K}$ melanocytes (Figure 4G). Further, we compared P56 WT and *Tyr-Nras*$^{Q61K}$ melanocytes on scRNA-seq. Upon combined analysis, all cells formed five clusters, M1 through M5 (Figure 4H; Tables S7, S8), and *Tyr-Nras*$^{Q61K}$ melanocytes were enriched in clusters M1 and M3 (Figure 4I). While all clusters shared core melanocyte lineage markers, such as *Mlna* and *Tyr*, a number of *in vitro* SASP factors and other *Tyr-Nras*$^{Q61K}$ melanocyte-enriched secretome genes, including *Spp1*, showed enrichment in cluster M3 (Figure 4J; Table S8).

*Spp1* was one of the top upregulated signaling transcripts in multiple nevus skin cell types on RNA-seq (Figure 4E). We confirmed this change at the protein level. On cytometry, osteopontin-secreting cells were significantly increased in P56 *Tyr-Nras*$^{Q61K}$ (20.6±3.7%; n=7) *vs.* WT skin (5.3±4.0%; n=6) (Figure 4K). Significantly increased osteopontin levels (nascent ~35 kDa and modified ~65 kDa forms) were detected in P56 mutant skin by western blot (Figure 4L; n=6 per genotype) and on immunostaining, with multiple cell types, including dermal melanocytes (Figure 4M) and myeloid cells being positive (Figures S16, S17). A broad increase in osteopontin-expressing cells was confirmed by lacZ staining in *Tyr-Nras*$^{Q61K}$*;Spp1*$^{+/-}$ *vs.* control *Spp1*$^{+/-}$ skin (Figure S18).

Next, we asked if osteopontin plays a functional role in the *Tyr-Nras*$^{Q61K}$ phenotype and if it is sufficient to induce a new hair cycle in WT mice. We generated *Tyr-Nras*$^{Q61K}$*;Spp1*$^{-/-}$ mice to test if osteopontin deletion rescues hair cycle quiescence. Indeed, compared to *Tyr-Nras*$^{Q61K}$ mice, whose HFs start cycling ectopically already at P23 (Figure S3B), ectopic anagen in *Tyr-Nras*$^{Q61K}$*;Spp1*$^{-/-}$ mice is prevented at P23 (Figure 4O) and P44 (Figure S19C). Ectopic anagen in double mutant mice resumed at a low rate only at P52 (Figure S19D) and then became more prominent at P56 and P69 (Figure S19E, S19F), albeit still below *Tyr-Nras*$^{Q61K}$*;Spp1*$^{+/-}$ control mouse levels (Figure 4R; n=6 per time point). We also showed that between P18 and P69, the hair cycle in *Spp1*$^{-/-}$ mutant mice progresses largely normally compared to WT mice (Figures 4N; S19). These results indicate that osteopontin is dispensable for normal hair cycle progression but is essential for hair cycle hyper-activation in nevus skin. Appearance of ectopic anagen in *Tyr-Nras*$^{Q61K}$*;Spp1*$^{-/-}$ mice after P52 indicates that other factors, possibly part of the senescent secretome, can compensate for osteopontin loss.

Considering that osteopontin upregulates in immune cells and fibroblasts at the edge of skin wounds (Liaw et al., 1998; Mori et al., 2008), we asked if it mediates a wound-induced hair cycle activation, when HFs enter premature anagen at the wound margin (Argyris, 1956; Wang et al., 2017b). A previous study implicated TNF as one of the signaling mediators of this phenomenon (Wang et al., 2017b). We now show that compared to WT mice (46.6±17.1 anagen HFs; n=8), *Spp1*$^{-/-}$ mice show

significantly fewer anagen HFs at the margin of 5 mm wounds 11 days post-wounding (8.1±3.2 anagen HFs; n=7) (Figure 4Q). Also, anagen was prominently induced 12 days after intradermal injection of SPP1-soaked beads in WT mice (40.2±23.1 anagen HFs; n=5), compared to BSA-soaked control beads (1.4±1.3 anagen HFs; n=5) (Figure 4R). Moreover, premature anagen was activated by P54 in *Tyr-rtTA;tetO-Spp1* mice, induced with doxycycline starting from P42. Compared to doxycycline-treated control mice, which remained in telogen, *Tyr-rtTA;tetO-Spp1* mice displayed broad anagen activation (Figure 6A, 6B). Therefore, osteopontin is sufficient to induce a new hair cycle in WT mice, and it mediates hair cycle hyper-activation in at least two skin states: melanocytic nevus and wound healing.

Considering the late activation of ectopic anagen in adult *Tyr-Nras$^{Q61K}$;Spp1$^{-/-}$* mice lacking osteopontin, we tested the hair growth-inducing effect of several other signaling factors enriched in *Tyr-Nras$^{Q61K}$* melanocytes: FSTL1, FGF7, GDF10 and IGFBP7 (Figures S20, S21). Consistent with a previous report by Yucel et al. (2013), FSTL1 induced significant anagen upon protein-soaked bead injection, while GDF10 and IGFBP7 showed a trend for anagen activation. We posit that the combined activity of multiple senescent secretome factors likely functions to augment the anagen-inducing effect of osteopontin, and that these factors compensate for *Spp1* genetic loss in the nevus mouse model. We also performed a series of functional experiments in *Tyr-Nras$^{Q61K}$* mice to examine the role of canonical WNT signaling in hair growth hyper-activation and found that it was not essential for the nevus phenotype (Text S2; Figures S22, S23).

***Immune cells contribute to the nevus secretome and hair growth hyper-activation***

Considering an emerging role for immune cells in hair cycle activation (Ali et al., 2017; Castellana et al., 2014; Chen et al., 2015; Lee et al., 2017; Wang et al., 2019; Wang et al., 2017b), we asked if and how the immune cell secretome is altered in nevus skin. Using RNA-seq, we examined skin-resident CD45$^{+}$ hematopoietic cells (Figure S24; Table S9) and tdTomato$^{+}$ myeloid cells isolated from *LysM–Cre;tdTomato* mice (Figure 5A, 5B; Table S10). To identify mutant-specific genes, we used the same analysis strategy as with melanocytes and compared P56 *Tyr-Nras$^{Q61K}$* cells to both P30 and P56 WT cells. *Tyr-Nras$^{Q61K}$* myeloid cells were enriched for multiple GO terms, including chemotaxis, proteolysis and chemokine signaling (Figure 5C; Table S10), and prominently upregulated secreted factors that belong to the senescent secretome (Figure 5D, F) – a feature validated by qRT-PCR (Figure 5E) and scRNA-seq. Upon combined scRNA-seq analysis, P56 WT and *Tyr-Nras$^{Q61K}$* myeloid cells formed four clusters, ML1 through ML4 (Figure 5G; Tables S11, S12), and *Tyr-Nras$^{Q61K}$* cells were enriched in cluster ML1 (63%) and depleted in ML3 (15%; Figure 5H). While all clusters shared myeloid marker genes, such as *Cd68* and *Tyrobp*, a number of secretome genes, including *Spp1*, were preferentially expressed in the ML1 cluster (Figure 5I; Table S12). Consistent with this finding, on bulk RNA-seq, *Tyr-Nras$^{Q61K}$* myeloid cells upregulated secretome genes shared with nevus melanocytes: *Igfbp2/7, Postn, Spp1* and *Timp1*. At the same time, they upregulated chemokines *Ccl4/5/6/9/17* and *Cxcl19/12*, interleukins *Il1a/1f9/10,* as well as *Mmp2/3/12/14*, which are otherwise not upregulated in nevus melanocytes (Figure 5D). We conclude

that the combined secretome of senescent melanocytes and myeloid cells distinctly enriches the signaling environment of nevus skin for multiple inflammatory pathway ligands and, most prominently, *Spp1*.

Next, we determined the relative impact of myeloid cells on the nevus hair growth phenotype. Consistent with our RNA-seq data, myeloid cells are known as a source and a target for osteopontin signaling in the context of inflammatory conditions, including in the skin (Giachelli et al., 1998; Liaw et al., 1998; Mori et al., 2008). We observed significantly more tdTomato$^{+}$ cells in the skin of P56 *Tyr-Nras$^{Q61K}$;LysM-Cre;tdTomato* mutants (568.3±77.7 cells/mm$^2$) *vs. LysM-Cre;tdTomato* control myeloid-specific reporter mice (451.1±94.8 cells/mm$^2$) (Figures 5J). *Spp1* deletion reduced myeloid infiltration of P56 *Tyr-Nras$^{Q61K}$;Spp1$^{-/-}$;LysM-Cre;tdTomato* skin (505.2±186.2 cells/mm$^2$) to the levels comparable with *Spp1$^{-/-}$;LysM-Cre;tdTomato* controls (427.8±98.8 cells/mm$^2$) (Figures 5K), while recombinant SPP1 injection to P47 *LysM-Cre;tdTomato* skin led to a significant increase in myeloid cell infiltration after 24 hrs (857.5±151.3 cells/mm$^2$) *vs.* BSA control (512.0±113.5 cells/mm$^2$) (Figures 5L). This suggests that osteopontin signaling contributes to myeloid cell recruitment to nevus skin.

Next, we depleted myeloid cells from nevus skin with doxycycline treatment of *Tyr-Nras$^{Q61K}$;LysM-Cre;Rosa-rtTA;tetO-DTA* mice. We observed significantly fewer ectopic anagen HFs after seven days of doxycycline treatment (2.9±5.1 anagen HFs/1 mm$^2$; n=4) *vs.* doxycycline-treated littermate control animals, lacking *tetO-DTA* (18.7±6.4 anagen HFs/1 mm$^2$; n=4) (Figure 5N, 5O). However, injection of DiI-labeled CD11b$^{+}$ myeloid cells, sorted from *Tyr-Nras$^{Q61K}$* skin, into telogen skin of *SCID* mice did not induce new anagen within 21 days (n=3; ~20,000 cells/injection) (Figure 5M). Likewise, in grafting assays, significant reduction in ectopic anagen HFs was observed only in *Tyr-Nras$^{Q61K}$;Spp1$^{-/-}$* to *SCID* skin grafts (18.7±6.6 anagen HFs/1 mm$^2$; n=6) as compared to *Tyr-Nras$^{Q61K}$* to *SCID* grafts (22.7±3.3 anagen HFs/1 mm$^2$; n=3). The rate of ectopic anagen in *Tyr-Nras$^{Q61K}$* skin grafted onto osteopontin-deficient *SCID;Spp1$^{-/-}$* mice (21±4.1 anagen HFs/1 mm$^2$; n=3) did not differ from that in *Tyr-Nras$^{Q61K}$* to *SCID* grafts (Figure 6C). We conclude that myeloid cells contribute to hair growth-inducing signals in nevus skin, but in isolation are insufficient to stimulate the hair cycle. Results of the skin grafting assays suggest that myeloid-produced osteopontin largely comes from skin-resident rather than blood-derived myeloid cells.

***CD44 receptor-mediated osteopontin effect on hair growth***

Next, we examined if the osteopontin receptor CD44 (Weber et al., 1996) mediates the nevus phenotype. *Cd44* was highly expressed in multiple skin cell types, including bulge and hair germ cells, both in *Tyr-Nras$^{Q61K}$* and control mice (Figure S25A). *Cd44* generates alternatively-spliced isoforms, including standard *Cd44s* and several variable *Cd44v* isoforms. RNA-seq analysis identified cell type-specific *Cd44* isoform enrichment patterns (Figure S25B). Bulge and hair germ cells were particularly

enriched for *Cd44v* isoforms containing exons *v6* and *v7*, previously implicated in mediating osteopontin signaling (reviewed in Ponta et al., 2003). We confirmed broad *Cd44* expression in the skin, including in bulge SCs by lacZ staining in *Tyr-Nras$^{Q61K}$;Cd44$^{+/-}$* and control *Cd44$^{+/-}$* reporter mice (Figure S26). Anagen induction in response to osteopontin-soaked beads was significantly suppressed in germline *Cd44$^{-/-}$* (4.8±3.0 anagen HFs; n=5) *vs.* WT mice (40.2±23.1 anagen HFs; n=5) (Figure 6D; same WT mice as in Figure 4R). Likewise, significantly fewer anagen HFs were induced at the wound margin of *Cd44$^{-/-}$* mutant (29.0±27.7 anagen HFs; n=5) *vs.* control mice (63.3±22.5 anagen HFs; n=6) (Figure 6E, 6E'). Furthermore, *Cd44* deletion in *Tyr-Nras$^{Q61K}$;Cd44$^{-/-}$* mice led to partial rescue of ectopic hair cycling, phenocopying the effect of *Spp1* deletion in the *Tyr-Nras$^{Q61K}$* background. All HFs in *Tyr-Nras$^{Q61K}$;Cd44$^{-/-}$* mice were in telogen at P44 (Figure 6F); occasional ectopic anagen HFs first appeared at P52, increasing thereafter (Figure 6G, 6H; S27). We also established that, similar to *Spp1* deletion alone, *Cd44* deletion alone does not significantly alter normal progression of the first two hair cycles. Lastly, we tested if the hair growth-activating effect of osteopontin requires CD44 signaling specifically on epithelial HF cells. We generated epithelial-specific constitutive *K14-Cre;Cd44$^{fl/fl}$* as well as tamoxifen-inducible *K14-CreER$^{T}$;Cd44$^{fl/fl}$* mice and injected them with osteopontin-soaked beads. Indeed, compared to osteopontin-treated control mice, telogen HFs both in *K14-Cre;Cd44$^{fl/fl}$* (4.2±2.9 anagen HFs (n=6) *vs.* 21±16.4 anagen HFs (n=4)) (Figure 6I) and induced *K14-CreER$^{T}$;Cd44$^{fl/fl}$* mice had significantly reduced anagen activation (5±1 anagen HFs (n=3) *vs.* 21.5±11.1 anagen HFs (n=4)) (Figure 6J). Therefore, the hair-growth activating effect of osteopontin in nevus skin requires epithelial CD44 signaling.

***Human hairy nevi upregulate osteopontin expression***

We also examined signaling aspects of hairy nevi in humans. Whole-tissue RNA-seq revealed prominent differences between hairy nevi and adjacent normal facial skin, and patient-to-patient variability (Figure 7A-C; Table S13). Nevi showed enrichment for melanogenesis genes *BCAN, DCT, GPR143, MITF, MLANA, MLPH, PMEL, TYR* and *TYRP1,* and consistent with *Tyr-Nras$^{Q61K}$* mouse data, they upregulated tumor suppressors *CDKN2A, GAS5, LZTS1, MIA* and mitosis markers *ANKRD53, MAD1L1, NEK6, PSRC1* (Figure 7D). Among secreted factors, they upregulated several TGFβ/BMP members *GDF1/10/11/15* and *BAMBI,* WNT modulators *DKKL1, FRZB,* as well as *CCL18, IL17D, PDGFD* and *SPP1* (Figure 7D; Table S13). *SPP1* was among upregulated secretome factors shared between human hairy nevi consistently across patients and *Tyr-Nras$^{Q61K}$* mouse melanocytes and myeloid cells (Figure 7E), which we validated by qRT-PCR (Figure 7E) and by immunostaining (Figure 7G-I'). Increased SPP1 expression was prominent in the dermis, where many SPP1$^{+}$ cells co-expressed myeloid marker CD11b (Figure 7I'). Also, many SPP1/TRP2 double-positive melanocytes were seen in nevus skin surrounding bulge and bulb regions of anagen HFs (Figure 7H'). Together, these data indicate that SPP1 overexpression correlates with hair growth hyper-activation in human nevi.

**Discussion**

In this work, we reveal that senescent cells prominently activate tissue-resident SCs and stimulate regeneration (Figure S28). Traditionally, accumulation of senescent cells is viewed as detrimental to regenerative potential and a sign of aging. Naturally, the large scale conversion of tissue progenitors toward a senescent state would reduce an organ's potential to renew and repair. Indeed, targeted genetic (Baker et al., 2016; Baker et al., 2011) and pharmacologic depletion (Chang et al., 2016) of senescent cells in mice delays the onset of age-related pathologies. At the same time, recent evidence points toward beneficial paracrine effects of senescent cells on progenitor cell activities. In the context of induced pluripotency, *in vivo* overexpression of Oct4/Sox2/Klf4/cMyc causes both cellular reprogramming and cellular senescence to occur in close proximity. By secreting interleukin IL6, senescent cells create a permissive signaling environment that improves the reprogramming efficiency of their neighbors (Mosteiro et al., 2016). Tissue injury, which generates an excess of senescent cells, further enhances this phenomenon (Chiche et al., 2017). Transient exposure of normal epithelial skin cells to SASP factors *in vitro* increases their stemness, and improves their morphogenetic potential in skin-reconstitution experiments (Ritschka et al., 2017). Cancer cells can exploit paracrine factors secreted by neighboring senescent cells to enhance their stemness and tumor progression (Ruhland et al., 2016; Yoshimoto et al., 2013).

We show that paracrine signals from senescent melanocytes hyper-activate normally quiescent HF SCs. This results in enhanced hair growth and produces a distinct, clinically-recognizable hairy nevus skin phenotype. Importantly, under normal conditions, melanocytes are not important regulators of HF SCs and hair regeneration. Thus, acquisition of senescence confers non-niche cells with novel niche-like properties. By the same accord, we posit that the acquisition of senescence by "professional" niche cells can endow them with new, constitutively-active properties. Future works should seek similar effects of cellular senescence on SC functions in other actively renewing organs, such as gut and bone marrow.

Paracrine effects of senescent cells are thought to be mediated by their secretome, a collection of signaling molecules enriched for inflammatory chemokines and interleukins (Coppe et al., 2008; Freund et al., 2010). Intriguingly, our transcriptomic analyses uncovered that top factors within the senescent melanocyte secretome *in vivo* only partially overlap with the core SASP factors *in vitro*. We posit that the default secretome of senescent cells alters *in vivo*, most likely in response to reciprocal interactions with other cell types in their neighborhood. We show that tissue-resident myeloid cells are one such cell type. Indeed, upon entering the nevus environment, myeloid cells change their transcriptome and overexpress multiple signaling factors, both unique and shared with the surrounding senescent melanocytes. We also show that inducible depletion of myeloid cells can partially reduce the hair growth hyper-activating effect of the nevus. Nevertheless, purified nevus-derived myeloid cells do not stimulate hair growth, suggesting that they play a secondary role in nevus-induced hair growth. We conclude that the unique secretome of senescent cell-enriched tissues is a collaborative result of leading

senescent and supportive immune cell activities. This finding parallels the hair growth-promoting effects of macrophages in other contexts, including in injury response-activating hair plucking (Chen et al., 2015) and wounding (Rahmani et al., 2018; Wang et al., 2017b). We posit that immune cells can modulate *in vivo* activities of senescent cells in other organs, beyond skin, and in other contexts, beyond regeneration. Future works should better delineate the crosstalk between senescent and immune cells *in vivo*.

Analysis of overexpressed signaling genes in nevus skin identified several new putative regulators of hair regeneration. We uncovered and validated the previously unrecognized hair growth-activating effect of osteopontin. Our expression data confirms the previously reported endogenous expression of *Spp1* in HF dermal papilla (Yu et al., 2001) and identifies it as one of the top upregulated signaling genes in multiple nevus skin cell types in mice and in human hairy nevi. Importantly, osteopontin has been identified as the top secretome factor produced by senescent fibroblasts in the context of inducing tumor progression (Pazolli et al., 2009). Our functional studies also demonstrate that the hair growth-promoting effect of osteopontin requires CD44 receptor signaling on epithelial cells. Future works will be necessary to test any synergistic effects of nevus-enriched signaling factors on the hair SC niche and how the combined effect of senescent secreted factors overcomes natural mechanisms of SC niche quiescence. In this context, our findings hold a therapeutic promise for regenerative disorders of the skin. Inspired by the naturally occurring condition of hairy nevus, our data points to future hair growth-stimulating therapies in which senescent cells or select senescent secretome factors are injected into hair loss-affected skin. Curiously, clinical cases describe hair loss-resistant pigmented nevi on the scalp of patients with alopecia, including alopecia universalis (Ruiz-Maldonado et al., 1993).

In conclusion, our study into the peculiar, yet poorly understood skin condition of hairy nevus led us to identify a distinct regulatory mechanism for adult SCs by tissue-resident senescent cells. These findings have far reaching implications for advancing our understanding of SC niche regulation and for developing new therapeutic strategies to regenerative disorders.

**Acknowledgements**

M.V.P. is supported by the NIH grants R01-AR067273, R01-AR069653, Edward Mallinckrodt Jr. Foundation, Pew Charitable Trust, LEO Foundation, UCI Applied Innovation POP grant; Q.N. and M.V.P. by the NIH grant U01-AR073159; Q.N., M.V.P., B.A. and X.W. by the NSF grant DMS1763272 and Simons Foundation Grant (594598, QN); M.V.P and B.A. by the NIH grant P30-AR075047; B.A. by the NIH grants R01-AR44882, R01-AR056439; X.W. by the CIHR fellowship MFE-123724; K.Y. by Yoshida Scholarship Foundation; J.W.O. by the Korea NRF grant 2016R1C1B1015211; H.L.L. by the NIH grant T32-CA009054;

C.F.G.-J. by the NSF grant DGE-1321846 and MBRS-IMSD grant; R.R. by the MBRS-IMSD grant GM055246; R.R.V. by the NSF grant DGE-1321846; J.T. by Trauma SFB 1149.

**Author contributions**

M.V.P. oversaw the project; X.W., M.V.P wrote the paper and produced figures; X.W., A.Q.P, T.K.N., H.Y.L., A.N., K.N.V., J.L.P., K.H.T., N.T., K.N.P., C.F.G.-J., L.H.P.W., H.-L.L., T.K. characterized mouse phenotypes; X.W., R.R., X.C., J.W.O. carried out cell and protein injection and skin grafting experiments, X.W., S.J(Jiang)., S.J(Jin)., Y.L., Z.D., R.D., R.M. J.L. carried out RNA-seq analyses; X(Xiaoyang).W., J.F., V.S., G.W. carried out cellular assays; X.W., K.Y., E.N.G., R.R.-V., S.J(Jahid)., P.V. carried out protein assays; K.J.M., D.A.L, B.A., A.M., Q.N., M.K., J.T., J.D.E., A.K.G. edited the paper.

**Declaration of interests**

M.V.P. is the inventor on a patent application filed by the University of California, Irvine describing the use of the senescent secretome for promoting hair growth.

**Figures and Figure legends**

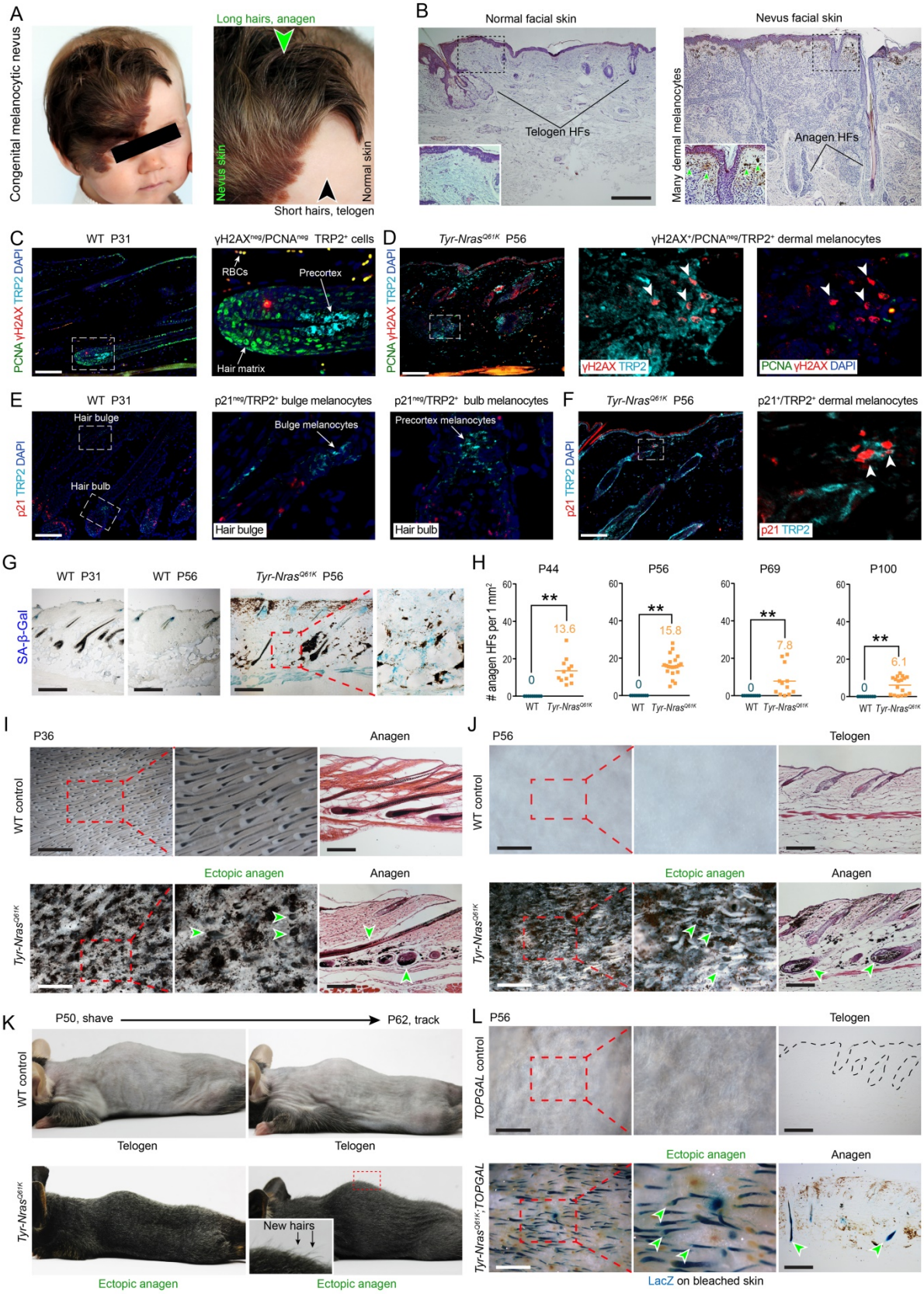
A
Congenital melanocytic nevus
Long hairs, anagen
Nevus skin
Normal skin
Short hairs, telogen
B
Normal facial skin
Nevus facial skin
Telogen HFs
Anagen HFs
Many dermal melanocytes
C
WT P31
γH2AXneg/PCNAneg TRP2+ cells
PCNA γH2AX TRP2 DAPI
RBCs
Precortex
Hair matrix
D
Tyr-NrasQ61K P56
γH2AX+/PCNAneg/TRP2+ dermal melanocytes
γH2AX TRP2
PCNA γH2AX DAPI
E
WT P31
p21neg/TRP2+ bulge melanocytes
p21neg/TRP2+ bulb melanocytes
p21 TRP2 DAPI
Hair bulge
Hair bulb
Bulge melanocytes
Precortex melanocytes
F
Tyr-NrasQ61K P56
p21+/TRP2+ dermal melanocytes
p21 TRP2
G
WT P31
WT P56
Tyr-NrasQ61K P56
SA-β-Gal
H
P44
P56
P69
P100
# anagen HFs per 1 mm2
**
13.6
15.8
7.8
6.1
0
WT
Tyr-NrasQ61K
I
P36
Anagen
WT control
Ectopic anagen
Anagen
Tyr-NrasQ61K
J
P56
Telogen
WT control
Ectopic anagen
Anagen
Tyr-NrasQ61K
K
P50, shave
P62, track
WT control
Telogen
Telogen
Tyr-NrasQ61K
New hairs
Ectopic anagen
Ectopic anagen
L
P56
Telogen
TOPGAL control
Ectopic anagen
Anagen
Tyr-NrasQ61K;TOPGAL
LacZ on bleached skin

**Figure 1: Hyper-activation of hair regeneration in nevus skin. (A)** Hair regeneration is prominently enhanced within congenital melanocytic nevus skin in humans (green arrowhead). **(B)** Facial HFs that commonly remain in telogen (left), activate and enter new anagen (right). Green arrowheads mark dermal melanin. **(C-F)** Compared to WT anagen skin **(C, E)**, *Tyr-Nras*$^{Q61K}$ skin at P56 contains many γH2AX$^{+}$/PCNA$^{neg}$/TRP2$^{+}$ **(D)** and p21$^{+}$/TRP2$^{+}$ **(F)** senescent melanocytes (arrowheads in insert). Also, see Figure S1. **(G)** Unlike WT P31 anagen and P56 telogen skin, P56 *Nras*$^{Q61K}$ skin contains many dermal senescent β-Gal+ cells (blue). **(H-J)** *Tyr-Nras*$^{Q61K}$ mice display enhanced hair regeneration. At all postnatal time points examined (Figures S3; n=3 each), including days P36 **(I)** and P56 **(J)**, *Tyr-Nras*$^{Q61K}$ skin contained many ectopic anagen HFs (green arrowheads). In contrast, HFs in WT mice collectively transitioned from anagen at P36 to telogen at P56. Ectopic anagen HFs are quantified in **H**. **(K)** Confirming continuous anagen, twelve days after shaving at P50, many new hairs grew in *Tyr-Nras*$^{Q61K}$, but not in WT mice. **(L)** At P56, *Tyr-Nras*$^{Q61K}$*;TOPGAL* mice (n=4), but not control *TOPGAL* mice (n=4) showed many lacZ$^{+}$ anagen HFs (green arrowheads). Scale bars: B – 500 um; C-F – 100 um; I, J, L (whole mount) – 1 mm; G, I, J, L (histology) – 200 μm.

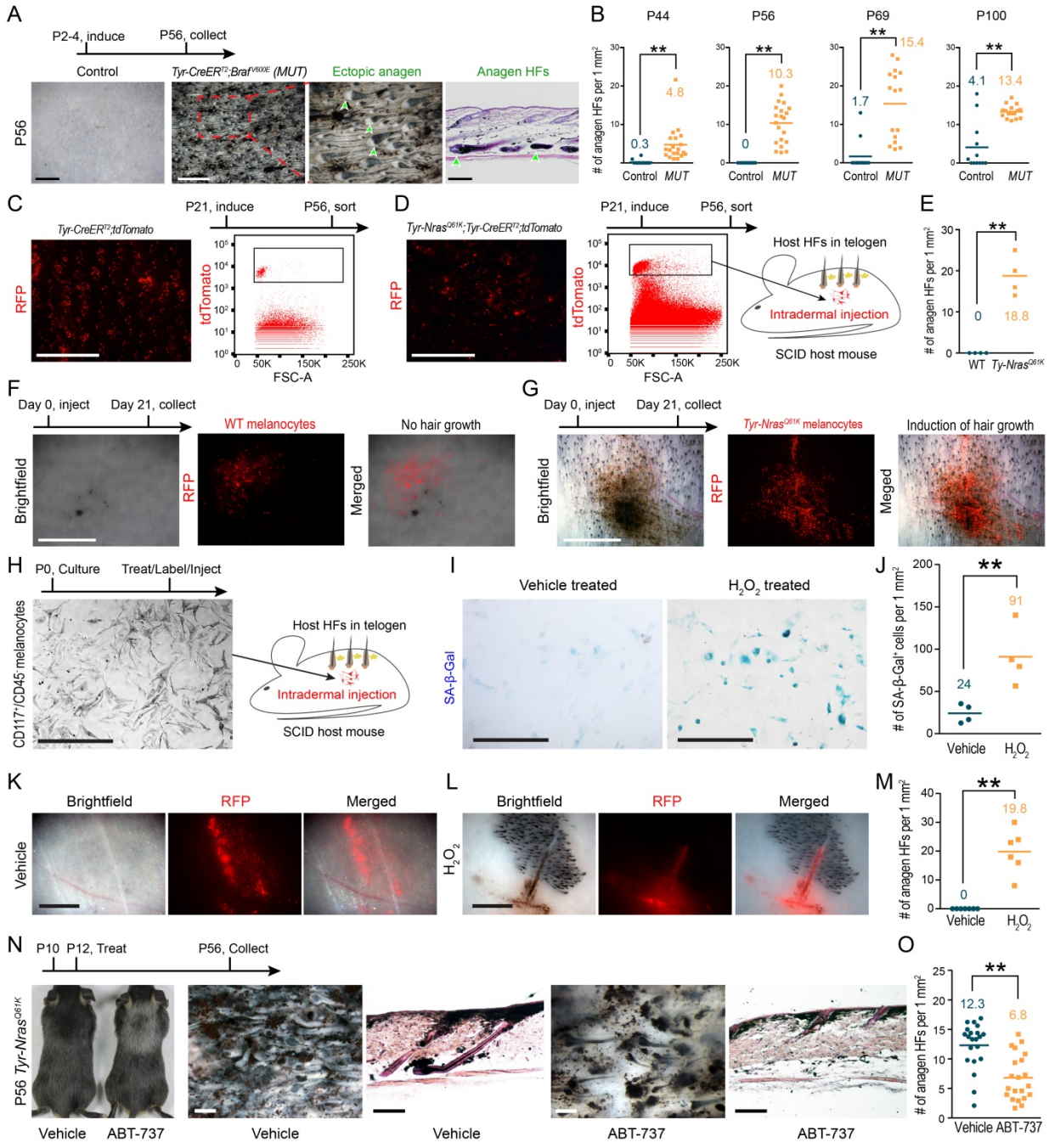
A
P2-4, induce
P56, collect
Control
Tyr-CreER^T2;Braf^V600E (MUT)
Ectopic anagen
Anagen HFs
P56
B
P44
P56
P69
P100
# of anagen HFs per 1 mm²
Control
MUT
C
Tyr-CreER^T2;tdTomato
P21, induce
P56, sort
RFP
tdTomato
FSC-A
D
Tyr-Nras^Q61K;Tyr-CreER^T2;tdTomato
Host HFs in telogen
Intradermal injection
SCID host mouse
E
WT
Ty-Nras^Q61K
F
Day 0, inject
Day 21, collect
WT melanocytes
No hair growth
Brightfield
Merged
G
Tyr-Nras^Q61K melanocytes
Induction of hair growth
Meged
H
P0, Culture
Treat/Label/Inject
CD117⁺/CD45⁻ melanocytes
I
Vehicle treated
H2O2 treated
SA-β-Gal
J
# of SA-β-Gal⁺ cells per 1 mm²
Vehicle
K
L
M
N
P10 P12, Treat
P56, Collect
P56 Tyr-Nras^Q61K
ABT-737
O

**Figure 2: Senescent melanocytes are required for hair growth hyper-activation. (A, B)** Compared to tamoxifen-induced control mice, induced *Tyr-CreER$^{T2}$;Braf$^{V600E}$* mutants showed prominent hair cycle hyper-activation. Representative P56 control and mutant skin samples are shown in **A**. Ectopic anagen HFs are marked with arrowheads in **A**, and quantified in **B**. Also, see Figure S5. **(C-G)** Melanocyte grafting experiment. Melanocyte lineage cells were isolated as tdTomato$^{+}$ cells from P56 *Tyr-CreER$^{T2}$;tdTomato* control **(C)** and *Tyr-Nras$^{Q61K}$;Tyr-CreER$^{T2}$;tdTomato* mutant skin **(D)** and intradermally injected into telogen skin of *SCID* mice. Also, see Figure S6. Mutant **(G)**, but not control tdTomato$^{+}$ cells **(F)** induced ectopic anagen 21 days after injection. Brightfield, fluorescent and merged images are shown. Induced anagen HFs are quantified in **E**. **(H-M)** $H_2O_2$-induced senescence experiment. Experimental design is shown in **H**. Senescence in primary CD117$^{+}$ newborn mouse melanocytes was induced by 2-hr exposure to $H_2O_2$ and confirmed with senescent β-Gal staining **(I, J)**. DiI-labeled $H_2O_2$-treated and normal control primary melanocytes were intradermally injected into telogen skin of *SCID* mice. $H_2O_2$-treated **(L)**, but not control cells **(K)** induced ectopic anagen 21 days after injection. Brightfield, fluorescent and merged images are shown. Induced anagen HFs are quantified in **M**. **(N, O)** Senescent cell depletion experiment. Compared to vehicle control, two subcutaneous ABT-737 treatments of *Tyr-Nras$^{Q61K}$* mice at P10 and P12 resulted in visible decrease in fur pigmentation and significant reduction in ectopic anagen HFs at P56 **(N)**. Ectopic anagen HFs are quantified in **O**. Scale bars: A (whole mount), K, L – 1 mm; C, D, F, G – 2 mm; A (histology) – 100 μm; H, I, N – 200 μm.

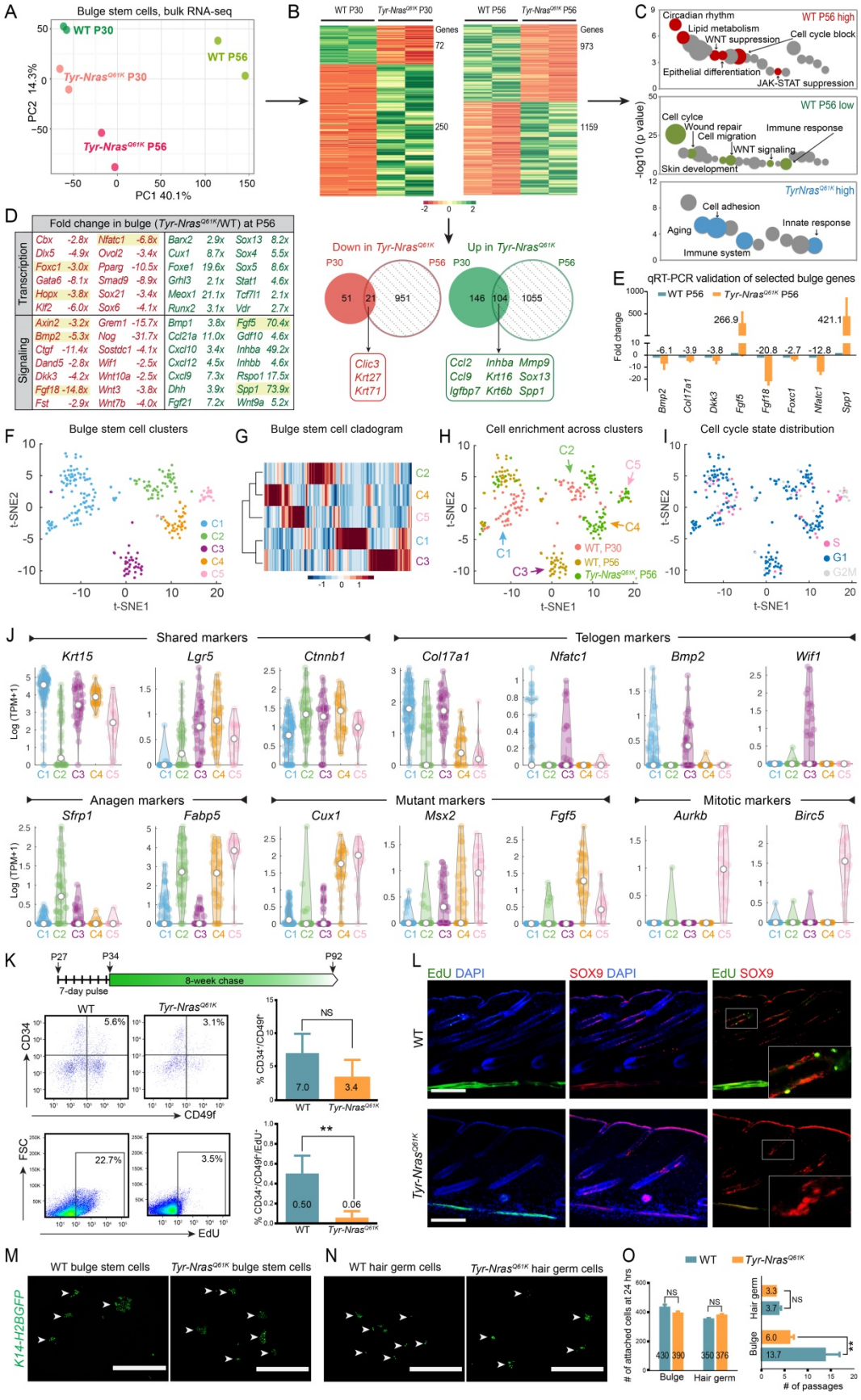
A
Bulge stem cells, bulk RNA-seq
WT P30
WT P56
Tyr-Nras^Q61K P30
Tyr-Nras^Q61K P56
PC1 40.1%
PC2 14.3%
B
WT P30
Tyr-Nras^Q61K P30
WT P56
Tyr-Nras^Q61K P56
Genes
72
250
973
1159
Down in Tyr-Nras^Q61K
Up in Tyr-Nras^Q61K
P30
P56
51
21
951
146
104
1055
Clic3
Krt27
Krt71
Ccl2
Inhba
Mmp9
Ccl9
Krt16
Sox13
Igfbp7
Krt6b
Spp1
C
WT P56 high
Circadian rhythm
Lipid metabolism
WNT suppression
Cell cycle block
Epithelial differentiation
JAK-STAT suppression
WT P56 low
Cell cylce
Wound repair
Cell migration
Immune response
WNT signaling
Skin development
Tyr-Nras^Q61K high
Cell adhesion
Aging
Innate response
Immune system
-log10 (p value)
D
Fold change in bulge (Tyr-Nras^Q61K/WT) at P56
Transcription
Signaling
Cbx -2.8x Nfatc1 -6.8x
Dlx5 -4.9x Ovol2 -3.4x
Foxc1 -3.0x Pparg -10.5x
Gata6 -8.1x Smad9 -8.9x
Hopx -3.8x Sox21 -3.4x
Klf2 -6.0x Sox6 -4.1x
Axin2 -3.2x Grem1 -15.7x
Bmp2 -5.3x Nog -31.7x
Ctgf -11.4x Sostdc1 -4.1x
Dand5 -2.8x Wif1 -2.5x
Dkk3 -4.2x Wnt10a -2.5x
Fgf18 -14.8x Wnt3 -3.8x
Fst -2.9x Wnt7b -4.0x
Barx2 2.9x Sox13 8.2x
Cux1 8.7x Sox4 5.5x
Foxe1 19.6x Sox5 8.6x
Grhl3 2.1x Stat1 4.6x
Meox1 21.1x Tcf7l1 2.1x
Runx2 3.1x Vdr 2.7x
Bmp1 3.8x Fgf5 70.4x
Ccl21a 11.0x Gdf10 4.6x
Cxcl10 3.4x Inhba 49.2x
Cxcl12 4.5x Inhbb 4.6x
Cxcl9 7.3x Rspo1 17.5x
Dhh 3.9x Spp1 73.9x
Fgf21 7.2x Wnt9a 5.2x
E
qRT-PCR validation of selected bulge genes
WT P56
Tyr-Nras^Q61K P56
Fold change
-6.1
-3.9
-3.8
266.9
-20.8
-2.7
-12.8
421.1
Bmp2
Col17a1
Dkk3
Fgf5
Fgf18
Foxc1
Nfatc1
Spp1
F
Bulge stem cell clusters
t-SNE1
t-SNE2
C1
C2
C3
C4
C5
G
Bulge stem cell cladogram
H
Cell enrichment across clusters
WT, P30
WT, P56
Tyr-Nras^Q61K, P56
I
Cell cycle state distribution
S
G1
G2M
J
Shared markers
Telogen markers
Krt15
Lgr5
Ctnnb1
Col17a1
Nfatc1
Bmp2
Wif1
Log (TPM+1)
Anagen markers
Mutant markers
Mitotic markers
Sfrp1
Fabp5
Cux1
Msx2
Fgf5
Aurkb
Birc5
K
P27
P34
P92
7-day pulse
8-week chase
WT
Tyr-Nras^Q61K
5.6%
3.1%
CD34
CD49f
NS
7.0
3.4
% CD34+/CD49f+
22.7%
3.5%
FSC
EdU
**
0.50
0.06
% CD34+/CD49f+/EdU+
L
EdU DAPI
SOX9 DAPI
EdU SOX9
WT
Tyr-Nras^Q61K
M
WT bulge stem cells
Tyr-Nras^Q61K bulge stem cells
K14-H2BGFP
N
WT hair germ cells
Tyr-Nras^Q61K hair germ cells
O
WT
Tyr-Nras^Q61K
# of attached cells at 24 hrs
NS
430
390
350
376
Bulge
Hair germ
Hair germ
Bulge
3.3
3.7
6.0
13.7
**
# of passages

**Figure 3: Hair stem cells within nevus skin lose quiescence. (A, B)** Bulk RNA-seq reveals prominent differences between *Tyr-Nras*$^{Q61K}$ and WT bulge SCs both at P30 (WT anagen) and P56 (WT telogen). PCA plot is shown in **A** and heatmaps of differentially expressed genes (DEGs) in **B**. Venn diagrams in **B** identify 21 downregulated and 104 upregulated genes specific to *Tyr-Nras*$^{Q61K}$. See Table S1. **(C)** Bubble charts showing enriched (red) and depleted (green) GO terms in P56 WT bulge SCs, and enriched GO terms in *Tyr-Nras*$^{Q61K}$ bulge SCs. Selected bubbles are colored and annotated. Bubble sizes correlate with gene numbers and their vertical position corresponds to significance. See Table S1. **(D)** List of selected downregulated (red) and upregulated (green) transcription and signaling factors at P56 and corresponding *Tyr-Nras*$^{Q61K}$/WT fold change values. Selected genes are highlighted. **(E)** qRT-PCR validation of selected DEGs from bulk RNA-seq data in **B**. **(F)** Combined tSNE analysis on scRNA-seq data for P30 and P56 WT and P56 *Tyr-Nras*$^{Q61K}$ bulge cells. Five clusters, C1 through C5, were identified and color-coded. **(G)** Unsupervised hierarchical clustering of average gene signatures on scRNA-seq data, showing relative cluster similarity. **(H)** tSNE plot color-coded by sample source. All samples contributed to shared cluster C1. Cluster C2 contains P30 WT and some P56 *Tyr-Nras*$^{Q61K}$ cells. Cluster C3 is specific to the P56 WT sample, while clusters C4 and C5 are specific to the P56 *Tyr-Nras*$^{Q61K}$ sample. **(I)** tSNE plot color-coded by inferred cell cycle state. Putative G1, S and G2/M cells are identified. **(J)** Violin plots for selected genes. Color coding matches cell cluster colors from **F**. Also, see Figures S10-S12 and Tables S2, S3. **(K)** EdU pulse (7 days) / chase (8 weeks) analysis on bulge SCs. While total numbers of CD34$^{+}$/CD49f$^{+}$ bulge SCs cells do not significantly differ between WT and *Tyr-Nras*$^{Q61K}$ mice (top), percentage of EdU$^{+}$ label-retaining SCs is reduced significantly in *Tyr-Nras*$^{Q61K}$ mutants (bottom). Also, see Figure S13. **(L)** Unlike WT HFs, *Tyr-Nras*$^{Q61K}$ HFs from the experiment in **K** lack EdU$^{+}$/SOX9$^{+}$ double-positive bulge SCs (yellow). **(M, N)** Viability and attachment rate at 24 hrs for *K14-H2B-GFP* expressing bulge and hair germ cells are similar between WT and *Tyr-Nras*$^{Q61K}$ mice. **(O)** Compared to WT, *Tyr-Nras*$^{Q61K}$ bulge SCs have prominently reduced serial passaging potential, while it is unaltered for hair germ progenitors. Scale bars: L – 100 μm; M – 1 mm.

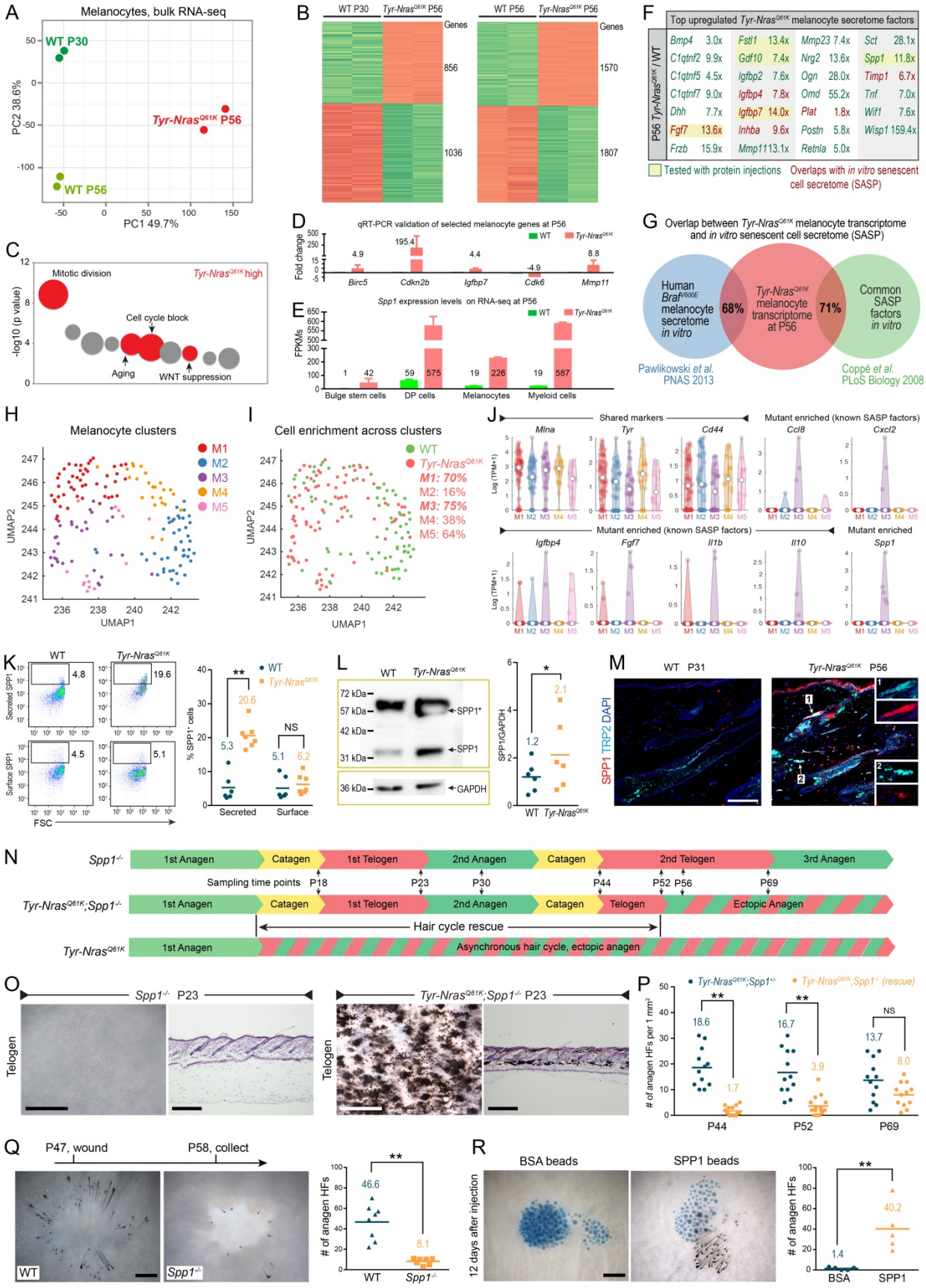
A
Melanocytes, bulk RNA-seq
WT P30
Tyr-Nras^Q61K P56
WT P56
PC2 38.6%
PC1 49.7%
B
WT P30
Tyr-Nras^Q61K P56
WT P56
Tyr-Nras^Q61K P56
Genes
856
1036
1570
1807
C
Mitotic division
Tyr-Nras^Q61K high
Cell cycle block
Aging
WNT suppression
-log10 (p value)
D
qRT-PCR validation of selected melanocyte genes at P56
WT
Tyr-Nras^Q61K
Fold change
4.9
195.4
4.4
-4.9
8.8
Birc5
Cdkn2b
Igfbp7
Cdk6
Mmp11
E
Spp1 expression levels on RNA-seq at P56
WT
Tyr-Nras^Q61K
FPKMs
1
42
59
575
19
226
19
587
Bulge stem cells
DP cells
Melanocytes
Myeloid cells
F
Top upregulated Tyr-Nras^Q61K melanocyte secretome factors
P56 Tyr-Nras^Q61K / WT
Bmp4 3.0x
C1qtnf2 9.9x
C1qtnf5 4.5x
C1qtnf7 9.0x
Dhh 7.7x
Fgf7 13.6x
Frzb 15.9x
Fstl1 13.4x
Gdf10 7.4x
Igfbp2 7.6x
Igfbp4 7.8x
Igfbp7 14.0x
Inhba 9.6x
Mmp11 13.1x
Mmp23 7.4x
Nrg2 13.6x
Ogn 28.0x
Omd 55.2x
Plat 1.8x
Postn 5.8x
Retnla 5.0x
Sct 28.1x
Spp1 11.8x
Timp1 6.7x
Tnf 7.0x
Wif1 7.6x
Wisp1 159.4x
Tested with protein injections
Overlaps with in vitro senescent cell secretome (SASP)
G
Overlap between Tyr-Nras^Q61K melanocyte transcriptome and in vitro senescent cell secretome (SASP)
Human Braf^V600E melanocyte secretome in vitro
68%
Tyr-Nras^Q61K melanocyte transcriptome at P56
71%
Common SASP factors in vitro
Pawlikowski et al. PNAS 2013
Coppé et al. PLoS Biology 2008
H
Melanocyte clusters
M1
M2
M3
M4
M5
UMAP2
UMAP1
I
Cell enrichment across clusters
WT
Tyr-Nras^Q61K
M1: 70%
M2: 16%
M3: 75%
M4: 38%
M5: 64%
UMAP2
UMAP1
J
Shared markers
Mutant enriched (known SASP factors)
Mutant enriched
Mlna
Tyr
Cd44
Ccl8
Cxcl2
Igfbp4
Fgf7
Il1b
Il10
Spp1
Log (TPM+1)
M1 M2 M3 M4 M5
K
WT
Tyr-Nras^Q61K
Secreted SPP1
Surface SPP1
FSC
4.8
19.6
4.5
5.1
% SPP1+ cells
Secreted
Surface
5.3
20.6
5.1
6.2
NS
L
WT
Tyr-Nras^Q61K
72 kDa
57 kDa
42 kDa
31 kDa
36 kDa
SPP1*
SPP1
GAPDH
SPP1/GAPDH
1.2
2.1
M
WT P31
Tyr-Nras^Q61K P56
SPP1 TRP2 DAPI
N
Spp1^-/-
1st Anagen
Catagen
1st Telogen
2nd Anagen
Catagen
2nd Telogen
3rd Anagen
Sampling time points
P18
P23
P30
P44
P52
P56
P69
Tyr-Nras^Q61K;Spp1^-/-
1st Anagen
Catagen
1st Telogen
2nd Anagen
Catagen
Telogen
Ectopic Anagen
Hair cycle rescue
Tyr-Nras^Q61K
1st Anagen
Asynchronous hair cycle, ectopic anagen
O
Spp1^-/- P23
Tyr-Nras^Q61K;Spp1^-/- P23
Telogen
P
Tyr-Nras^Q61K;Spp1^+/-
Tyr-Nras^Q61K;Spp1^-/- (rescue)
# of anagen HFs per 1 mm^2
18.6
1.7
16.7
3.9
13.7
8.0
NS
P44
P52
P69
Q
P47, wound
P58, collect
WT
Spp1^-/-
# of anagen HFs
46.6
8.1
R
BSA beads
SPP1 beads
12 days after injection
# of anagen HFs
1.4
40.2
BSA
SPP1

**Figure 4: Distinct secretome of senescent melanocytes contains osteopontin that promotes hair growth. (A, B)** Bulk RNA-seq reveals prominent differences between *Tyr-Nras*$^{Q61K}$ and WT melanocytes at P30 and P56. PCA plot is shown in **A** and heatmaps of DEGs in **B**. P56 *Tyr-Nras*$^{Q61K}$ cells (red) were compared to P30 and P56 WT cells (green). See Table S6. **(C)** Bubble chart showing enriched GO terms in *Tyr-Nras*$^{Q61K}$ melanocytes. Selected bubbles are colored and annotated. See Table S6. **(D)** qRT-PCR validation of selected DEGs from bulk RNA-seq data in **B**. **(E)** Absolute FPKM values for *Spp1* in distinct skin cell types at P56. **(F)** List of secretome factors specifically upregulated in *Tyr-Nras*$^{Q61K}$ melanocytes and corresponding *Tyr-Nras*$^{Q61K}$/WT fold change values at P56. Selected genes are highlighted. **(G)** Venn diagram showing the degree of overlap between the P56 *Tyr-Nras*$^{Q61K}$ melanocyte transcriptome and a published *in vitro* human senescent melanocyte secretome (blue, 68%) and core *in vitro* SASP factors (green, 71%). **(H)** Combined UMAP analysis on scRNA-seq data for P56 WT and *Tyr-Nras*$^{Q61K}$ melanocytes. Five clusters, M1 through M5, were identified and color-coded. **(I)** UMAP plot color-coded by sample source. Contribution from *Tyr-Nras*$^{Q61K}$ melanocytes (red cells) was the highest to clusters M1 (70%) and M3 (75%). **(J)** Violin plots for selected genes. Color coding matches cell cluster colors from **H**. See Tables S7, S8. **(K)** On flow cytometry, P56 *Tyr-Nras*$^{Q61K}$ skin contains significantly more SPP1-secreting, but not surface-positive cells than WT. Left – representative FACS plots, right – quantification. **(L)** On Western blot, P56 *Tyr-Nras*$^{Q61K}$ skin contains significantly increased levels of nascent (~35 kDa) and modified (~65 kDa) SPP1 than WT. Left – representative Western blot images, right – quantification. **(M)** Compared to WT anagen skin (left), *Tyr-Nras*$^{Q61K}$ skin at P56 contains many SPP1$^{+}$/TRP2$^{+}$ melanocytes (inserts on right). Also, see Figures S16, S17. **(N-P)** *Tyr-Nras*$^{Q61K}$*;Spp1*$^{-/-}$ mice lacking *Spp1* show partial rescue of hair cycle quiescence. Summary of hair cycle phases in *Spp1*$^{-/-}$ *vs. Tyr-Nras*$^{Q61K}$*;Spp1*$^{-/-}$ *vs. Tyr-Nras*$^{Q61K}$ mice is shown on **N**. Hair cycle phases are color-coded as follows: anagen (green), catagen (yellow), telogen (red), ectopic anagen (red and green stripes). Representative P23 *Spp1*$^{-/-}$ (left) and *Tyr-Nras*$^{Q61K}$*;Spp1*$^{-/-}$ skin samples (right), both in synchronized telogen, are shown on **O**. Also, see Figures S18, S19. Quantification of ectopic anagen HFs in *Tyr-Nras*$^{Q61K}$*;Spp1*$^{-/-}$ (orange) *vs. Tyr-Nras*$^{Q61K}$*;Spp1*$^{+/-}$ littermate control mice (blue) at P44, P52 and P69 is shown on **P** (n=6 per time point). **(Q)** *Spp1*$^{-/-}$ mice (n=7) showed significantly reduced efficiency of hair cycle activation 11 days after wounding compared to WT mice (n=8). Left – representative images, right – quantification. **(R)** Unlike BSA controls (n=5), SPP1-soaked beads (blue; n=5) induced ectopic anagen in WT telogen skin. Left – representative samples, right –quantification. Scale bars: M – 100 μm; O (histology) – 200 μm; O (whole mount), Q, R – 500 μm.

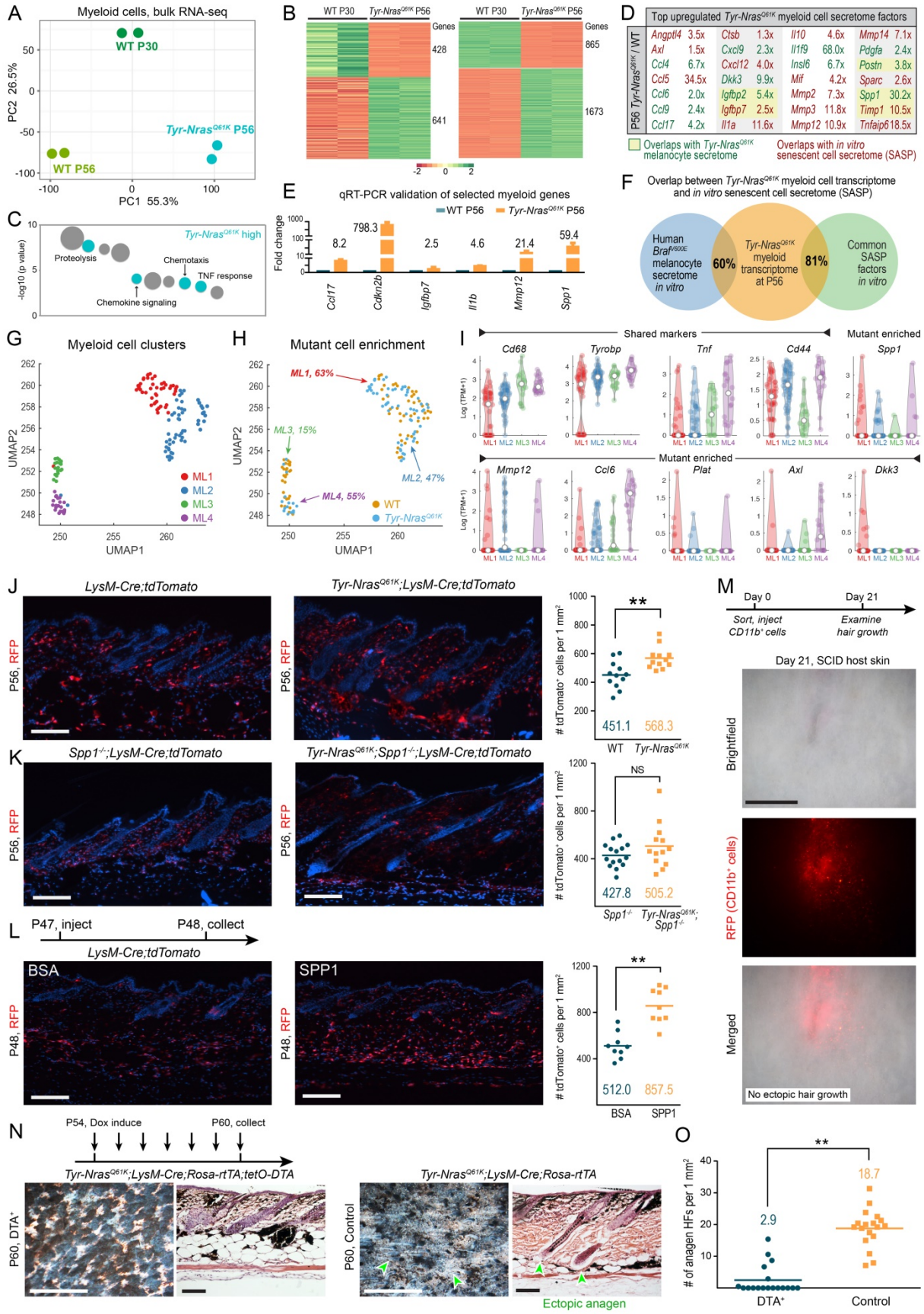
A
Myeloid cells, bulk RNA-seq
WT P30
Tyr-Nras^Q61K P56
WT P56
PC2 26.5%
PC1 55.3%
B
WT P30
Tyr-Nras^Q61K P56
Genes
428
641
865
1673
D
Top upregulated Tyr-Nras^Q61K myeloid cell secretome factors
P56 Tyr-Nras^Q61K / WT
Angptl4 3.5x
Axl 1.5x
Ccl4 6.7x
Ccl5 34.5x
Ccl6 2.0x
Ccl9 2.4x
Ccl17 4.2x
Ctsb 1.3x
Cxcl9 2.3x
Cxcl12 4.0x
Dkk3 9.9x
Igfbp2 5.4x
Igfbp7 2.5x
Il1a 11.6x
Il10 4.6x
Il1f9 68.0x
Insl6 6.7x
Mif 4.2x
Mmp2 7.3x
Mmp3 11.8x
Mmp12 10.9x
Mmp14 7.1x
Pdgfa 2.4x
Postn 3.8x
Sparc 2.6x
Spp1 30.2x
Timp1 10.5x
Tnfaip6 18.5x
Overlaps with Tyr-Nras^Q61K melanocyte secretome
Overlaps with in vitro senescent cell secretome (SASP)
C
Tyr-Nras^Q61K high
Proteolysis
Chemotaxis
TNF response
Chemokine signaling
-log10 (p value)
E
qRT-PCR validation of selected myeloid genes
WT P56
Tyr-Nras^Q61K P56
Fold change
8.2
798.3
2.5
4.6
21.4
59.4
Ccl17
Cdkn2b
Igfbp7
Il1b
Mmp12
Spp1
F
Overlap between Tyr-Nras^Q61K myeloid cell transcriptome and in vitro senescent cell secretome (SASP)
Human Braf^V600E melanocyte secretome in vitro
60%
Tyr-Nras^Q61K myeloid transcriptome at P56
81%
Common SASP factors in vitro
G
Myeloid cell clusters
UMAP2
UMAP1
ML1
ML2
ML3
ML4
H
Mutant cell enrichment
ML1, 63%
ML3, 15%
ML2, 47%
ML4, 55%
WT
Tyr-Nras^Q61K
I
Shared markers
Mutant enriched
Cd68
Tyrobp
Tnf
Cd44
Spp1
Mmp12
Ccl6
Plat
Axl
Dkk3
Log (TPM+1)
J
LysM-Cre;tdTomato
Tyr-Nras^Q61K;LysM-Cre;tdTomato
P56, RFP
# tdTomato+ cells per 1 mm2
451.1
568.3
WT
Tyr-Nras^Q61K
K
Spp1-/-;LysM-Cre;tdTomato
Tyr-Nras^Q61K;Spp1-/-;LysM-Cre;tdTomato
NS
427.8
505.2
Spp1-/-
Tyr-Nras^Q61K; Spp1-/-
L
P47, inject
P48, collect
LysM-Cre;tdTomato
BSA
SPP1
P48, RFP
512.0
857.5
M
Day 0
Day 21
Sort, inject CD11b+ cells
Examine hair growth
Day 21, SCID host skin
Brightfield
RFP (CD11b+ cells)
Merged
No ectopic hair growth
N
P54, Dox induce
P60, collect
Tyr-Nras^Q61K;LysM-Cre;Rosa-rtTA;tetO-DTA
Tyr-Nras^Q61K;LysM-Cre;Rosa-rtTA
P60, DTA+
P60, Control
Ectopic anagen
O
# of anagen HFs per 1 mm2
2.9
18.7
DTA+
Control

**Figure 5: Nevus myeloid cells augment the melanocyte secretome and contribute to hair growth activation. (A, B)** Bulk RNA-seq revealed prominent differences between *Tyr-Nras*$^{Q61K}$ and WT myeloid cells at P30 and P56. PCA plot is shown in **A** and heatmap of DEGs in **B**. P56 *Tyr-Nras*$^{Q61K}$ cells (blue) were compared to P30 and P56 WT cells (green). See Table S10. **(C)** Bubble chart showing enriched GO terms in *Tyr-Nras*$^{Q61K}$ myeloid cells. Selected bubbles are colored and annotated. See Table S10. **(D)** List of secretome factors specifically upregulated in *Tyr-Nras*$^{Q61K}$ myeloid cells and corresponding *Tyr-Nras*$^{Q61K}$/WT fold change values at P56. Selected genes are highlighted. **(E)** qRT-PCR validation of selected DEGs from bulk RNA-seq data in **B**. **(F)** Venn diagram showing the degree of overlap between P56 *Tyr-Nras*$^{Q61K}$ myeloid transcriptome and published *in vitro* human senescent melanocyte secretome (blue, 60%) and core *in vitro* SASP factors (green, 81%). **(G)** Combined UMAP analysis on scRNA-seq data for P56 WT and *Tyr-Nras*$^{Q61K}$ myeloid cells. Four clusters, ML1 through ML4, were identified and color-coded. **(H)** UMAP plot color-coded by sample source. Contribution from *Tyr-Nras*$^{Q61K}$ myeloid cells (orange cells) is the highest to clusters ML1 (63%) and the lowest in ML3 (15%). **(I)** Violin plots for selected genes. Color coding matches cell cluster colors from **G**. See Tables S11, S12. **(J)** P56 *Tyr-Nras*$^{Q61K}$*;LysM-Cre;tdTomato* skin is significantly enriched for RFP$^{+}$ myeloid cells compared to control. Data quantification on the right. **(K)** Deletion of *Spp1* in *Tyr-Nras*$^{Q61K}$ mice led to reduced numbers of RFP$^{+}$ myeloid cells in P56 skin compared to control *Spp1*$^{-/-}$ mutants. Data quantification is on the right. **(L)** SPP1 injection resulted in significant myeloid cell infiltration of the skin at 24 hrs compared to BSA control. Data quantification is on the right. **(M)** Injection of DiI-labeled CD11b$^{+}$ sorted myeloid cells from *Tyr-Nras*$^{Q61K}$ skin into telogen skin of *SCID* mice failed to induce ectopic anagen by day 21. Brightfield, fluorescent and merged images of the representative injection site are shown. **(N)** Inducible depletion of myeloid cells in day P54 *Tyr-Nras*$^{Q61K}$ mice (left) significantly reduced ectopic anagen HFs on day 6 compared to control (right). **(O)** Quantification of data from **N**. Scale bars: J, K, L and N (histology) – 100 μm; M, N (whole mount) – 1 mm.

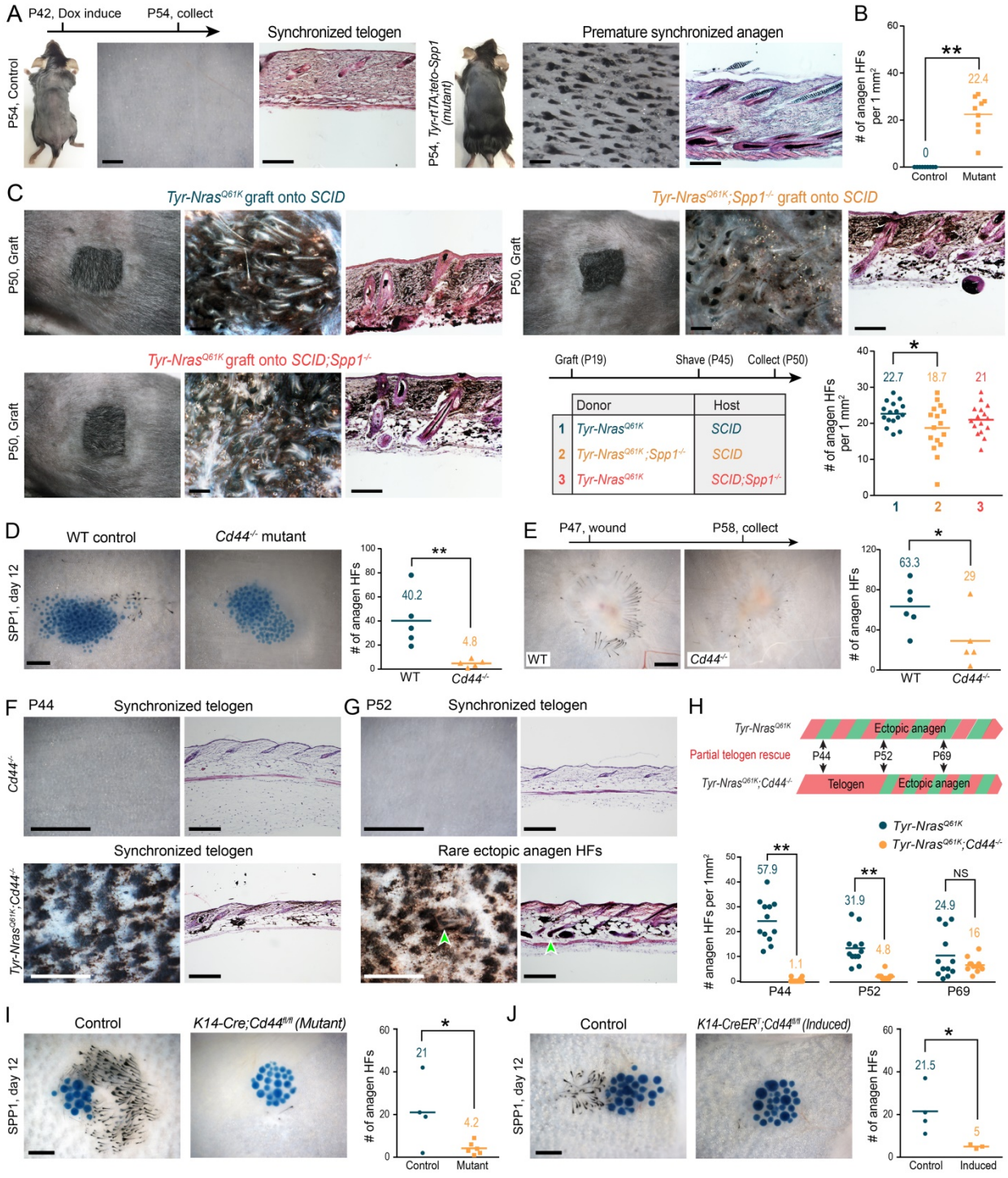
A
P42, Dox induce
P54, collect
Synchronized telogen
Premature synchronized anagen
P54, Control
P54, Tyr-rtTA;teto-Spp1 (mutant)
B
# of anagen HFs per 1 mm²
22.4
0
Control
Mutant
C
Tyr-Nras^Q61K graft onto SCID
Tyr-Nras^Q61K;Spp1^-/- graft onto SCID
Tyr-Nras^Q61K graft onto SCID;Spp1^-/-
P50, Graft
Graft (P19)
Shave (P45)
Collect (P50)
Donor
Host
1 Tyr-Nras^Q61K SCID
2 Tyr-Nras^Q61K;Spp1^-/- SCID
3 Tyr-Nras^Q61K SCID;Spp1^-/-
22.7
18.7
21
D
WT control
Cd44^-/- mutant
SPP1, day 12
40.2
4.8
WT
Cd44^-/-
E
P47, wound
P58, collect
63.3
29
F
P44
Synchronized telogen
Cd44^-/-
Tyr-Nras^Q61K;Cd44^-/-
G
P52
Synchronized telogen
Rare ectopic anagen HFs
H
Tyr-Nras^Q61K
Ectopic anagen
Partial telogen rescue
Tyr-Nras^Q61K;Cd44^-/-
Telogen
P44
P52
P69
# anagen HFs per 1mm²
57.9
1.1
31.9
4.8
24.9
16
NS
I
Control
K14-Cre;Cd44^fl/fl (Mutant)
21
4.2
J
Control
K14-CreER^T;Cd44^fl/fl (Induced)
21.5
5

**Figure 6: Effect of osteopontin on hair growth depends on CD44. (A, B)** P54 *Tyr-rtTA;tetO-Spp1* but not control doxycycline-treated mice display premature anagen activation. Representative mice are shown on **A** and data quantification on **B**. **(C)** Results of skin grafting assays: *Tyr-Nras$^{Q61K}$* to *SCID* (blue), *Tyr-Nras$^{Q61K}$;Spp1$^{-/-}$* to *SCID* (orange), *Tyr-Nras$^{Q61K}$* to *SCID;Spp1$^{-/-}$* (red). Whole mount and histological images of representative grafts are shown. Ectopic anagen data quantification is lower right. **(D)** *Cd44$^{-/-}$* mice showed significantly reduced anagen activation in response to SPP1-soaked beads compared to WT (same WT as in Figure 4R). Representative samples are on the left, data quantification is on the right. **(E)** *Cd44$^{-/-}$* mice showed significantly reduced wound-induced hair cycle activation compared to WT. Representative wounds are on the left, data quantification is on the right. **(F, G)** *Tyr-Nras$^{Q61K}$;CD44$^{-/-}$* mice lacking *Cd44* showed partial rescue of hair cycle quiescence. At P44, *Tyr-Nras$^{Q61K}$;Cd44$^{-/-}$* HFs are in coordinated telogen **(F)**. Only rare ectopic anagen HFs were present at P52 **(G)**. Also, see Figure S19. **(H)** Summary of hair cycle phases in *Tyr-Nras$^{Q61K}$;Cd44$^{-/-}$ vs. Tyr-Nras$^{Q61K}$* mice (top) and quantification of ectopic anagen HFs in *Tyr-Nras$^{Q61K}$ vs. Tyr-Nras$^{Q61K}$;Cd44$^{-/-}$* mice (bottom). Double mutants showed significantly reduced ectopic anagen at P44 and P52. **(I, J)** Both constitutive epithelial-specific *K14-Cre;Cd44$^{fl/fl}$* **(I)**, and tamoxifen induced *K14-CreER$^{T}$;Cd44$^{fl/fl}$* mice **(J)** showed significantly reduced anagen activation in response to SPP1-soaked beads compared to control mice. Representative samples are on the left on **I** and **J**, data quantification is on the right. Scale bars: A, C, F (histology), G (histology) – 200 µm; I, J – 300 µm; D, E – 500 µm; F, G (whole mount) – 1 mm.

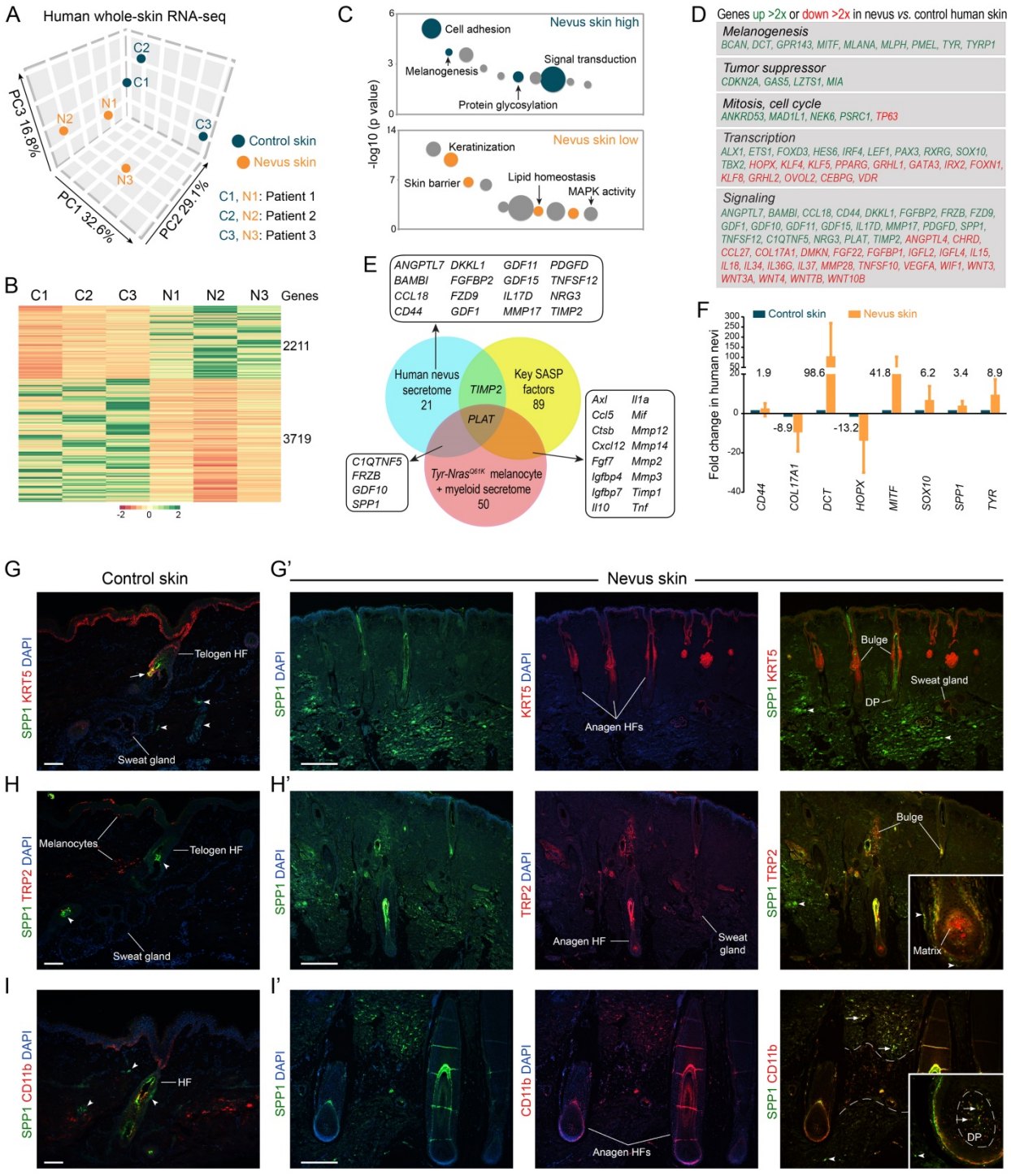
A
Human whole-skin RNA-seq
C2
C1
N1
N2
C3
N3
PC3 16.8%
PC1 32.6%
PC2 29.1%
Control skin
Nevus skin
C1, N1: Patient 1
C2, N2: Patient 2
C3, N3: Patient 3
B
C1 C2 C3 N1 N2 N3 Genes
2211
3719
-2 0 2
C
Nevus skin high
Cell adhesion
Melanogenesis
Signal transduction
Protein glycosylation
-log10 (p value)
Nevus skin low
Keratinization
Skin barrier
Lipid homeostasis
MAPK activity
D
Genes up >2x or down >2x in nevus vs. control human skin
Melanogenesis
BCAN, DCT, GPR143, MITF, MLANA, MLPH, PMEL, TYR, TYRP1
Tumor suppressor
CDKN2A, GAS5, LZTS1, MIA
Mitosis, cell cycle
ANKRD53, MAD1L1, NEK6, PSRC1, TP63
Transcription
ALX1, ETS1, FOXD3, HES6, IRF4, LEF1, PAX3, RXRG, SOX10, TBX2, HOPX, KLF4, KLF5, PPARG, GRHL1, GATA3, IRX2, FOXN1, KLF8, GRHL2, OVOL2, CEBPG, VDR
Signaling
ANGPTL7, BAMBI, CCL18, CD44, DKKL1, FGFBP2, FRZB, FZD9, GDF1, GDF10, GDF11, GDF15, IL17D, MMP17, PDGFD, SPP1, TNFSF12, C1QTNF5, NRG3, PLAT, TIMP2, ANGPTL4, CHRD, CCL27, COL17A1, DMKN, FGF22, FGFBP1, IGFL2, IGFL4, IL15, IL18, IL34, IL36G, IL37, MMP28, TNFSF10, VEGFA, WIF1, WNT3, WNT3A, WNT4, WNT7B, WNT10B
E
ANGPTL7 DKKL1 GDF11 PDGFD
BAMBI FGFBP2 GDF15 TNFSF12
CCL18 FZD9 IL17D NRG3
CD44 GDF1 MMP17 TIMP2
Human nevus secretome 21
TIMP2
Key SASP factors 89
PLAT
C1QTNF5
FRZB
GDF10
SPP1
Tyr-Nras^Q61K melanocyte + myeloid secretome 50
Axl Il1a
Ccl5 Mif
Ctsb Mmp12
Cxcl12 Mmp14
Fgf7 Mmp2
Igfbp4 Mmp3
Igfbp7 Timp1
Il10 Tnf
F
Control skin
Nevus skin
Fold change in human nevi
1.9
-8.9
98.6
-13.2
41.8
6.2
3.4
8.9
CD44
COL17A1
DCT
HOPX
MITF
SOX10
SPP1
TYR
G
Control skin
G'
Nevus skin
SPP1 KRT5 DAPI
Telogen HF
Sweat gland
SPP1 DAPI
KRT5 DAPI
Anagen HFs
SPP1 KRT5
Bulge
Sweat gland
DP
H
H'
SPP1 TRP2 DAPI
Melanocytes
Telogen HF
Sweat gland
SPP1 DAPI
TRP2 DAPI
Anagen HF
Sweat gland
SPP1 TRP2
Bulge
Matrix
I
I'
SPP1 CD11b DAPI
HF
SPP1 DAPI
CD11b DAPI
Anagen HFs
SPP1 CD11b
DP

**Figure 7: Human nevi feature a unique secretome enriched for osteopontin. (A, B)** Bulk RNA-seq reveals prominent differences between hairy nevi and adjacent normal facial skin in humans. PCA is shown in **A** and heatmap of DEGs in **B**. **(C)** Bubble chart showing enriched (blue) and depleted (orange) GO terms in human nevi. Also, see Table S13. **(D)** Selected upregulated (green) and downregulated (red) DEGs in nevus *vs.* normal skin. **(E)** Comparisons of human nevus secretome (blue) with combined *Tyr-Nras*$^{Q61K}$ mouse myeloid and melanocyte secretome (red) and published *in vitro* SASP (yellow). **(F)** qRT-PCR validation of selected DEGs from bulk RNA-seq data in **B**. **(G, G')** SPP1 (green) and KRT5 (red) expression in human skin. In normal skin, SPP1 is seen in telogen HFs (arrow in **G**) and in scattered dermal cells (arrowheads in **G**). In nevus skin, many dermal cells are SPP1-positive (arrowheads in **G'**). **(H, H')** SPP1 (green) and TRP2 (red) co-staining. In normal skin, TRP2-positive melanocytes do not express SPP1 **(H)**. In nevus skin, many double positive cells are seen in HF bulge and matrix **(H')**. **(I, I')** SPP1 (green) and CD11b (red) co-staining. In normal skin, CD11b-positive myeloid cells do not express SPP1**(I)**. Nevus skin contains many double positive dermal myeloid cells (arrows in **I'**). Scale bars: G, H, I – 100 μm; G', H', I' – 500 μm.

**References**


Ackermann, J., Frutschi, M., Kaloulis, K., McKee, T., Trumpp, A., and Beermann, F. (2005). Metastasizing melanoma formation caused by expression of activated N-RasQ61K on an INK4a-deficient background. Cancer research *65*, 4005-4011.

Ali, N., Zirak, B., Rodriguez, R.S., Pauli, M.L., Truong, H.A., Lai, K., Ahn, R., Corbin, K., Lowe, M.M., Scharschmidt, T.C*., et al.* (2017). Regulatory T Cells in Skin Facilitate Epithelial Stem Cell Differentiation. Cell *169*, 1119-1129 e1111.

Aoki, H., Tomita, H., Hara, A., and Kunisada, T. (2015). Conditional Deletion of Kit in Melanocytes: White Spotting Phenotype Is Cell Autonomous. The Journal of investigative dermatology *135*, 1829-1838.

Argyris, T.S. (1956). The effect of wounds on adjacent growing or resting hair follicles in mice. AMA Arch Pathol *61*, 31-36.

Baker, D.J., Childs, B.G., Durik, M., Wijers, M.E., Sieben, C.J., Zhong, J., Saltness, R.A., Jeganathan, K.B., Verzosa, G.C., Pezeshki, A*., et al.* (2016). Naturally occurring p16(Ink4a)-positive cells shorten healthy lifespan. Nature *530*, 184-189.

Baker, D.J., Wijshake, T., Tchkonia, T., LeBrasseur, N.K., Childs, B.G., van de Sluis, B., Kirkland, J.L., and van Deursen, J.M. (2011). Clearance of p16Ink4a-positive senescent cells delays ageing-associated disorders. Nature *479*, 232-236.

Bosenberg, M., Muthusamy, V., Curley, D.P., Wang, Z., Hobbs, C., Nelson, B., Nogueira, C., Horner, J.W., 2nd, Depinho, R., and Chin, L. (2006). Characterization of melanocyte-specific inducible Cre recombinase transgenic mice. Genesis *44*, 262-267.

Castellana, D., Paus, R., and Perez-Moreno, M. (2014). Macrophages contribute to the cyclic activation of adult hair follicle stem cells. PLoS biology *12*, e1002002.

Chang, J., Wang, Y., Shao, L., Laberge, R.M., Demaria, M., Campisi, J., Janakiraman, K., Sharpless, N.E., Ding, S., Feng, W.*, et al.* (2016). Clearance of senescent cells by ABT263 rejuvenates aged hematopoietic stem cells in mice. Nat Med *22*, 78-83.

Chen, C.C., Wang, L., Plikus, M.V., Jiang, T.X., Murray, P.J., Ramos, R., Guerrero-Juarez, C.F., Hughes, M.W., Lee, O.K., Shi, S.*, et al.* (2015). Organ-level quorum sensing directs regeneration in hair stem cell populations. Cell *161*, 277-290.

Chiche, A., Le Roux, I., von Joest, M., Sakai, H., Aguin, S.B., Cazin, C., Salam, R., Fiette, L., Alegria, O., Flamant, P.*, et al.* (2017). Injury-Induced Senescence Enables In Vivo Reprogramming in Skeletal Muscle. Cell stem cell *20*, 407-414 e404.

Coppe, J.P., Patil, C.K., Rodier, F., Sun, Y., Munoz, D.P., Goldstein, J., Nelson, P.S., Desprez, P.Y., and Campisi, J. (2008). Senescence-associated secretory phenotypes reveal cell-nonautonomous functions of oncogenic RAS and the p53 tumor suppressor. PLoS biology *6*, 2853-2868.

Cotsarelis, G., Sun, T.T., and Lavker, R.M. (1990). Label-retaining cells reside in the bulge area of pilosebaceous unit: implications for follicular stem cells, hair cycle, and skin carcinogenesis. Cell *61*, 1329-1337.

Demaria, M., Ohtani, N., Youssef, S.A., Rodier, F., Toussaint, W., Mitchell, J.R., Laberge, R.M., Vijg, J., Van Steeg, H., Dolle, M.E.*, et al.* (2014). An essential role for senescent cells in optimal wound healing through secretion of PDGF-AA. Dev Cell *31*, 722-733.

Dhomen, N., Reis-Filho, J.S., da Rocha Dias, S., Hayward, R., Savage, K., Delmas, V., Larue, L., Pritchard, C., and Marais, R. (2009). Oncogenic Braf induces melanocyte senescence and melanoma in mice. Cancer Cell *15*, 294-303.

Dikovskaya, D., Cole, J.J., Mason, S.M., Nixon, C., Karim, S.A., McGarry, L., Clark, W., Hewitt, R.N., Sammons, M.A., Zhu, J.*, et al.* (2015). Mitotic Stress Is an Integral Part of the Oncogene-Induced Senescence Program that Promotes Multinucleation and Cell Cycle Arrest. Cell Rep *12*, 1483-1496.

Driskell, R.R., Giangreco, A., Jensen, K.B., Mulder, K.W., and Watt, F.M. (2009). Sox2-positive dermal papilla cells specify hair follicle type in mammalian epidermis. Development *136*, 2815-2823.

Feng, T., Meng, J., Kou, S., Jiang, Z., Huang, X., Lu, Z., Zhao, H., Lau, L.F., Zhou, B., and Zhang, H. (2019). CCN1-Induced Cellular Senescence Promotes Heart Regeneration. Circulation *139*, 2495-2498.

Festa, E., Fretz, J., Berry, R., Schmidt, B., Rodeheffer, M., Horowitz, M., and Horsley, V. (2011). Adipocyte lineage cells contribute to the skin stem cell niche to drive hair cycling. Cell *146*, 761-771.

Freund, A., Orjalo, A.V., Desprez, P.Y., and Campisi, J. (2010). Inflammatory networks during cellular senescence: causes and consequences. Trends Mol Med *16*, 238-246.

Giachelli, C.M., Lombardi, D., Johnson, R.J., Murry, C.E., and Almeida, M. (1998). Evidence for a role of osteopontin in macrophage infiltration in response to pathological stimuli in vivo. Am J Pathol *152*, 353-358.

Greco, V., Chen, T., Rendl, M., Schober, M., Pasolli, H.A., Stokes, N., Dela Cruz-Racelis, J., and Fuchs, E. (2009). A two-step mechanism for stem cell activation during hair regeneration. Cell stem cell *4*, 155-169.

Hsu, Y.C., and Fuchs, E. (2012). A family business: stem cell progeny join the niche to regulate homeostasis. Nat Rev Mol Cell Biol *13*, 103-114.

Hsu, Y.C., Li, L., and Fuchs, E. (2014). Emerging interactions between skin stem cells and their niches. Nat Med *20*, 847-856.

Joost, S., Zeisel, A., Jacob, T., Sun, X., La Manno, G., Lonnerberg, P., Linnarsson, S., and Kasper, M. (2016). Single-Cell Transcriptomics Reveals that Differentiation and Spatial Signatures Shape Epidermal and Hair Follicle Heterogeneity. Cell Syst *3*, 221-237 e229.

Kunisada, T., Yoshida, H., Yamazaki, H., Miyamoto, A., Hemmi, H., Nishimura, E., Shultz, L.D., Nishikawa, S., and Hayashi, S. (1998). Transgene expression of steel factor in the basal layer of epidermis promotes survival, proliferation, differentiation and migration of melanocyte precursors. Development *125*, 2915-2923.

Laberge, R.M., Sun, Y., Orjalo, A.V., Patil, C.K., Freund, A., Zhou, L., Curran, S.C., Davalos, A.R., Wilson-Edell, K.A., Liu, S.*, et al.* (2015). MTOR regulates the pro-tumorigenic senescence-associated secretory phenotype by promoting IL1A translation. Nature cell biology *17*, 1049-1061.

Lee, P., Gund, R., Dutta, A., Pincha, N., Rana, I., Ghosh, S., Witherden, D., Kandyba, E., MacLeod, A., Kobielak, K.*, et al.* (2017). Stimulation of hair follicle stem cell proliferation through an IL-1 dependent activation of gammadeltaT-cells. Elife *6*.

Liaw, L., Birk, D.E., Ballas, C.B., Whitsitt, J.S., Davidson, J.M., and Hogan, B.L. (1998). Altered wound healing in mice lacking a functional osteopontin gene (spp1). The Journal of clinical investigation *101*, 1468-1478.

Michaloglou, C., Vredeveld, L.C., Soengas, M.S., Denoyelle, C., Kuilman, T., van der Horst, C.M., Majoor, D.M., Shay, J.W., Mooi, W.J., and Peeper, D.S. (2005). BRAFE600-associated senescence-like cell cycle arrest of human naevi. Nature *436*, 720-724.

Mori, R., Shaw, T.J., and Martin, P. (2008). Molecular mechanisms linking wound inflammation and fibrosis: knockdown of osteopontin leads to rapid repair and reduced scarring. The Journal of experimental medicine *205*, 43-51.

Mosteiro, L., Pantoja, C., Alcazar, N., Marion, R.M., Chondronasiou, D., Rovira, M., Fernandez-Marcos, P.J., Munoz-Martin, M., Blanco-Aparicio, C., Pastor, J.*, et al.* (2016). Tissue damage and senescence provide critical signals for cellular reprogramming in vivo. Science *354*.

Muller-Rover, S., Handjiski, B., van der Veen, C., Eichmuller, S., Foitzik, K., McKay, I.A., Stenn, K.S., and Paus, R. (2001). A comprehensive guide for the accurate classification of murine hair follicles in distinct hair cycle stages. The Journal of investigative dermatology *117*, 3-15.

Pawlikowski, J.S., McBryan, T., van Tuyn, J., Drotar, M.E., Hewitt, R.N., Maier, A.B., King, A., Blyth, K., Wu, H., and Adams, P.D. (2013). Wnt signaling potentiates nevogenesis. Proceedings of the National Academy of Sciences of the United States of America *110*, 16009-16014.

Pazolli, E., Luo, X., Brehm, S., Carbery, K., Chung, J.J., Prior, J.L., Doherty, J., Demehri, S., Salavaggione, L., Piwnica-Worms, D.*, et al.* (2009). Senescent stromal-derived osteopontin promotes preneoplastic cell growth. Cancer research *69*, 1230-1239.

Plikus, M.V., Baker, R.E., Chen, C.C., Fare, C., de la Cruz, D., Andl, T., Maini, P.K., Millar, S.E., Widelitz, R., and Chuong, C.M. (2011). Self-organizing and stochastic behaviors during the regeneration of hair stem cells. Science *332*, 586-589.

Plikus, M.V., and Chuong, C.M. (2014). Macroenvironmental regulation of hair cycling and collective regenerative behavior. Cold Spring Harb Perspect Med *4*, a015198.

Plikus, M.V., Mayer, J.A., de la Cruz, D., Baker, R.E., Maini, P.K., Maxson, R., and Chuong, C.M. (2008). Cyclic dermal BMP signalling regulates stem cell activation during hair regeneration. Nature *451*, 340-344.

Ponta, H., Sherman, L., and Herrlich, P.A. (2003). CD44: from adhesion molecules to signalling regulators. Nat Rev Mol Cell Biol *4*, 33-45.

Rahmani, W., Liu, Y., Rosin, N.L., Kline, A., Raharjo, E., Yoon, J., Stratton, J.A., Sinha, S., and Biernaskie, J. (2018). Macrophages promote wound-induced hair follicle regeneration in a CX3CR1 and TGFbeta1 dependent manner. The Journal of investigative dermatology.

Ritschka, B., Storer, M., Mas, A., Heinzmann, F., Ortells, M.C., Morton, J.P., Sansom, O.J., Zender, L., and Keyes, W.M. (2017). The senescence-associated secretory phenotype induces cellular plasticity and tissue regeneration. Genes & development *31*, 172-183.

Roh, M.R., Eliades, P., Gupta, S., and Tsao, H. (2015). Genetics of melanocytic nevi. Pigment Cell Melanoma Res *28*, 661-672.

Ruhland, M.K., Loza, A.J., Capietto, A.H., Luo, X., Knolhoff, B.L., Flanagan, K.C., Belt, B.A., Alspach, E., Leahy, K., Luo, J.*, et al.* (2016). Stromal senescence establishes an immunosuppressive microenvironment that drives tumorigenesis. Nat Commun *7*, 11762.

Ruiz-Maldonado, R., Tamayo, L., and Duran, C. (1993). Hairy pigmented congenital naevocellular naevus in a patient with alopecia universalis. Clin Exp Dermatol *18*, 162-163.

Sarig, R., Rimmer, R., Bassat, E., Zhang, L., Umansky, K.B., Lendengolts, D., Perlmoter, G., Yaniv, K., and Tzahor, E. (2019). Transient p53-Mediated Regenerative Senescence in the Injured Heart. Circulation *139*, 2491-2494.

Scadden, D.T. (2014). Nice neighborhood: emerging concepts of the stem cell niche. Cell *157*, 41-50.

Sennett, R., and Rendl, M. (2012). Mesenchymal-epithelial interactions during hair follicle morphogenesis and cycling. Semin Cell Dev Biol *23*, 917-927.

Storer, M., Mas, A., Robert-Moreno, A., Pecoraro, M., Ortells, M.C., Di Giacomo, V., Yosef, R., Pilpel, N., Krizhanovsky, V., Sharpe, J.*, et al.* (2013). Senescence is a developmental mechanism that contributes to embryonic growth and patterning. Cell *155*, 1119-1130.

Wang, E.C.E., Dai, Z., Ferrante, A.W., Drake, C.G., and Christiano, A.M. (2019). A Subset of TREM2(+) Dermal Macrophages Secretes Oncostatin M to Maintain Hair Follicle Stem Cell Quiescence and Inhibit Hair Growth. Cell stem cell *24*, 654-669 e656.

Wang, Q., Oh, J.W., Lee, H.L., Dhar, A., Peng, T., Ramos, R., Guerrero-Juarez, C.F., Wang, X., Zhao, R., Cao, X.*, et al.* (2017a). A multi-scale model for hair follicles reveals heterogeneous domains driving rapid spatiotemporal hair growth patterning. Elife *6*.

Wang, X., Chen, H., Tian, R., Zhang, Y., Drutskaya, M.S., Wang, C., Ge, J., Fan, Z., Kong, D., Wang, X.*, et al.* (2017b). Macrophages induce AKT/beta-catenin-dependent Lgr5(+) stem cell activation and hair follicle regeneration through TNF. Nat Commun *8*, 14091.

Weber, G.F., Ashkar, S., Glimcher, M.J., and Cantor, H. (1996). Receptor-ligand interaction between CD44 and osteopontin (Eta-1). Science *271*, 509-512.

Yang, H., Adam, R.C., Ge, Y., Hua, Z.L., and Fuchs, E. (2017). Epithelial-Mesenchymal Micro-niches Govern Stem Cell Lineage Choices. Cell *169*, 483-496 e413.

Yosef, R., Pilpel, N., Tokarsky-Amiel, R., Biran, A., Ovadya, Y., Cohen, S., Vadai, E., Dassa, L., Shahar, E., Condiotti, R.*, et al.* (2016). Directed elimination of senescent cells by inhibition of BCL-W and BCL-XL. Nat Commun *7*, 11190.

Yoshimoto, S., Loo, T.M., Atarashi, K., Kanda, H., Sato, S., Oyadomari, S., Iwakura, Y., Oshima, K., Morita, H., Hattori, M.*, et al.* (2013). Obesity-induced gut microbial metabolite promotes liver cancer through senescence secretome. Nature *499*, 97-101.

Yu, D.W., Yang, T., Sonoda, T., Gong, Y., Cao, Q., Gaffney, K., Jensen, P.J., Freedberg, I.M., Lavker, R.M., and Sun, T.T. (2001). Osteopontin gene is expressed in the dermal papilla of pelage follicles in a hair-cycle-dependent manner. The Journal of investigative dermatology *117*, 1554-1558.

Yucel, G., Altindag, B., Gomez-Ospina, N., Rana, A., Panagiotakos, G., Lara, M.F., Dolmetsch, R., and Oro, A.E. (2013). State-dependent signaling by Cav1.2 regulates hair follicle stem cell function. Genes & development *27*, 1217-1222.

## Supplemental Information

**Signaling by senescent cells hyper-activates the skin stem cell niche**

Xiaojie Wang *et al.*

**Supplemental Text**

**Text S1: RNA-seq analysis of *Tyr-Nras$^{Q61K}$* hair germ and dermal papilla cells.**

Compared to WT control, P56 *Tyr-Nras$^{Q61K}$* hair germ cells upregulated transcriptional factors, including *Grhl3, Meis2, Ovol1, Sox6/15,* canonical (*Wnt3/3a/7b/10a*) and non-canonical WNT ligands (*Wnt5a/5b/11/16*), multiple cytokines *Ccl1/2/7/20/27a/27b,* interleukins *Il1a/1b/1f5/1f9/6/24/34* and chemokines *Cxcl9/16*. They downregulated transcriptional factors *Id1/2/4, Lhx2, Sox5/13, Tbx1;* multiple WNT components: *Dkk3, Fzd2/3/7/8, Lgr4/5, Lef1, Lrp6, Tcf7l1/12, Wnt7a/10b, Wif1;* and Hedgehog members *Gli1/2, Ptch1/2* (Figure S14; Table S4). This RNA-seq signature indicates complex changes in the WNT pathway, inhibitory changes in the Hedgehog pathway, and prominent activation of inflammatory signaling.

P56 *Tyr-Nras$^{Q61K}$* dermal papilla cells upregulated transcriptional factors *Alx4, Hey1/2, Msx1/2, Pax1, Pitx2, Sox18, Tbx5/18;* BMP components: *Bmp4, Bambi, Id1, Sostdc1;* WNT components: *Fzd4/10, Rspo1/3/4, Sfrp1/4, Wnt5b;* as well as *Fgf7/10, Spp1* and cytokines *Cxcl1/5/9/12/14*. They downregulated transcriptional and epigenetic factors *Ezh2, Hdac5/9, Stat2/3/5a, Zeb1;* BMP components: *Chrdl1, Grem1;* WNT components *Dkk3, Fzd9, Wnt6/10a/16;* as well as *Dhh* and *Pdgfa* (Figure S15; Table S5). This RNA-seq signature indicates complex changes in WNT and BMP pathways, activation of hair growth-promoting FGF ligands, and cytokines, including *Spp1.*

**Text S2: WNT signaling is dispensable for hair cycle hyper-activation in nevus skin.**

Ectopic hair cycling in nevus skin resembles the phenotype of *K14-Wnt7a* mice overexpressing WNT ligand (Plikus et al., 2011). WNT signaling is also important in physiological hair cycle activation (Choi et al., 2013; Greco et al., 2009; Lien et al., 2014; Lowry et al., 2005) and it is elevated and drives early stages of melanocytic nevus formation (Pawlikowski et al., 2013). Consistently, we found foci of WNT reporter-active cells in the dermis of *Tyr-Nras$^{Q61K}$;TOPGAL* mice (Figure 1L; S22A). At the same time, RNA-seq analysis suggests that neither *Tyr-Nras$^{Q61K}$* melanocytes nor myeloid cells overexpress canonical WNT ligands (Figure 4F, 5E). To establish a role for WNT signaling in a nevus hair cycle phenotype, we blocked its activity using several mouse models. We targeted WNT signaling from melanocytes by either overexpressing its antagonist *Dkk1* or ablating *Wls*, necessary for WNT ligand secretion. Both *Tyr-Nras$^{Q61K}$;Tyr–rtTA;tetO-Dkk1* mice (n=3; induced from P5) and *Tyr-Nras$^{Q61K}$;Tyr-CreER$^{T2}$;Wls$^{fl/fl}$* mice (n=3; induced for two days at P5) continued to show prominent ectopic anagen at P21 and P56 (Figures S22B, S23A). We also induced broad *Dkk1* overexpression in *Tyr-Nras$^{Q61K}$;K5-rtTA;tetO-Dkk1* mice (n=2; induced from P0). However, this also failed to supress ectopic hair cycling (Figure S23B). At the same time, normal hair cycle activation was prevented in induced *K5-rtTA;tetO-Dkk1* control mice (n=2)

consistent with Choi et al. (2013). Therefore, we conclude that hair cycle hyper-activation in nevus skin does not critically rely on WNT signaling.

## Supplemental Figures

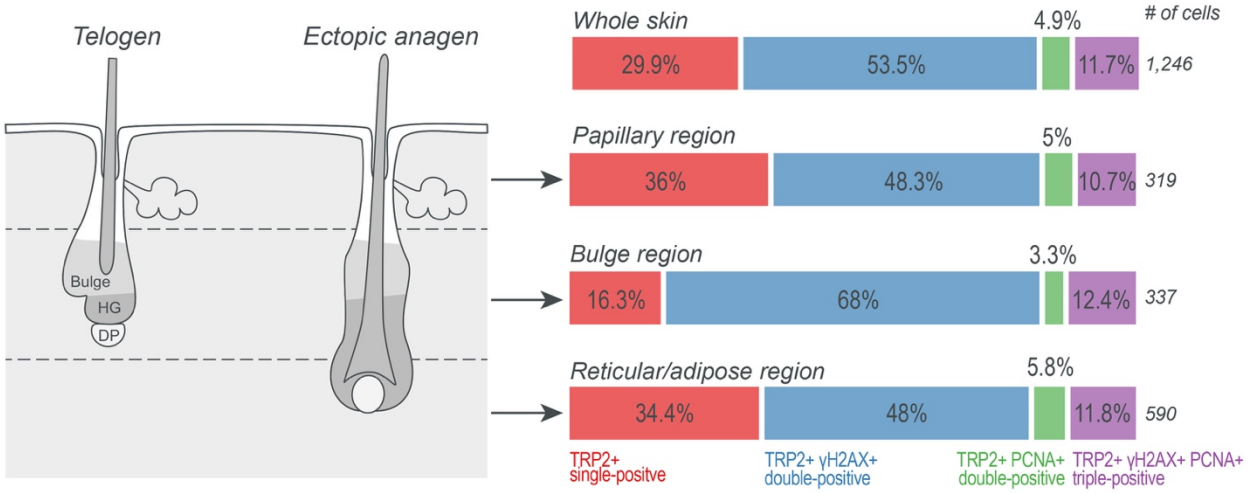


**Figure S1: Abundance and distribution of senescent melanocytes in P56 *Tyr-Nras$^{Q61K}$* skin.** Quantification results of TRP2, γH2AX and PCNA co-immunostaining data. Senescent melanocytes were identified as TRP2$^{+}$/γH2AX$^{+}$/PCNA$^{neg}$ (i.e. non-proliferative γH2AX$^{+}$ melanocytes; blue). Proliferative melanocytes include TRP2$^{+}$/γH2AX$^{+}$/PCNA$^{+}$ (purple) and TRP2$^{+}$/γH2AX$^{neg}$/PCNA$^{+}$ cells (green). The remaining TRP2$^{+}$/γH2AX$^{neg}$/PCNA$^{neg}$ cells were considered quiescent melanocytes (red). A total of 1,246 melanocytes were quantified and quantification was performed separately on melanocytes in the papillary region, bulge and reticular/adipose regions. On average, 53.5% of all melanocytes in P56 *Tyr-Nras$^{Q61K}$* skin were identified as senescent and their highest proportion (68%) was present in the bulge region. See main Figure 1D.

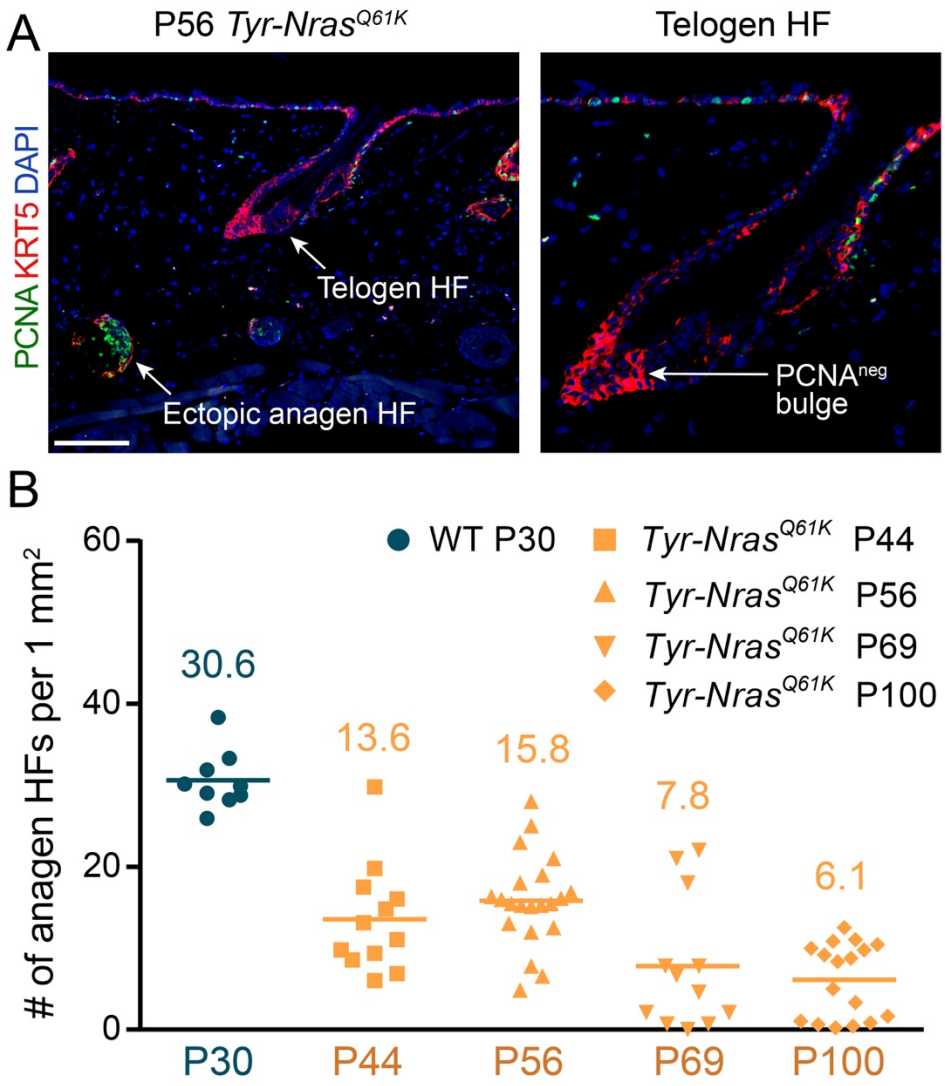


**Figure S2: *Tyr-Nras*$^{Q61K}$ skin contains a mixture of telogen and anagen hair follicles. (A)** Co-immunostaining for PCNA (green) and KRT5 (red) shows presence of non-proliferating telogen HFs in P56 *Tyr-Nras*$^{Q61K}$ skin. **(B)** Quantification of anagen HF density in *Tyr-Nras*$^{Q61K}$ skin at different postnatal time points (orange) relative to P30 WT skin (blue), where all hair follicles are in anagen. Anagen HF density in WT skin at P30 is 30.6±3.6 HFs/mm$^2$. In *Tyr-Nras*$^{Q61K}$ skin the values are as follows: P44 – 13.6±6.7 (44% of P30 WT); P56 – 15.8±5.6 (52%); P69 – 7.8±8.1 (26%); P100 – 6.1±4.6 (20%). Size bar: A – 100 µm.

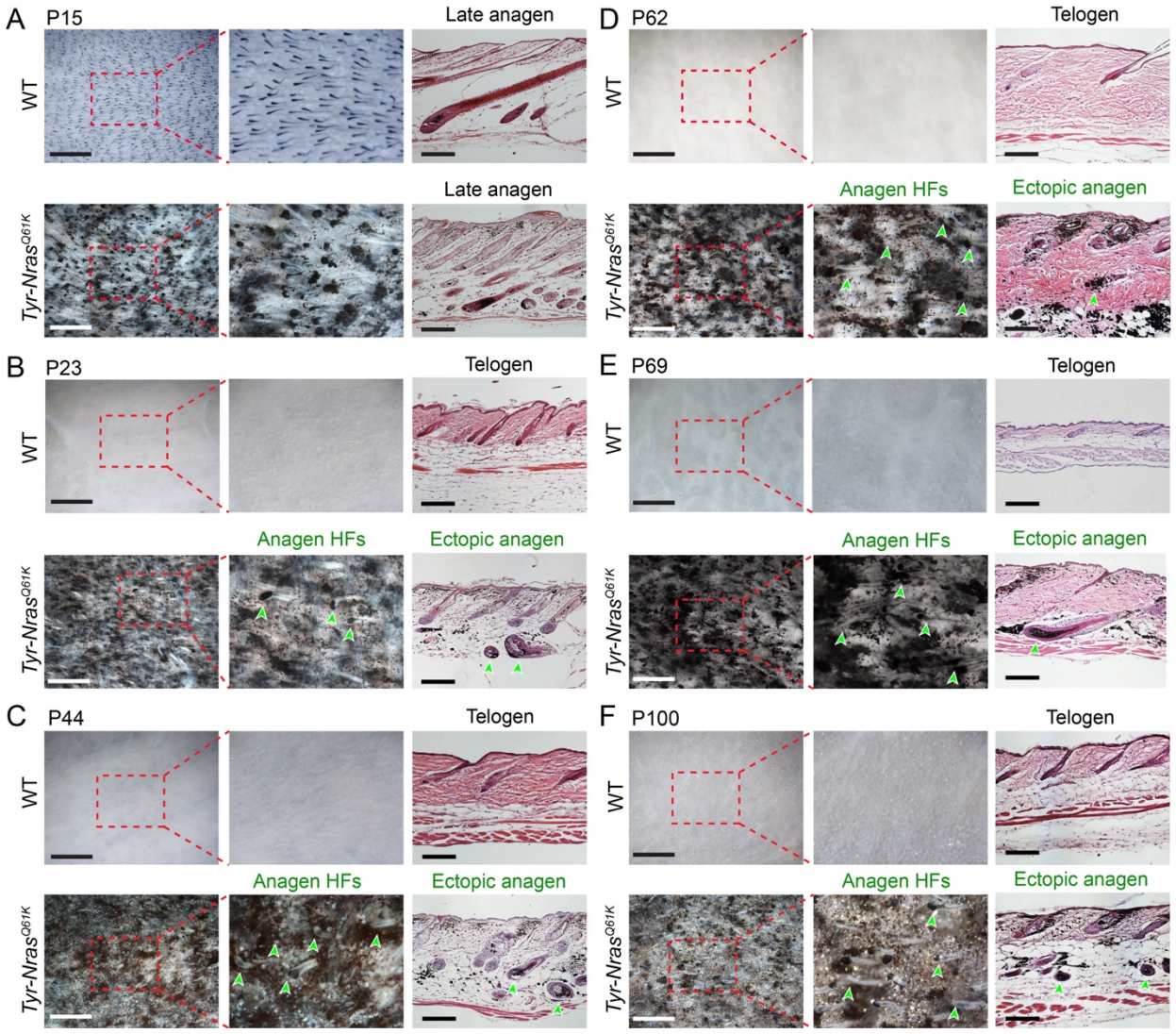


**Figure S3: *Tyr-Nras$^{Q61K}$* mice exhibit ectopic hair regeneration.** At all postnatal time points examined, the dorsal skin of *Tyr-Nras$^{Q61K}$* mice contains many ectopic anagen HFs. In WT control mice, HFs are in first anagen at day P15 **(A)**, in first telogen at P23 **(B)**, in extended second telogen at P44 **(C)**, P62 **(D)**, P69 **(E)**, and in third telogen at P100 **(F).** In contrast, at all of the above time points, *Tyr-Nras$^{Q61K}$* skin contains many ectopic anagen HFs (green arrowheads). For each time point, both whole mount (left) and histology samples (right) are shown. Also, see main Figure 1H-J. Scale bars: A-F (whole mount) – 1 mm; A-F (histology) – 200 µm.

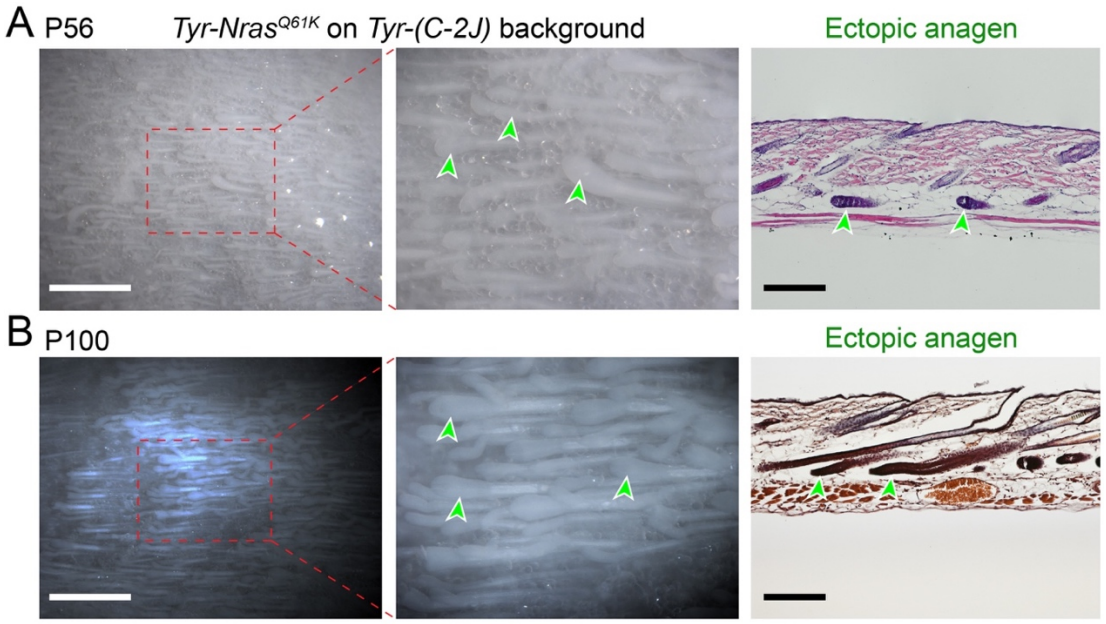


**Figure S4: Albino *Tyr-Nras*$^{Q61K}$ mice maintain an ectopic hair regeneration phenotype.** *Tyr-Nras*$^{Q61K}$ mice crossed onto an albino *Tyr(C-2J)* background, carrying a mutation in the tyrosinase gene, continued to display ectopic anagen HFs (green arrowheads) both at P56 **(A)** and P100 **(B)**. For each time point, both whole mount (left) and histology samples (right) are shown. Scale bars: A, B (whole mount) – 1 mm; A, B (histology) – 200 µm.

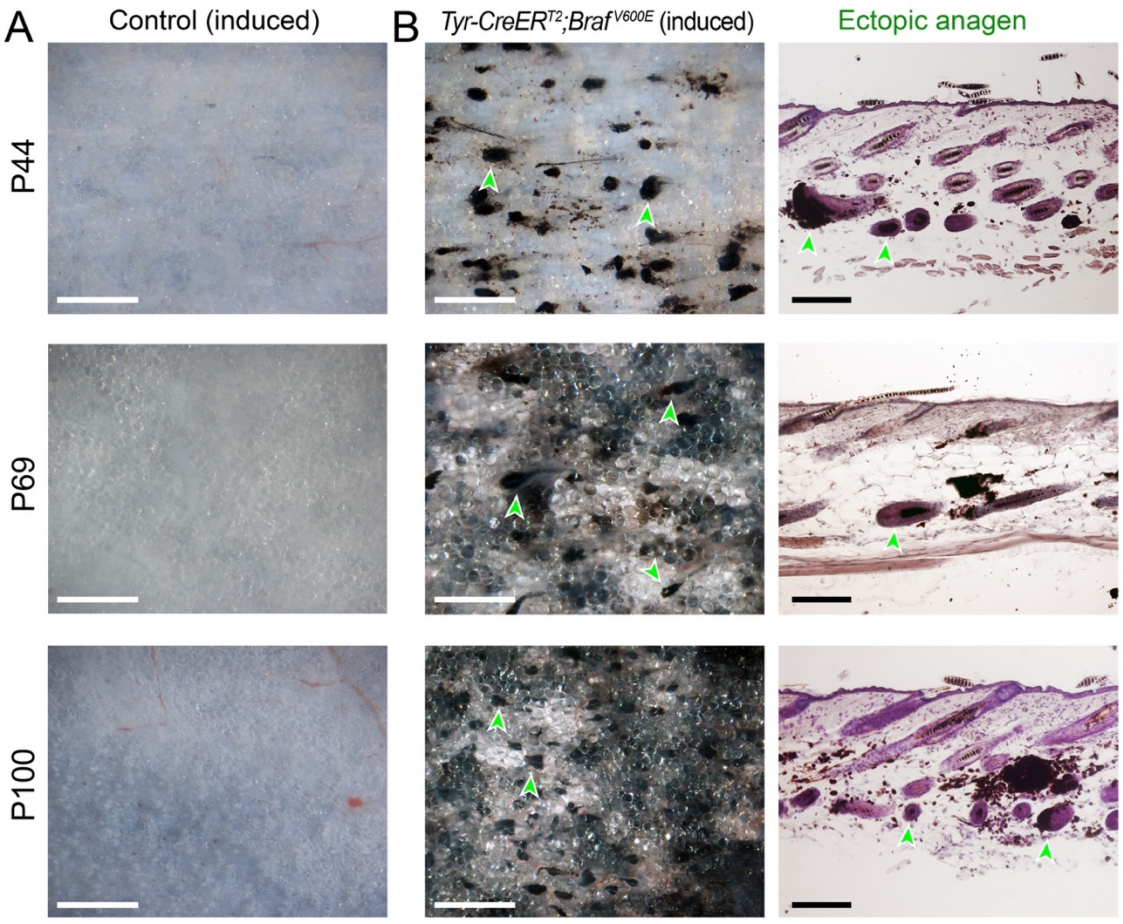


**Figure S5: *Tyr-CreER$^{T2}$;Braf$^{V600E}$* mice exhibit ectopic hair regeneration.** At all postnatal time points examined (P44, P69 and P100), dorsal skin in induced *Tyr-CreER$^{T2}$;Braf$^{V600E}$* mice contained many ectopic anagen HFs (green arrowheads) **(B)**. In contrast, HFs in induced control mice at the above time points were in telogen **(A)**. For each time point, whole mount samples and histology samples (for *Tyr-CreER$^{T2}$;Braf$^{V600E}$* mice) are shown. Also, see main Figure 2A-B. Anagen HF density in *Tyr-CreER$^{T2}$;Braf$^{V600E}$* were as follows (in HFs/mm$^2$): P44 – 4.8±1.5 (16% of P30 WT); P56 – 10.3±3.0 (34%); P69 – 15.4±6.9 (50%); P100 – 13.3±1.8 (20%). Scale bars: A, B (whole mount) – 500 µm; B (histology) – 200 µm.

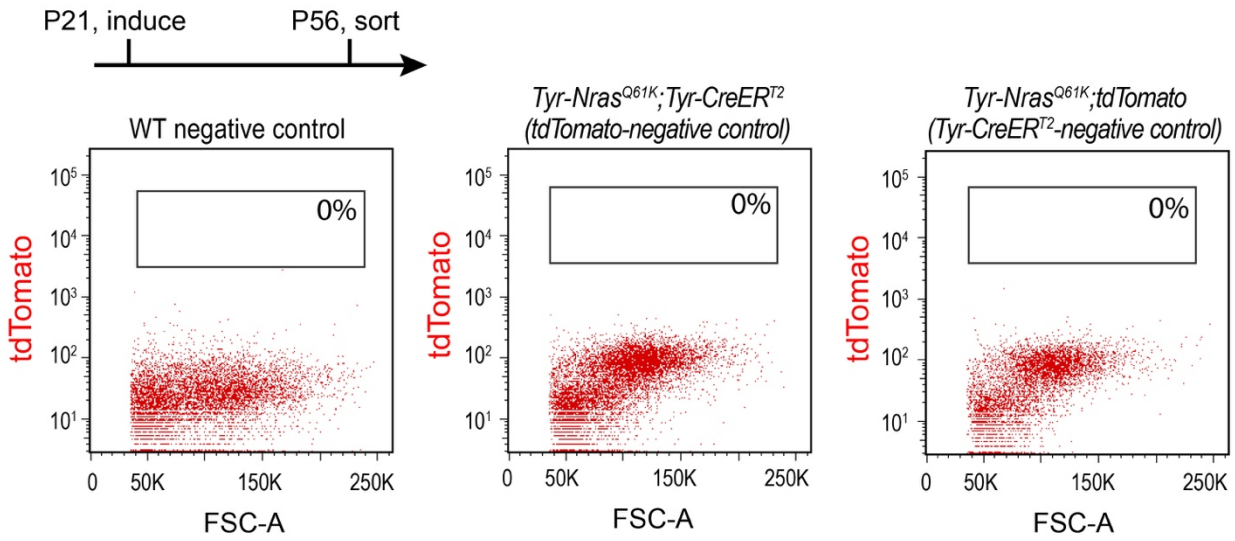


**Figure S6: Negative controls for melanocyte cell lineage sorting strategy.** Representative FACS plots are shown for WT negative control (left), *Tyr-Nras$^{Q61K}$;Tyr-CreER$^{T2}$* negative control (center) and *Tyr-Nras$^{Q61K}$;tdTomato* negative control (right). In all cases, mice were tamoxifen-induced at P21 and skin cells were analyzed at P56. As expected, no tdTomato$^{+}$ cells were detected in all controls.

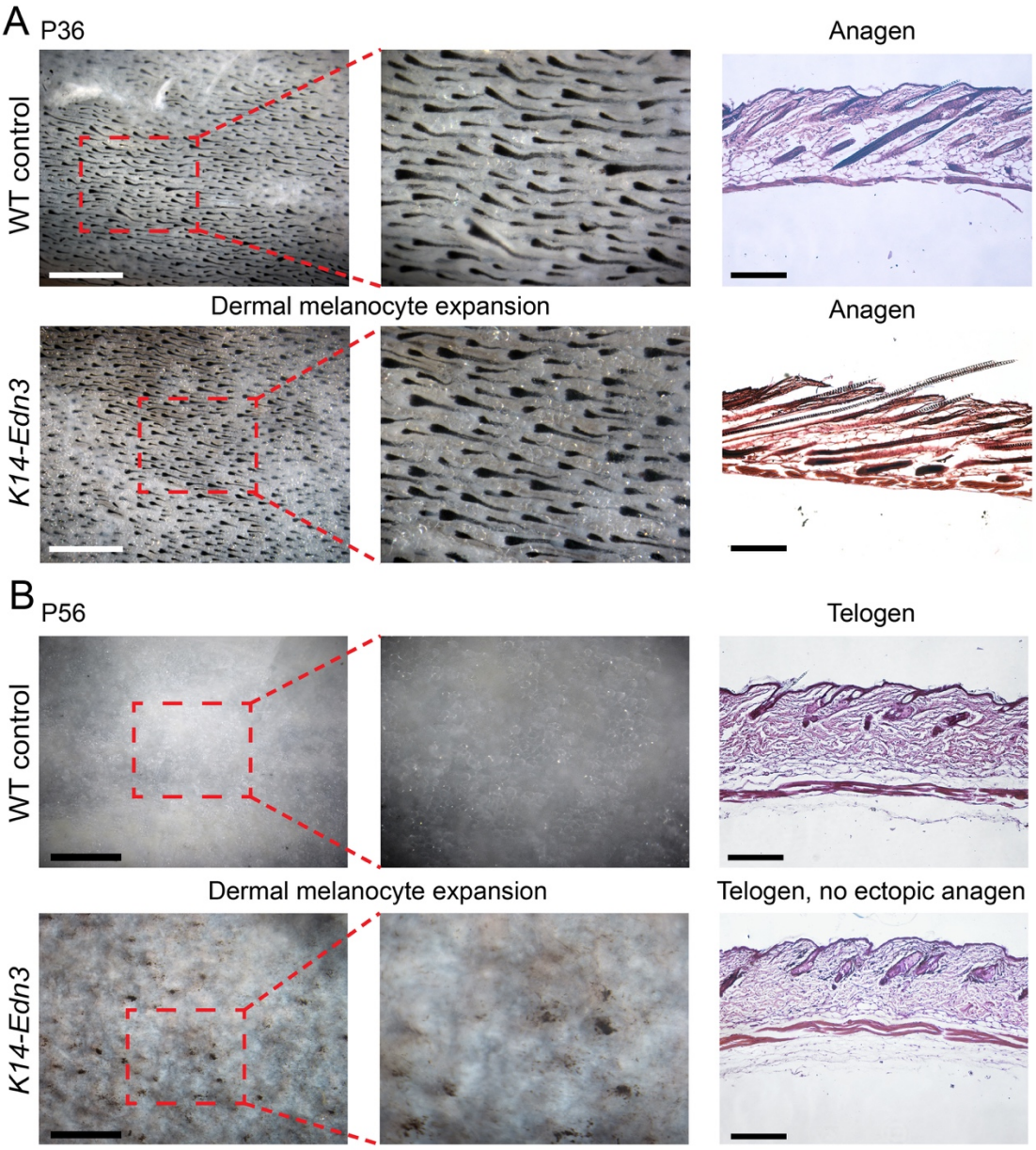


**Figure S7: *K14-Edn3* mouse model for non-senescent melanocyte expansion displays a normal hair cycle.** Similar to control mice, *K14-Edn3* mice with dermal melanocyte expansion are in synchronized anagen at P36 **(A)** and synchronized telogen at P56 **(B)**. Scale bars: A, B (whole mount) – 1 mm; A, B (histology) – 200 µm.

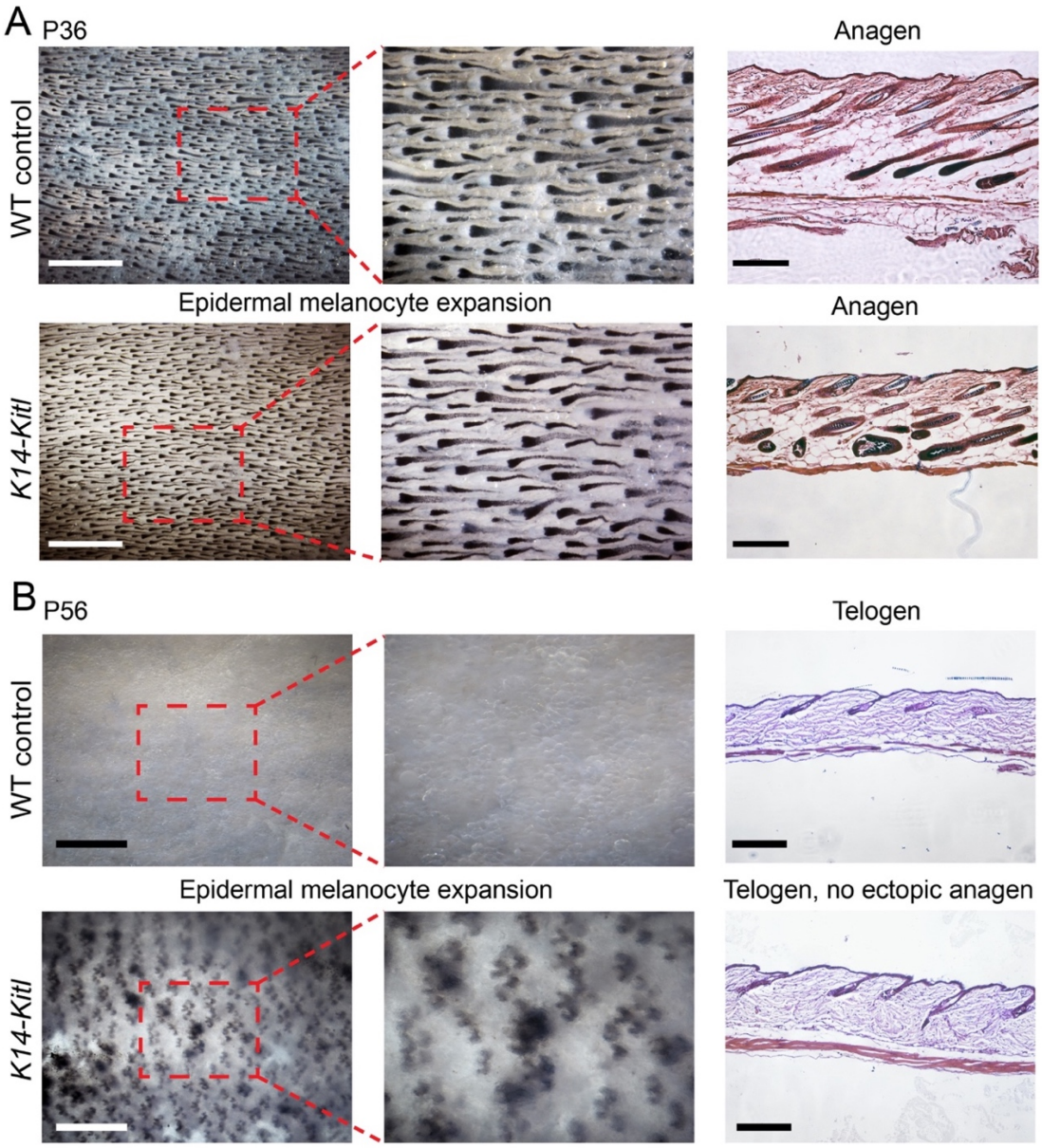


**Figure S8: *K14-Kitl* mouse model for non-senescent melanocyte expansion displays a normal hair cycle.** Similar to control mice, *K14-Kitl* mice with epidermal melanocyte expansion are in synchronized anagen at P36 **(A)** and synchronized telogen at P56 **(B)**. Scale bars: A, B (whole mount) – 1 mm; A, B (histology) – 200 µm.

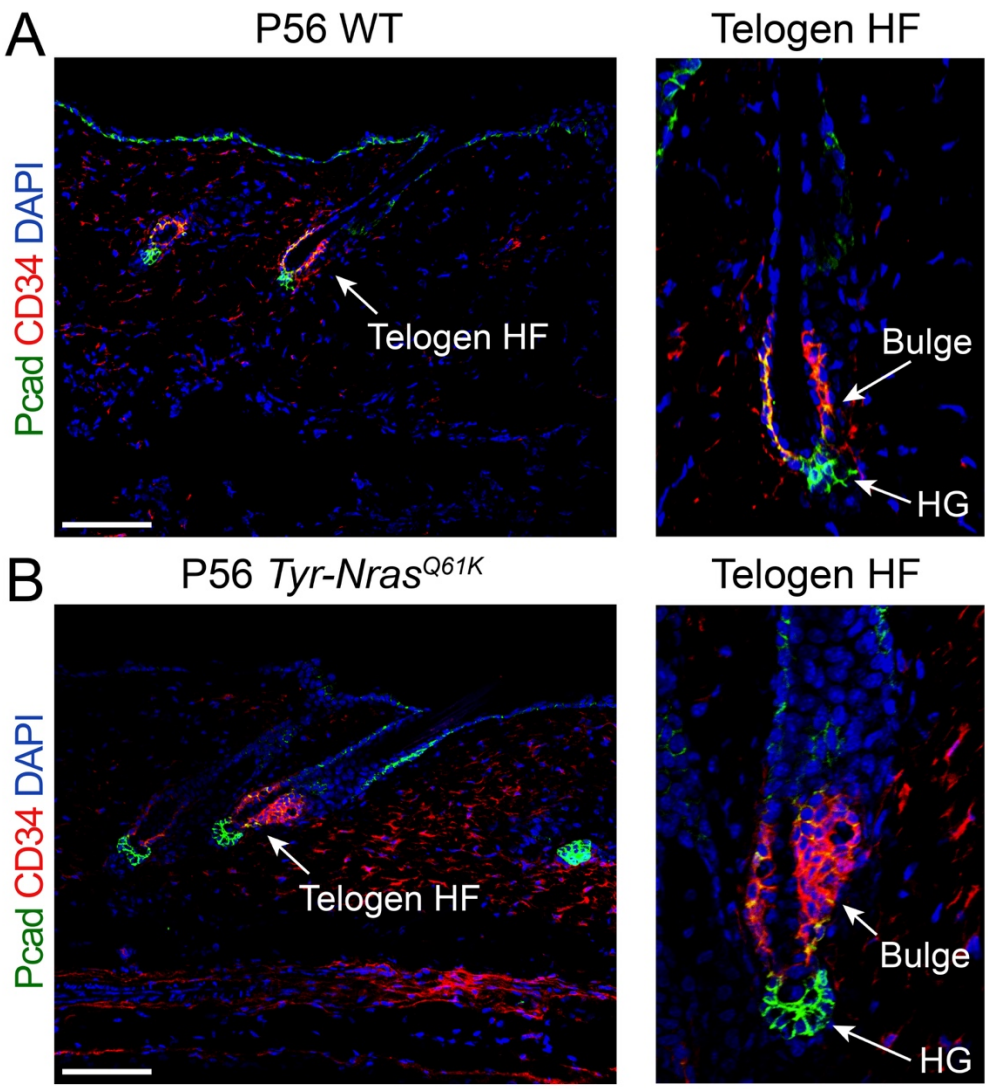


**Figure S9: *Tyr-Nras*$^{Q61K}$ telogen hair follicles maintain normal expression patterns of bulge and hair germ markers.** Co-immunostaining for CD34 (red) and Pcad (green) showed that their expression pattern in *Tyr-Nras*$^{Q61K}$ telogen HFs **(B)** is consistent with that in WT telogen HFs **(A)** – bulge is CD34$^{+}$ and Pcad$^{low}$, while hair germ (HG) is CD34$^{neg}$ and Pcad$^{high}$. Scale bars: A, B – 100 µm.

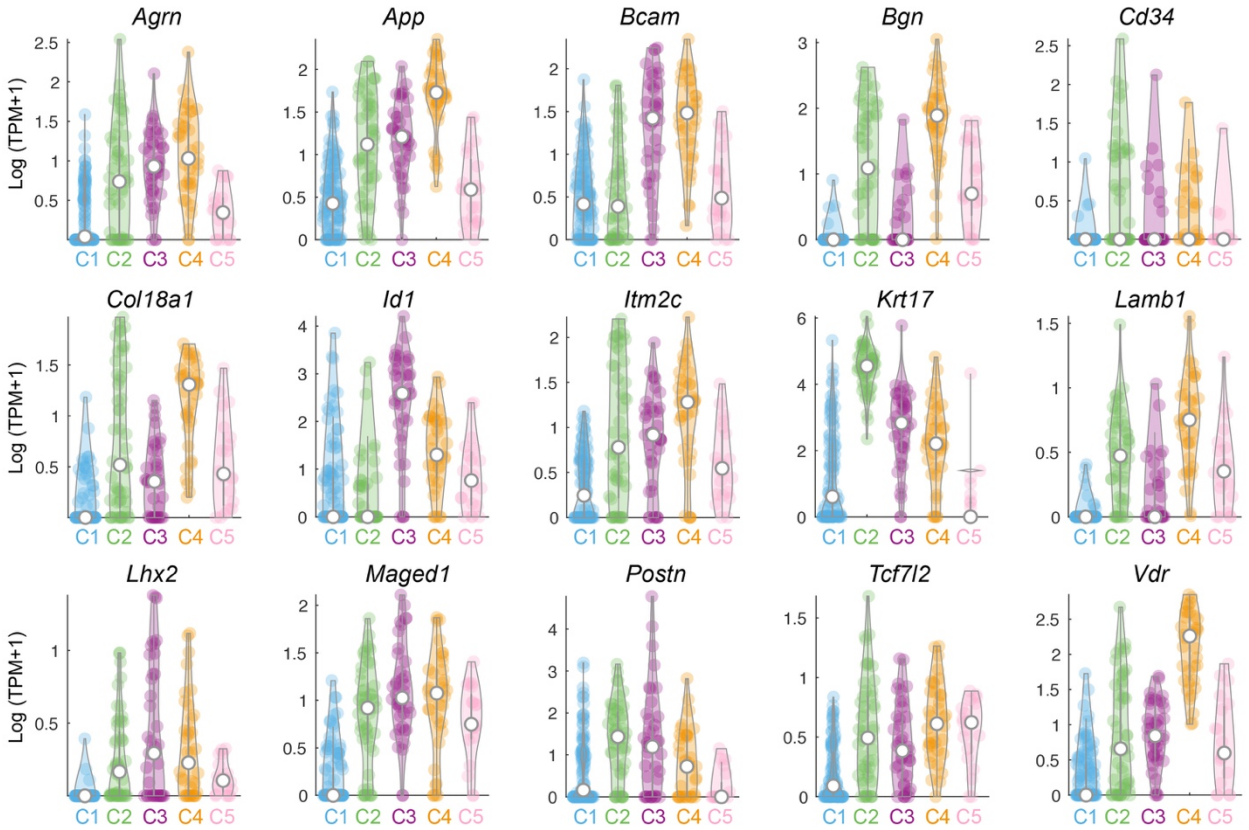


**Figure S10: Expression patterns of outer bulge markers on single-cell RNA-seq.** Violin plots for established outer bulge markers are shown. Cell clusters are color-coded according to main Figure 3F and are as follows: C1 – inner bulge cells, present in P30 and P56 WT samples and in P56 *Tyr-Nras*$^{Q61K}$ sample; C2 – anagen-specific outer bulge cells, present in P30 WT and P56 *Tyr-Nras*$^{Q61K}$ samples; C3 – telogen-specific outer bulge cells, present in P56 WT sample; C4 and C5 – outer bulge cells specific to *Tyr-Nras*$^{Q61}$ sample. Markers show enriched expression in outer bulge clusters C2, C3 and C4. Mutant C5 cluster, which is enriched for G2/M cells, shows variable marker expression. Normalized expression is shown along the Y-axis.

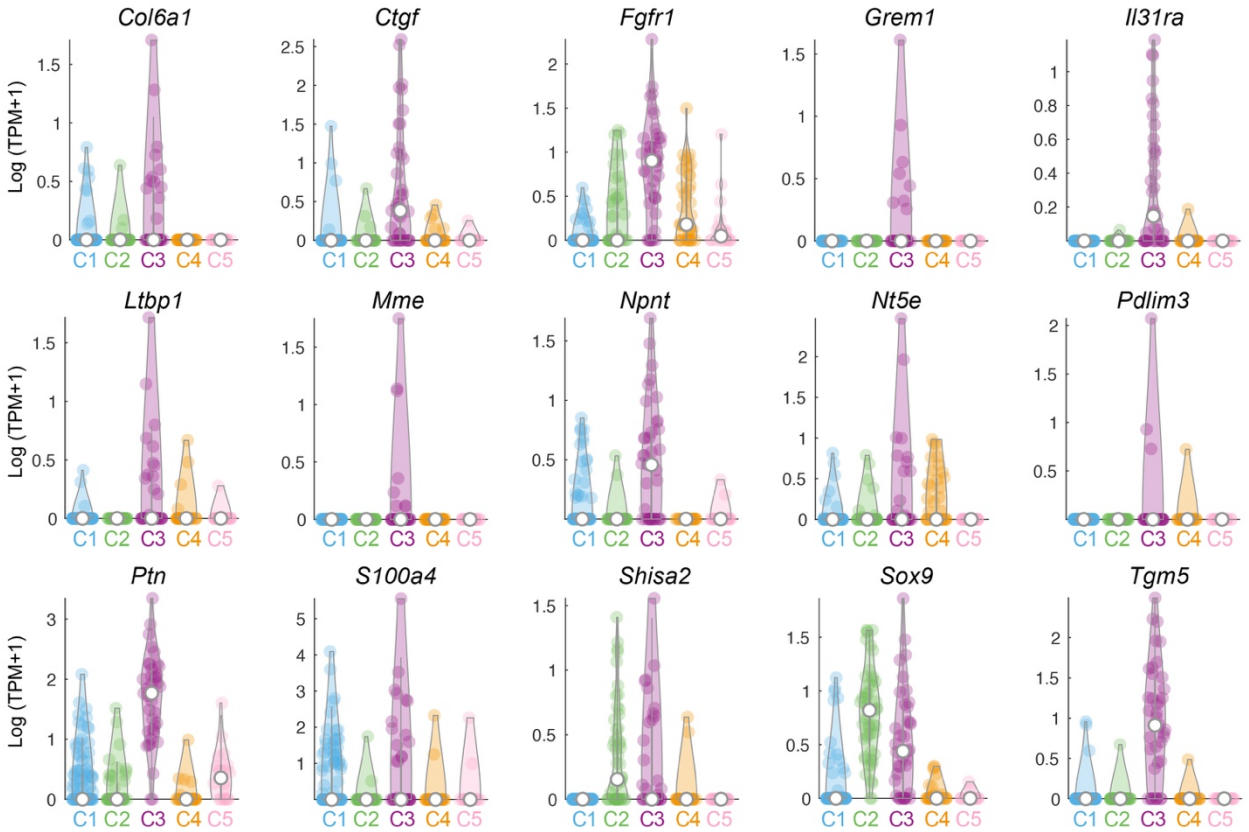


**Figure S11: Expression patterns of telogen-phase outer bulge markers on single-cell RNA-seq.** Violin plots for telogen-phase outer bulge markers are shown. Cell clusters are color-coded according to main Figure 3F and are as follows: C1 – inner bulge cells, present in P30 and P56 WT samples and in P56 *Tyr-Nras*$^{Q61K}$ sample; C2 – anagen-specific outer bulge cells, present in P30 WT and P56 *Tyr-Nras*$^{Q61K}$ samples; C3 – telogen-specific outer bulge cells, present in P56 WT sample; C4 and C5 – outer bulge cells specific to *Tyr-Nras*$^{Q61}$ sample. Markers show enriched expression in telogen-specific WT outer bulge cluster C3 and are depleted from anagen-specific outer bulge cluster C2 and from mutant-specific outer bulge clusters C4 and C5. Normalized expression is shown along the Y-axis.

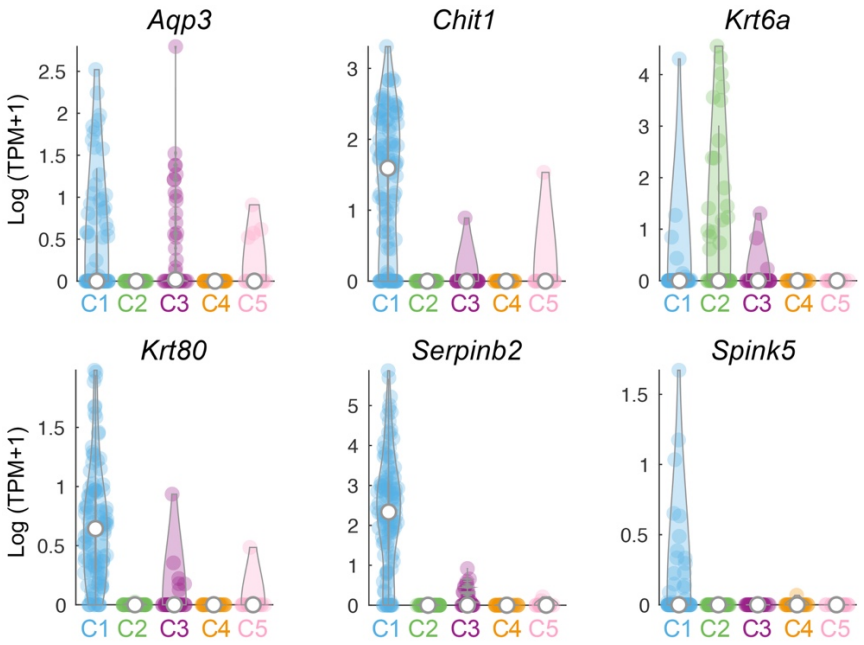


**Figure S12: Expression patterns of inner bulge markers on single-cell RNA-seq.** Violin plots for established inner bulge markers are shown. Cell clusters are color-coded according to main Figure 3F and are as follows: C1 – inner bulge cells, present in P30 and P56 WT samples and in P56 *Tyr-Nras*$^{Q61K}$ sample; C2 – anagen-specific outer bulge cells, present in P30 WT and P56 *Tyr-Nras*$^{Q61K}$ samples; C3 – telogen-specific outer bulge cells, present in P56 WT sample; C4 and C5 – outer bulge cells specific to *Tyr-Nras*$^{Q61}$ sample. Markers show enriched expression in inner bulge cluster C1. Normalized expression is shown along the Y-axis.

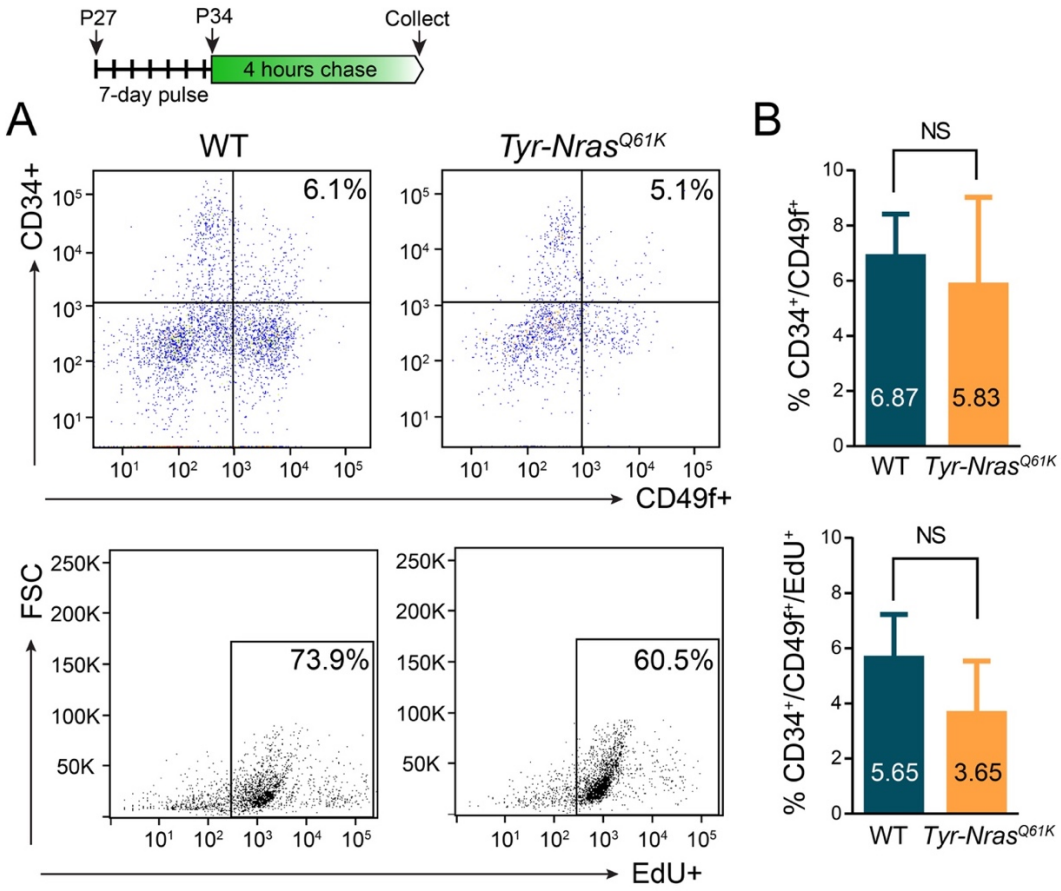


**Figure S13: EdU-labeling efficiency for bulge stem cells is consistent between WT control and *Tyr-Nras*$^{Q61K}$ mice. (A)** Representative FACS plots for EdU$^{+}$ bulge stem cells are shown for P34 WT control (left) and *Tyr-Nras*$^{Q61K}$ mice (right) following 4 hrs of chase after 7 days of daily EdU administration. **(B)** Quantification of all bulge stem cells (top) as well as EdU+ bulge stem cells (bottom) reveals lack of significant differences in labeling efficiency between WT control (blue) and *Tyr-Nras*$^{Q61K}$ mice (orange).

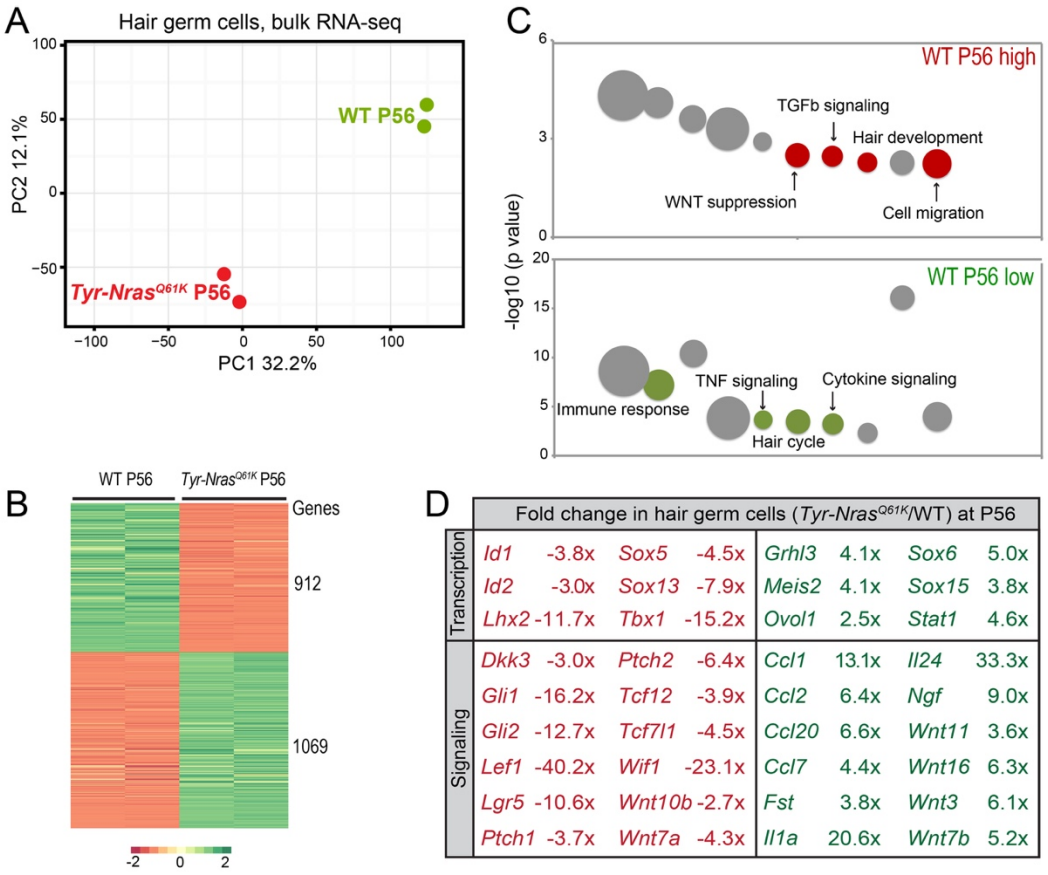


**Figure S14: Gene expression changes in *Tyr-Nras*$^{Q61K}$ hair germ progenitors. (A, B)** Bulk RNA-seq analysis on P56 hair germ progenitor cells revealed prominent differences between *Tyr-Nras*$^{Q61K}$ and WT control mice. PCA is shown on **(A)** and heatmap of differentially expressed genes on **(B)**. WT samples are color-coded green and *Tyr-Nras*$^{Q61K}$ samples – red. Multiple downregulated and upregulated genes were identified and are listed in Table S4. **(C)** Bubble charts showing differentially enriched (red) and depleted (green) gene ontology terms in P56 WT hair germ cells. Selected bubbles are colored and annotated. Also see Table S4. **(D)** Selected transcription and signaling factors differentially expressed between P56 *Tyr-Nras*$^{Q61K}$ and WT hair germ cells are shown. Genes downregulated and upregulated in *Tyr-Nras*$^{Q61K}$ hair germ cells are shown in red and green respectively. Expression level fold change is indicated for each gene.

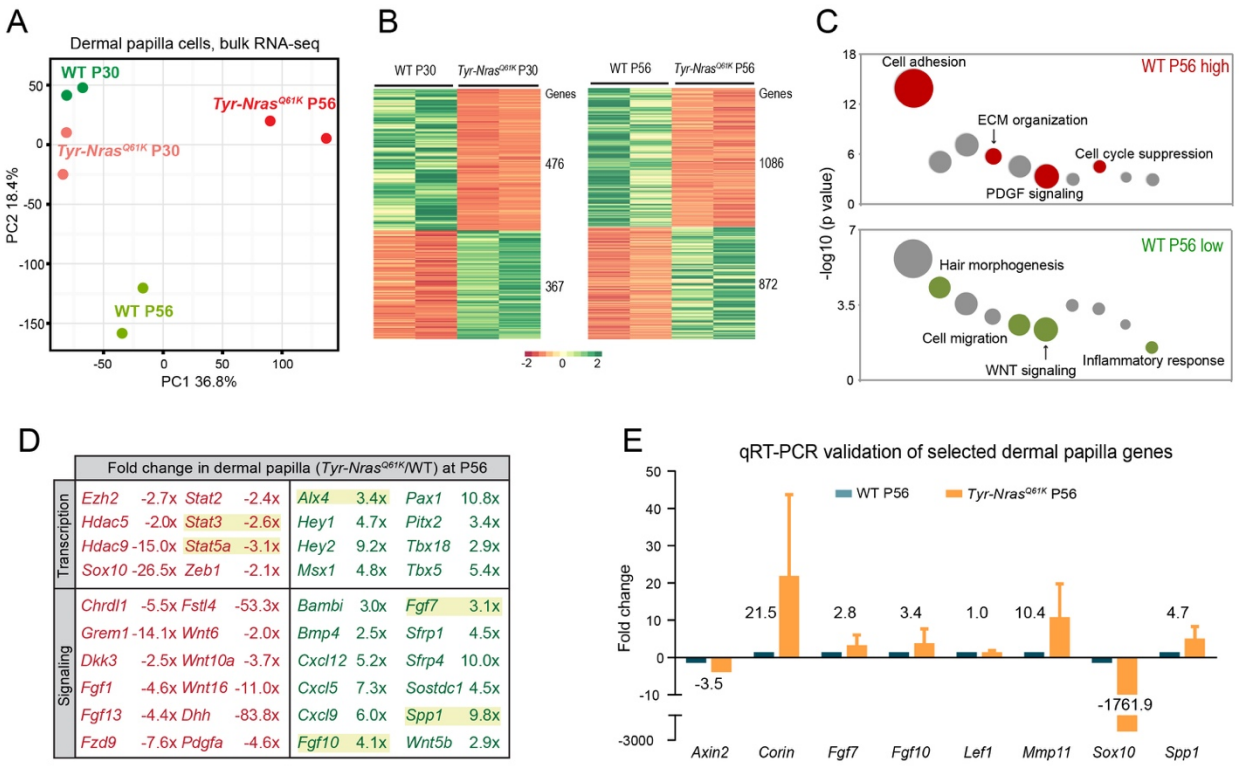


**Figure S15: Gene expression changes in *Tyr-Nras$^{Q61K}$* dermal papilla cells. (A, B)** Bulk RNA-seq analysis on dermal papilla cells revealed prominent differences between *Tyr-Nras$^{Q61K}$* and WT control mice both at P30, when control hair follicles are in synchronous anagen, and at P56, when control hair follicles are in synchronous telogen. PCA is shown on **(A)** and heatmap of differentially expressed genes on **(B)**. WT samples are color-coded green and *Tyr-Nras$^{Q61K}$* samples – red. Multiple downregulated and upregulated genes were identified at both time points and are listed in Table S5. **(C)** Bubble charts showing differentially enriched (red) and depleted (green) gene ontology terms in P56 WT dermal papilla cells. Selected bubbles are colored and annotated. Also see Table S5. **(D)** Selected transcription and signaling factors differentially expressed between P56 *Tyr-Nras$^{Q61K}$* and P56 WT dermal papilla cells are shown. Genes downregulated and upregulated in P56 *Tyr-Nras$^{Q61K}$* dermal papilla cells are shown in red and green respectively. Expression level fold change is indicated for each gene. Selected genes are highlighted with yellow. **(E)** qRT-PCR validation of eight selected differentially expressed genes from bulk RNA-seq data on P56 dermal papilla cells. Relative fold change in *Tyr-Nras$^{Q61K}$ vs.* WT control samples is shown.

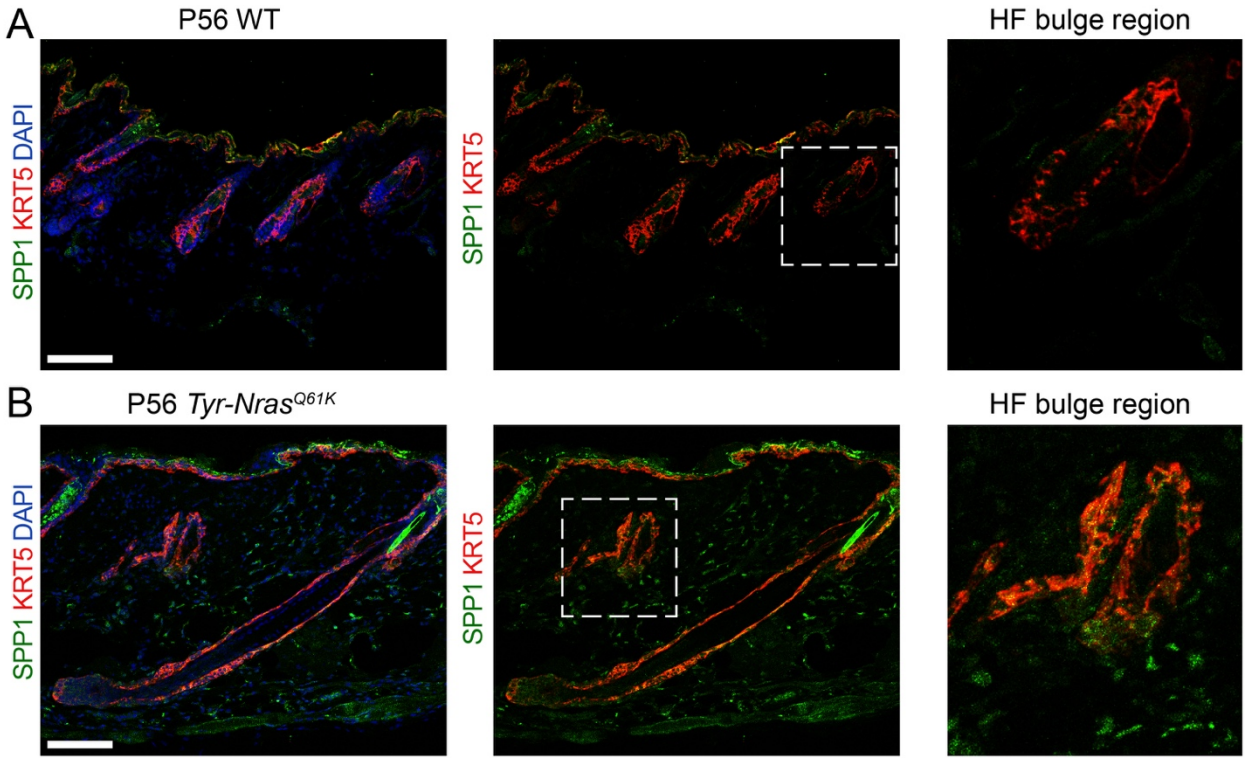


**Figure S16: SPP1 expression is increased in *Tyr-Nras*$^{Q61K}$ nevus skin.** Co-immunostaining for KRT5 (red) and SPP1 (green) in P56 WT (top panels) and *Tyr-Nras*$^{Q61K}$ skin (bottom panels). *Tyr-Nras*$^{Q61K}$ skin shows prominently increased SPP1 expression in the dermal compartment, including around the hair follicle bulges (inserts). Scale bars: A, B – 100 µm.

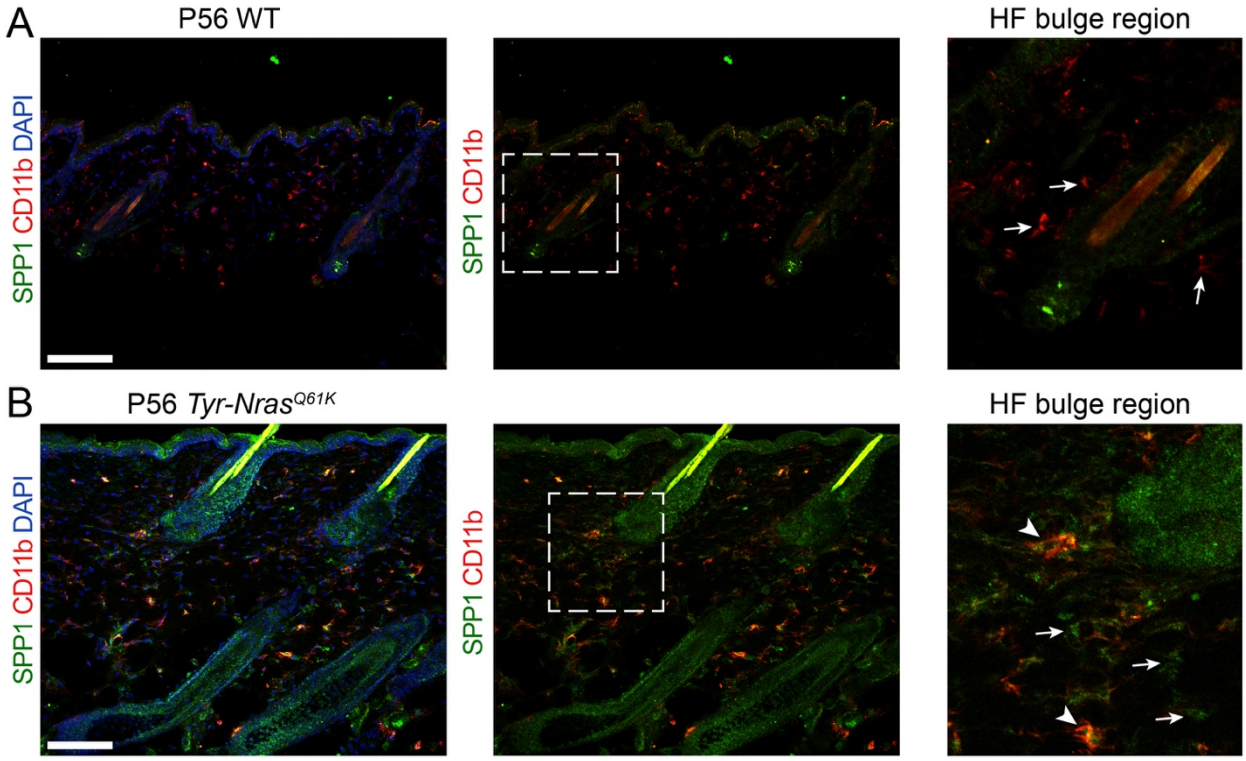


**Figure S17: SPP1 expression is increased in myeloid cells in *Tyr-Nras*$^{Q61K}$ nevus skin.** Co-immunostaining for CD11b (red) and SPP1 (green) in P56 WT (top panels) and *Tyr-Nras*$^{Q61K}$ skin (bottom panels). *Tyr-Nras*$^{Q61K}$ skin shows prominently increased SPP1 expression, including in CD11b+ myeloid cells (arrowheads) around the hair follicle bulges (inserts). SPP1$^{neg}$ myeloid cells are marked with arrows. Scale bars: A, B – 100 µm.

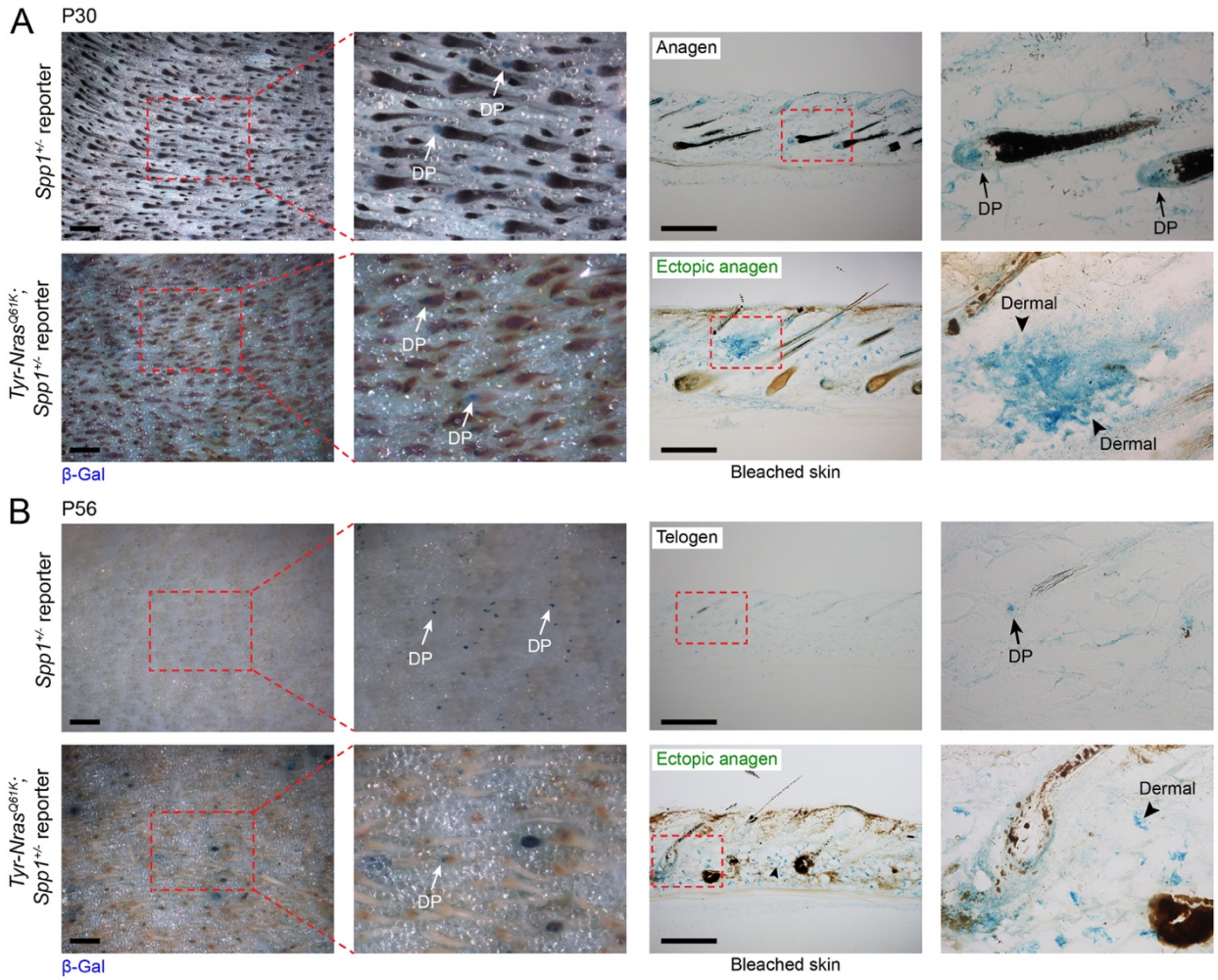


**Figure S18: *Spp1* reporter activity is increased in *Tyr-Nras*$^{Q61K}$ nevus skin. (A, B)** LacZ staining (blue) in *Tyr-Nras*$^{Q61K}$*;Spp1*$^{+/-}$ *vs.* control *Spp1*$^{+/-}$ reporter mice shows a broad increase in the distribution of *Spp1*-expressing skin cells, especially in the dermal compartment both at P30 **(A)** and P56 **(B)**. Dermal and dermal papilla (DP) expression sites are marked. For each panel, whole mount and histology samples are shown on the left and on the right, respectively. Scale bars: A, B (whole mount) – 500 µm; A, B (histology) – 200 µm.

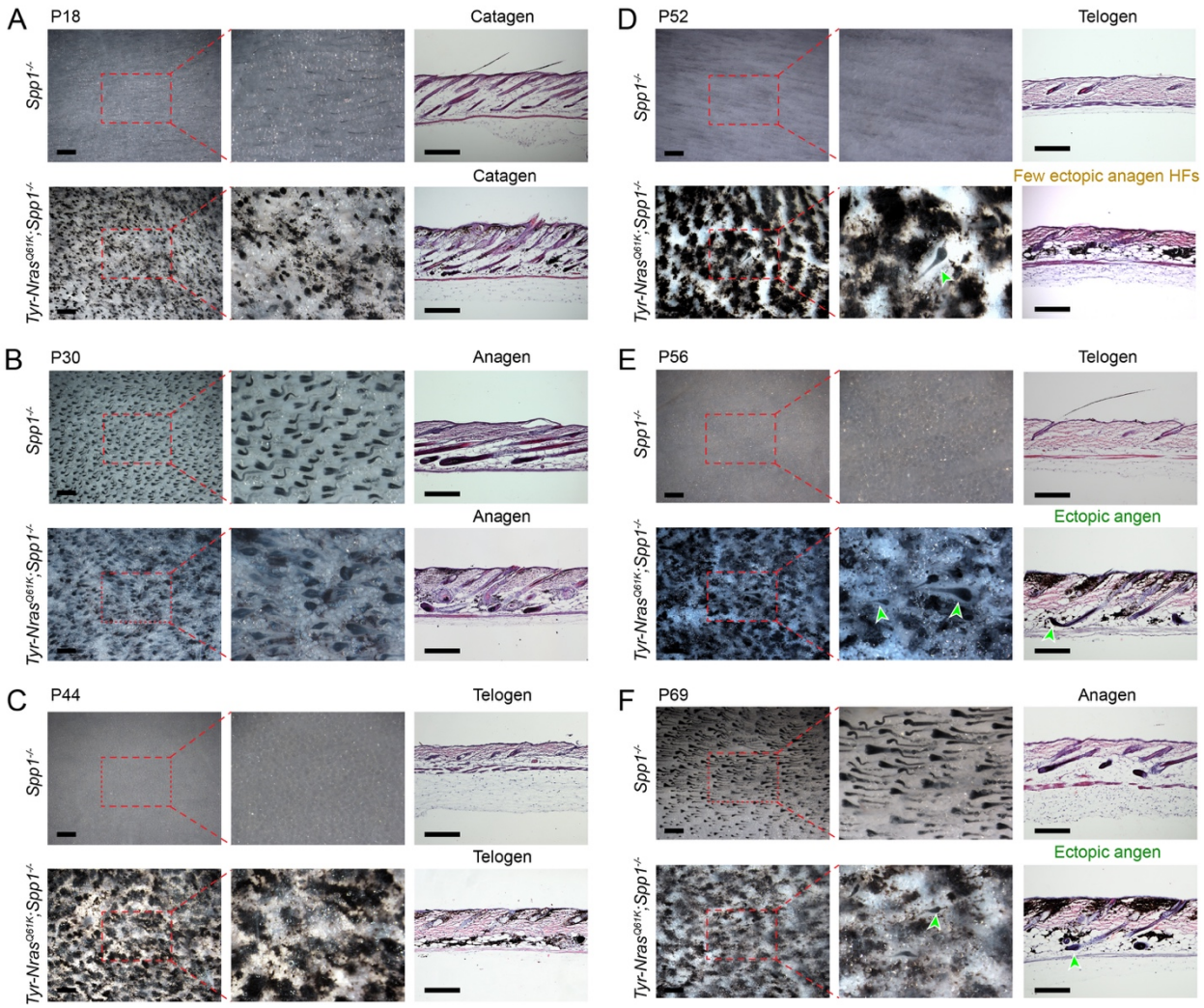


**Figure S19: *Spp1* deletion partially rescues hair cycle quiescence in *Tyr-Nras$^{Q61K}$* mice. (A-F)** *Tyr-Nras$^{Q61K}$;Spp1$^{-/-}$* mice show partial rescue of hair cycle quiescence. Unlike *Tyr-Nras$^{Q61K}$* mice (see Figures 1; S3, S4), *Tyr-Nras$^{Q61K}$;Spp1$^{-/-}$* animals show synchronized first telogen at P23 (see main Figure 4N) and synchronized second telogen at P44 **(C)**. Ectopic hair cycling resumes at P52, albeit at a very low rate **(D)**, and then becomes prominent at P56 **(E)** and P69 **(F)**. For each time point, *Spp1$^{-/-}$* control and *Tyr-Nras$^{Q61K}$;Spp1$^{-/-}$* mutant skin samples are shown. Whole mount samples are shown on the right and histology on the left of each panel. For quantification, see main Figure 4P. Scale bars: A-F (whole mount) – 500 µm; A-F (histology) – 200 µm.

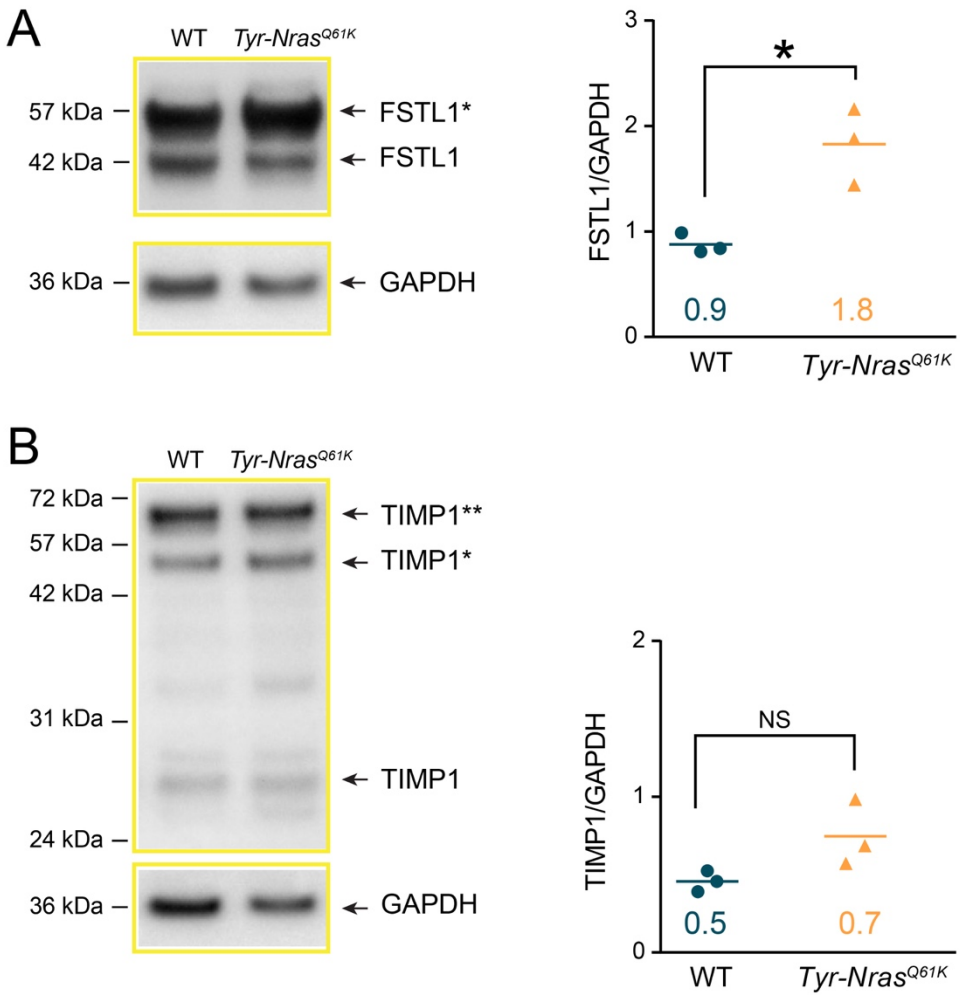


**Figure S20: Western blot measurements of FSTL1 and TIMP1 in *Tyr-Nras$^{Q61K}$* nevus skin.** On western blot, P56 *Tyr-Nras$^{Q61K}$* skin shows increased levels of FSTL1 **(A)**, but not significantly changed levels of TIMP1 compared to P56 WT control **(B)**. On **(A)** and **(B)**, representative western blot images and measurements of optical density relative to GAPDH are shown on the left and right, respectively.

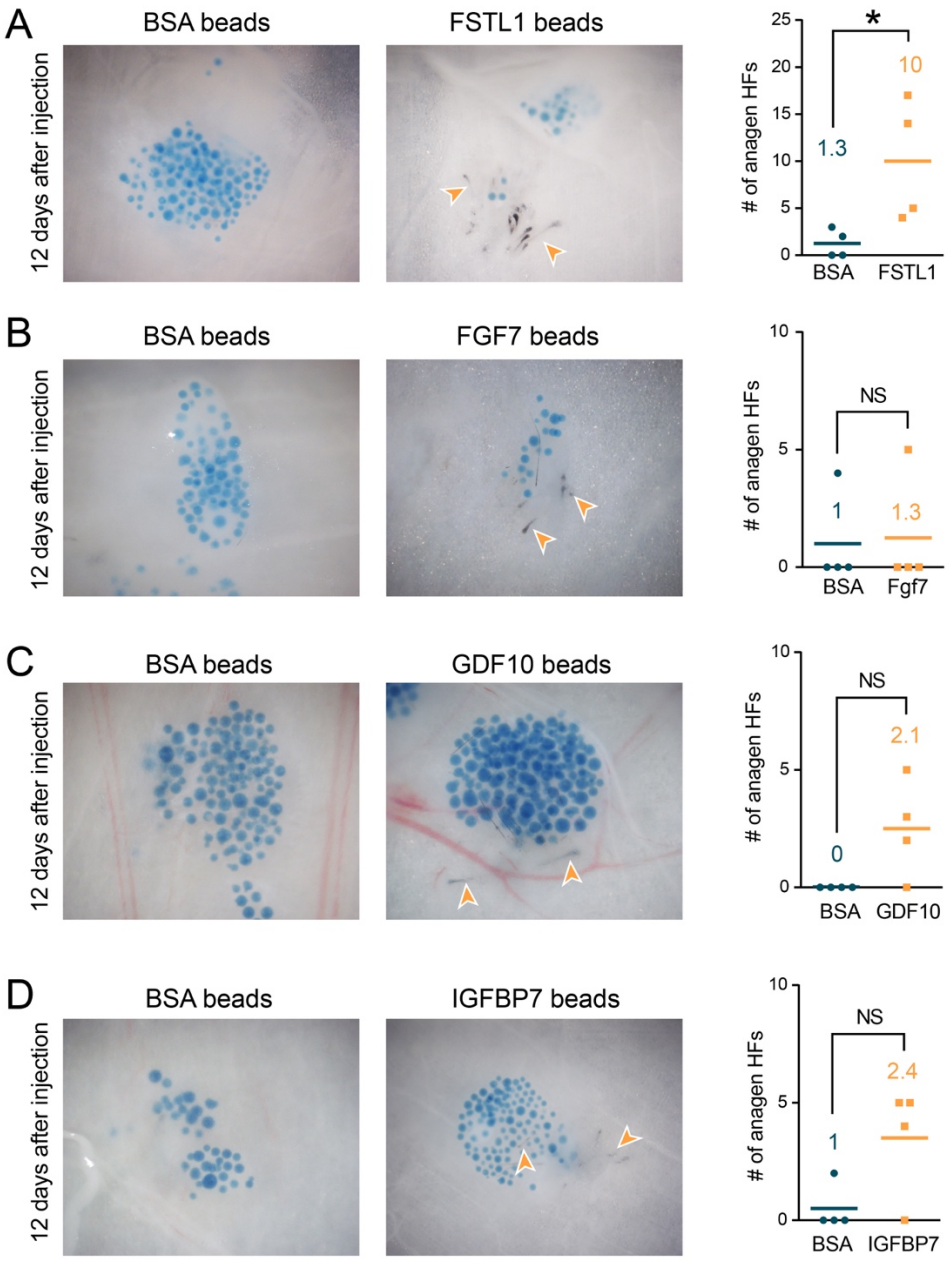


**Figure S21: Assessment of hair growth-stimulating effect of selected nevus secretome factors.** Hair growth stimulating effects of FSTL1 **(A)**, FGF7 **(B)**, GDF10 **(C)** and IGFBP7 **(D)** were tested in recombinant protein-soaked agarose bead micro-injection experiments. For all proteins, hair growth-inducing effect was examined on whole mount 12 days after bead micro-injection and was compared to BSA-soaked beads (negative control). On all panels, representative whole mount images are shown on the left and anagen HF quantification on the right. Anagen HFs are marked with arrowheads. Statistically significant hair growth stimulation was observed for FSTL1.

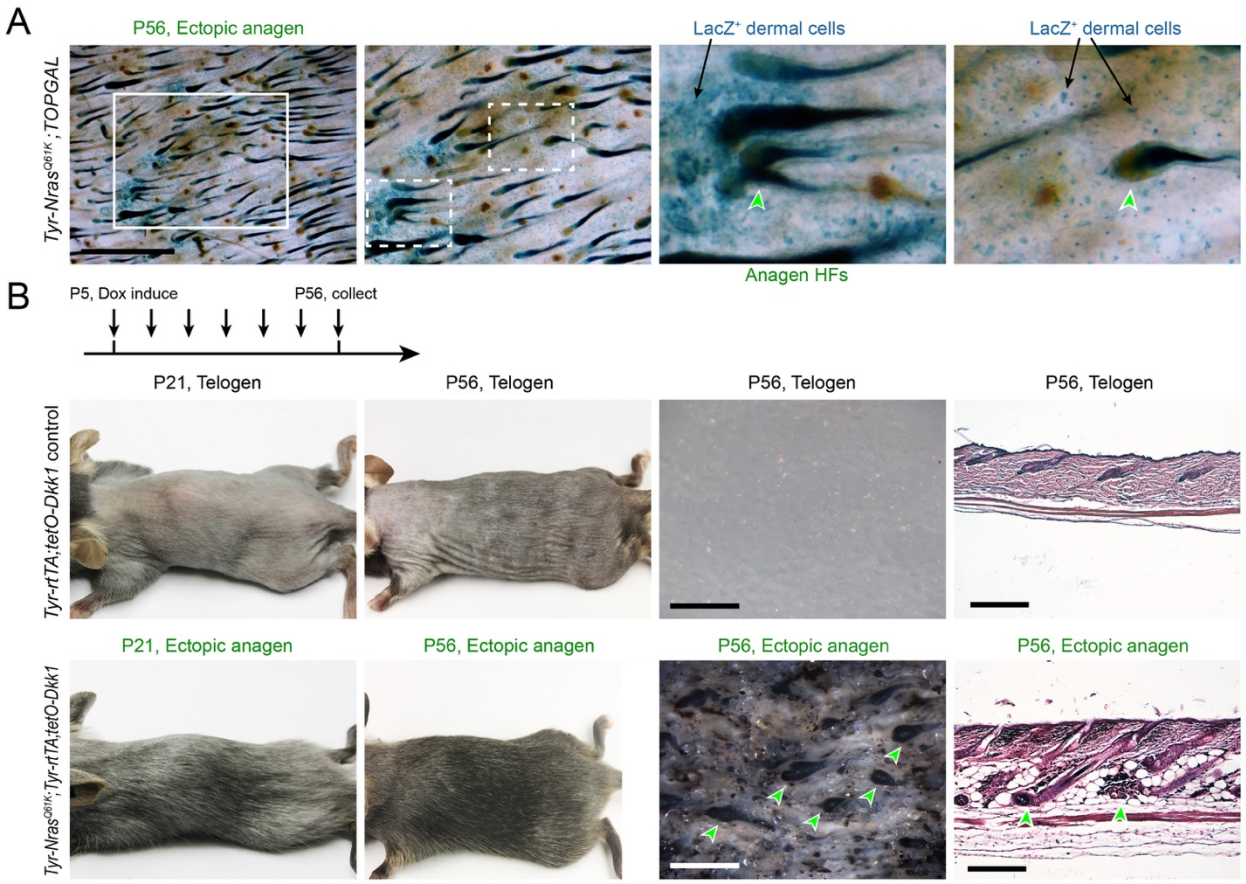


**Figure S22: Reduction in WNT signaling does not rescue hair cycle quiescence in *Tyr-Nras*$^{Q61K}$ mice. (A)** P56 *Tyr-Nras*$^{Q61K}$*;TOPGAL* WNT reporter mice show scattered lacZ-positive dermal cells (blue) as well as foci of lacZ-positive cells. Ectopic anagen HFs are marked with arrowheads. **(B)** Compared to doxycycline-induced *Tyr–rtTA;tetO-Dkk1* mice, inducible activation of DKK1 expression in melanocytes of *Tyr-Nras*$^{Q61K}$*;Tyr–rtTA;tetO-Dkk1* mice did not rescue ectopic hair cycling, characteristic of *Tyr-Nras*$^{Q61K}$ mice (see Figures 1; S3, S4). Mice shown on the left were shaved and photographed at P21 and then at P56. Corresponding P56 skin samples, both whole mount and histology, are shown on the right. Ectopic anagen HFs are marked with arrowheads. Scale bars: A – 2 mm; B (whole mount) – 1 mm; B (histology) – 200 µm.

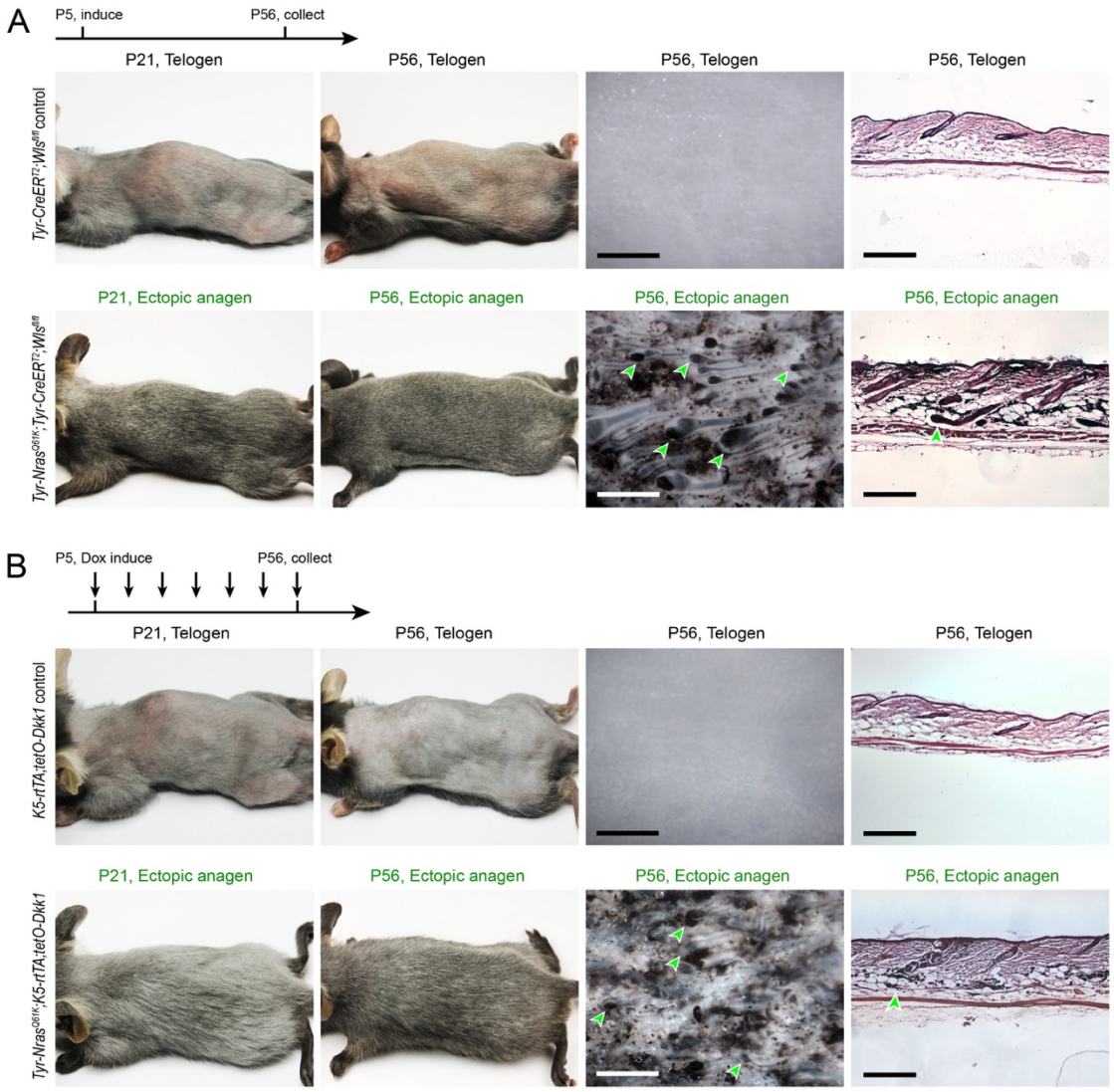


**Figure S23: Reduction in WNT signaling does not rescue hair cycle quiescence in *Tyr-Nras$^{Q61K}$* mice. (A)** Compared to tamoxifen-induced *Tyr-CreER$^{T2}$;Wls$^{fl/fl}$* mice, inducible activation of WLS deletion in *Tyr-Nras$^{Q61K}$;Tyr-CreER$^{T2}$;Wls$^{fl/fl}$* mutant mice did not rescue ectopic hair cycling, characteristic of *Tyr-Nras$^{Q61K}$* mice (see Figures 1; S3, S4). **(B)** Compared to doxycycline-induced *K5-rtTA;tetO-Dkk1* mice, inducible activation of DKK1 expression in skin epithelium of *Tyr-Nras$^{Q61K}$;K5-rtTA;tetO-Dkk1* mice did not rescue ectopic hair cycling. On **(A)** and **(B)**, mice shown on the left were shaved and photographed at P21 and then at P56. Corresponding P56 skin samples, both whole mount and histology, are shown on the right. Ectopic anagen HFs are marked with arrowheads. Scale bars: A, B (whole mount) – 1 mm; A, B (histology) – 200 µm.

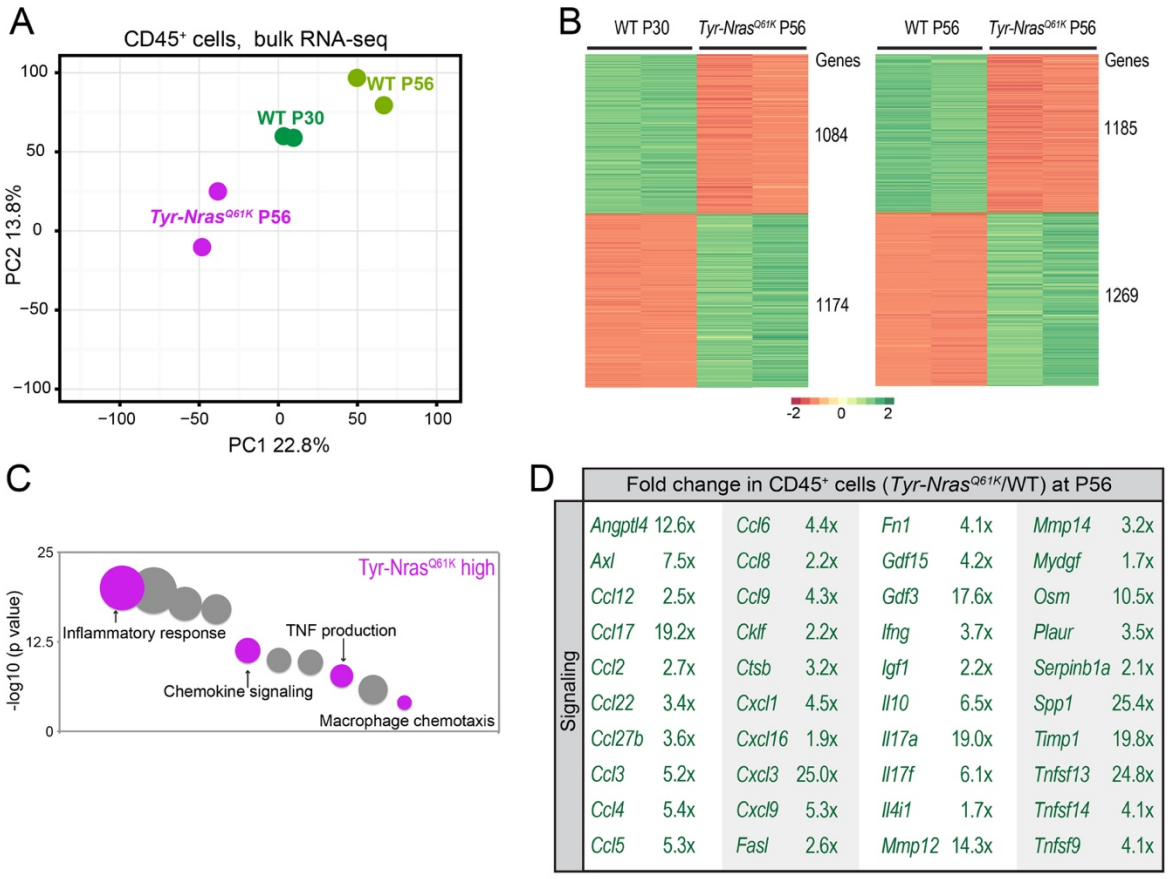


**Figure S24: Gene expression changes in *Tyr-Nras*$^{Q61K}$ CD45-expressing skin cells. (A, B)** Bulk RNA-seq analysis on CD45-expressing skin cells revealed differences between *Tyr-Nras*$^{Q61K}$ and WT control mice. P56 *Tyr-Nras*$^{Q61K}$ cells were compared to both P30 and P56 WT cells. PCA is shown on **(A)** and heatmap of differentially expressed genes on **(B)**. WT samples are color-coded green and *Tyr-Nras*$^{Q61K}$ samples – purple. Multiple downregulated and upregulated genes were identified and are listed in Table S9. **(C)** Bubble chart showing differentially enriched gene ontology terms in *Tyr-Nras*$^{Q61K}$ CD45-expressing skin cells. Selected bubbles are colored and annotated. Also see Table S9. **(D)** Selected signaling factors differentially enriched in P56 *Tyr-Nras*$^{Q61K}$ CD45-expressing skin cells *vs.* P56 WT CD45-expressing skin cells are shown. Expression level fold change is indicated for each gene.

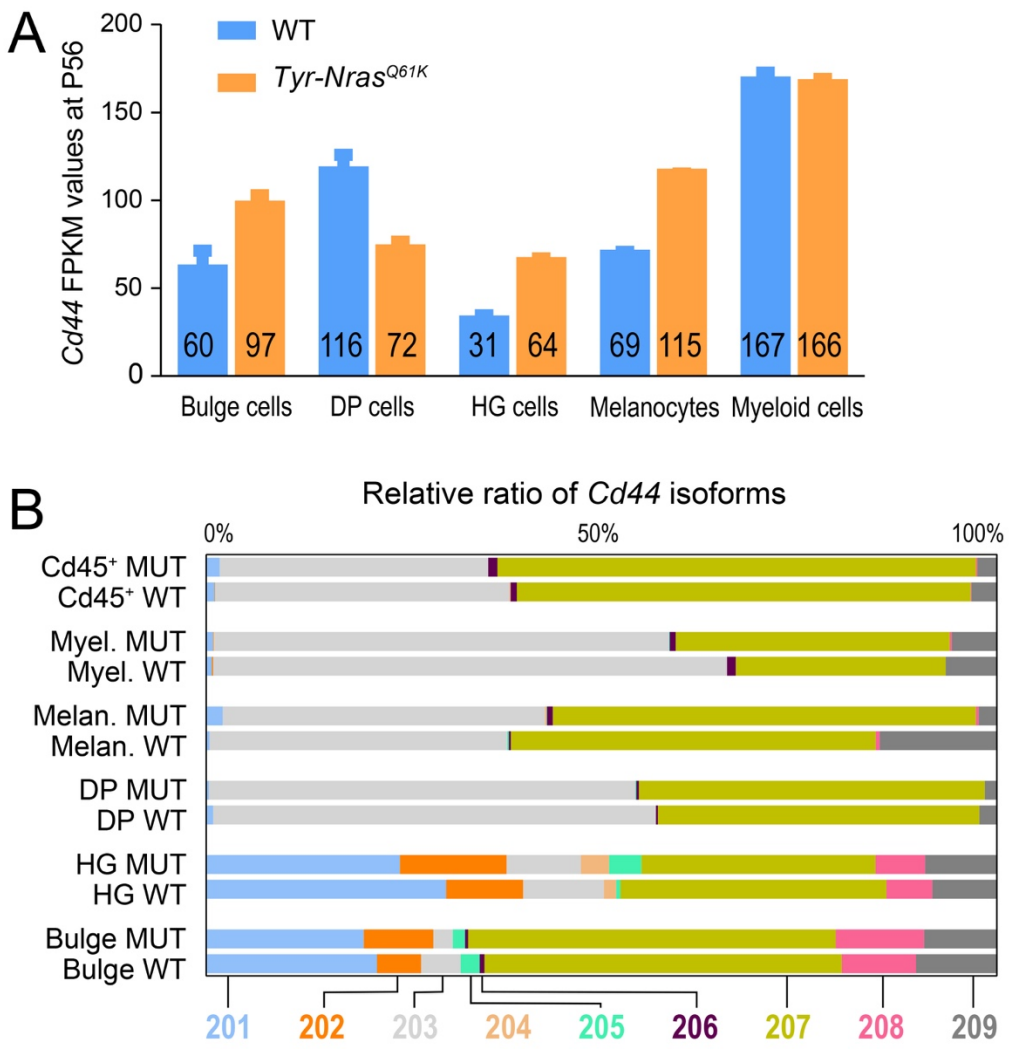


**Figures S25. *Cd44* expression levels and isoform distribution patterns in distinct skin cell types. (A)** *Cd44* is prominently expressed on bulk RNA-seq in tested skin cell types both in P56 WT control (blue) and *Tyr-Nras*$^{Q61K}$ mice (orange). Average *Cd44* FPKM values are shown. DP – dermal papilla, HG – hair germ. **(B)** Relative abundance of *Cd44* isoforms established from full-length bulk RNA-seq. Isoforms are numbered using conventional nomenclature and indicated along the X-axis. Skin cell types are listed along the Y-axis. WT – wild type cells, MUT – *Tyr-Nras*$^{Q61K}$ mutant cells. Bulge and hair germ (HG) cells show distinct isoform distribution patterns from the rest of the skin cell types. They are enriched for isoforms 201, 202, 205 and 208.

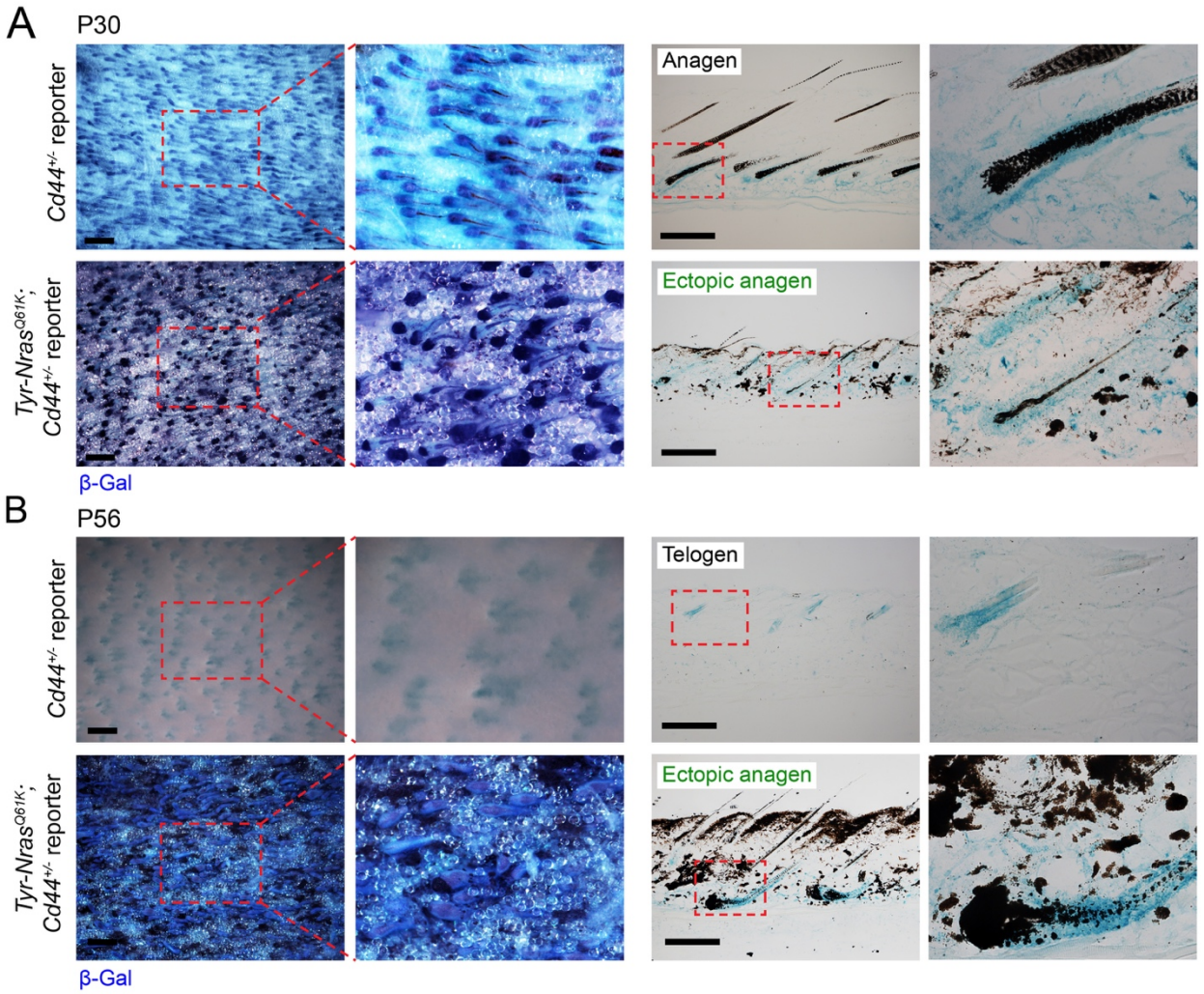


**Figure S26: Reporter activity shows broad distribution of *Cd44* expression in skin. (A, B)** LacZ staining (blue) in *Tyr-Nras$^{Q61K}$;Cd44$^{+/-}$ vs.* control *Cd44$^{+/-}$* reporter mice shows broad distribution of *Cd44*-positive cells in the skin, both in epithelial and dermal compartments, at P30 **(A)** and P56 **(B)**. For each panel, whole mount and histology samples are shown on the left and on the right, respectively. Scale bars: A, B (whole mount) – 500 µm; A, B (histology) – 200 µm.

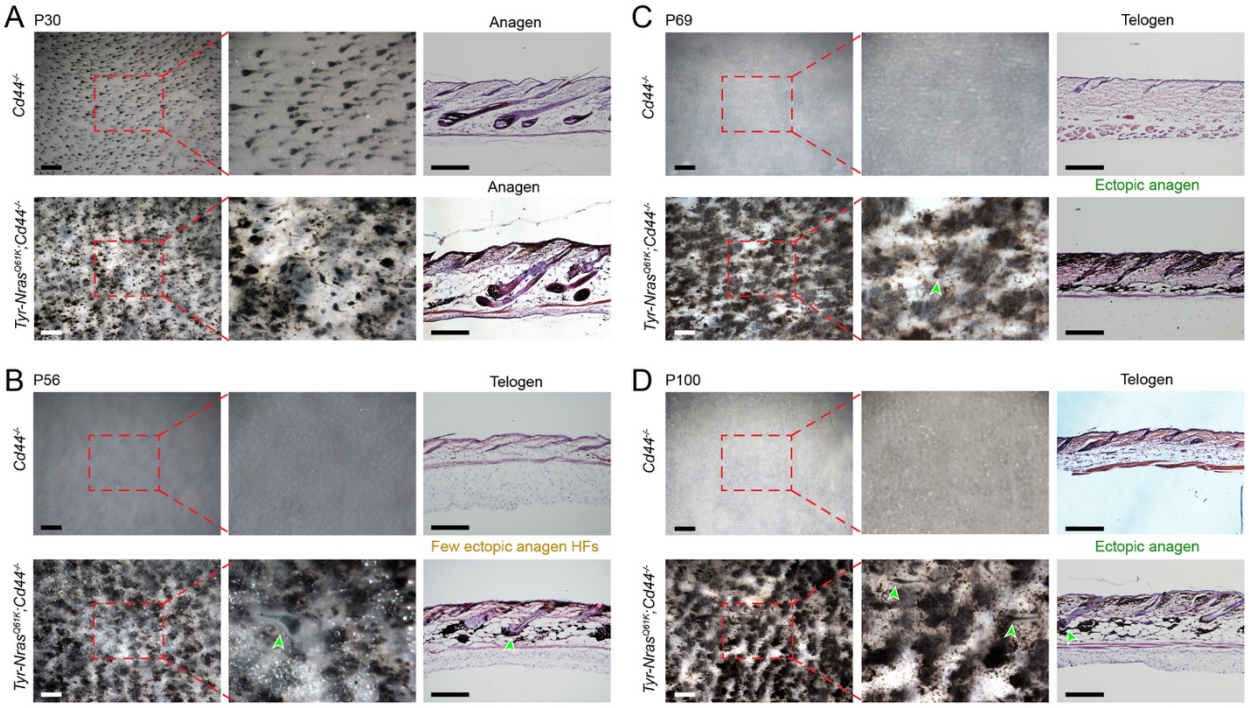


**Figure S27: *Cd44* deletion partially rescues hair cycle quiescence in *Tyr-Nras$^{Q61K}$* mice. (A-D)** *Tyr-Nras$^{Q61K}$;Cd44$^{-/-}$* mice show partial rescue of hair cycle quiescence. Unlike *Tyr-Nras$^{Q61K}$* mice (see Figures 1; S3, S4), *Tyr-Nras$^{Q61K}$;Cd44$^{-/-}$* animals show synchronized second telogen at P44 (see main Figure 6F) and only very occasional ectopic anagen HFs at P52 (see main Figure 6G) and P56 **(B)**. Ectopic anagen HFs become more prevalent on P69 **(C)** and P100 **(D)**. For each time point, *Cd44$^{-/-}$* control and *Tyr-Nras$^{Q61K}$;Cd44$^{-/-}$* mutant skin samples are shown. Whole mount samples are shown on the right and histology on the left of each panel. For quantification, see main Figure 6H. Scale bars: A-D (whole mount) – 500 µm; A-D (histology) – 200 µm.

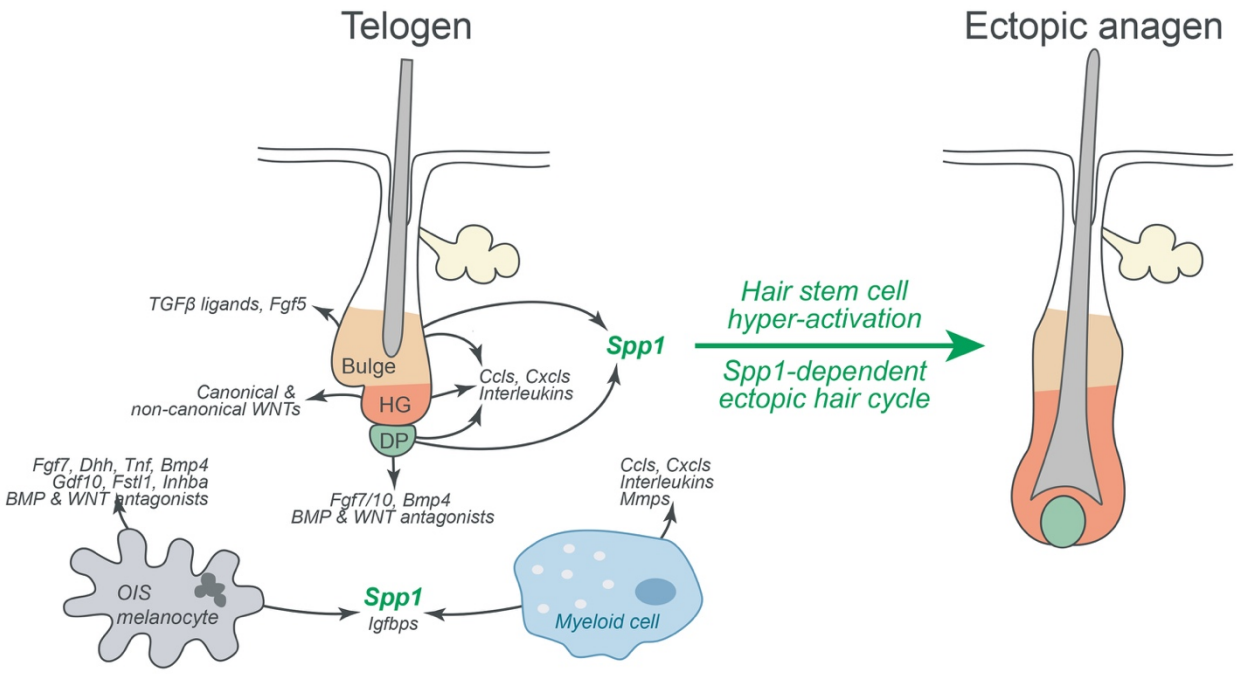


**Figure S28: Model of nevus secretome-induced hair cycle hyper-activation.** Selected secretome factors enriched in key nevus skin cell types are shown: bulge stem cells (yellow), hair germ progenitors (orange), dermal papilla cells (green), melanocytes (grey) and myeloid cells (blue). SPP1, which is prominently over-expressed in nevus skin and is sufficient and necessary to drive hair cycle hyper-activation is highlighted. The latter is dependent on bulge stem cell hyper-activation in telogen hair follicles.

**Supplemental Tables**

**Table S1:** Differential gene expression and GO analysis on bulk RNA-seq data from mouse bulge stem cells.

**Table S2:** Single-cell RNA-seq data from mouse bulge stem cells.

**Table S3:** Marker genes for mouse bulge stem cell clusters from single-cell RNA-seq data.

**Table S4:** Differential gene expression and GO analysis on bulk RNA-seq data from mouse hair germ progenitors.

**Table S5:** Differential gene expression and GO analysis on bulk RNA-seq data from mouse dermal papilla cells.

**Table S6:** Differential gene expression and GO analysis on bulk RNA-seq data from mouse skin melanocyte lineage cells.

**Table S7:** Single-cell RNA-seq data from mouse skin melanocyte lineage cells.

**Table S8:** Marker genes for mouse skin melanocyte lineage cell clusters from single-cell RNA-seq data.

**Table S9:** Differential gene expression and GO analysis on bulk RNA-seq data from mouse skin $CD45^{+}$ hematopoietic cells.

**Table S10:** Differential gene expression and GO analysis on bulk RNA-seq data from mouse skin myeloid cells.

**Table S11:** Single-cell RNA-seq data from mouse skin myeloid cells.

**Table S12:** Marker genes for mouse skin myeloid cell clusters from single-cell RNA-seq data.

**Table S13:** Differential gene expression and GO analysis on bulk RNA-seq data from hairy nevi and adjacent normal facial human skin.

**Table S14:** Primer sequence for real time PCR.

## Supplemental References


Choi, Y.S., Zhang, Y., Xu, M., Yang, Y., Ito, M., Peng, T., Cui, Z., Nagy, A., Hadjantonakis, A.K., Lang, R.A.*, et al.* (2013). Distinct functions for Wnt/beta-catenin in hair follicle stem cell proliferation and survival and interfollicular epidermal homeostasis. Cell stem cell *13*, 720-733.

Greco, V., Chen, T., Rendl, M., Schober, M., Pasolli, H.A., Stokes, N., Dela Cruz-Racelis, J., and Fuchs, E. (2009). A two-step mechanism for stem cell activation during hair regeneration. Cell stem cell *4*, 155-169.

Lien, W.H., Polak, L., Lin, M., Lay, K., Zheng, D., and Fuchs, E. (2014). In vivo transcriptional governance of hair follicle stem cells by canonical Wnt regulators. Nature cell biology *16*, 179-190.

Lowry, W.E., Blanpain, C., Nowak, J.A., Guasch, G., Lewis, L., and Fuchs, E. (2005). Defining the impact of beta-catenin/Tcf transactivation on epithelial stem cells. Genes & development *19*, 1596-1611.

Pawlikowski, J.S., McBryan, T., van Tuyn, J., Drotar, M.E., Hewitt, R.N., Maier, A.B., King, A., Blyth, K., Wu, H., and Adams, P.D. (2013). Wnt signaling potentiates nevogenesis. Proceedings of the National Academy of Sciences of the United States of America *110*, 16009-16014.

Plikus, M.V., Baker, R.E., Chen, C.C., Fare, C., de la Cruz, D., Andl, T., Maini, P.K., Millar, S.E., Widelitz, R., and Chuong, C.M. (2011). Self-organizing and stochastic behaviors during the regeneration of hair stem cells. Science *332*, 586-589.